Vertical load was applied uniformly over the entire top surface of the plate, and the load was increased in increments. For each load increment, the equilibrium state of the problem was determined. Because of the continuously hardening postyield behavior of Titanium Grade 7, equilibrium could be achieved for any vertical load. However, at a certain load level, the region of the plate between the stiffener and the support over the legs snaps through. Usually, the failure criteria for Titanium Grade 7 are reached when the plate snaps through, indicating that the plates would tear at the contact with the bulkheads or longitudinal stiffeners.

6.4.3.1.3 Damage and Failure Criteria

As was discussed in Section 6.2.1, the damage area is defined as the area on the inner and outer surfaces of the drip shield plate where the residual tensile stresses or the stresses due to long-term load exceed the threshold of 80% of the yield strength for Titanium Grade 7 at 60°C (253 MPa). The damage areas on the inner and outer surfaces are added irrespective of their geometrical relation and potential overlap, although the overlapping surfaces should not be counted twice. Stress contours and damage areas for 10-mm-thick plate, Case 2 boundary conditions, and a pressure of 1,620 kPa are illustrated in Figure 6-40. The drip shield plots in this figure are oriented similarly to those in Figure 6-39. The symmetry planes are along the closer (or lower in the presented view) and the left edge.

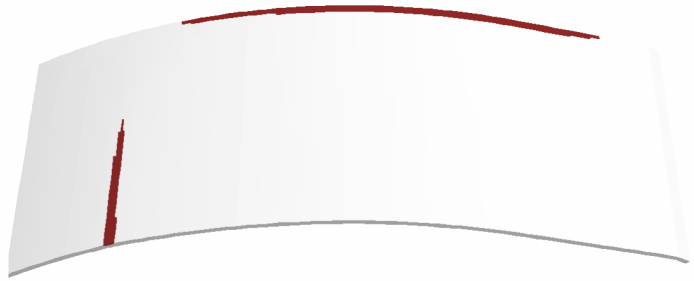

a) Damage Areas

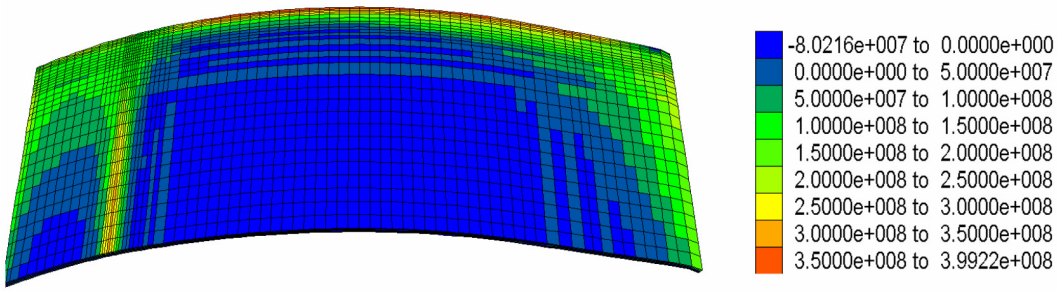

b) Maximum Stress (Pa) Contours

Output DTN: MO0701DRIPSHLD.000, file *\case2\10mm\plate-1.6200e+006.sav*.

NOTES: The damage area is the inner or outer surface of the drip shield plate with maximum stress greater than 80% of the yield strength of Titanium Grade 7. Damage area is shown in brown color. Compressive stresses are negative.

Figure 6-40. Damage Areas and Maximum Stress Contours in the 10-mm-Thick Drip Shield Plate for Case 2 Boundary Conditions and a Pressure of 1,620 kPa

Criteria based on both accumulated plastic strain and maximum stress were used to determine the plate failure. The plate failure load was considered to be the smaller load that indicated plate failure from either of two criteria. If either failure criterion is reached anywhere in the simulated domain (i.e., in any element of the numerical representation), the plate is considered to fail.

When the Titanium Grade 7 failure criterion based on ultimate strain is checked, the maximum plastic shear strain (used as a hardening parameter in FLAC3D calculations) is multiplied by $\sqrt{4/3}$ and then compared with ultimate plastic strain, ε_{up}, from Table 6-134. (The plastic shear strain, which is the time integral of the square root of the second invariant of deviatoric strain rate, is multiplied by $\sqrt{4/3}$ to be equivalent to effective strain. More discussion on this topic is provided in Section 6.5.1.2.3.)

Yielding of the Tresca material is controlled by the maximum principal stress difference, $(\sigma_1 - \sigma_3)$, not by the magnitude of the major principal stress, σ_1. Under uniaxial stress conditions, the minor principal stress, σ_3, is zero, and the maximum principal stress, the maximum deviatoric stress, and the Tresca criterion are equivalent. Under general triaxial stress conditions, the Tresca criterion can indicate material failure when the maximum principal stress is either smaller (if σ_3 is compressive) or greater (if σ_3 is tensile) than the ultimate tensile strength. The plate was considered to fail when either the maximum tensile stress or the tensile stress difference reached the rupture strength of the material.

Failure criteria based on maximum stress difference and strain are equivalent. For example, contours of maximum principal stress for Case 2 boundary conditions and for a 5-mm-thick plate loaded by a vertical pressure of 860 kPa are shown in Figure 6-41. The maximum stress at the support above the bulkhead (434 MPa) exceeds the tensile strength of 396 MPa. However, the effective strain is less than the rupture strain of Titanium Grade 7. The rupture strain is exceeded in the next load increment, as indicated in Figure 6-42, which is a contour plot of plastic shear strain at a vertical stress of 880 kPa. At this load level, the plate snaps through. The effect of the boundary conditions at the support above the bulkhead can also be seen in Figure 6-42. Because the plate is not restrained in the lateral direction, it moves considerably inward in failure state.

Fracture initiation and propagation through the plates were not analyzed.

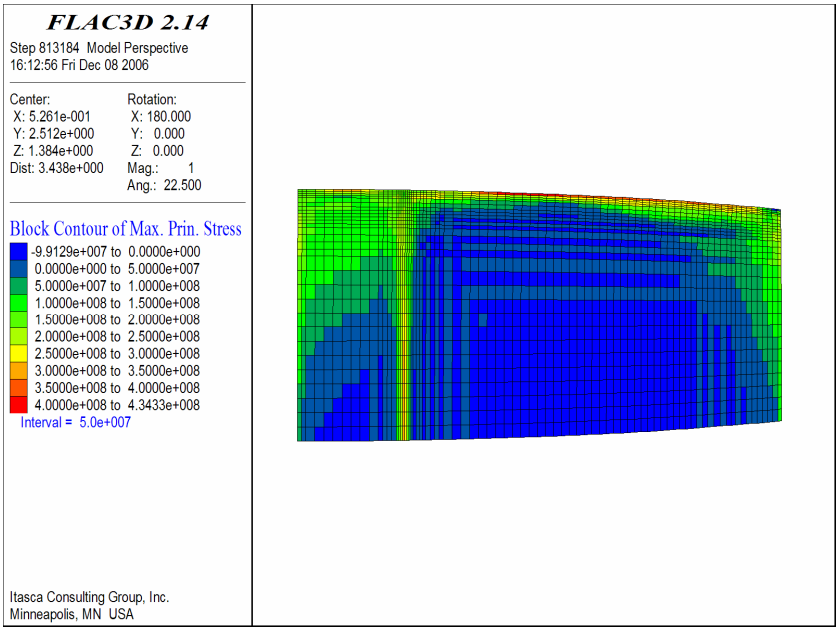

Output DTN: MO0701DRIPSHLD.000, file *\case2\5mm\Plate-8.6000e+005.sav*.

NOTE: View from above. Compressive stresses are negative.

Figure 6-41. Contours of Maximum Principal Stress (Pa) in the 5-mm-Thick Drip Shield Plate for Case 2 Boundary Conditions and a Vertical Stress of 860 kPa

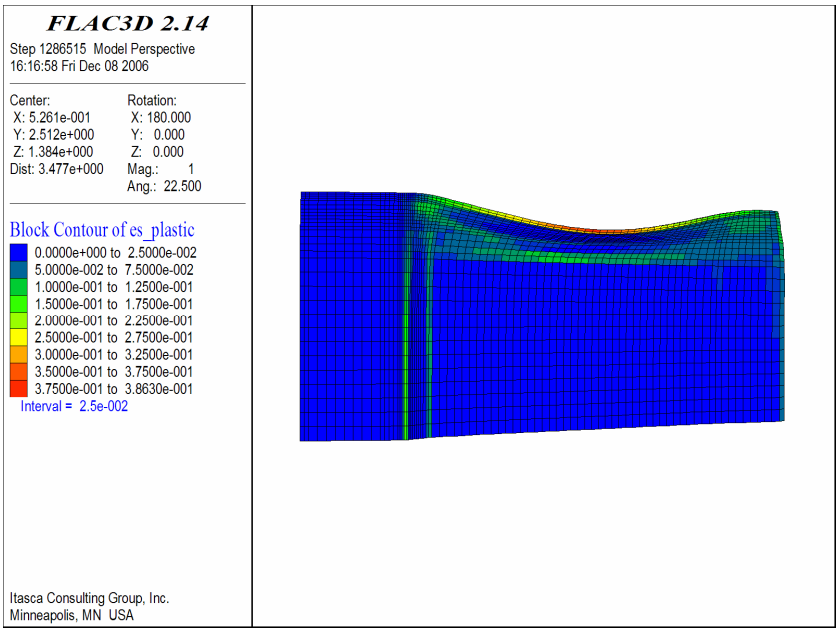

Output DTN: MO0701DRIPSHLD.000, file *\case2\5mm\Plate-8.6000e+005.sav*.

NOTE: View from above. Compressive stresses are negative.

Figure 6-42. Contours of Plastic Shear Strain in the 5-mm-Thick Drip Shield Plate for Case 2 Boundary Conditions and a Vertical Stress of 880 kPa

6.4.3.1.4 Results

The damage areas in the drip shield plates as functions of pressure for three plate thicknesses and two boundary conditions are shown in Figure 6-43. This figure shows the damage area in the analyzed region of the drip shield plate. Assuming uniformly distributed load over the entire drip shield, the total damage area in the drip shield plates is 20 times the values indicated in Figure 6-43.[3] The figure indicates monotonic increase in the damage area as a function of the increase in pressure and the decrease in plate thickness. In all cases, the damage increases relatively gradually as a function of pressure until the pressure approaches the plate failure pressure, when the damage area jumps suddenly. Similarly, the boundary conditions do not have a significant effect on the damage area, while the pressure is relatively small compared to failure pressure. However, Case 2 boundary conditions generally result in greater damage (compared to Case 1 boundary conditions), which is the expected trend. The apparent deviation from this trend, which occurs for 15-mm-thick plates at pressures greater than 2.5 MPa, is due to the finer load increment used for Case 2 boundary conditions. However, those results are irrelevant because the plate fails at approximately 2.5 MPa (Table 6-135).

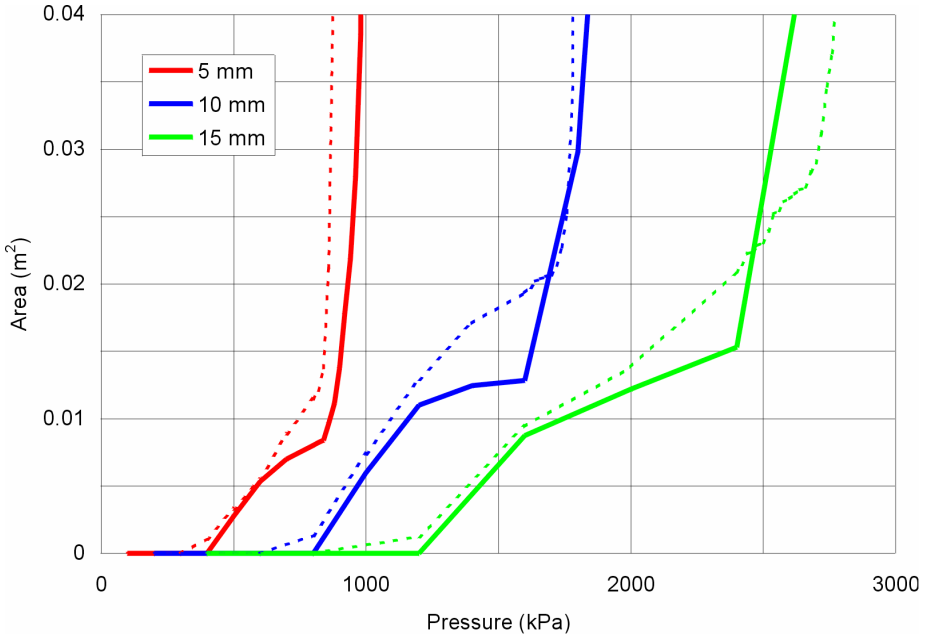

Output DTN: MO0703PADSBLOC.000, file *DS plate damage due to distributed loads.xls*, sheet "scale 1."

NOTES: The solid line is for the Case 1 boundary condition; the dashed line is for the Case 2 boundary condition.

The reported results are for the analyzed segment of the drip shield crown plate (i.e., the segment between the bulkheads, the plane of symmetry between the bulkheads, the middle stiffener, and the drip shield shoulder). To obtain the damage for the entire drip shield, the results need to be multiplied by 20.

The damage areas on the inner and outer surfaces are added irrespective of their geometrical relation and potential overlap, although the overlapping surfaces should not be counted twice.

Figure 6-43. Damage Areas in the Drip Shield Plate as a Function of Uniform Load for Different Plate Thicknesses and Boundary Conditions

[3] The analysis was conducted for one-quarter of a segment. There are five segments on a drip shield.

Table 6-135. Fragility of the Drip Shield Plate as a Function of Plate Thickness and Boundary Conditions

Plate Thickness (mm)	Failure Loads (kPa)	
	Case 1 Boundary Conditions	Case 2 Boundary Conditions
5	1,086	740
10	1,911	1,609
15	2,668	2,438

Output DTN: MO0701DRIPSHLD.000, file *summary DS plate fragility.xls.*

The evolution of effective plastic strain, the maximum stress and maximum stress difference as functions of load for all three plate thickness, and both cases of boundary conditions are shown in Figures 6-44 through 6-47. The ultimate strain and stress are also indicated in the plots. For the Case 1 boundary conditions (Figures 6-44 and 6-45), the stress state is predominantly uniaxial at the support where the stresses are maximum. Consequently, the ultimate load determined from the three criteria is very similar. For Case 2 boundary conditions (Figures 6-46 and 6-47) the biaxiality of stresses causes the maximum principal stress to exceed the ultimate tensile strength of Titanium Grade 7, while the effective strain and the stress difference are less than the corresponding failure thresholds. In order to account for the stress biaxiality effect on failure condition, the failure load for Case 2 boundary conditions was determined based on the maximum stress. This criterion was used when the criterion based on the maximum stress (not strain or stress difference) resulted in a smaller failure load. (For example, the maximum principal stresses (dashed lines in Figure 6-47) intersect ultimate stress (black solid line) at lower pressures than the critical pressure based on stress difference (colored solid lines) or strain as indicated in Figure 6-46.)

All plate fragility results are summarized in Figure 6-48 and Table 6-135, which show the drip shield plate-failure load as a function of plate thickness and boundary conditions. Two boundary conditions were analyzed to address uncertainty in load distribution between the neighboring drip shield segments. The results show that the limit loads increase with plate thickness. Considering bending stresses only, the limit load is expected to be proportional to the square of the plate thickness. However, the shear and membrane forces make the relation between limit load and plate thickness almost linear. The Case 1 boundary conditions make the plate stronger as they include lateral constraint on the drip shield.

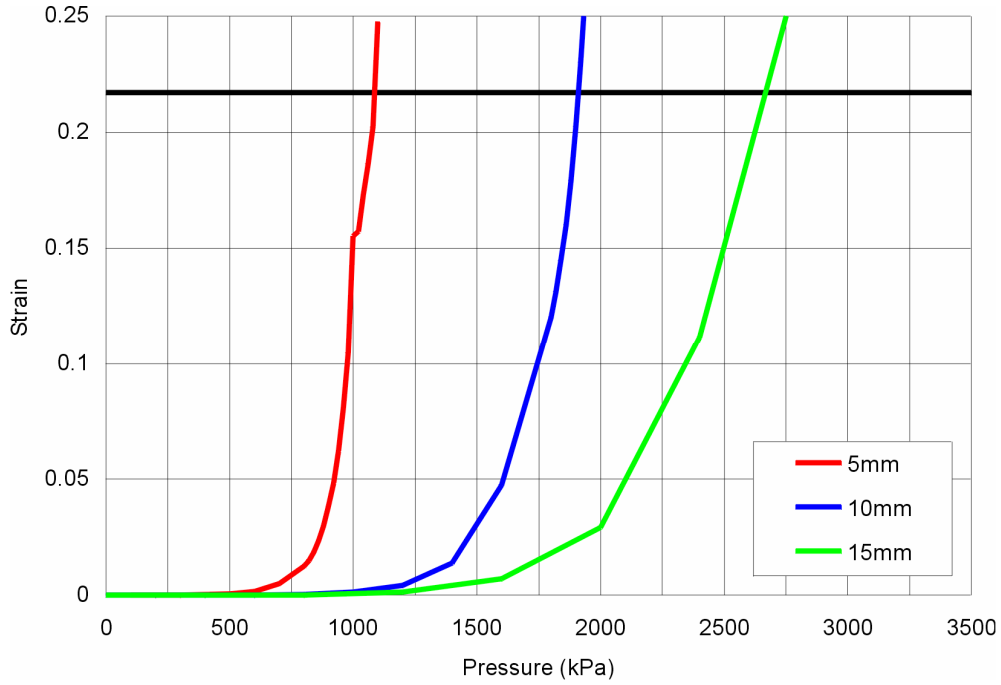

Output DTN: MO0701DRIPSHLD.000, file *drip shield plate fragility\summary\summary 3d fixed.xls,* sheet "ch plate 3d strain."

NOTE: Ultimate stress is indicated by the solid horizontal black line.

Figure 6-44. Maximum Effective Plastic Strain in the Drip Shield Plate as Function of Load: Case 1 Boundary Conditions

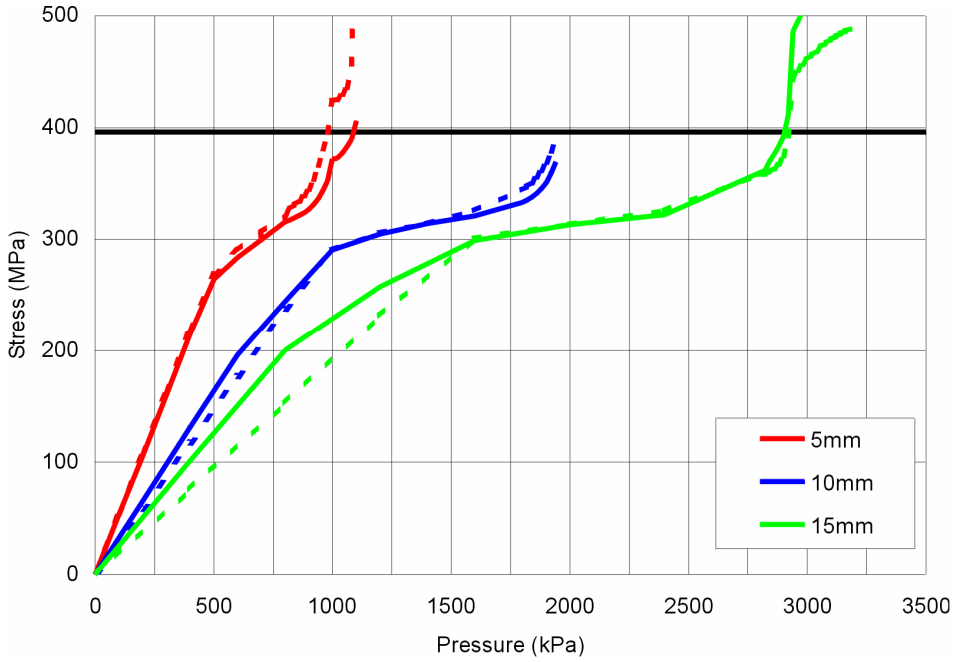

Output DTN: MO0701DRIPSHLD.000, file *drip shield plate fragility\summary\summary 3d fixed.xls*, sheet "ch plate 3d stress."

NOTE: Ultimate stress is indicated by the solid horizontal black line. Maximum principal stress is shown by dashed lines; maximum stress difference is shown by solid lines.

Figure 6-45. Maximum Principal Stress and Maximum Stress Difference in the Drip Shield Plate as Function of Load: Case 1 Boundary Conditions

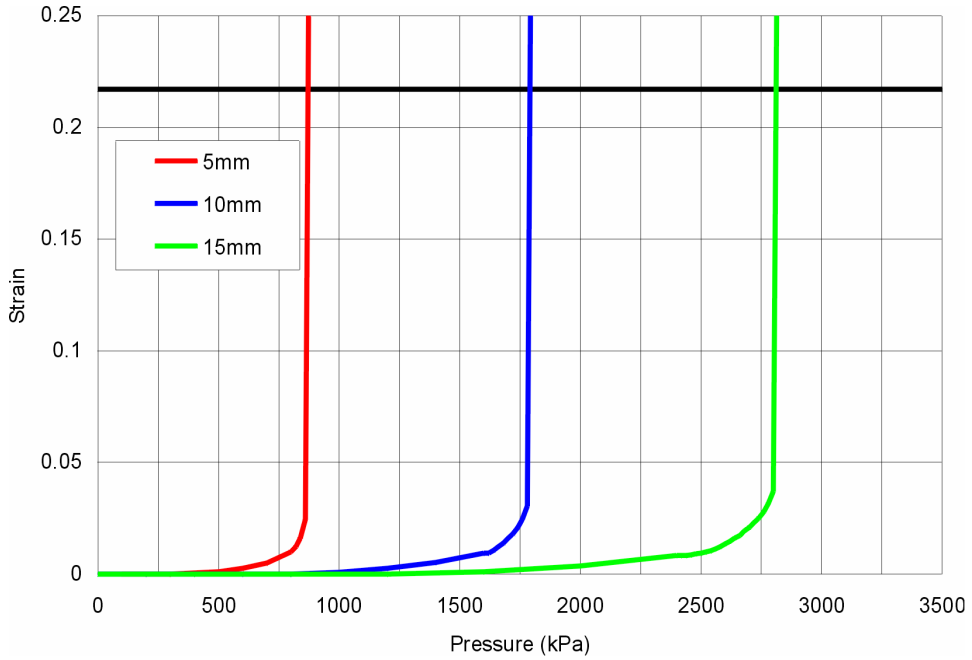

Output DTN: MO0701DRIPSHLD.000, file *drip shield plate fragility**summary**summary 3d free laterally.xls*, sheet "ch plate 3d strain."

NOTE: Ultimate stress is indicated by the solid horizontal black line.

Figure 6-46. Maximum Effective Plastic Strain in the Drip Shield Plate as Function of Load: Case 2 Boundary Conditions

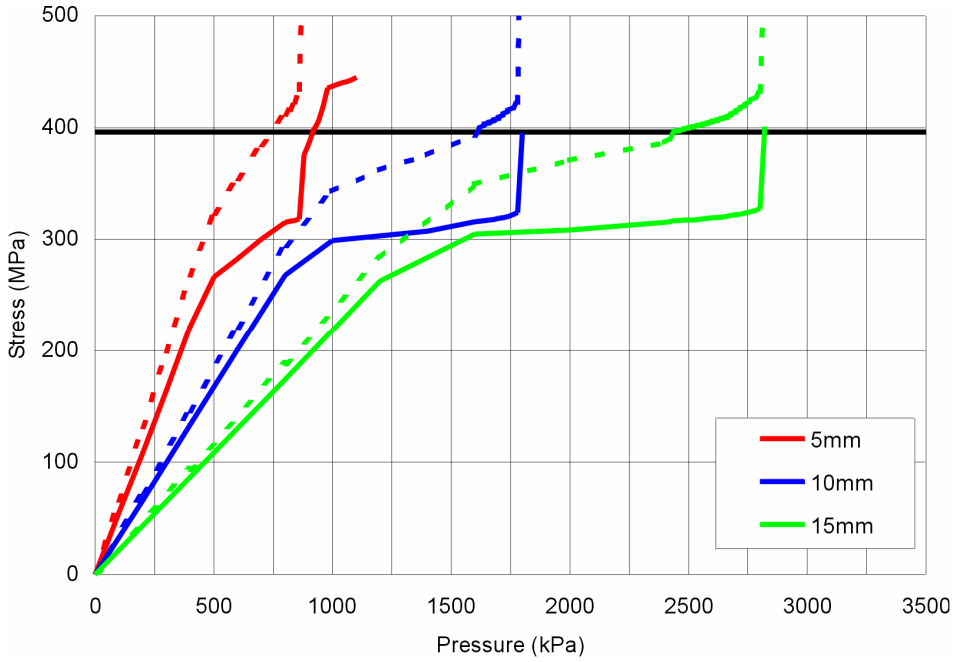

Output DTN: MO0701DRIPSHLD.000, file *\drip shield plate fragility\summary\summary 3d free laterally7.xls*, sheet "ch plate 3d stress."

NOTE: Ultimate stress is indicated by the solid horizontal black line. Maximum principal stress is shown by the dashed lines; maximum stress difference is shown by the solid lines.

Figure 6-47. Maximum Principal Stress and Maximum Stress Difference in the Drip Shield Plate as Function of Load: Case 2 Boundary Conditions

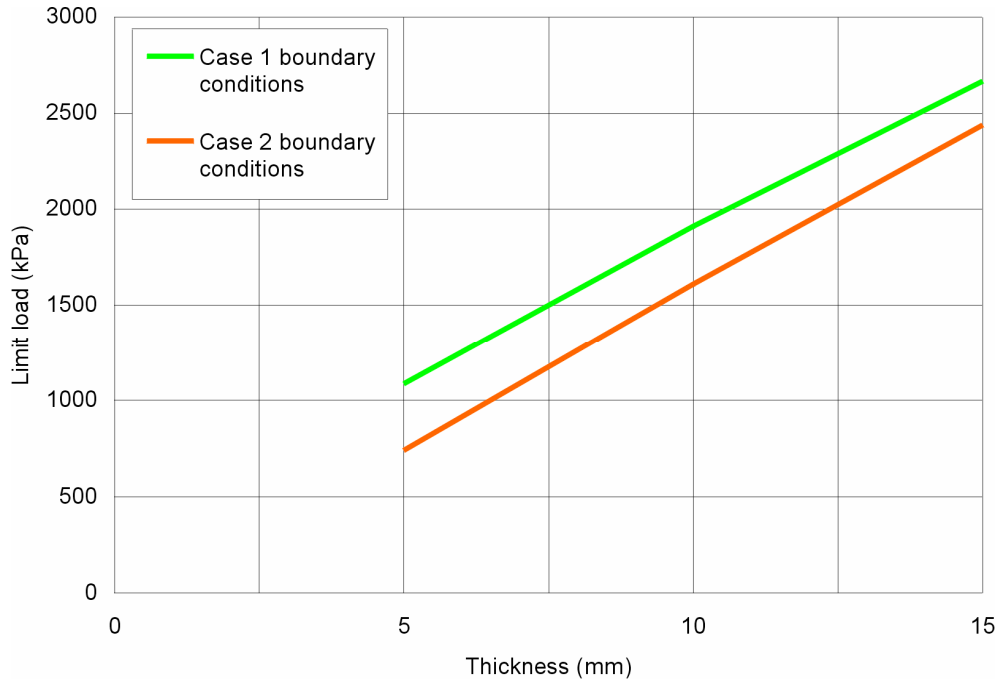

Output DTN: MO0701DRIPSHLD.000, file *\drip shield plate fragility\summary\summary DS plate fragility.xls*, sheet "ch limit load."

Figure 6-48. Fragility of the Drip Shield Plate as a Function of Plate Thickness and Boundary Conditions

6.4.3.2 Analyses for Drip Shield Framework Fragility

6.4.3.2.1 Purpose

In this section the fragility of the drip shield framework is investigated by quasi-static analysis in which vertical loading on the drip shield crown is increased monotonically until the structure fails or other failure criteria are reached. The purpose of this analysis is to determine a vertical failure load for use in *Seismic Consequence Abstraction* (SNL 2007 [DIRS 176828]). This failure load can be correlated to the ground motion PGA using the relation in Equation 6-1 in order to determine a probability distribution for the ground motion intensity or the PGV level at which the framework collapses.

The vertical PGA of the ground motion at which the drip shield framework collapses is related to the limit (ultimate) load, p_{ult}, and the vertical static load of the rubble in the collapsed drift, p, by the simple formula of Equation 6-1. The same formula is used in fragility analysis of the drip shield plates (Section 6.4.3.1).

A three-dimensional model was used and calculations were conducted for the initial geometry with dimensions specified in the design documents, and for two additional geometries in which the plates and all other structural components of the drip shield are thinned by 5 mm and 10 mm relative to the design geometry to account for two stages of uniform corrosion during the postclosure period.

6.4.3.2.2 Numerical Representation

The analysis was carried out using FLAC3D V. 2.14 numerical code.

6.4.3.2.2.1 Geometry and Boundary Conditions

The initial geometry of the drip shield is shown in Figure 6-49. The geometry of the drip shield numerical representation is generated based on specifications from sources listed in Table 4-1. Groups 1, 2, 7 and 8 are Titanium Grade 7; groups 4, 6, 10, and 12 are Titanium Grade 24. The mechanical properties of Titanium Grades 7 and 24 are listed in Table 6-134. Groups 9 and 11 are rigid surfaces representing the invert and the pallet, respectively. Due to the repetitive nature of the design, only one segment of the drip shield was included in the analysis of drip shield stability under static rubble load. In the initial configuration, the drip shield rests on the invert under its own weight. The invert and the pallet are fixed and rigid in all calculations. Initially, the drip shield is not in contact with the two vertical, planar surfaces (shown in light-green color in Figure 6-49) that represent the physical restraint of the pallet; however, sufficient deformation of the legs can cause interaction between the drip shield and the pallet. Symmetry boundary conditions (no displacements parallel to the axis of the drip shield and no rotation in the direction along the drip shield outline in the vertical cross section normal to the drip shield longitudinal axis) were assigned along the boundaries on the vertical planes that define the drip shield segment boundaries.

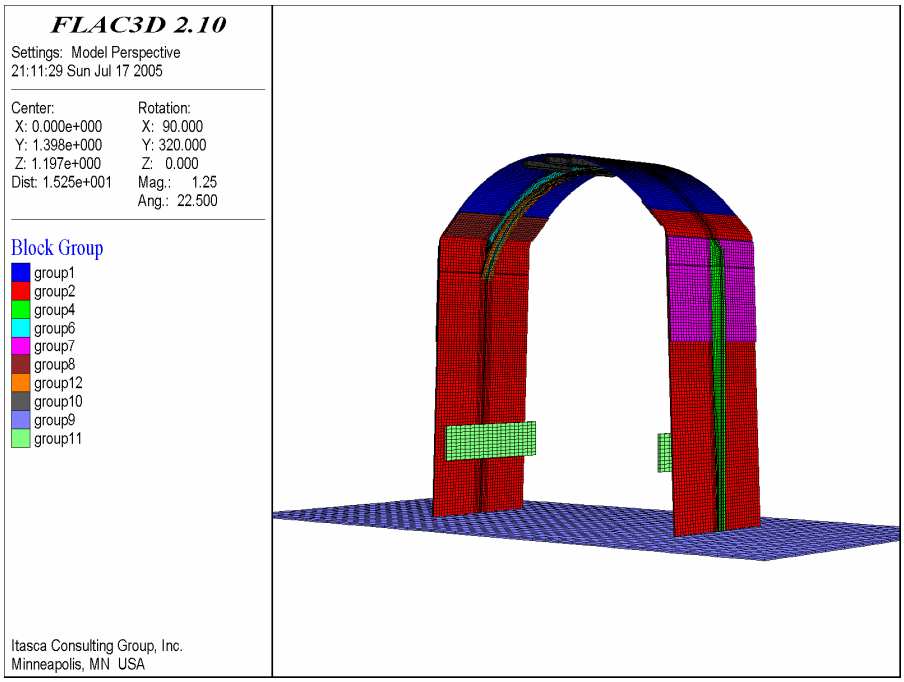

Source: Created for illustrative purposes only, from FLAC3D save file in output DTN: MO0701DRIPSHLD.000, *drip shield framework fragility/average load/15mm/grid3.sav*, by plotting block group geometry.

NOTE: Groups 1, 2, 7, and 8 are Titanium Grade 7; groups 4, 6, 10, and 12 are Titanium Grade 24. Groups 9 and 11 are rigid surfaces representing the invert and pallet, respectively.

Figure 6-49. Geometry of the Drip Shield Showing Groups of Elements Representing Different Parts of the Structure

Figure 6-50 is a detailed cross section of the drip shield crown through the bulkhead. The plate is shown in dark blue; red and green represent the bulkhead; and light blue represents the longitudinal stiffeners.

Different drip shield structural components will be welded together in such a way that any relative motion between those components will be prevented (i.e., the welds will not fail before any of the welded components). Therefore, all structural components (groups) in the numerical representation are rigidly connected.

The drip shield fragility calculations were conducted for the initial geometry with dimensions specified in the design documents (Table 4-1), and for two additional geometries in which the plates and all other structural components of the drip shield are thinned by 5 mm and 10 mm relative to the design geometry to account for two stages of uniform corrosion.

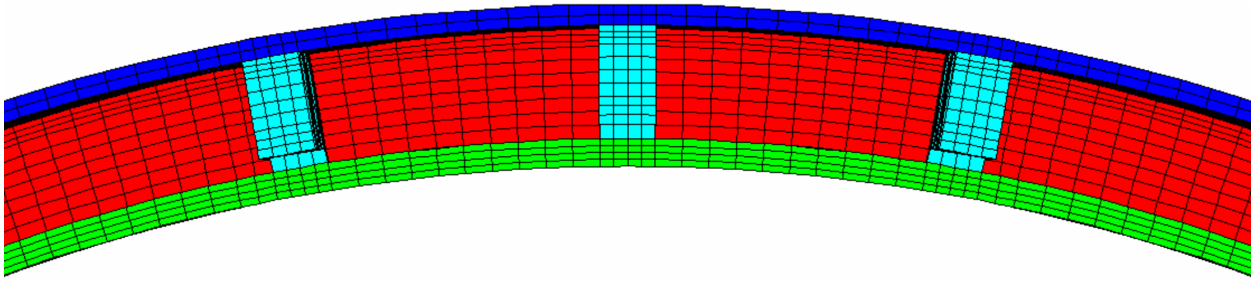

Source: Created for illustrative purposes only, from FLAC3D save file in output DTN: MO0701DRIPSHLD.000, *drip shield framework fragility/average load/15mm/grid3.sav*, by plotting block group geometry.

NOTE: Dark blue represents the plate (Titanium Grade 7); light blue areas are the longitudinal stiffeners (Titanium Grade 24); red and green areas are the bulkheads (Titanium Grade 24).

Figure 6-50. Geometry of the Drip Shield Showing Groups of Elements Representing Different Parts of the Structure: Crown Detail

6.4.3.2.2.2 Rubble Loads on the Drip Shield

Rocks falling on the drip shield will consist of blocks of irregular shapes and various sizes. The typical size distribution for these blocks is expected to range from 0.1 m to 0.3 m (BSC 2004 [DIRS 166107], Section 6.4.1.1). The manner in which the rock blocks fall and compact around the drip shield is a random process. The static load of the fallen rock mass will be transferred to the drip shield through contacts among the rocks and between the rocks and the drip shield (a large number of localized contacts that are nearly point loads).

The distribution of the point loads on the drip shield will vary significantly, both in location and in magnitude, due to the stochastic nature of drift degradation. The variability in point loads was analyzed previously in *Mechanical Assessment of the Drip Shield Subject to Vibratory Motion and Dynamic and Static Rock Loading* (BSC 2004 [DIRS 169753], Figure 5-33). In this earlier work, six realizations of simulated rock collapse onto the drip shield were conducted for fully collapsed drifts, and the results showed variability of almost 50% in the average pressure applied by the rubble to the drip shield.

To conservatively account for variability in the loads on the drip shield, a new series of simulations was conducted that utilizes results from the study mentioned above. In particular, a drip shield stability analysis was conducted in which the pressure in a particular outline interval (Figure 6-51) was applied along the entire length of the segment in the three-dimensional model. In this simulation the pressure distribution along the drip shield surface was discretized over 30 intervals of approximately equal length, as indicated in Figure 6-51. Note that the even-numbered outline intervals are omitted to improve visibility. The pressure distribution did not vary in the longitudinal (z) direction.

The limit load for the drip shield is not only a function of the magnitude of the load—it is also a function of its distribution. The fragility of the drip shield framework (i.e., the limit load at which the framework fails) was determined using the load distributions based on two load distributions that were derived from *Mechanical Assessment of the Drip Shield Subject to Vibratory Motion and Dynamic and Static Rock Loading* (BSC 2004 [DIRS 169753], Figure 5-33). These were (a) rock-load realization 3, which was selected as the most severe load realization among the six generated cases in the previous study, and (b) an average of the six loads used in the previous study. The rubble loads are summarized in Table 6-136. Although the table lists average pressures for the legs and the crown, the actual pressure distribution for 30 outline intervals was used in the calculations.

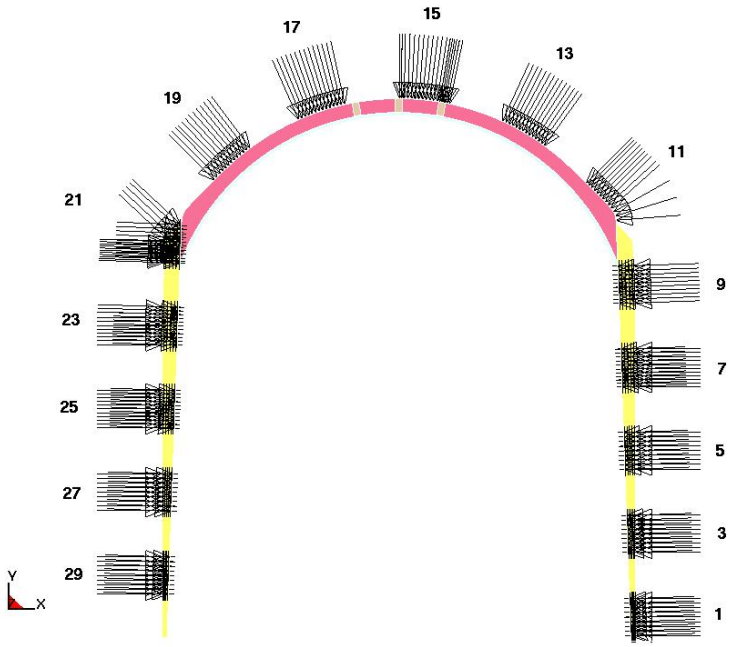

Source: BSC 2004 [DIRS 170791], Figure 5.

NOTE: The pressure applied to even-numbered outline intervals is removed for purposes of clarity.

Figure 6-51. Application of the Static Pressure of the Fallen Rock Mass on the Drip Shield

Table 6-136. Average Pressure Values on the Drip Shield for Quasi-Static Drift Degradation (Rock Size 0.2 m)

Realization	Pressure (kPa)		
	Left Leg	Top (Crown)	Right Leg
1	41.54	108.91	58.76
2	19.15	147.07	19.33
3	31.35	154.81	6.69
4	57.23	129.75	128.81
5	69.69	112.73	105.43
6	32.97	113.87	52.19
Average	41.99	127.86	61.87

Source: DTN: MO0407MWDDSLCR.000 [DIRS 170873], file *final drip shield quasi-static pressure.xls*, sheet "data." Block size taken from BSC 2004 [DIRS 169753], Section 5.2.5.1.

NOTE: The source DTN provides pressures only for the average of the loading realizations. The other averages are calculated from the outline interval pressures provided in the DTN.

In assessing the factor of safety of the drip shield with respect to the rubble static load in *Mechanical Assessment of the Drip Shield Subject to Vibratory Motion and Dynamic and Static Rock Loading* (BSC 2004 [DIRS 169753], Section 5.4.3.1), an increase in the density of rubble in the two-dimensional analysis of drip shield–rubble interaction was used as a method to generate increased rubble loads on the drip shield. This new load distribution was then applied to the three-dimensional, elastic-plastic representation of the drip shield to assess its stability for increased load level. Although load distribution was determined from the coupled rubble-drip shield analysis, the drip shield stability analysis was uncoupled, and all loads were fixed, dead loads.

The loading in this analysis also incorporated a passive (reactive) pressure to emulate the load of rubble on the sides of the drip shield during deformation. That is, as the structure began to deform excessively, displacing toward the rubble, the passive (reactive) pressures of the rubble increased, confining the structure and making it more stable. In the approach used here, initial load realizations (load realization 3 and the average of six load realizations) were modified to account for the increased rubble load. The vertical load on the drip shield (load in outline intervals 11 through 20 in Figure 6-51) was gradually increased proportionally to the initial load distribution. The initial lateral loads on the drip shield legs were not changed. However, the effect of the passive rubble loads was accounted for using the methodology described in Section 6.4.4.2.2.3. The analysis presented in *Mechanical Assessment of the Drip Shield Subject to Vibratory Motion and Dynamic and Static Rock Loading* (BSC 2004 [DIRS 169753], Section 5.4.3) does not account for that effect and, thus, underestimates the stability and strength of the structure.

6.4.3.2.2.3 Interaction between the Drip Shield and the Rubble

The rubble load on the drip shield is not simply the dead weight of the rubble but is the consequence of the mechanical interaction between the drip shield and the rubble accumulated along the sides and on top of the drip shield. Due to the shear resistance of the rubble (mostly

caused by friction among the rough rubble particles) coupled with the deformation of the drip shield, some of the weight of the rubble located above the drip shield is transferred to the invert and the drift walls by stress-arching through the rubble. Some of the loads on the sides of the drip shield are passive loads caused by lateral deformation of the legs of the drip shield under the vertical load on the crown. These passive loads tend to provide confinement to the legs of the drip shield, preventing lateral deformation or "leaning" of the structure. As the drip shield deforms with the increase in load, the loads will change due to interaction with the surrounding rubble. Deformation of the drip shield will alter both active and passive loads (pressures) of the rubble on the drip shield. The active pressure when the rubble is moving toward the structure most likely will decrease due to increased stress-arching in the rubble. In general, the passive pressure when the structure is moving toward the rubble will increase.

To account for the interaction between the drip shield and the surrounding rubble, as well as the change of load on the drip shield during increase in the vertical load, it generally is necessary to simulate concurrently (i.e., fully coupled) the three-dimensional deformation of the drip shield and the surrounding rubble. This coupling is accounted for in an approximate way as follows. The reactive pressures of the rubble, resulting from the large deformation of the drip shield, are generated and applied on the sides of the drip shield in locations at which the drip shield is moving toward the rubble. The pressures on the crown of the drip shield do not change in this approximation, irrespective of the deformation of the drip shield. The pressures generated by interaction between the drip shield and the rubble were applied on the side of the drip shield, and superimposed on the initial pressures only where the drip shield moved toward the rubble; elsewhere, the pressure did not change.

The mechanical interaction between the rubble and the drip shield is represented by elastic springs (Figure 6-52) that act in compression only and are calibrated to simulate the approximate deformability of the rubble. The springs are connected to every node of the drip shield legs. The stiffness of the springs is calculated using Equation 6-2:

$$k_n = E\,A / w \qquad \text{(Eq. 6-2)}$$

where E is the approximate Young's modulus of the rubble; w is the distance between the drip shield leg and the intact drift wall, and A is the interacting drip shield surface area associated with the node. (In other words, if a bar w long, with Young's modulus E and cross-sectional area A is loaded on one end by force F, while the other end is fixed, the loaded end will displace $\Delta w = F / k_n$.)

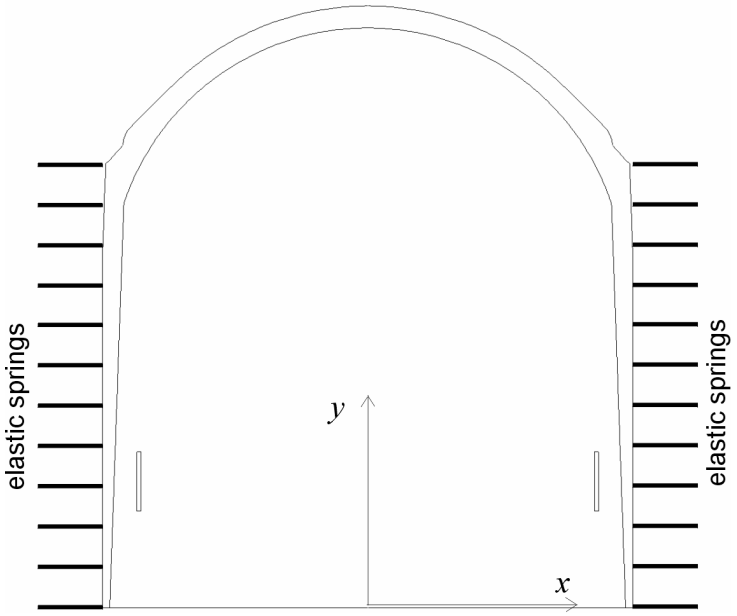

Source: BSC 2005 [DIRS 174715], Figure 5.4-3.

NOTE: The interaction is represented by a series of elastic springs that represent the rubble and its connection to the drip shield.

Figure 6-52. Interaction between the Drip Shield and the Rubble along the Sides of the Drip Shield

The effective elastic modulus of the rubble was estimated by conducting confined numerical-compression tests of collapsed rubble generated during the six realizations of drift collapse and drip shield rubble loading. These numerical compression tests were supplemented by estimates of elastic properties for rockfall taken from the literature. The analysis of rubble properties is reported in *Mechanical Assessment of the Waste Package Subject to Vibratory Ground Motion* (BSC 2005 [DIRS 173172], Attachment IX). The value of 50 MPa represents the lower bound of the initial tangent of Young's modulus of the rubble at confinement greater than 100 kPa. Analysis of drift collapse shows (e.g., BSC 2004 [DIRS 166107], Figure 6-171) that most of the rockfall comes from the drift crown. The rubble fills the space between the drip shield and the drift wall, reducing—or even preventing—deterioration of the walls. The maximum initial horizontal distance from the drip shield to the drift wall (before rockfall) is approximately 1.5 m. Accounting for some rockfall from the walls, the distance between the drip shield and the stable drift wall is taken, conservatively, to be 2.5 m. Softer springs provide less confinement (i.e., allow more deformation of the structure, making it more likely to buckle). Consequently, selected Young's modulus values underestimate the stiffness of the rubble, while the distance between the drip shield and the drift wall is overestimated (see Equation 6-2).

The force in a spring representing rubble is given by Equation 6-3:

$$F = \begin{cases} -k_n u_h & \text{if } x_p\, u_h > 0 \\ 0 & \text{otherwise} \end{cases} \qquad \text{(Eq. 6-3)}$$

where x_p is the x coordinate of the node, and u_h is the horizontal displacement of the node. The practical interpretation of this equation is that, when the drip shield moves toward the rubble, a compressive interactive force is developed; however, when the drip shield and rubble move apart, no force is developed.

6.4.3.2.3 Results

Analyses of drip shield collapse were completed for three drip shield geometries. The geometry of the initial drip shield configuration is shown in Figure 6-49. The loads were increased initially in increments equal to the initial pressures on the drip shield crown. At a particular pressure level, the drip shield collapses or a failure criterion is reached. The pressure increment was refined to 20% of the initial pressure increment within the final increment when the drip shield collapsed. Effective plastic strain, maximum stress, and maximum stress difference were monitored during the simulation. Because the rubble pressure varies along the drip shield outline, the load distribution is characterized by the average pressure on the drip shield crown. The actual failure pressure is calculated by interpolating between the discrete points in the load-effective plastic strain plots. The plot for load realization 3 is shown in Figure 6-53. The failure loads, determined on the basis of effective plastic strains, maximum stress or maximum stress difference, are practically the same in the case of drip shield framework fragility. In all cases, the ultimate strains or stresses are reached when buckling occurs, which is indicated by an almost vertical line representing the effective plastic strain as a function of pressure (shown in Figure 6-53).

Typical drip shield framework modes of failure are illustrated in Figures 6-54 to 6-56. In the initial configuration, the drip shield bulkhead snaps through approximately in the middle of the span (Figure 6-54). Uniform reduction in the thickness of the drip shield structural components weakens the lower part of the drip shield legs. Consequently, the mode of failure of the thinned drip shield structure is buckling of the legs, as shown in Figures 6-55 and 6-56. These results are consistent with the analysis and discussion in Section 6.4.4, which demonstrate that the main failure mode of the drip shield framework, when the emplacement drifts are subjected to strong seismic ground motions, is buckling of the drip shield legs.

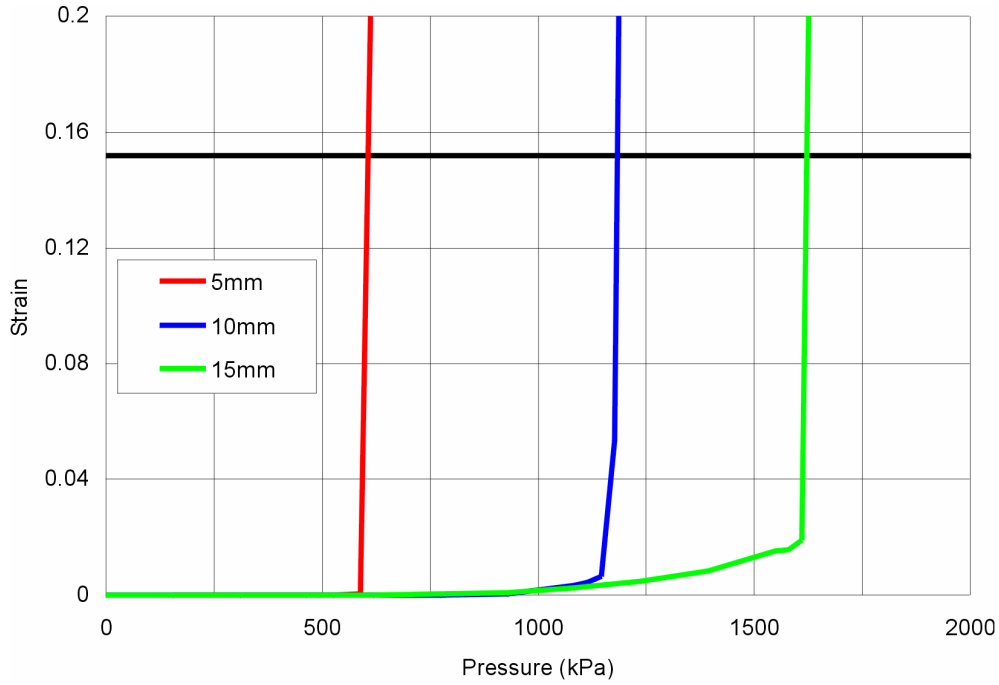

Output DTN: MO0701DRIPSHLD.000, file *summary load 3.xls*, chart "ch frame 3d strain."

NOTE: Thickness of all drip shield structural components is reduced by the same amount as the thickness of the plates.

Figure 6-53. Maximum Effective Plastic Strain in the Drip Shield Framework as a Function of Load for Different Plate Thicknesses: Rubble Load Realization 3

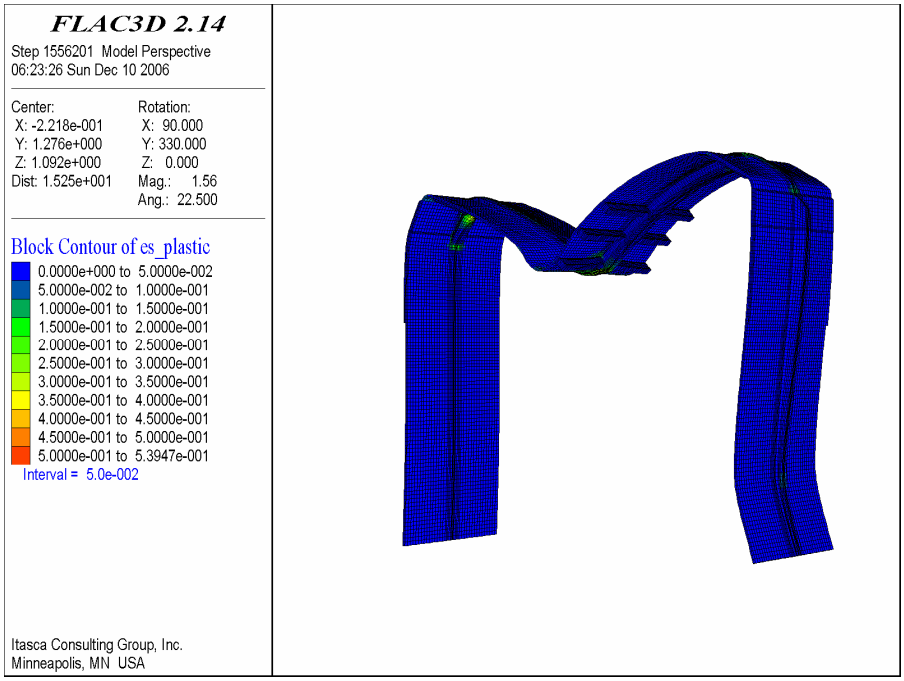

Output DTN: MO0701DRIPSHLD.000, file *average load\15mm\eq_lf134.sav*.

Figure 6-54. Deformed Shape and Contours of Plastic Shear Strain in the Failure State for the Initial Thickness of the Drip Shield Components

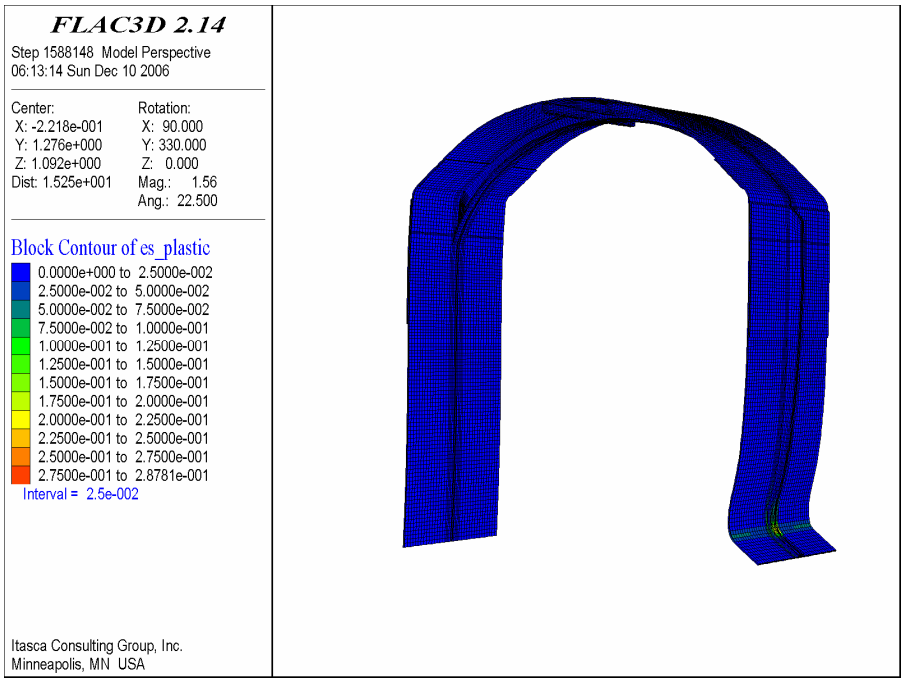

Output DTN: MO0701DRIPSHLD.000, file *average load\10mm\eq_lf86.sav*.

Figure 6-55. Deformed Shape and Contours of Plastic Shear Strain in the Failure State for the Drip Shield Components Thinned 5 mm

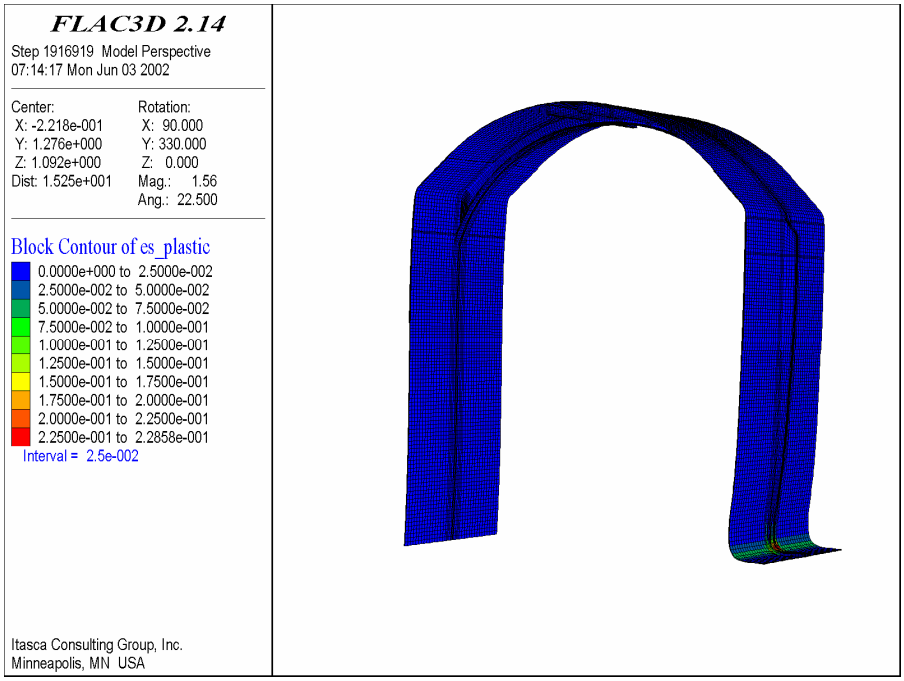

Output DTN: MO0701DRIPSHLD.000, file *\average load\5mm\eq_lf40.sav*.

Figure 6-56. Deformed Shape and Contours of Plastic Shear Strain in the Failure State for the Drip Shield Components Thinned 10 mm

Drip shield fragility curves are shown in Figure 6-57 (and discrete points on the curves are listed in Table 6-137) as functions of drip shield geometry for both load realization 3 and a load representing the average of the six load realizations. These curves are expressed with respect to thickness of the plates, and it is important to note that in these simulations all other drip shield structural components are thinned by the same amount. The fragility curves show that the limiting load increases almost linearly with increased thickness of the structural components. The load realization does not have a significant effect on the limit of the drip shield. Such a trend is a consequence of the confining effect of the rubble reactive pressure along the drip shield legs. The asymmetry of loading is compensated for by an increase in reactive rubble pressures as the drip shield structure starts deforming excessively to one side.

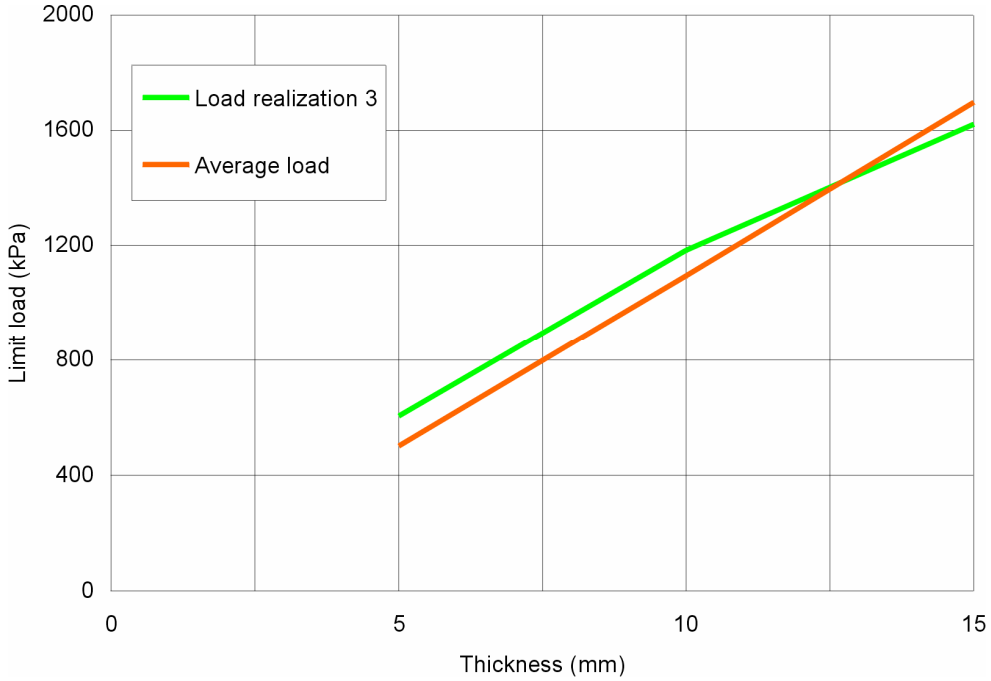

Output DTN: MO0701DRIPSHLD.000, file *summary DS framework fragility.xls*, chart "ch limit load."

NOTE: The thickness of all drip shield structural components is reduced by the same amount as the thickness of the plates.

Figure 6-57. Fragility of the Drip Shield Framework as a Function of Plate Thickness and Load Realization

Table 6-137. Fragility of the Drip Shield Framework as a Function of Drip Shield Configuration and Load Distribution

Plate Thickness (mm)	Failure Loads (kPa)	
	Load Realization 3	Average Load
5	606	501
10	1,183	1,094
15	1,622	1,698

Output DTN: MO0701DRIPSHLD.000, file *summary DS framework fragility.xls*.

6.4.4 Drip Shield Failure Modes

6.4.4.1 Purpose of Drip Shield Failure Mode Analysis

This section describes the results of the dynamic analysis of the modes of failure of the drip shield framework and interaction of the drip shield with surrounding rubble during strong seismic ground motion. A two-dimensional dynamic analysis of the coupled drip shield–rubble mechanical interaction during seismic ground motions is carried out for selected ground motions. Results presented in this section are used to confirm drip shield framework failure loads and failure modes obtained with the quasi-static fragility analysis presented in Section 6.4.3.2.

Motion of the drip shield and its interaction with rubble and objects inside the drip shield (i.e., the waste package and the pallet) during seismic ground motion, particularly at the 2.44 m/s and 4.07 m/s PGV levels, will be extremely complex. Although the initial rubble load is predominantly vertical, seismic ground motion can cause significant horizontal loading. The shape of the drip shield structure is designed to withstand the vertical loading, but the drip shield is vulnerable to horizontal loading. As a result of the fluctuation of loading histories in both the vertical and horizontal directions during seismic ground motion, the drip shield components will be subjected to complex stress histories. The quasi-static fragility analysis (Section 6.4.3.2) is conducted in such a way that the vertical load was gradually increased as an active load on the drip shield crown, while the lateral load increased as the passive load resulting from the simple approximation of interaction between the drip shield legs and surrounding rubble. Such an approximation can affect estimates of both failure loads and failure modes.

It is important to verify that the approximation predicts the correct failure mode of the structure. Interaction between the drip shield and the waste package, as well as future performance of the waste package, will be affected significantly by the drip shield failure mode. If the drip shield crown fractures, the sharp edges of the bulkhead will contact the waste package, and the rubble load will be transferred to the waste package, possibly tearing the OCB. However, if the drip shield legs fail, the conditions of waste package failure will be less favorable because the waste package would be loaded by the relatively smooth surface of the bulkhead.

6.4.4.2 Numerical Representation

A three-dimensional dynamic analysis of drip shield interaction with the surrounding rubble that includes sufficient details of the drip shield geometry to assess drip shield failure and a sufficiently large rock mass volume to simulate drift collapse would be very time-consuming. Thus, it was decided to analyze the problem using a two-dimensional approximation implemented in the numerical code UDEC V. 3.1, which previously has been used to analyze drift degradation in the lithophysal rock mass (BSC 2004 [DIRS 166107], Section 6.4.2) and is appropriate for assessment of drip shield stability. A geometrical representation of the emplacement drift similar to that used to analyze drift collapse in *Drift Degradation Analysis* (BSC 2004 [DIRS 166107], Section 6.4) is applied here. The rock mass is represented as an assembly of polygonal blocks, initially bonded together. The joints between the blocks have finite shear and tensile strengths and can fail as dictated by stresses in the rock mass. Failing of the joints between the blocks represents fracturing of the rock mass and formation of blocks that fall under gravity to accumulate on the drift floor and around the waste package as rubble. Representation of different lithophysal rock-mass qualities and an analysis of rockfall using this approach are described in detail in *Drift Degradation Analysis* (BSC 2004 [DIRS 166107], Section 6.4). Because the objective of the analyses discussed here is assessment of the potential for and modes of drip shield failure, relatively detailed representation of the drip shield geometry is included in the geometrical representation. The numerical representation of the drip shield surrounded by rubble at three different length scales is shown in Figure 6-58.

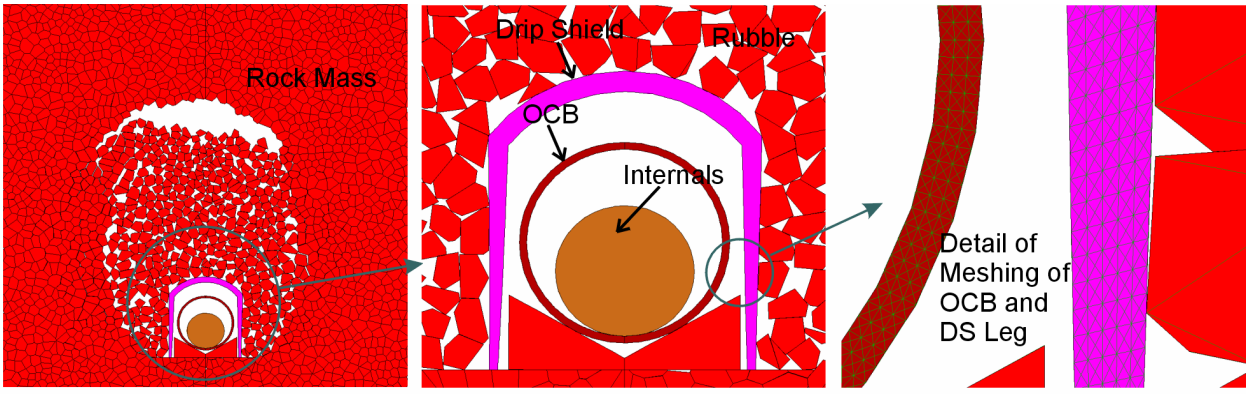

Source: Created for illustrative purposes only.

NOTE: DS = drip shield; OCB = outer corrosion barrier.

Figure 6-58. Geometrical Representation Used in the Analysis of the Mechanical Interaction between the Drip Shield and the Rubble During Seismic Ground Motions

The analysis is carried out in a plane perpendicular to the drift axis. There are few consequences of the two-dimensional approximation. The ground-motion component normal to the plane of analysis is not considered. The analysis is carried out for the vertical and one horizontal component (H1) of ground motion acting normal to the drift axis. The component of ground motion neglected in this analysis (H2) has only a second-order effect on drip shield–rubble interaction. Two-dimensional, plane strain approximation implies that the represented objects extend infinitely in the out-of-plane direction (i.e., normal to the plane of analysis). In reality, the size of the rubble block in the out-of-plane direction is on the order of its size in the plane of analysis. Instead of line loads at contacts between rubble blocks and the drip shield that extend infinitely in the out-of-plane direction, the distribution and magnitude of the loads change along the drip shield. The length scale over which the rubble load changes is equal to the typical block size (i.e., 0.1 m to 0.3 m), which is much smaller than the drip shield length or width. Consequently, the effect of randomly varying the load on a small scale is equivalent, with respect to the large-scale deformation of the drip shield, to (relatively) uniformly distributed loading. Two-dimensional approximation overestimates the nonuniformity of the rubble load on the drip shield, as well as its magnitude of deformation and magnitude of induced stresses.

6.4.4.3 Geometrical and Mechanical Representation of Different Model Components

The lithophysal rock mass is represented as an assembly of polygonal elastic blocks, as shown in Figure 6-58, initially bonded together along the joints and having finite tensile and shear strengths. Based on lithophysae and joint spacing, the average block size of 0.3 m is consistent with the typical block size of the lithophysal rock mass (between 0.1 m and 0.3 m as discussed in Section 6.4.1.1 of *Drift Degradation Analysis* (BSC 2004 [DIRS 166107])). Based on its quality, the lithophysal rock mass is divided into five categories, labeled 1 through 5. Lithophysal rock mass Category 3 is used for all calculations, since this rock category represents the intermediate estimate of the mechanical properties of the lithophysal rock mass. The micro-mechanical properties for bonded joints and intact blocks, calibrated to the large-scale

mechanical properties of the Category 3 lithophysal rock mass, are found in Table 4-4. Because of the random nature of the block geometry used to represent the rock mass, different realizations of block geometry, as controlled by random-number-generator seeds, were generated and analyzed. Four different random number-generator seeds, 4, 9, 14, and 2, were used in the calculations. The reasoning for selection of those particular numbers is provided in Section 6.4.4.5.

The mechanical behavior of the OCB (Alloy 22) and structural components of the drip shield (titanium plate and frame members) are represented by the Tresca strain-hardening constitutive relation. The Tresca constitutive relation is a special case of the Mohr-Coulomb relation, in which the friction angle is zero and tensile failure cutoff is not used (i.e., the tensile strength is set to be infinitely large). It is a well-known fact that metals are pressure-insensitive materials (unlike soils and rocks), and therefore von Mises or Tresca constitutive relations are more appropriate than Mohr-Coulomb (Popov 1968 [DIRS 181340], pp. 316 to 319). The yield and strain-hardening parameters used in UDEC were set in such a way that the uniaxial stress-strain response of the material follows a bi-linear curve characterized by Young's modulus, yield strength, and postyield tangent modulus.

The waste package OCB can interact with the drip shield during strong seismic ground motion (impacts) and in case of large deformation of the drip shield could provide back pressure and limit its further deformation. Therefore, the OCB is included in this analysis although assessment of deformation and damage of the OCB is not the focus of this analysis. The TAD-bearing waste package was considered in the analysis as it is the most common type of waste package to be emplaced in the repository (DTN: MO0702PASTREAM.001 [DIRS 179925]). The OCB is the only component of the waste package explicitly represented in the analysis. The inner OCB diameter is 1,830.7 mm (Table 4-2). (The radius of 915.3 mm is used as the actual input in the calculations, obtained by rounding the input to four significant digits.) A 25.4-mm thickness of the Alloy 22 OCB (Table 4-7) is analyzed in these calculations. (No thickness reduction due to uniform corrosion was considered.) The small thickness of the OCB wall is a critical factor for determination of the maximum stable calculation time step. In order to increase the critical time-step and shorten the calculation times, the OCB thickness and the minimum element size of the OCB were increased. However, at the same time, the Young's modulus, yield strength, and ultimate strength of the OCB representation were modified in such a way that flexural stiffness and bending moment versus curvature of the modified (increased thickness) cross section are the same as, or underestimate, those of the actual cross section. The axial stiffness of the modified cross section is considerably smaller than that of the actual cross section. However, the axial stiffness has a negligible effect on deformation of the OCB. Derivation of equivalent geometrical and mechanical properties of the OCB is documented in Appendix B. The list of UDEC input parameters used to represent the mechanical behavior of Alloy 22 is provided in Table 6-138.

Table 6-138. UDEC Input Parameters Used to Represent the Mechanical Behavior of Alloy 22 in Analysis of Drip Shield–Rubble Interaction

Parameter	Derivation	Value
Bulk modulus (K)	$K = \frac{E}{3(1-2\nu)}$	7.51 GPa
Shear modulus (G)	$G = \frac{E}{2(1+\nu)}$	3.91 GPa
Cohesion (c)	$c = \frac{\sigma_y}{2}$	23.5 MPa
Cohesion corresponding to 100% of strain (c_1)	$c_1 = \frac{\sigma_1}{2}$	153.5 MPa
Plastic shear strain corresponding to 100% of strain (ε_{p1})	$\varepsilon_{p1} = 1 - \frac{\sigma_y}{E}$	0.995

Source: Poisson's ratio, $\nu = 0.278$, is taken from Table 4-3. Young's modulus, $E = 10$ GPa, the yield strength, $\sigma_y = 47.1$ MPa, and the stress corresponding to 100% of effective strain, $\sigma_1 = 307$ MPa, are derived in Appendix B for equivalent representation of the OCB with increased thickness from 0.0254 m to 0.0694 m.

Although the drip shield is a three-dimensional structure with continuous plates supported by bulkheads and support beams at 1.071-m spacing, investigation of drip shield fragility using a quasi-static approach (Section 6.4.3.2) indicates that the drip shield deforms practically as a two-dimensional structure. In this analysis, deformation and failure of the drip shield framework are approximated with a two-dimensional representation. A cross section of the drip shield (which includes plates and bulkhead or support beam) is approximated by a rectangular cross section with a given height in the two-dimensional representation. The height of the cross section and the mechanical properties (i.e., Young's modulus, yield and ultimate strengths) of the drip shield representation were calculated in such a way that flexural stiffness and bending moment versus curvature of the approximating rectangular cross section match or underestimate those of the actual cross section.

The methodology of approximation and validation of approximation are discussed and documented in detail in Appendix B. The approximations were calculated in the middle of the bulkhead and in the top and bottom of the legs. The approximating cross section in the middle of the bulkhead was used for entire crown width. The height of the approximation in the legs varies linearly between the top and bottom of the legs. The stiffness properties (Young's modulus and Poisson's ratio) are the same in both the crown and legs, but different yield and ultimate strengths are assigned to the crown and the legs. In all cases, the height of the approximation is slightly greater than the total height of the actual cross section. Consequently, for the same curvature, the maximum strains in the two-dimensional approximation overestimate the maximum strain in the actual cross sections. The geometrical and mechanical properties of the characteristic cross sections of the two-dimensional approximations for three drip shield

configurations with different levels of thinning of the components by uniform corrosion (as derived in Appendix B) are listed Table 6-139.

Table 6-139. Equivalent Geometrical Characteristics and Mechanical Properties of Drip Shield Components in Analysis of Drip Shield–Rubble Interaction

Configuration	Density (kg/m^3)	Crown					Legs	
		Height (m)	Yield Strength σ_y (MPa)	Ultimate Strength σ_u (MPa)	Height (Top) (m)	Height (Bottom) (m)	Yield Strength σ_y (MPa)	Ultimate Strength σ_u (MPa)
Initial	675	0.202	28	35	0.183	0.079	31	38
5 mm thinned	548	0.182	27	34	0.161	0.059	30	38
10 mm thinned	386	0.157	23	35	0.137	0.040	25	35

Source: All variables in the table are derived and validated in Appendix B. The files used in the derivation of the values in the table are in output DTN: MO0701DRIPSHLD.000, folder "\drip shield failure modes\2D approximation\."

NOTE: Young's modulus, E, is 3.3 GPa in all cases.

The actual UDEC input parameters used for mechanical representation of drip shield behavior in the coupled dynamic analysis of drip shield–rubble interaction are listed in Tables 6-140, 6-141, and 6-142 for the initial configuration, the configuration thinned by 5 mm, and the configuration thinned by 10 mm, respectively.

Table 6-140. UDEC Input Parameters Used to Represent the Mechanical Behavior of the Drip Shield in the Initial Configuration in Analysis of Drip Shield–Rubble Interaction

Parameter	Derivation	Crown	Legs
Bulk modulus (K)	$K = \frac{E}{3(1-2\nu)}$	3.44 GPa	3.44 GPa
Shear modulus (G)	$G = \frac{E}{2(1+\nu)}$	1.23 GPa	1.23 GPa
Cohesion (c)	$c = \frac{\sigma_y}{2}$	14 MPa	15.5 MPa
Cohesion corresponding to 100% of strain (c_1)	$c_1 = \frac{1}{2}\left[\sigma_y + \frac{\sigma_u - \sigma_y}{\varepsilon_u - \frac{\sigma_y}{E}}\left(1 - \frac{\sigma_y}{E}\right)\right]$	36.9 MPa	38.5 MPa
Plastic shear strain corresponding to 100% of strain (ε_{p1})	$\varepsilon_{p1} = 1 - \frac{\sigma_y}{E}$	0.992	0.991

Source: Poisson's ratio, $\nu = 0.34$, and ultimate elongation, $\varepsilon_u = 0.16$, are taken from Tables 4-6 and A-2. Other variables are taken from Table 6-139.

Table 6-141. UDEC Input Parameters Used to Represent the Mechanical Behavior of the Drip Shield in the Configuration Thinned by 5 mm in Analysis of Drip Shield–Rubble Interaction

Parameter	Derivation	Crown	Legs
Bulk modulus (K)	$K = \frac{E}{3(1-2\nu)}$	3.44 GPa	3.44 GPa
Shear modulus (G)	$G = \frac{E}{2(1+\nu)}$	1.23 GPa	1.23 GPa
Cohesion (c)	$c = \frac{\sigma_y}{2}$	13.5 MPa	15 MPa
Cohesion corresponding to 100% of strain (c_1)	$c_1 = \frac{1}{2}\left[\sigma_y + \frac{\sigma_u - \sigma_y}{\varepsilon_u - \frac{\sigma_y}{E}}\left(1 - \frac{\sigma_y}{E}\right)\right]$	36.4 MPa	41.3 MPa
Plastic shear strain corresponding to 100% of strain (ε_{p1})	$\varepsilon_{p1} = 1 - \frac{\sigma_y}{E}$	0.992	0.991

Source: Poisson's ratio, $\nu = 0.34$, and ultimate elongation, $\varepsilon_u = 0.16$, are taken from Tables 4-6 and A-2. Other variables are taken from Table 6-139.

Table 6-142. UDEC Input Parameters Used to Represent the Mechanical Behavior of the Drip Shield in the Configuration Thinned by 10 mm in Analysis of Drip Shield–Rubble Interaction

Parameter	Derivation	Crown	Legs
Bulk modulus (K)	$K = \frac{E}{3(1-2\nu)}$	3.44 GPa	3.44 GPa
Shear modulus (G)	$G = \frac{E}{2(1+\nu)}$	1.23 GPa	1.23 GPa
Cohesion (c)	$c = \frac{\sigma_y}{2}$	11.5 MPa	12.5 MPa
Cohesion corresponding to 100% of strain (c_1)	$c_1 = \frac{1}{2}\left[\sigma_y + \frac{\sigma_u - \sigma_y}{\varepsilon_u - \frac{\sigma_y}{E}}\left(1 - \frac{\sigma_y}{E}\right)\right]$	50.4 MPa	45.1 MPa
Plastic shear strain corresponding to 100% of strain (ε_{p1})	$\varepsilon_{p1} = 1 - \frac{\sigma_y}{E}$	0.993	0.992

Source: Poisson's ratio, $\nu = 0.34$, and ultimate elongation, $\varepsilon_u = 0.16$, are taken from Table 4-6 and A-2. Other variables are taken from Table 6-139.

The mechanical and geometrical representations of the waste package internals and the emplacement pallet are identical to those used in the analysis of the waste package surrounded by rubble (documented in Section 6.5.1.2.2).

6.4.4.4 Sequence of Analysis and Boundary Conditions

The analysis of the drip shield surrounded by rubble was carried out in four stages. The boundary conditions and modes of calculations (i.e., quasi-static and dynamic) were changed between different stages of analysis.

In the first calculation step, carried out under quasi-static conditions, the initial equilibrium under the actions of gravity and in situ stresses in the rock was calculated. (As discussed in *Drift Degradation Analysis* (BSC 2004 [DIRS 166107], Section 6.3.1.1), the principal stresses were considered to be vertical and horizontal. The magnitude of the vertical stress was taken to be 7 MPa; the horizontal stress was 3.5 MPa.) Because the strength of a Category 3 lithophysal rock mass was used, equilibrium was achieved for a stable initial outline of the emplacement drift (i.e., no rockfall took place). In this stage of calculation, the bottom and vertical boundaries of the calculation domain were fixed. A constant vertical stress, equal to overburden weight, was applied on the top boundary.

Rockfall is induced in the second stage of the calculations, also carried out under quasi-static conditions. Because in situ rock stresses are insufficient to cause significant fracturing of a Category 3 lithophysal rock mass, fracturing is induced by artificially reducing the cohesive and tensile strengths of the joints between the polygonal blocks (calibrated to Category 3 rock mass strength) to 0.1% of their initial values. The loose blocks formed by fractures emanating from the drift wall fall under gravity and accumulate on the drift floor, around and on top of the drip shield. The drip shield is set to behave elastically during the rockfall. The impacts of the blocks do not cause any plastic deformation of the drip shield. After the rockfall stops, or once a stable drift profile is achieved, an additional substep is conducted in which elastic–plastic properties are assigned to the drip shield and a new equilibrium point is calculated. In this step, inelastic deformation of the drip shield could take place under static rubble load. The geometry of the numerical representation at the end of the second stage for a particular realization of block geometry (with the random number-generator seed equal to 9) is shown in Figure 6-58.

The third stage of the calculations is carried out dynamically. During this stage, non-reflecting boundary conditions were applied at the top and bottom boundaries of the domain. (Nonreflecting boundary conditions dissipate incident P- and S-waves approximating their spatial divergence without their reflection back into the analyzed domain.) The free-field boundaries were applied on the vertical domain boundaries.[4] Incoming ground motions, propagating vertically upward, were applied at the base of the domain. Although the ground motions are provided as displacement, velocity, and acceleration histories, the boundary condition at the base of the model is applied as the stress history. The stress histories at the base are generated based on velocity histories and are equivalent to the velocity histories. (Static and

[4] The free-field boundaries are non-reflecting boundaries which account for free-field motion. In other words, motion of the boundaries synchronous with free-field motion is not dissipated.

dynamic boundary conditions are discussed and validated in *Drift Degradation Analysis* (BSC 2004 [DIRS 166107], Section 6.4.2.1).) Only those portions of ground-motion time histories bracketed by the 15% and 85% points in energy buildup measured by the Arias intensity were simulated (Assumption 5.17, Section 5). For each three-component set of ground motions, these points were determined for each component (H1, H2, and V); then, the earliest 15% point and the latest 85% point were used to define the duration for that set of ground motions. Time histories between the 15% and 85% thresholds were inspected visually, and thresholds were moved (the lower threshold was always decreased and the upper threshold always increased) to ensure that the ground motions do not start or end with relatively large velocities.

In the fourth, and final, stage of the simulation, the numerical representation was simulated to represent static equilibrium after completion of the dynamic simulation of seismic ground motions. All outside boundaries were fixed, and this stage of simulation was carried out quasi-statically.

6.4.4.5 Summary of Simulations

In all, 24 simulations were carried out. Three different drip shield geometries were analyzed to assess the effect of uniform corrosion on the drip shield performance: (a) the initial configuration (15 mm plate thickness), (b) the configuration in which all components are thinned by 5 mm (10 mm plate thickness), and (c) the configuration in which all components are thinned by 10 mm (5 mm plate thickness). Each configuration was analyzed for four sets of ground motion time histories at two PGV levels: 2.44 m/s and 4.07 m/s. The ground motion time histories at the 4.07 m/s PGV levels were derived by rescaling the available ground motions at the 5.35 m/s PGV level. (The scaling factor is 4.07/5.35 = 0.761.) Each ground motion included time histories in three coordinate directions. However, only one horizontal component H1 and the associated vertical component were used in the calculations (i.e., horizontal component H2 was not used). The ground motion time histories were selected from the set of 17 time histories available at each PGV level, and included time histories 3, 7, 9, and 13. In particular, ground motion 9 has the largest vertical PGA, ground motion 3 has a very large horizontal PGA (H1 component), and ground motions 7 and 3 have the largest vertical PGV. Ground motion 9 has the largest Arias intensity (Kramer 1996 [DIRS 103337]) as documented in *Drift Degradation Analysis* (BSC 2004 [DIRS 166107], Tables X-8 and X-10). Ground motion 13 has the largest power spectral density as documented in *Drift Degradation Analysis* (BSC 2004 [DIRS 166107], Tables X-13 and X-15). The vertical PGAs for analyzed ground motions are listed in Table 6-143. These PGAs are not inputs for the calculations. They are used at the end of this section to compare the results of quasi-static and dynamic drip shield framework fragility analysis.

Table 6-143. Vertical PGAs for Ground Motions Used in the Waste Package–Rubble Interaction Analyses

Ground Motion Realization	Vertical PGA for 2.44 m/s PGV Level (g)	Vertical PGA for 4.07 m/s PGV Level (g)[a]	Start Time(s)	End Time(s)
3	6.53	13.31	2.04	4.30
7	7.81	15.93	5.23	12.00
13	3.14	6.41	2.93	11.90
9	12.87	26.26	0.84	6.60

[a] Obtained by rescaling histories at the 5.35 m/s PGV level (DTN: MO0403AVTMH107.003 [DIRS 168892], folder ats.zip, files *mat03v.ats*, *mat07v.ats*, *mat09v.ats,* and *mat13v.ats*) by 4.07/5.35=0.761.

Sources: DTN: MO0403AVDSC106.001 [DIRS 168891], folder ats.zip, files *mat03v.ats*, *mat07v.ats*, *mat09v.ats,* and *mat13v.ats*.

NOTE: Times taken from output DTN: MO0701DRIPSHLD.000, file *\drip shield failure modes\dynamic simulations\5mm\inputs\1e-6\times.fis*.

Each of the analyzed ground motions was paired with a realization of block geometry. Pairing was done using the same Latin Hypercube sampling that was generated for simulations of the waste package surrounded with rubble (Section 6.5; the pairings are specifically discussed in Section 6.5.1.4.1).[5] The drip shield–rubble interaction was simulated for realizations 4, 11, 13, and 17 (i.e., ground motions 3, 7, 13, and 9, respectively) as listed in Table 6-144.

Table 6-144. Pairing of Rock Structure Realization and Ground Motion Realization Indices

Realization (Case) Number	Ground Motion Number	Random-Number-Generator Seed for Joint Pattern
4	3	4
11	7	9
13	13	14
17	9	2

Output DTN: MO0704SIPAWPSR.000, file *udec_sampling_17_results.xls*.

The 24 simulations conducted for this analysis are listed in Table 6-145. In the following discussion, specific pairings of rock structure and ground motion realizations are referenced using the rock structure index or case number.

[5] Because of limited number of simulations, the objective of the analysis was not to determine the entire range of responses but to focus on the most intense ground motions.

Table 6-145. List of Realizations for Dynamic Analysis of Drip Shield Failure Mechanism

Trial #	Realization (Case) Number	Ground Motion Number	Random-Number-Generator Seed for Joint Pattern	PGV (m/s)	Component Thinning (mm)
1	4	3	4	2.44	10
2	11	7	9	2.44	10
3	13	13	14	2.44	10
4	17	9	2	2.44	10
5	4	3	4	2.44	5
6	11	7	9	2.44	5
7	13	13	14	2.44	5
8	17	9	2	2.44	5
9	4	3	4	2.44	0
10	11	7	9	2.44	0
11	13	13	14	2.44	0
12	17	9	2	2.44	0
13	4	3	4	4.07	10
14	11	7	9	4.07	10
15	13	13	14	4.07	10
16	17	9	2	4.07	10
17	4	3	4	4.07	5
18	11	7	9	4.07	5
19	13	13	14	4.07	5
20	17	9	2	4.07	5
21	4	3	4	4.07	0
22	11	7	9	4.07	0
23	13	13	14	4.07	0
24	17	9	2	4.07	0

Source: Compiled and presented for illustrative purposes only.
NOTE: PGV = peak ground velocity.

6.4.4.6 Results

Results presented in this section demonstrate that buckling of the drip shield legs is the main potential failure mode of the drip shield framework when the emplacement drifts are subjected to strong seismic ground motions.

The calculations provide the final configuration of the emplacement drift and the objects located inside the drift (i.e., the drip shield and the waste package), including the residual stresses and accumulated strains. Stability of the drip shield is assessed based on the plastic shear strains. (Detailed discussion of the plastic shear strain and its relation to the effective strains is provided in Section 6.5.1.2.3) The plastic shear strain, which is the hardening parameter used in the UDEC formulation of plasticity and the variable that can be contoured by UDEC, if multiplied by $\sqrt{4/3}$ (Section 6.5.1.2.3), becomes the effective plastic strain and can be compared with the ultimate plastic strain (or elongation) in assessing rupture potential.

In the majority of the calculations, the maximum plastic shear strain, usually greater than the failure limit, is at the bottom of the legs in the contact region, where the legs are resting on the invert or the rubble. An example of the initial configuration, Case 4 at the 2.44 m/s PGV level, is shown in Figure 6-59. Although details of the geometry at the bottom of the drip shield legs are not included in this numerical representation, the results of the calculations indicate that the bottom of the legs, where relatively large forces will be transferred through a relatively small area, will undergo significant damage and distortion. Because the large deformation and plastic strains are localized to the contact area, the observed damage at the bottom of the legs will not affect the overall stability and performance of the drip shield structure.

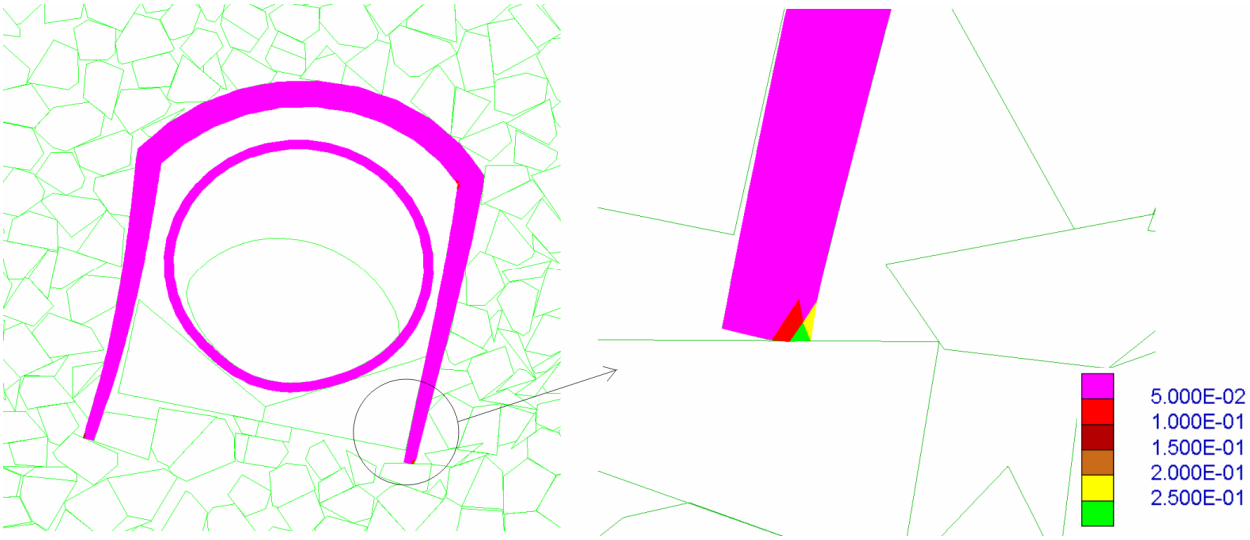

Output DTN: MO0701DRIPSHLD.000, file *\initial\2.44m_s\case4\case4seed4_eqfin.sav*.

Figure 6-59. Contours of Plastic Shear Strain in the Drip Shield with Details of the Bottom of the Drip Shield Leg for Case 4, Initial Configuration at the 2.44 m/s PGV Level

Deformed drip shield shapes and contours of the plastic shear strain for all analyzed cases are summarized in Figures 6-60 to 6-62 for the initial configuration, the configuration with all components thinned 5 mm, and the configuration with all components thinned 10 mm. For the cases in which the drip shield undergoes significant distortion, the maximum effective plastic strains and location of occurrence are indicated in the figures. The drip shield fails when the extensile effective plastic strain exceeds the ultimate plastic strain. The ultimate plastic strain of Titanium Grade 24 is used here because it is smaller than the value for Titanium Grade 7 and, therefore, results in underestimation of the framework strength. The ultimate plastic strain for Titanium Grade 24 is $\varepsilon_{up} = \varepsilon_u - \sigma_y / E = 0.16 - 862/112377 = 0.152$. The values are taken from Tables 4-6 and A-2. In Table 4-6, E is modulus of elasticity and σ_y is the yield strength.

The first observation from the calculation results is that the drip shield structure never fails as a result of snap-through in the middle of the crown. Only in Case 11, at the 4.07 m/s PGV for all geometrical configurations, are there indications of failure in the crown, but it occurs in the corner, near the connection between the crown and the legs. With the exception of two cases (Cases 11 and 17, at the 4.07 m/s PGV level for the configuration with the components thinned by 10 mm) in which the legs fail at the higher location, the drip shield fails by buckling of the legs near the bottom (i.e., 20 cm to 30 cm from the leg bottom). Figure 6-63 shows the results for three analyzed cases for the configuration of the waste package, the pallet, and the rubble around the drip shield.

A summary of drip shield stability assessment based on comparison of dynamic simulations and estimates from the quasi-static drip shield fragility analysis is provided in Table 6-146. This table provides a comparison of the drip shield framework fragility based on three-dimensional quasi-static analysis (Section 6.4.3.2) and two-dimensional dynamic analysis discussed in this section. The quasi-static analysis indicates the drip shield framework fails if the load limit (taken from Figure 6-57 or Table 6-137) is less than the ultimate load (computed using Equation 6-1 and the maximum vertical PGA for that ground motion also included in Table 6-146); otherwise, "stable" is indicated. Failure for the dynamic analyses is determined from inspection of the cross sections shown in Figures 6-60 to 6-62. Whenever the maximum tensile strains anywhere in the drip shield numerical representation are greater than the ultimate plastic strain (0.152), the drip shield is considered to "fail." (The accumulated plastic strains are positive, regardless of extension or compression. The compression or tension is determined based on position relative to the neutral axis of a bent beam.) As Table 6-146 shows, the quasi-static approach is in agreement with fully coupled dynamic approach or underestimates stability of the drip shield covered with rubble during strong seismic ground motions for all cases except Case 13 at 4.07 m/s PGV level, 10 mm and 15 mm plate thicknesses.

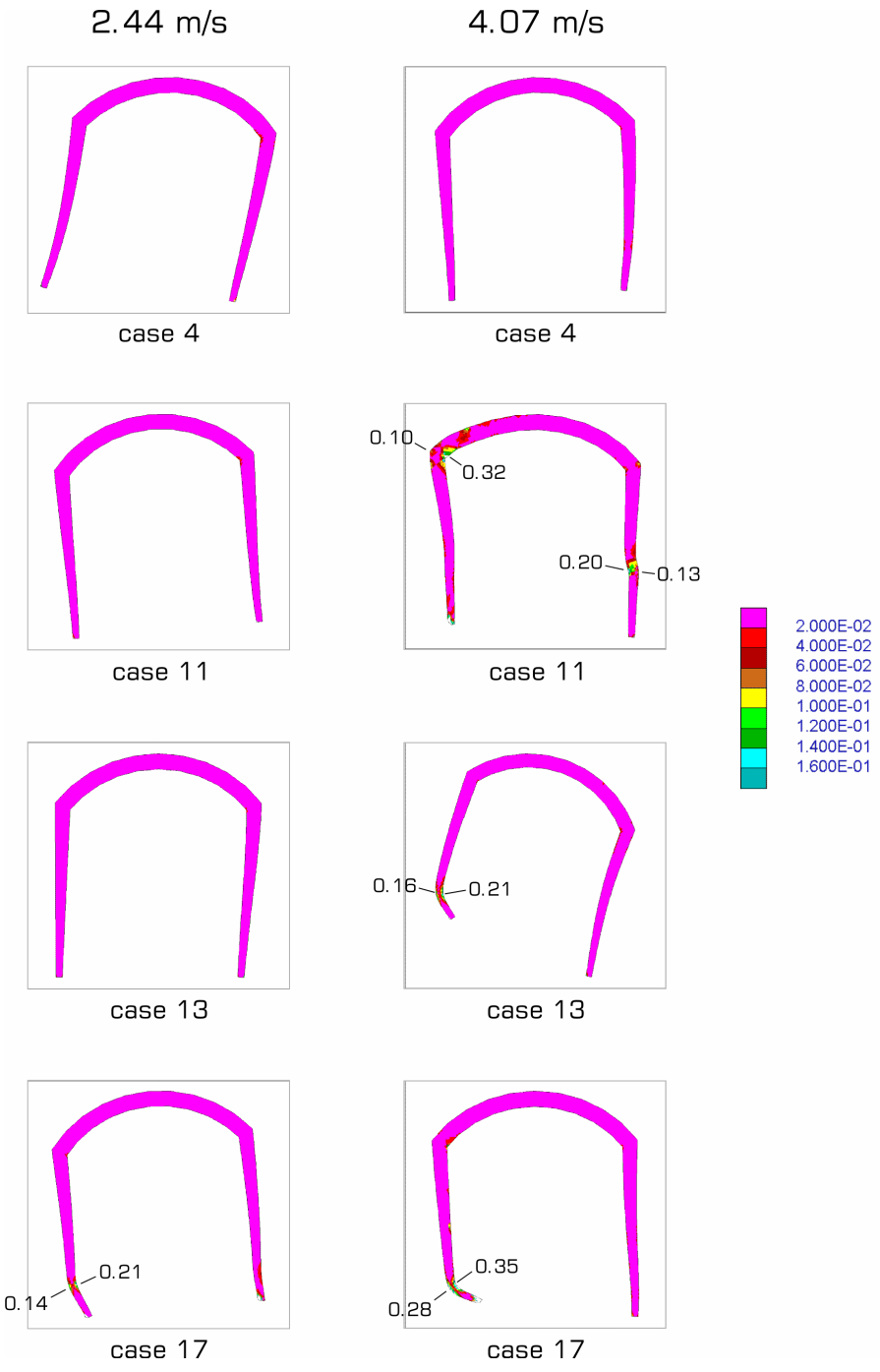

Output DTN: MO0701DRIPSHLD.000, files *\initial\2.44m_s\case4\case4seed4_eqfin.sav, \initial\4.07m_s\case4\case4seed4_eqfin.sav, \initial\2.44m_s\case11\case11seed9_eqfin.sav, \initial\4.07m_s\case11\case1seed9_eqfin.sav, \initial\2.44m_s\case13\case13seed14_eqfin.sav, \initial\4.07m_s\case13\case13seed14_eqfin.sav, \initial\2.44m_s\case17\case17seed2_eqfin.sav, \initial\4.07m_s\case17\case17seed2_eqfin.sav*.

NOTE: The maximum effective plastic strains (obtained by multiplying the plastic shear strains by $\sqrt{4/3}$) are indicated in some cases where large distortion occurred.

Figure 6-60. Deformed Drip Shield Geometries and Contours of Plastic Shear Strain for the Initial Drip Shield Configuration (Plate Thickness 15mm)

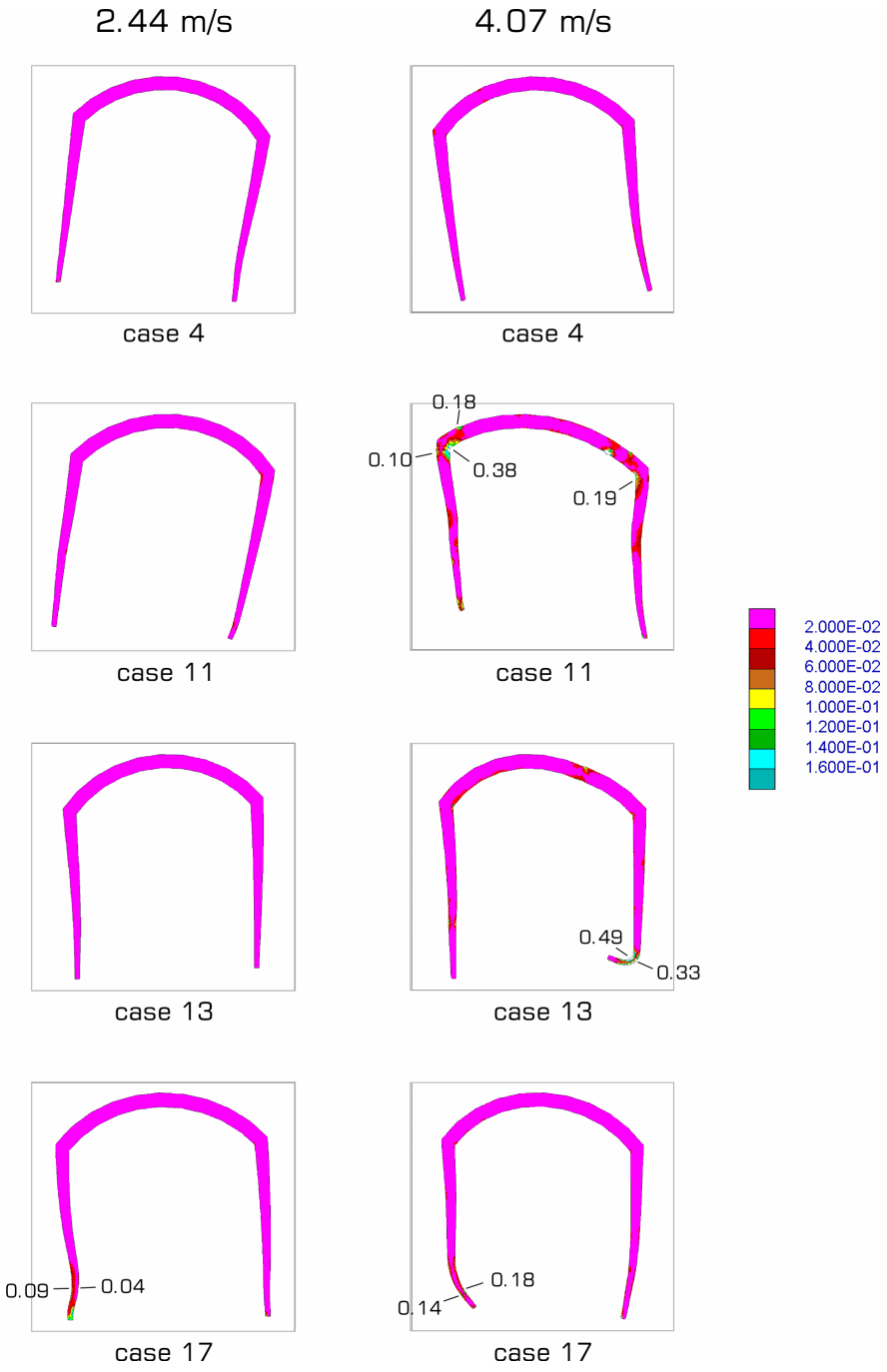

Output DTN: MO0701DRIPSHLD.000, files *\5mm\2.44m_s\case4\case4seed4_eqfin.sav, \5mm\4.07m_s\case4\case4seed4_eqfin.sav, \5mm\2.44m_s\case11\case11seed9_eqfin.sav, \5mm\4.07m_s\case11\case1seed9_eqfin.sav, \5mm\2.44m_s\case13\case13seed14_eqfin.sav, \5mm\4.07m_s\case13\case13seed14_eqfin.sav, \5mm\2.44m_s\case17\case17seed2_eqfin.sav, \5mm\4.07m_s\case17\case17seed2_eqfin.sav*.

NOTE: The maximum effective plastic strains (obtained by multiplying the plastic shear strains by $\sqrt{4/3}$) are indicated several cases where large distortion occurred.

Figure 6-61. Deformed Drip Shield Geometries and Contours of Plastic Shear Strain for the Drip Shield Configuration with Components Thinned by 5 mm (Plate Thickness 10mm)

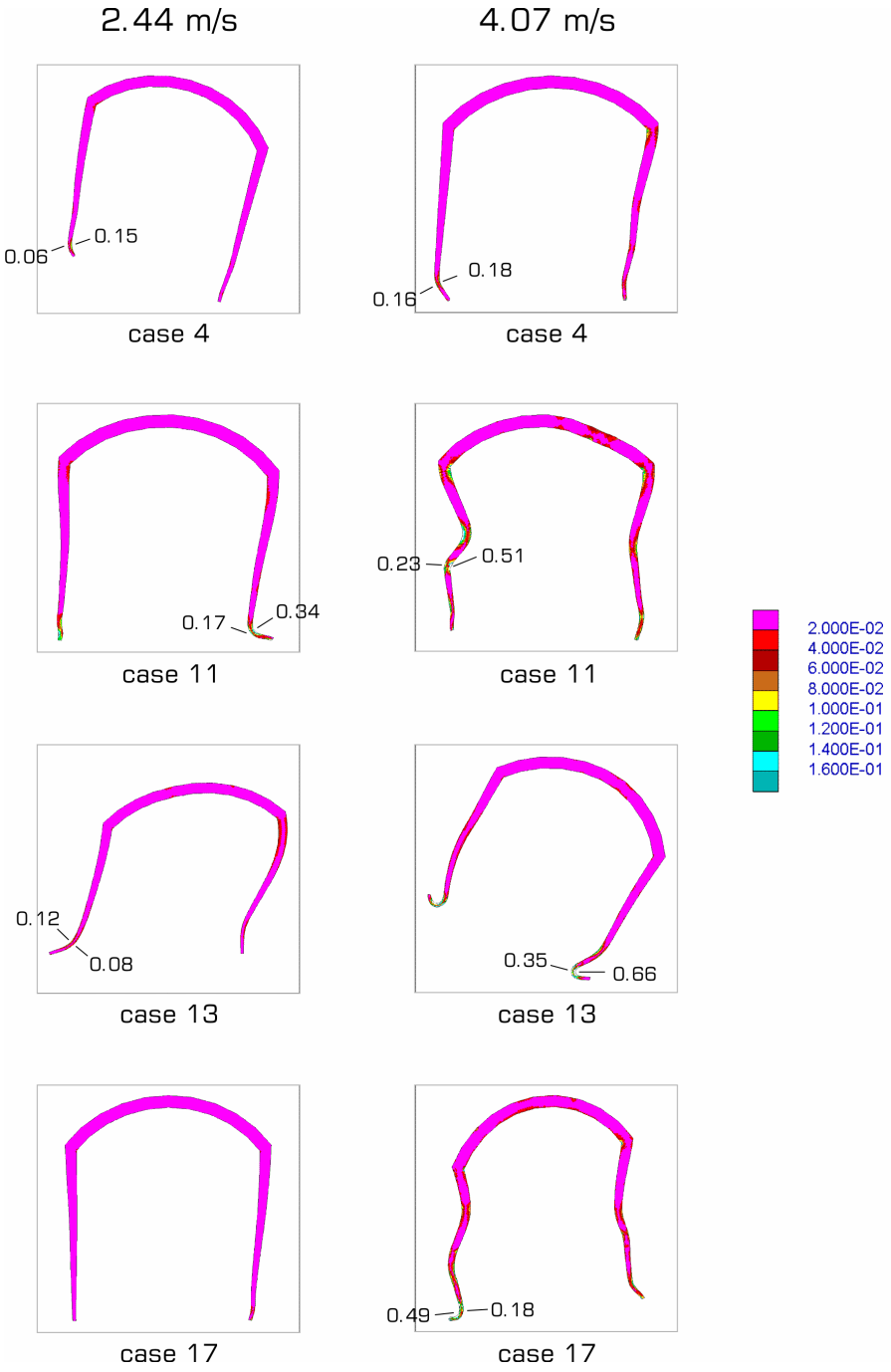

Output DTN: MO0701DRIPSHLD.000 files *\10mm\2.44m_s\case4\case4seed4_eqfin.sav, \10mm\4.07m_s\case4\case4seed4_eqfin.sav, \1omm\2.44m_s\case11\case11seed9_eqfin.sav, \10mm\4.07m_s\case11\case1seed9_eqfin.sav, \10mm\2.44m_s\case13\case13seed14_eqfin.sav, \10mm\4.07m_s\case13\case13seed14_eqfin.sav, \10mm\2.44m_s\case17\case17seed2_eqfin.sav, \10mm\4.07m_s\case17\case17seed2_eqfin.sav*.

NOTE: The maximum effective plastic strains (obtained by multiplying the plastic shear strains by $\sqrt{4/3}$) are indicated in several cases where large distortion occurred.

Figure 6-62. Deformed Drip Shield Geometries and Contours of Plastic Shear Strain for the Drip Shield Configuration, with Components Thinned by 10 mm (Plate Thickness 5 mm)

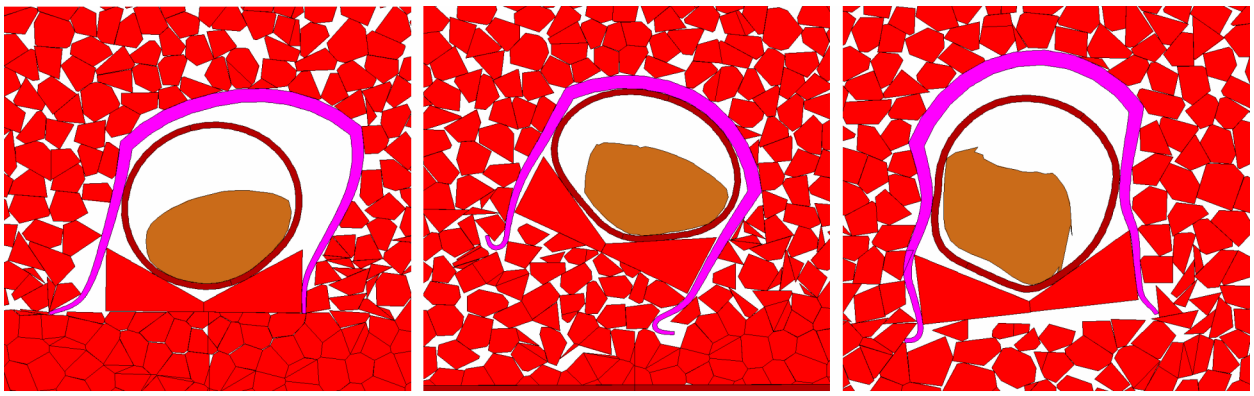

PGV 2.44 m/s; case 13 | PGV 4.07 m/s; case 13 | PGV 4.07 m/s; case 17

Output DTN: MO0701DRIPSHLD.000, files *\10mm\2.44m_s\case13\case13seed14_eqfin.sav, \10mm\4.07m_s\case13\case13seed14_eqfin.sav, and \10mm\4.07m_s\case17\case17seed2_eqfin.sav*.

Figure 6-63. Configuration of Drip Shield, Rubble, Waste Package and Pallet at the End of Selected Simulations for the Geometry Thinned by 10 mm (component thickness 5 mm)

Table 6-146. Comparison of the Drip Shield Stability Assessment Based on Two-Dimensional Dynamic and Three-Dimensional Quasi-Static Analyses

				Initial Configuration, 15-mm Plate Thickness		5-mm-Thinned Configuration, 10-mm Plate Thickness		10-mm-Thinned Configuration, 5-mm Plate Thickness	
Case	PGV Level (m/s)	Vertical PGA (g)[a]	Ultimate Load p_{ul} (kPa)[b]	Fragility Analysis (Load Limit 1698 kPa[c])	Dynamic Analysis (Fig. 6-60)	Fragility Analysis (Load Limit 1094 kPa[c])	Dynamic Analysis (Fig. 6-61)	Fragility Analysis (Load Limit 501 kPa[c])	Dynamic Analysis (Fig. 6-62)
4	2.44	6.53	963	stable	stable	stable	stable	fails	stable
11	2.44	7.81	1,126	stable	stable	fails	stable	fails	fails
13	2.44	3.14	529	stable	stable	stable	stable	fails	stable
17	2.44	12.87	1,773	fails	stable	fails	stable	fails	stable
4	4.07	13.31	1,830	fails	stable	fails	stable	fails	fails
11	4.07	15.93	2,165	fails	fails	fails	fails	fails	fails
13	4.07	6.41	947	stable	fails	stable	fails	fails	fails
17	4.07	26.26	3,485	fails	fails	fails	stable	fails	fails

Sources: [a] Table 6-143.

[b] Computed as $p_{ul} = p(1+\mathrm{PGA})$ in Equation 6-1, where p is static rubble pressure, taken from Table 6-136, average top (vertical) pressure.

[c] Quasi-static limit loads taken from Table 6-137 and Figure 6-57 for average rubble load distribution.

NOTE: PGA = peak ground acceleration; PGV = peak ground velocity.

6.4.5 Kinematic Analyses for Waste Package-to-Drip Shield Impacts

The analysis presented in this section provides a characterization of the interactions between the waste package and drip shield in response to postclosure ground motions for an emplacement drift that has partially or completely collapsed and "pinned" the drip shield in place. The primary area of concern is the potential tearing of welds and associated rupture of the drip shield

as a result of a waste package longitudinally impacting an internal bulkhead (rib) of the drip shield.

The potential damage to the waste package as a result of impacts with the drip shield has previously been shown (BSC 2005 [DIRS 173247], Section 6.5.3.1) to be significantly lower than damage due to a waste package having an end-to-end impact with an adjacent waste package. Although the waste package does not experience significant damage from impacts with the drip shield, there is the potential for tearing of welds between the drip shield plates and its framework and tearing of the plates themselves when the edge or lip of a waste package longitudinally impacts or "clips" an internal rib on the underside of the drip shield. The potential for this type of tearing failure is assessed through the three-dimensional kinematic calculations. These calculations characterize the frequency and impact velocity between the TAD-bearing and codisposal waste packages and the internal ribs of the drip shield.

This analysis supports an assessment of the importance of waste package-to-drip shield impacts for the seismic scenario class (SNL 2007 [DIRS 176828]). A previous assessment was performed for the potential for drip shield failure from waste package impacts (BSC 2005 [DIRS 173172], Attachment VI) and found that (a) each of the drip shield components remained within its true ultimate strength through all but one of the impact scenarios, and (b) a bulkhead could fail at the point of impact if it is clipped by a waste package. It should be noted that this is a low-probability event (BSC 2005 [DIRS 173172], Section VI-3.7).

Section 6.3.2.1 describes models for the kinematic analyses of multiple waste packages with the objective of determining damaged area and rupture probability for the waste packages. As those analyses were aimed at quantifying waste package-to-waste package and waste package-to-pallet impacts, the bulkheads and bulkhead flanges at the top of the drip shield were not modeled. The drip shield was modeled as a surface that is uniform in the direction along the drift. For the analyses described in this section, the kinematic model with multiple waste packages was modified to include ribs that represent the drip shield bulkheads and bulkhead flanges.

The goal of this analysis is to determine the frequency and impact velocity between waste packages and the bulkhead structures. As the analysis is kinematic in nature, the detailed geometry of the bulkhead structures was of secondary importance and certain simplifications were employed to create a more efficient simulation. The longitudinal stiffeners were omitted and the combination of bulkhead and bulkhead flange are represented as ribs that are modeled as shells. The drip shield ribs have a uniform thickness of 44.5 mm (1.75 in), and the contact thickness is defined such that the ribs protrude approximately 55.9 mm (2.2 in) below the drip shield surface. The ribs are spaced at 1097.3-mm (43.2-in) intervals, a distance which is based on the average spacing between the bulkheads. The lowest point of the ribs at the crown of the drip shield is approximately 2717.8 mm (107 in) above the invert, which represents the height from the invert to the bulkhead and bulkhead flange. This geometry is an approximation of the drip shield dimensions (BSC 2004 [DIRS 170791], Attachment I).

Figure 6-64 shows the drip shield ribs, protruding below the top of the drip shield (not shown). With the exception of the addition of the drip shield ribs, the kinematic analyses are identical to those described in Section 6.3.2.1 for the 13-waste-package configuration. Impacts of the five central waste packages with the drip shield ribs were quantified. The five central packages

consist of the three central TAD-bearing waste packages and the two central codisposal waste packages. The primary concern of these analyses was quantifying "tearing" types of impacts between the waste packages and drip shield ribs. Figure 6-65 illustrates this differentiation.

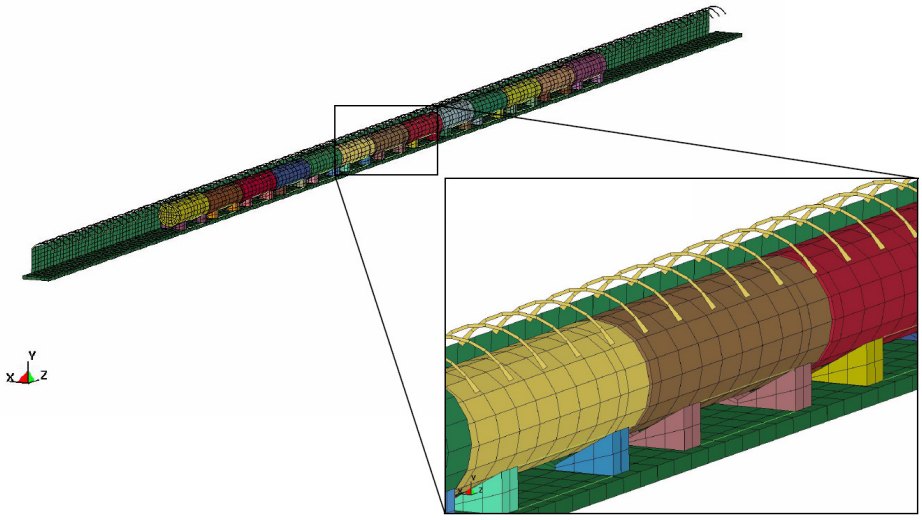

Output DTN: LL0704PA041SPC.026, file *Figures_Mech_Assessment_AMR.tar.gz*.

Figure 6-64. Thirteen-Waste-Package Configuration with Drip Shield Ribs for Focus on the Central Five TAD-Bearing and Codisposal Waste Packages

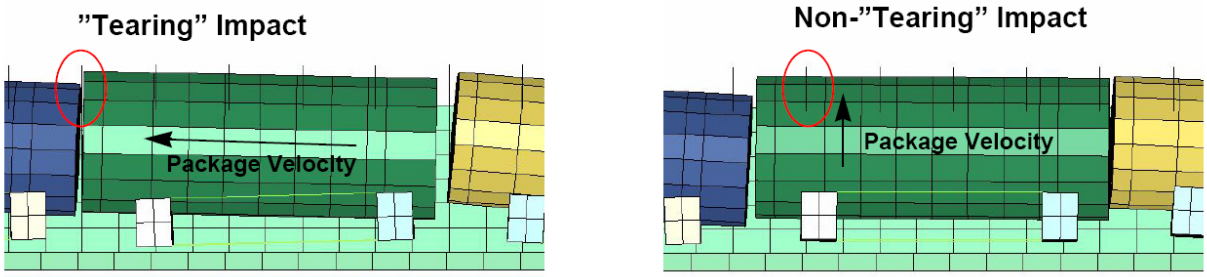

Output DTN: LL0704PA051SPC.026, file *Figures_Mech_Assessment_AMR.tar.gz*.

Figure 6-65. Illustration of the Difference between "Tearing" and Non-"Tearing" Impacts

To quantify the frequency and impact velocity of "tearing" impacts, contact pairs were defined between the two end surfaces of each waste package and the collection of drip shield ribs. Observation of a nonzero contact force for any of the waste packages of interest (H through L, as shown in Figure 6-10) indicated a "tearing" impact with a drip shield rib. By noting the time of impact and determining the drip shield and waste package velocities at the immediately preceding time step, relative impact velocities were calculated. Only the z-component (along the drift) of velocity was calculated, as this is the measure of the tearing force on the drip shield rib.

Kinematic analyses were conducted for peak ground motion velocities of 1.05 m/s, 2.44 m/s, and 4.07 m/s. A full set of calculations (realizations 1-17) was performed for 4.07 m/s PGV. For

1.05 and 2.44 m/s PGV, reduced sets of calculations were performed. The reduced sets were justified based on observations of the 13-waste-package configuration kinematic calculations of Section 6.3. In these calculations, if the waste packages of interest (H to L) never contacted the top of the drip shield, then it could safely be assumed that they would also not contact the drip shield ribs. An important point in this regard is that the drip shield representation in the calculations of Section 6.3 is lowered to the position of the bottom of the longitudinal stiffeners, less than one inch above the bottom of bulkheads. Thus, lack of contact with the top of the drip shield indicates that no waste package reaches that height, which is approximately the same as the bottom of the drip shield ribs.

Table 6-147 summarizes the contact postprocessing results from the 13-waste-package configuration kinematic calculations of Section 6.3. Note that this table overestimates the number of realizations with potential for a "tearing" waste package-to-drip shield rib impact. Positive contact results in these cases indicate contact at any point along the drip shield, and not necessarily at a point or with a waste package velocity vector that would cause a "tearing" impact. It should be noted that the evaluation of whether contact occurs is not necessary at the 0.40 m/s PGV level for other than realizations 3 and 10, since only those two realizations had any impacts between the central five waste packages and the top of the drip shield at the higher 1.05 m/s PGV level.

Table 6-147. Summary of the Occurrence of Impacts between Waste Packages and the Drip Shield

	PGV (m/s)		
Realization	**2.44**	**1.05**	**0.40**
1	No	No	–
2	No	No	–
3	Yes	Yes	No
4	Yes	No	–
5	No	No	–
6	No	No	–
7	Yes	No	–
8	No	No	–
9	No	No	–
10	Yes	Yes	No
11	No	No	–
12	No	No	–
13	No	No	–
14	No	No	–
15	Yes	No	–
16	No	No	–
17	No	No	–

Output DTN: LL0704PA050SPC.025, file *WPDS_kinematic_analyses_summary.xls,* sheet "WP-DS Contact."

NOTE: Based on the kinematic analyses of the 13-waste-package-configuration in Section 6.3.

Tables 6-148, 6-149, and 6-150 summarize the observed "tearing" impacts between drip shield ribs and waste packages H through L for analyses with PGV of 1.05 m/s, 2.44 m/s, and 4.07 m/s,

respectively. Full details of impact times and impact velocities for all analyses are located in output DTN: LL0704PA050SPC.025.

Table 6-148. Summary of Impacts between the Five Central Waste Packages (H to L) and the Drip Shield Ribs for 1.05 m/s PGV

Realization	Number of Impacts	Number of Impacts withVelocity Greater Than			Maximum Impact Velocity (m/s)
		2 m/s	3 m/s	4 m/s	
3	2	0	0	0	0.501
10	0	0	0	0	–
Total	**2**	**0**	**0**	**0**	**NA**

LL0704PA050SPC.025, file *WPDS_kinematic_analyses_summary.xls,* sheet "All Impacts Summary."

Table 6-149. Summary of Impacts between the Five Central Waste Packages (H to L) and the Drip Shield Ribs for 2.44 m/s PGV

Realization	Number of Impacts	Number of Impacts with Velocity Greater Than			Maximum Impact Velocity (m/s)
		2 m/s	3 m/s	4 m/s	
3	0	0	0	0	–
4	1	0	0	0	0.501
7	0	0	0	0	–
10	4	0	0	0	0.994
15	2	0	0	0	0.383
Total	**7**	**0**	**0**	**0**	**NA**

Output DTN: LL0704PA050SPC.025, file *WPDS_kinematic_analyses_summary.xls,* sheet "All Impacts Summary."

Table 6-150. Summary of Impacts between the Five Central Waste Packages (H to L) and the Drip Shield Ribs for 4.07 m/s PGV

Realization	Number of Impacts	Number of Impacts with Velocity Greater Than			Maximum Impact Velocity (m/s)
		2 m/s	3 m/s	4 m/s	
1	0	0	0	0	–
2	0	0	0	0	–
3	2	1	0	0	2.614
4	7	1	1	0	3.071
5	1	1	1	0	3.315
6	2	0	0	0	1.615
7	0	0	0	0	–
8	0	0	0	0	–
9	0	0	0	0	–
10	13	2	0	0	2.694
11	0	0	0	0	–
12	5	1	1	1	4.301
13	0	0	0	0	–
14	4	1	1	0	3.419
15	11	0	0	0	1.958
16	1	1	1	1	4.782
17	2	1	0	0	2.802
Total	**48**	**9**	**5**	**2**	**NA**

Output DTN: LL0704PA050SPC.025, file *WPDS_kinematic_analyses_summary.xls,* sheet "All Impacts Summary."

6.4.6 Effect of Uneven Invert Settlement on Drip Shield Stability

6.4.6.1 Purpose

This task responds to an AIN from the NRC (Key Technical Issue Agreement Total System Performance Assessment and Integration 2.02, Comment J-2 (Kokajko 2005 [DIRS 177025], pp. 5 to 6 of enclosure).

This section presents an analysis of the effect of settlement of the invert during the postclosure period on the stability of the drip shield when subjected to seismic ground motion. The emplacement drift invert will be filled initially with leveled, crushed tuff, as illustrated in Figure 6-66. Carbon steel profiles, forming a framework imbedded in the crushed tuff, will corrode gradually (Assumption 5.18, Section 5), resulting in settlement of the crushed tuff in the invert. Seismic ground motion also will cause the invert to deform. Relatively low-intensity seismic shaking will cause the invert to settle. On the other hand, strong ground motions can cause large deformation of tuff particles, possibly resulting in bulking of the tuff in the invert and certainly changing the invert configuration. As a result the drip shield will not be resting on the planar, horizontal surface. From the perspective of drip shield stability, the most unfavorable result will be that the uneven settlement of the invert tilts the entire drip shield structure. There is a high degree of uncertainty in the deformation of the invert as a function of time and location, since it will depend on the rate of steel corrosion, the frequency and magnitude of seismic events, and the evolution of the rubble volume accumulated on the crushed tuff in the invert and on the drip shield. Rather than estimating the magnitude of uneven settlement, the drip shield stability analysis was carried out over a range of values bounding the settlement that can reasonably be expected to occur. The simulations were conducted for five different magnitudes of settlement (5 cm, 10 cm, 15 cm, 20 cm, and 25 cm) for two realizations of static rubble loading.

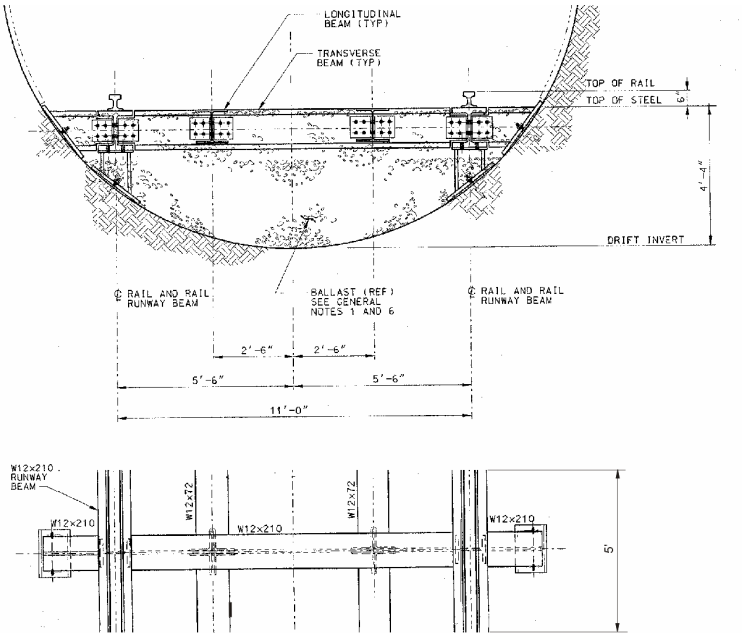

Source: SNL 2007 [DIRS 179354], Section 4.1.1, Table 4-1, item 02-07.

Figure 6-66. Drip Shield Support Elements in an Invert

The maximum magnitude of uneven settlement of the crushed tuff in the invert was estimated based on the geometry of the tuff in the invert and the volume of the steel components that will be initially built into the invert. (Degradation of the steel components due to corrosion is considered to be a main cause for settlement of the crushed tuff in invert.) The effect of different levels (including the maximum, bounding magnitudes) of uneven settlement on the stability of the drip shield was analyzed in three-dimensional calculations. The effect of uneven settlement was analyzed for static rubble load.

The calculations of the effect of uneven settlement on structural integrity and stability of the drip shield were carried out using a qualified version of the finite-difference program FLAC3D V. 2.1.

6.4.6.2 Numerical Representation

As in the previous analyses (BSC 2004 [DIRS 169753], Section 5.2.2.3), only one section of the drip shield is analyzed (Figure 6-67). The drip shield geometry used in the investigation is the same as that used in *Creep Deformation of the Drip Shield* (BSC 2005 [DIRS 174715], Section 5.4.1.1), except that the entire representation was rotated to account for uneven settlement. The geometry of the drip shield (and the representations of the invert and the pallet) was rotated around the bottom of one leg, which was kept fixed to allow for specified displacement of the settling end.

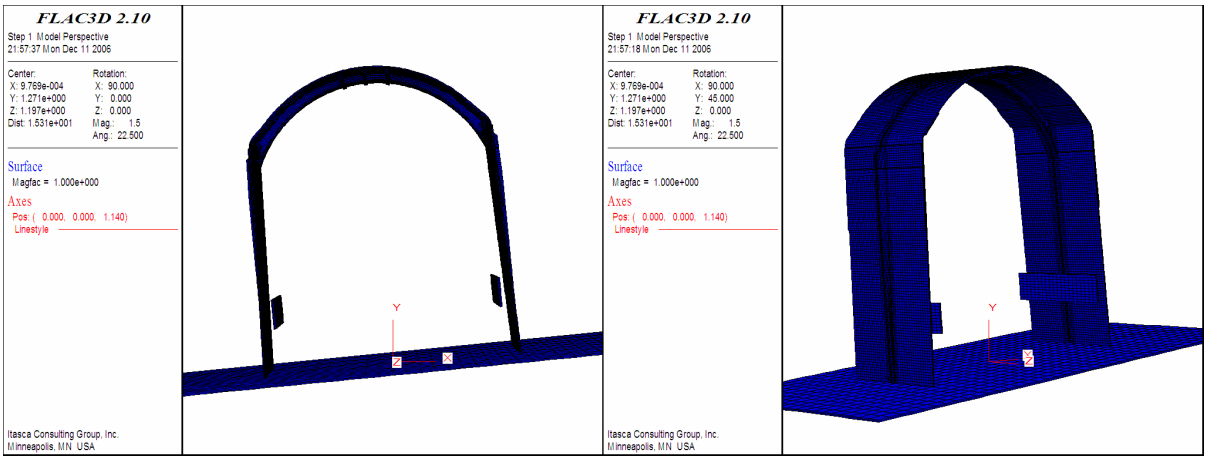

Source: Created for illustrative purposes only.

Figure 6-67. Geometry of the Drip-Shield Numerical Representation Used for Analysis of the Effect of Uneven Invert Settlement

Two static rubble-load realizations were used in the analysis. These were taken from the earlier analysis (BSC 2004 [DIRS 169753]) and were (a) load realization 3, which had the greatest vertical loading, and (b) load realization 4, which had the greatest lateral loading (see Table 6-149). The direction of rotation and uneven settlements for each load realization were selected depending on the direction of the rubble loading and drip shield deformation (Figure 6-68). Although the drip shield structure was rotated, the loads specified for 30 outline intervals (as illustrated in Figure 6-51) were not. Rather, they were applied in the same direction as before the rotation. (If the loads were rotated together with the structure, the conditions of

drip shield stability would remain unchanged, because gravity loading is relatively small.) Simulations were conducted in the large strain mode using the same mesh (discretized geometry) and boundary conditions as in *Creep Deformation of the Drip Shield* (BSC 2005 [DIRS 174715], Section 5.4.1). No interaction of the drip shield with surrounding rubble was considered in these calculations (i.e., all loads are dead loads that did not change as a function of drip shield deformation).

The potential for invert settlement due to corrosion of steel profiles was estimated by assuming total degradation of the steel structural elements (Assumption 5.18, Section 5). Transverse support beams are placed every five feet (Table 4-1). Thus, the total volume of the material in the invert is estimated for a representative five-foot-long segment of the invert, shown in Figure 6-66.

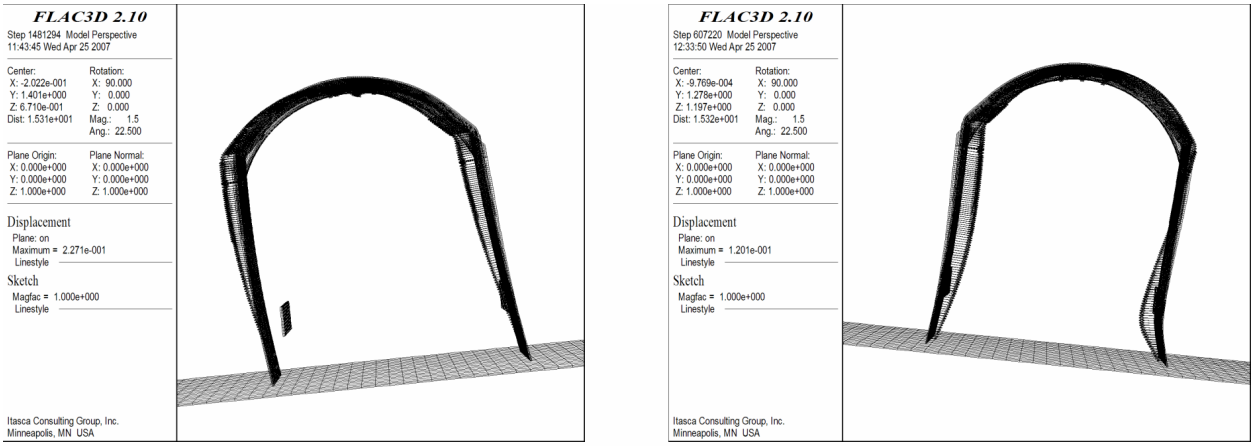

a) realization 3 b) realization 4

Output DTN: MO0701DRIPSHLD.000, files *\realization 3\solve_25L/sav* and *\realization 4\solve_25R.sav*.

Figure 6-68. Displacement Vector Fields (m) from Two Simulations of the Effect of Invert Settlement on Drip Shield Stability

The volumes of the longitudinal and transverse steel support beams beneath the drip shield were calculated based on information in *Total System Performance Assessment Data Input Package for Requirements Analysis for EBS In-Drift Configuration* (SNL 2007 [DIRS 179354], Section 4.1.1, Table 4-1, item 02-07) and cross-sectional properties (AISC 1995 [DIRS 114107], pp. 1-28 and 1-30). The volume of two 5-ft-long (1.524 m) longitudinal W12 × 72 beams is 0.04148 m^3; the volume of two 5-ft-long W12 × 210 runway beams is 0.12152 m^3. The transverse W12 × 210 beam is 4.698 m long and has a volume of 0.18731 m^3. Finally, two transverse beam supports, which are W10 × 100 profiles, have a volume of 0.01431 m^3. In the representative volume, the total volume of steel is 0.364 m^3 (two longitudinal beams, two runway beams, one transverse beam and two transverse beam supports), which corresponds to 5.5% of the total volume of material supporting the drip shield.

Because of their relatively small volume, degradation of steel support components due to corrosion does not have a significant impact on the potential for uneven settlement of the drip shield. Shifting of the crushed rock due to earthquakes or uneven settlement of the invert itself would have a much larger effect. Considering the total thickness of approximately 1.01 m for

the crushed tuff underneath the drip shield legs in the design illustrated in Figure 6-66, the maximum value of 0.25 m used in the calculations is an upper bound on the possible magnitudes of uneven settlement. Furthermore, the settlement of crushed tuff in the invert will be spatially variable, both in cross section (which is analyzed here as the cause for inclination of the drip shield) and along the emplacement drift. The drip shield is a three-dimensional structure 5.805 m long. Furthermore, adjacent drip shield sections are interlocked. The spatial variation in uneven settlement will occur on a length scale smaller than drip shield length. Consequently, uneven settlement will not cause the entire drip shield to tilt. Instead, the drip shield will arch over the regions of large settlement of the crushed tuff.

The material properties of Titanium Grades 7 and 24 at 150°C temperature used in the simulations are taken from *Creep Deformation of the Drip Shield* (BSC 2005 [DIRS 174715], Table 5.2-1). The FLAC3D input properties used in the mechanical representation of Titanium Grades 7 and 24 are listed in Table 6-151.

Table 6-151. FLAC3D Input Parameters Used to Represent the Mechanical Behavior of Titanium Grades 24 and 7 in the Analysis of the Effect of Invert Settlement on Drip Shield Stability

Property		Titanium Grade 24	Titanium Grade 7
Bulk modulus (K)	$K = \frac{E}{3(1-2\nu)}$	111.81GPa	105.21GPa
Shear modulus (G)	$G = \frac{E}{2(1+\nu)}$	39.49GPa	37.69GPa
Cohesion (c)	$c = \frac{\sigma_y}{2}$	341 MPa	89 MPa
Plastic shear strain corresponding to 100% of strain (ε_{p1})	$\varepsilon_{p1} = 1 - \frac{\sigma_y}{E}$	0.994	0.998

Source: BSC 2005 [DIRS 174715], Table 5.2-1.

NOTE: E is the Young's modulus; ν is the Poisson's ratio; σ_y is the yield strength; and E_t is the postyield tangent modulus of Titanium Grades 24 and 7 at 150°C.

6.4.6.3 Results

All simulations show a stable response for settlements of 5 cm, 10 cm, 15 cm, 20 cm, and 25 cm on the left side of the drip shield for rubble load realization 3 and on the right side of the drip shield for rubble load realization 4. Maximum drip shield displacement reaches a magnitude of 22.71 cm (for the 25-cm settlement), with a horizontal middle-of-the-crown displacement of 21.75 cm. The same magnitude of imposed settlement load as in realization 4 causes maximum drip shield displacement of 12.12 cm, with the horizontal component of the middle-of-the-crown displacement equal to 9.56 cm. Maximum displacements, maximum stresses, and stress differences from all simulations are summarized in Table 6-152. Positive horizontal displacement is to the right. Deformation patterns for two external-loading scenarios

are depicted in Figure 6-68. For a given loading, the displacement pattern is the same for all settlement values; only the displacement magnitudes are different.

Table 6-152. Summary of the Effect of Uneven Settlement on Drip Shield Stability

Realization	Settlement [cm]	Maximum Stress σ_1 Titanium Grade 24 [MPa]	σ_1-σ_3 Titanium Grade 24 [MPa]	Maximum Stress σ_1 Titanium Grade 7 [MPa]	σ_1-σ_3 Titanium Grade 7 [MPa]	Horizontal Crest Displacement [cm]
3	0	411	414	239	175	−15.88
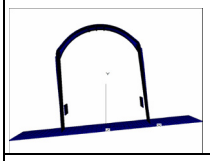	5	430	433	223	161	−16.58
	10	485	488	249	170	−19.25
	15	510	513	258	168	−20.09
	20	529	533	267	174	−20.88
	25	554	558	274	174	−21.75
4	0	283	498	227	178	4.22
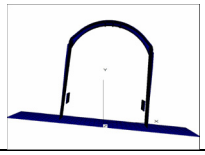	5	296	518	217	172	4.26
	10	338	551	222	172	5.59
	15	380	604	240	174	6.85
	20	434	675	286	178	8.83
	25	447	675	293	179	9.56

Output DTN: MO0701DRIPSHLD.000, 3_4_5.zip. files *\realization 3\solve_5L.sav, \realization 3\solve_10L.sav, \realization 3\solve_15L.sav, \realization 3\solve_20L.sav, \realization 3\solve_25L.sav, \realization 4\solve_5R.sav, \realization 4\solve_10R.sav, \realization 4\solve_15R.sav,* and *\realization 4\solve_20R.sav, \realization4\solve_25R.sav*.

Source: DTN: MO0508SPACREEP.000 [DIRS 179984].

NOTE: The table as it is does not exist in the DTN listed as the source; however the values can be extracted from the submitted files.

Stresses show consistent pattern, and maximum magnitudes are reached for the cases with maximum settlements. Principal stresses for the 25-cm settlement case and load realization 3 are shown in Figure 6-69. The maximum compression for this loading case is 468 MPa on the flange of the bulkhead (Figure 6-69a), while the maximum tensile stress reaches 554 MPa in the vertical support beams, as shown in Figure 6-69b.

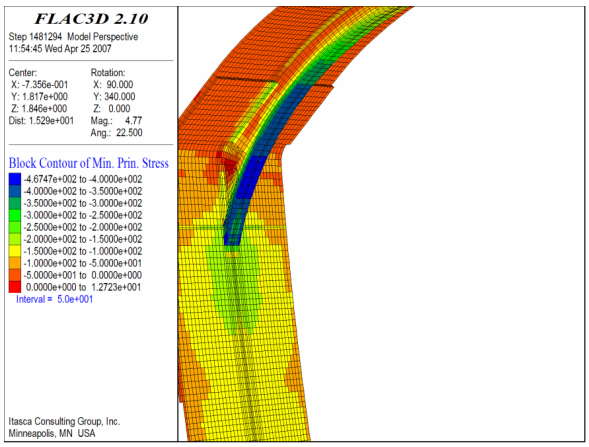

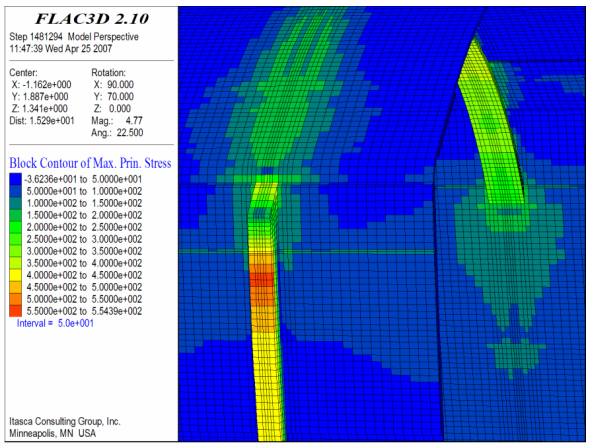

a) minimum principal stress

b) maximum principal stress

Output DTN: MO0701DRIPSHLD.000, file *\realization 3\solve_25L.sav*.

Figure 6-69. Minimum and Maximum Principal Stresses (Pa) in the Drip Shield for Load Realization 3, 25-cm Settlement

For load realization 4, with a 25-cm settlement, the maximum tensile stress of 447 MPa is smaller than that reached for the same amount of settling for load realization 3. Maximum compression reaches 675 MPa in the vertical support beam (Figure 6-70a), while maximum tension is in the upper fiber of the crown beam (Figure 6-70b and c).

In all cases, the stresses in Titanium Grades 7 and 24 are smaller than the true tensile strengths of those materials at 150°C; the tensile strength values are 347 MPa for Titanium Grade 7 and 982 MPa for Titanium Grade 24 (BSC 2004 [DIRS 168993], Section 5.1.2). Thus, settlement of the invert is not expected to materially alter the drip shield function.

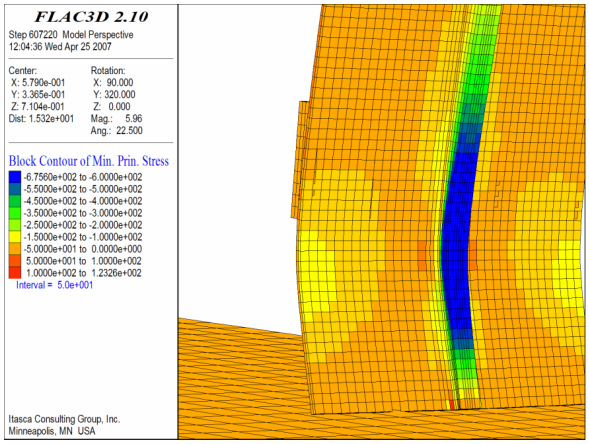

a) minimum principal stress

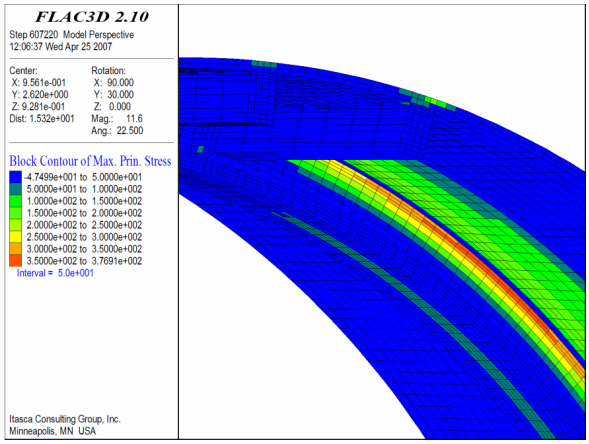

b) maximum principal stress, view 1

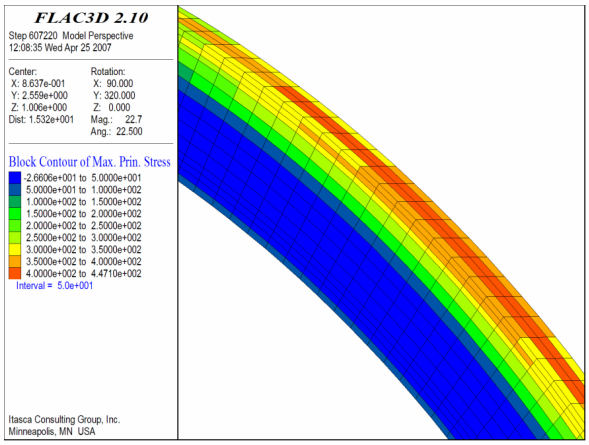

c) maximum principal stress, view 2

Output DTN: MO0701DRIPSHLD.000, file *\realization 4\solve_25R.sav*.

Figure 6-70. Minimum and Maximum Principal Stresses (Pa) in the Drip Shield for Load Realization 4, 25-cm Settlement

6.4.7 Analysis for Drip Shield Fragility and Damage Due to Impact of Large Blocks

6.4.7.1 Purpose

The number of joint sets, their spacing, and their orientation in the rock mass define the size and shape of the blocks that potentially can become unstable when emplacements drifts are subjected to different loads. Joint spacing in the nonlithophysal units is greater than joint spacing in the lithophysal units. Consequently, potential rockfall in the nonlithophysal rock mass will consist of much larger blocks than in the lithophysal rock mass. The impact of large blocks into the drip shield, as they fall after being dislodged, could cause damage to and even failure of the drip shield plates and the structural components of the drip shield framework (i.e., bulkheads, support beams, and stiffeners). Because approximately 15% of the emplacement drifts will be located in

the nonlithophysal units and because *Drift Degradation Analysis* (BSC 2004 [DIRS 166107], Section 6.3.1.2.3) indicates that strong seismic ground motions (particularly for PGVs equal to or greater than 1 m/s) will cause significant rockfall in the nonlithophysal units, block impacts into the drip shield were analyzed, and damage and potential for drip shield failure (either tearing of the plates or failure of the structural components) was estimated. The purpose of the analyses was to generate lookup tables for damage area and strain in the drip shield as functions of block energy and thickness of the drip shield plates and framework. The lookup tables were generated for damage area, maximum strain in the plates, and maximum strain in the structural components of the framework.

6.4.7.2 Numerical Representation

The numerical code FLAC3D V. 2.14 was used in this analysis. Three different drip shield configurations were considered: (1) the initial configuration (with dimensions as specified in the design documents); (2) the configuration with all structural components thinned by 5 mm; and (3) the configuration with all structural components thinned by 10 mm. Different configurations are referred to by plate thickness (i.e., 15 mm, 10 mm, and 5 mm). Each configuration is analyzed for seven block-impact energies (i.e., combinations of block mass and velocity). The mechanical properties of Titanium Grade 7 (for plates) and Titanium Grade 24 (for framework components), interpolated for 60°C and as listed in Table 6-134, were used in the calculations.

6.4.7.2.1 Drip Shield Geometry and Boundary Conditions

The mesh used in the previous analyses of block impact into the drip shield (BSC 2004 [DIRS 168993], Section 5.5) was modified for the analyses described here. Three views of the mesh are shown in Figure 6-71. The original mesh assumed only symmetry plane 2 (a vertical plane along the drip shield axis through the middle of the crown) indicated in view B in Figure 6-71. Thus, all five segments of the drip shield were included in the representation. However, the drip shield has another plane of symmetry, which is indicated as symmetry plane 1 (a vertical plane perpendicular to the drip shield axis in the middle of the drip shield) in view A in Figure 6-71. Symmetry plane 1 was not used in the original calculations because of the asymmetry of falling rock with respect to that plane. (Rock is not shown in Figure 6-71.) To optimize the simulations, the falling blocks are assumed to have a cubical shape (discussed further in Section 6.4.7.2.2), allowing one more symmetry condition to be used (with respect to symmetry plane 1). Therefore, the geometrical representation includes only one-quarter of the drip shield.

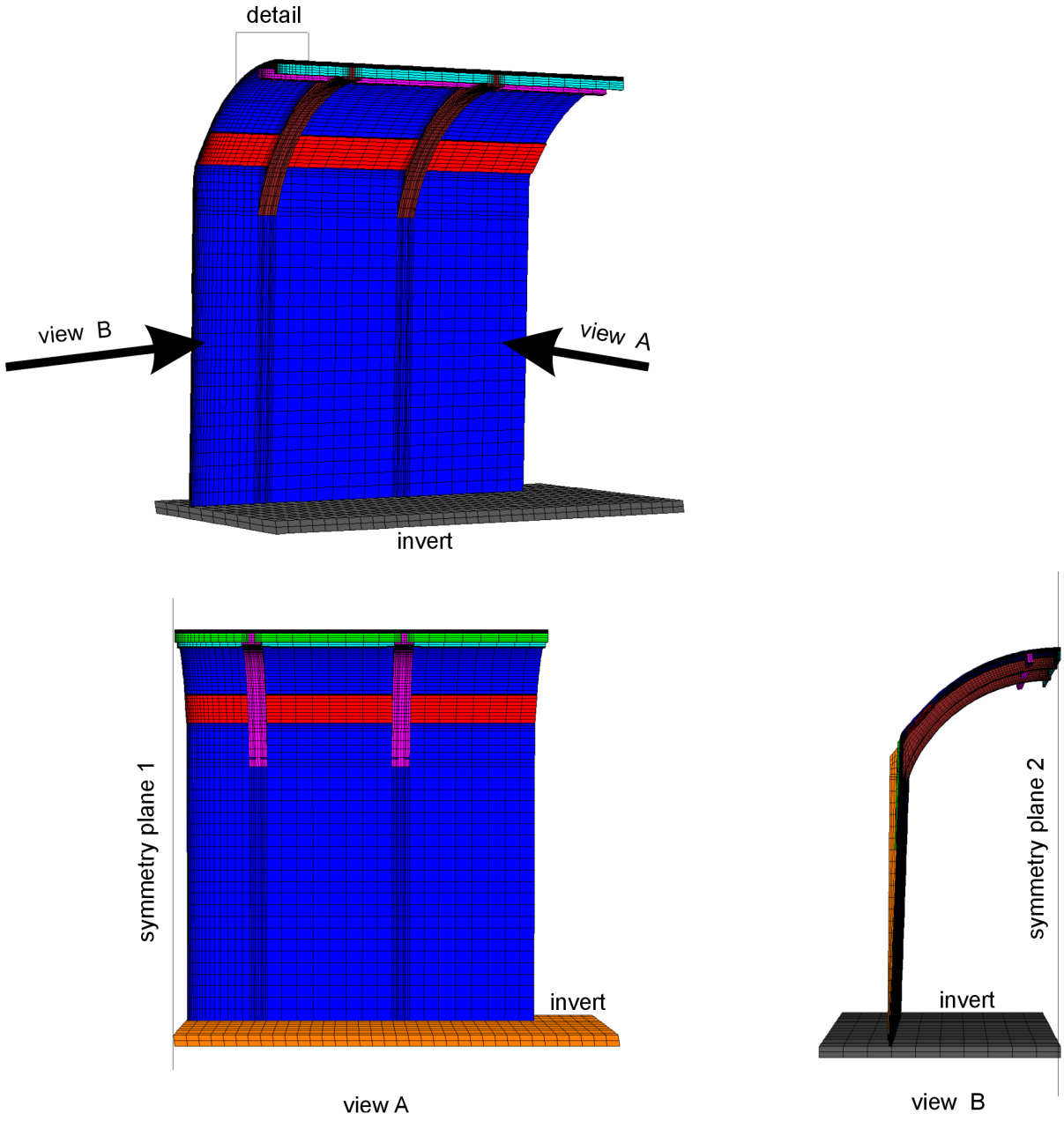

Source: Created for illustrative purposes only, from FLAC3D save file in output DTN: MO0704DSFLAC3D.000, file *15mm/grid input/grid+2mm.sav*, by plotting block group geometry.

NOTE: Detail in top graphic is shown in Figure 6-72.

Figure 6-71. Three Views of the Geometrical Representation of the Drip Shield with Indications of the Symmetry Planes Used

A detailed view of mesh and the discretization of the plates and longitudinal stiffeners at the impact location is shown in Figure 6-72. There are five layers per plate thickness throughout the geometrical representation. The mesh at the impact location is also refined in the plane view in both longitudinal and transverse directions. The suitability of this mesh for impact simulations is demonstrated in *Drip Shield Structural Response to Rock Fall* (BSC 2004 [DIRS 168993], Section 6).

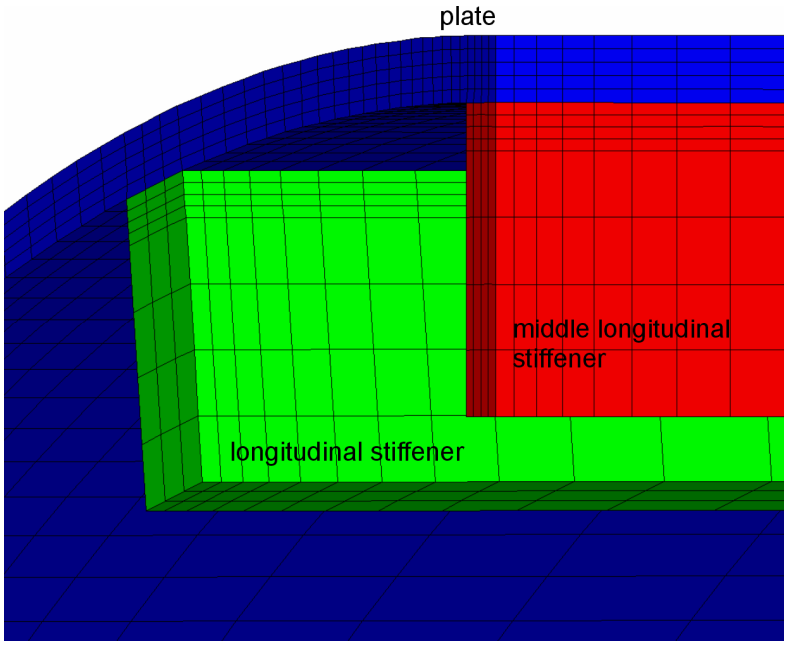

Source: Created for illustrative purposes only, from FLAC3D save file in output DTN: MO0704DSFLAC3D.000, *15mm/grid input/grid +2mm.sav*, by plotting block group geometry.

Figure 6-72. Detail of Mesh in the Plate and Longitudinal Stiffener in the Drip Shield Crown at the Location of Intersection of Two Symmetry Planes (indicated in Figure 6-71)

The drip shield is resting by its own weight on the invert, which is represented as a rigid, horizontal surface with two layers of solid brick elements (Assumption 5.2, Section 5). There is a frictional interface between the invert and the drip shield legs. A friction coefficient of 0.4 is assigned to the interface (Assumption 5.4, Section 5). The symmetry conditions are applied to the grid points on the symmetry planes. Displacement of the points lying on the symmetry planes is constrained in the direction perpendicular to the symmetry planes. The end at which the drip shield is interlocked with the adjacent drip shield is represented as a stress-free boundary. The interaction with the adjacent drip shield has a second-order effect on drip shield deformation caused by impact in the middle of the drip shield.

Three different drip shield configurations were analyzed using different geometrical representations. Because the plates and the framework beams were approximated using the solid brick elements, the effect of thinning of the components was accounted for by modifying the geometrical representation (i.e., generating a new mesh). The effect of uniform corrosion is represented by the reduction in thickness of both plates and beams. Only for support beams, which are close to a square shape in cross section, are both thickness and height reduced to account for uniform corrosion.

6.4.7.2.2 Representation of Rock Blocks

Rockfall analysis in the nonlithophysal units was conducted for different PGV levels (BSC 2004 [DIRS 166107], Section 6.3). Because the purpose of the analysis described here was to generate lookup tables, the rock block masses and their velocities were selected such that their energies span the entire range of the impact energies observed from the rockfall calculations.

The analyzed blocks, impact velocities, and energies are listed in Table 6-153. In order to avoid the need for extrapolation, the maximum analyzed block-impact energy is the maximum impact energy recorded in any of the rockfall calculations irrespective of PGV level. The maximum impact energy of 706,914 J is recorded at the 5.35 m/s PGV for a block of 28.29 mT impacting the drip shield with a velocity of 7.07 m/s (rock block 1 from Table 6-153). The smallest analyzed impact energy of 84 J (rock block 7), which is expected to result in no damage, corresponds to the 20th percentile for the 1.05 m/s PGV level. The 99.9th, 99th, 90th, 70th, and 40th percentiles (rock blocks 2 through 6, respectively) for the 1.05 m/s PGV level provide a reasonable spread of impact energies for interpolation. Comparison of the percentiles for the selected impact energies at different PGV levels is shown in Table 6-154.

Table 6-153. Analyzed Impact Block Masses and Velocities

Rock Block	Case	PGV Level (m/s)	Volume (m^3)	Mass (mT)	Velocity (m/s)	Impact Energy (J)
1	42	5.35	11.7	28.29	7.07	706,914
2	40	1.05	3.11	7.49	4.81	86,559
3	50	1.05	0.771	1.86	4.50	18,846
4	56	1.05	0.157	0.38	4.24	3,412
5	34	1.05	0.061	0.15	3.58	949
6	49	1.05	0.056	0.14	1.83	228
7	59	1.05	0.054	0.13	1.14	84

Source: DTN: MO0703PASDSTAT.001 [DIRS 182878], file *Nonlith Damage Abstraction for DS.xls*, worksheet "Data Catalogs."

NOTES: Block 1 is based solely on the 5.35 m/s PGV level which occurs below the 1×10^{-8} annual exceedance frequency on the bounded hazard curve that is the basis for TSPA and is beyond the level considered in TSPA by NRC regulation.

PGV = peak ground velocity.

Table 6-154. Comparison of Percentiles for Selected Impact Energy at Different PGV Levels

Impact Energy (J)	PGV Levels		
	1.05 m/s	2.44 m/s	5.35 m/s
706,914	–	–	100
86,559	99.9	99.8	99.7
18,846	99	98	96
3,412	90	85	77
949	70	62	48
228	40	28	18
84	20	12	8

Source: DTN: MO0703PASDSTAT.001 [DIRS 182878], file *Nonlith Damage Abstraction for DS.xls*, worksheet "Data Catalogs."

NOTE: PGV = peak ground velocity.

The shape of the rock blocks that can become unstable can vary considerably. However, compared to block impact energy (i.e., mass and velocity), which is the dominant factor, the shape of the blocks has a second-order effect on deformation and damage of the drip shield during impact. Therefore, to simplify the analysis and reduce the number of parameters to be varied, the blocks were considered to have cubical shapes (Assumption 5.19, Section 5). One advantage of a cubical block shape is that symmetry plane 1 could be used (Figure 6-71), reducing the size of the analyzed domain by half. Geometrical representation, including both the drip shield and rock block 5 (from Table 6-153), is shown in Figure 6-73. In all calculations, the block edge impacts the middle of the crown. The center of mass of the block and the impact locations are co-linear with the vertical impact velocity. The vertical impact in the middle of the crown was selected because the previous calculations (BSC 2004 [DIRS 168993], Table 6-2) showed that vertical impact resulted in a larger damage area than rockfall impact into the drip shield shoulder or into the drip shield sidewall. Corner impact certainly would result in greater damage of the plates than edge impact. However, if the block corner impacts the drip shield first, the probability is very small that the center of mass of the block and the impact location will be co-linear with impact velocity. Consideration of such a low-probability corner impact would result in overprediction of damage to the drip shield. Instead, all analyses were carried out for direct-edge impact (Assumption 5.12, Section 5), as illustrated for rock block 5 in Figure 6-73.

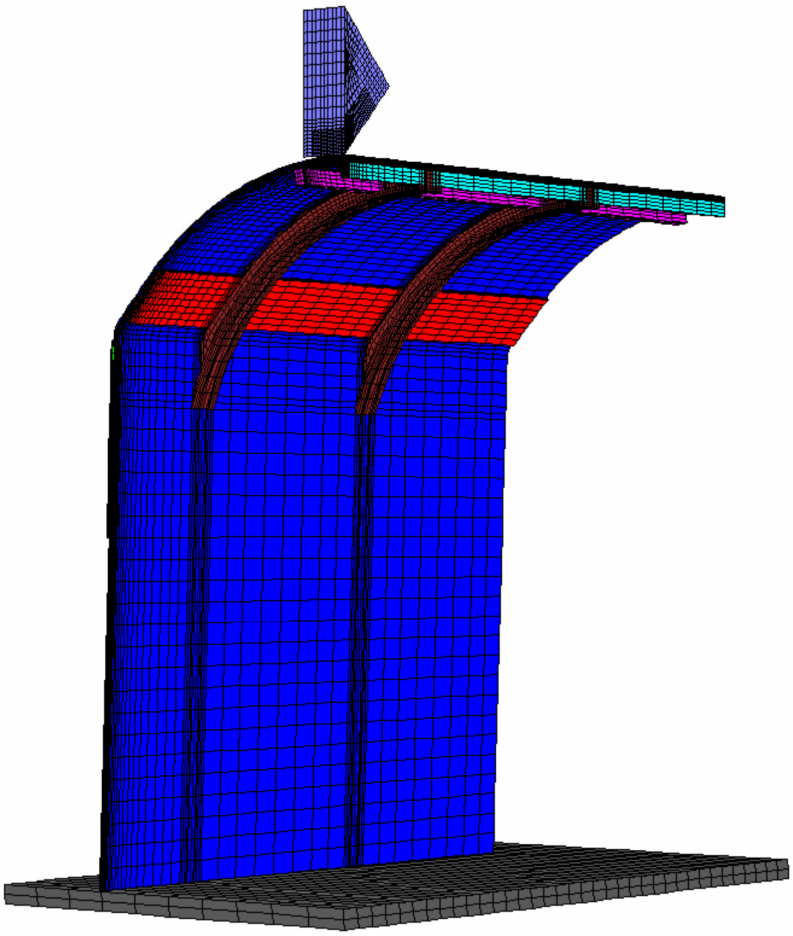

Source: Created for illustrative purposes only, from FLAC3D save file in output DTN: MO0704DSFLAC3D.000, *15mm/rock5/outputs/final_dynamic.sav*, by plotting block group geometry.

Figure 6-73. Rock Block 5 Impact into the Drip Shield

Discretization of the rock blocks is gradually refined toward the point of initial contact of the block with the drip shield in such a way that a sufficiently fine grid, which can represent deformation of the rock realistically, is achieved at the impact location. The rock blocks are represented as linearly elastic–perfectly plastic Tresca materials as discussed in *Drip Shield Structural Response to Rock Fall* (BSC 2004 [DIRS 168993], Section 5.4.1). The uniaxial compressive strength (290 MPa) and other mechanical properties of the rock blocks are provided in Table 4-4. In reality, intact tuff blocks are expected to exhibit brittle response, particularly when subjected to the tensile stress field expected near the impact location. (The Tresca constitutive relation does not include the tension cutoff typical of rock materials.) Also, the uniaxial compressive strength of 290 MPa overestimates the average intact-block strength in the nonlithophysal rock mass. The approximations of the constitutive relation and rock strength result in underestimating the damage and deformation in the rock and, consequently, overestimating the damage and deformation of the drip shield plates and other drip shield structural components.

The interaction between the rock and the drip shield takes place through the frictional interfaces placed on the upper surface of the drip shield crown plate and on the rock surface that can come in the contact with the plate. A friction coefficient of 0.4 was assigned to the interfaces (Assumption 5.4, Section 5).

6.4.7.2.3 Sequence of Analysis

The simulations were carried out in three steps. In the first step, which was conducted quasi-statically, the stresses in the drip shield were initialized for the weight of the drip shield under gravity. There was no interaction between the rock block and the drip shield during this step. The second step was carried out dynamically. No damping, except for natural damping due to friction in the interfaces and inelastic constitutive behavior, was applied in the simulation. The block was initially placed such that the edge almost touched the drip shield crown, and its vertical velocity was initialized to the specified value (indicated in Table 6-153). The deformed geometries and stress contours during impact of rock block 2 into the drip shield configuration with 15-mm-thick plates are shown in Figures 6-74 and 6-75. The impact was simulated until the rock block bounced off the drip shield. When the block was no longer in contact with the drip shield, the block was deleted, and, in the third step, the drip shield was simulated quasi-statically until it reached equilibrium. The damage areas were reported based on the stresses in the final equilibrium state.

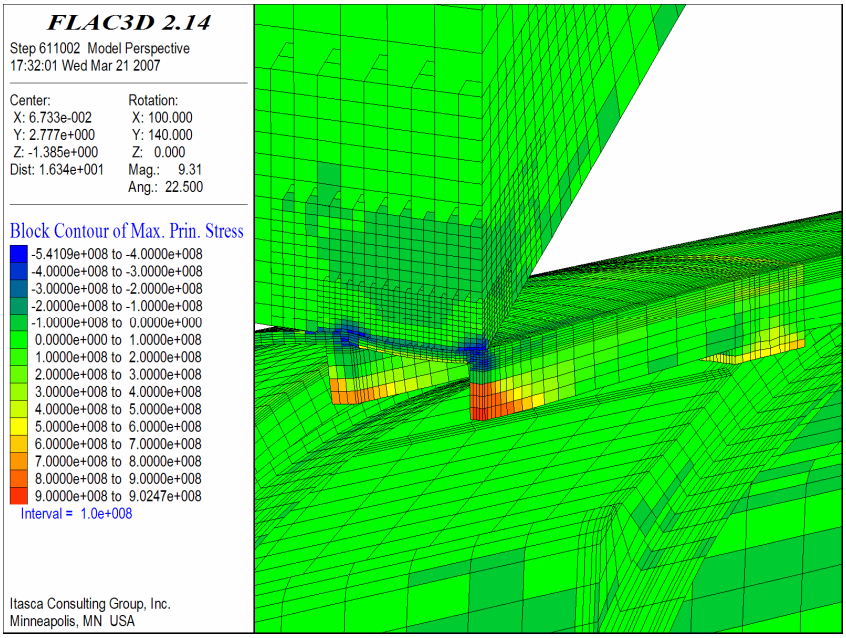

Output DTN: MO0705IMPACTST.000, file *stresses-view1.pcx.*

Figure 6-74. Contours of Major Principal Stress (Pa) During Impact of Rock Block 2 into the Drip Shield Configuration with 15-mm-Thick Plates

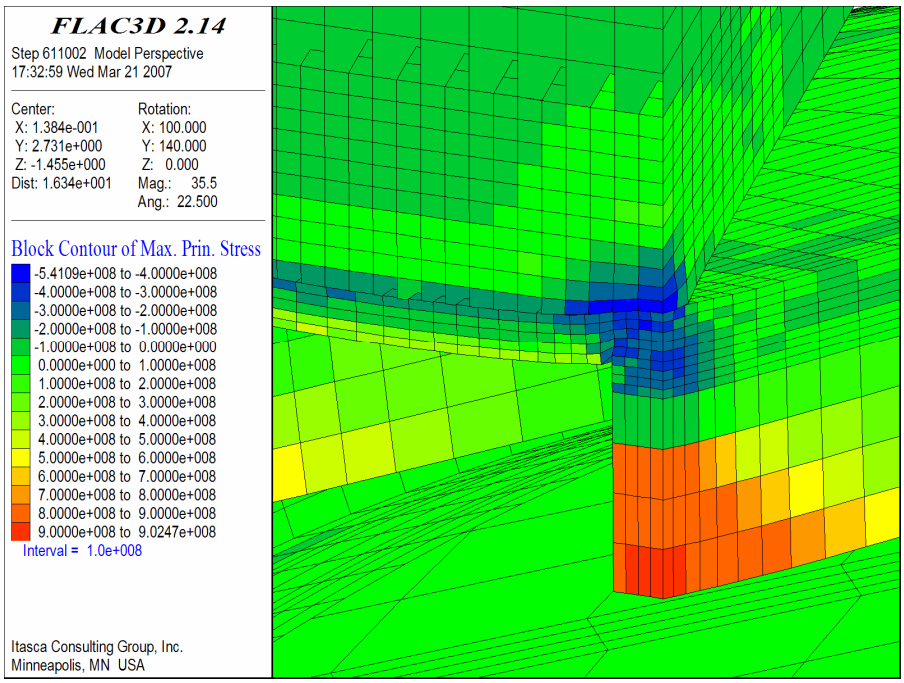

Output DTN: MO0705IMPACTST.000, file *stresses-view2.pcx*.

Figure 6-75. Contours of Major Principal Stress (Pa) During Impact of Rock Block 2 into the Drip Shield Configuration with 15-mm-Thick Plates: Detail of the Impact Location

6.4.7.3 Summary of the Large-Block Impact Calculations

The objectives of the calculations were to determine, for a given drip shield configuration and impact energy, (1) the potential for failure of the drip shield framework structural components, (2) the potential for failure of the drip shield plates, and, (3) in the case that impact does not cause failure (rupture or tear) of any of the drip shield components, the damage area in the drip shield plates.

The longitudinal stiffeners are the drip shield framework structural components most affected by large rock-block impact (see stress contours in Figure 6-74), because the rock first impacts the stiffeners in the middle of the span between the bulkheads. The potential for failure of the stiffeners was assessed based on (tensile) effective plastic strains compared to the ultimate (rupture) plastic strain. The ultimate plastic strain for Titanium Grade 24 is 0.152 (Table 6-134). For beams, the stress-free boundaries (i.e., the bottom and lateral surfaces of a beam) impose constraints, making the stress state in the middle of span of the beam basically uniaxial. Consequently, the triaxiality factor for the longitudinal stiffeners is 1.0. The calculated maximum extensional strains in the stiffeners for different rock blocks and different drip shield configurations are listed in Table 6-155. The results indicate that the maximum effective plastic strain in the longitudinal stiffener exceeds the ultimate plastic strain for Titanium Grade 24 in the case of rock block 1 impact irrespective of the drip shield configuration. This implies that the stiffener would fail. Although the maximum strain is in the middle stiffener, the ultimate plastic strain is exceeded in all stiffeners, as illustrated in Figure 6-76. This numerical representation can be used for prediction of the onset of failure.

Table 6-155. Maximum Effective Plastic Strains in the Drip Shield Longitudinal Stiffeners Due to Rock Block Impact

Rock Block	Plate Thickness		
	5 mm	10 mm	15 mm
1	—	0.274	0.247
2	0.084	0.067	0.044
3	0.005	—	—

Output DTN: MO0703PADSBLOC.000, file *DS damage due to large block impacts.xls,* worksheet *max stiffener plastic strains*.

NOTES: The case for the impact of rock block 1 into the drip shield configuration with a 5-mm-thick plate was stopped before completion because of numerical problems. The maximum effective plastic strains for this case will certainly be greater than 0.274, which was the maximum strain predicted for the drip shield configuration with 10 mm plate thickness.

The maximum plastic strains, where not listed (except for the impact by rock block 1 into drip shield configuration with 5-mm-thick plates), are less than 0.005.

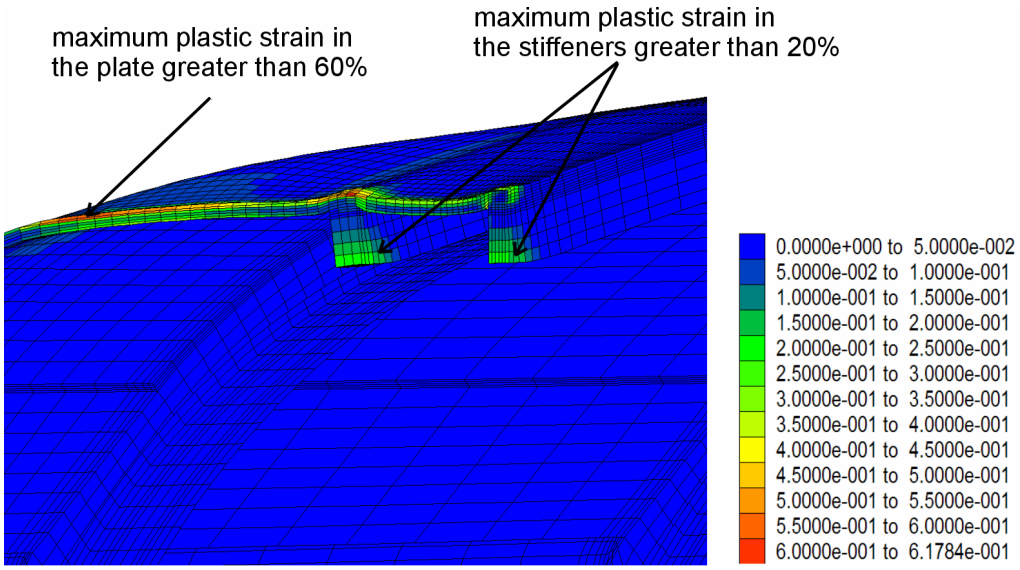

Output DTN: MO0704DSFLAC3D.000, file *\15mm\rock1\outputs\final.sav*.

Figure 6-76. Contours of Plastic Shear Strains in the Case of Rock Block 1 Impact into the Drip Shield Configuration with 15-mm-Thick Plates

The conclusion from the calculations is that rock block 1 would cause the stiffeners to fail. The maximum plastic strains for all other cases indicate that the drip shield framework (and stiffeners) would withstand the impact without failure. The maximum stiffener displacement for impact of rock block 1 is 20.4 cm. For all other cases the maximum stiffener displacement is 4.2 cm. When compared to the initial clearance between the drip shield and the waste package of 36 cm, no contact between the drip shield and the waste package is predicted. However, for the impact of rock block 1 (which fails the drip shield stiffeners), the complete failure process of the drip shield has yet to be calculated. It is possible that the deformation of the drip shield may

increase such that the drip shield contacts the waste package. As the drip shield continues to deform, energy of the rock block impact will be dissipated and any potential impact of the drip shield into the waste package will be at a substantially reduced velocity.

Should the drip shield impact the waste package, there may be a damage area based on residual stress, similar to the damage areas determined from a waste package impacting a support pallet (Section 6.3) or a collapsed drip shield bearing on the waste package (Section 6.5.2). It is expected that any contact between the drip shield and the waste package as a result of an impact by rock block 1 will be spread over a large area, resulting in insignificant deformations to waste packages with intact internals, and fairly small deformations to waste packages with degraded internals. From the discussion of potential rupture of degraded waste packages in Section 6.3.3.2 (based on the observation of large deformations) it is possible to conclude that, should rock block 1 cause the drip shield to contact the waste package, the consequence would be limited to a residual stress damage area and there would be no rupture of the waste package. It is important to note that Block 1 is based solely on the 5.35 m/s PGV level, which occurs below the 1×10^{-8} annual exceedance frequency on the bounded hazard curve that is the basis for TSPA, and is beyond the level considered in TSPA by NRC regulation.

Stress corrosion cracking in the drip shield plates (Titanium Grade 7) and framework structural components (Titanium Grade 29) can occur when the residual stresses due to loading conditions (such as big block impacts onto the drip shield or static and dynamic loads of rock rubble accumulated on the top and along the sides of the drip shield) exceed the residual stress threshold for initiation of stress corrosion cracking. The resulting network of stress corrosion cracks is not included in the compliance case for the license application because advective flow through stress corrosion cracks on the drip shield is excluded in FEP 2.1.03.10.0B, Advection of Liquids and Solids Through Cracks in the Drip Shield, so the presence of a crack network does not compromise the ability of the drip shield to divert seepage away from the waste package.

However, stress corrosion cracking in the structural components of the drip shield framework may have an effect on its mechanical strength and integrity. The potential for stress corrosion cracking to degrade the mechanical integrity of the drip shield has not been included in the structural response calculations for the seismic scenario. The presence of cracks in the drip shield framework could reduce its ultimate plastic load capacity in response to static rockfall loading and vibratory ground motion. However, the ultimate plastic load capacity has not been reduced because of the conservatisms in the structural response calculations that support the seismic damage abstractions. These conservatisms include: (1) the spread in the vertical component of the ground motion (important because the fragility curves for drip shield failure are a direct function of the vertical component of the peak ground acceleration) is overestimated by the current sets of postclosure ground motions (SNL 2007 [DIRS 176828], Appendix C); and (2) the ultimate plastic load capacity is based on a quasi-static approach, which is usually conservative relative to fully dynamic analyses, in the sense that it underestimates the plastic load capacity relative to dynamic calculations of drip shield response (see Section 6.4.4.6). The combined effect of these conservatisms is expected to be more significant for structural response than the potential reduction in plastic load capacity from the presence of stress corrosion cracks.

Although the stiffeners take the greater proportion of the impact force, the impact causes significant deformation of the drip shield plates (Figure 6-75). The maximum effective plastic strains in the drip shield plates are listed in Table 6-156. The reported maximum strains are tensile strains. The maximum shear strains, particularly at the impact location, at the portion of the plate sitting on the longitudinal stiffener, often exceed the values reported in Table 6-156; however, they are not reported here because only tensile strains can cause plate tearing. Inspection of stress states at the location and the time at which maximum strains are achieved indicate biaxial tension, for which the triaxiality factor is 0.5 (see Appendix A). Consequently, based on the Titanium Grade 7 properties listed in Table A-1, the ultimate plastic strain is corrected for the triaxiality factor as follows:

$$\varepsilon_{up}^{TF} = 0.5\,\varepsilon_u - \frac{\sigma_y}{E} = 0.5 \cdot 0.22 - \frac{316}{105000} = 0.107\,. \qquad \text{(Eq. 6-4)}$$

Comparing the maximum plastic strains from Table 6-160 with the ultimate plastic strain, the calculations indicate that rock blocks 1 and 2 will tear the drip shield plate regardless of the plate thickness. Rock block 3 will tear only the 5-mm-thick plate.

Table 6-156. Maximum Effective Plastic Strains in the Drip Shield Plates Due to Rock Block Impact

	Plate Thickness		
Rock Block	**5 mm**	**10 mm**	**15 mm**
1	–	0.753	0.655
2	0.256	0.212	0.114
3	0.164	0.068	0.041
4	0.096	0.024	0.005
5	0.039	0.005	0.000
6	0.001	0.000	0.000
7	0.000	0.000	0.000

Output DTN: MO0703PADSBLOC.000, file *DS damage due to large block impacts.xls,* worksheet "max plate plastic strains."

NOTES: The case for rock block 1 impact into the drip shield configuration with a 5-mm-thick plate was stopped before completion because of numerical problems.

The strains shown in the table are tensile strains.

The damage area of the drip shield plate is defined as the inner and outer surface of the drip shield plate where the residual, major principal stress is greater than 80% of the Titanium Grade 7 yield strength (i.e., 252.8 MPa). The damage areas for different rock blocks and drip shield plate thickness are summarized in Table 6-157 for one-quarter of the drip shield. (The damage area for the entire drip shield is four times the values in the table.) An illustration of the damage area and the contours of the major principal stress for rock block 1 impact into the drip shield configuration with 15-mm plate thickness is shown in Figure 6-77. When the damage areas on the inner and outer surfaces overlap, the damage area should be counted only once. However, in the results presented in Table 6-157, the damage areas on the inner and the outer surfaces are added, irrespective of their geometrical relation. This approximation overestimates

the total damage area, though not significantly, because the damage areas on the inner and the outer surfaces rarely overlap.

Table 6-157. Damage Areas (m^2) in the Drip Shield Plates Due to Rock Block Impact

Rock Block	Plate Thickness		
	5 mm	10 mm	15 mm
1	—	2.72×10^{-2}	2.30×10^{-2}
2	3.61×10^{-2}	8.27×10^{-3}	1.59×10^{-2}
3	3.27×10^{-3}	3.32×10^{-3}	1.15×10^{-3}
4	4.80×10^{-4}	6.17×10^{-4}	2.79×10^{-4}
5	8.08×10^{-5}	0.000	0.000
6	0.000	0.000	0.000
7	0.000	0.000	0.000

Output DTN: MO0703PADSBLOC.000, file *DS damage due to large block impacts.xls*, worksheet "damage area."

NOTES: The case for rock block 1 impact into the drip shield configuration with 5-mm-thick plate was stopped before completion because of numerical problems.

The damage areas in the table are for one-quarter of the drip shield. The damage area for the entire drip shield can be obtained by multiplying the numbers in the table by 4.

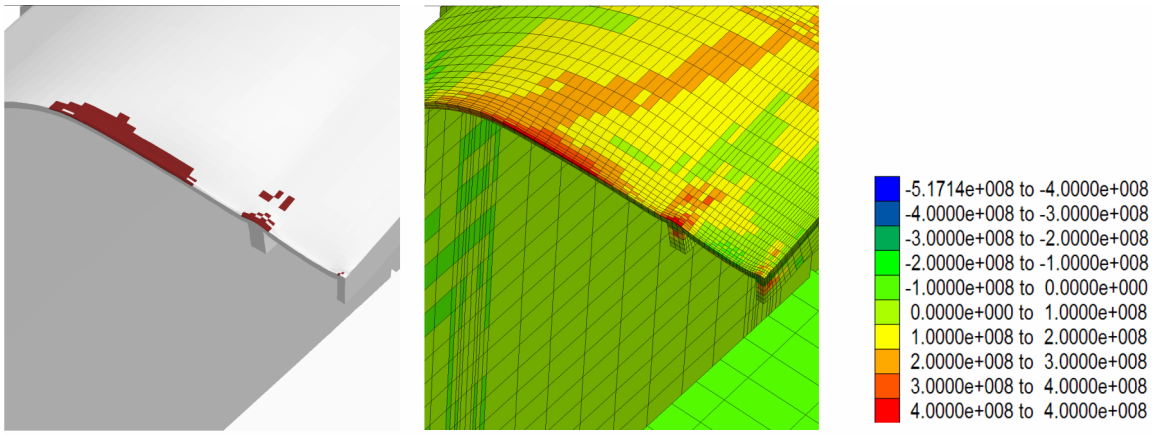

a) Damage Areas b) Maximum Stress (Pa) Contours

Output DTN: MO0704DSFLAC3D.000, file *\15mm\rock1\outputs\final.sav*.

NOTES: The damage area is the inner or outer surface of the drip shield plate with maximum stress greater than 80% of the yield strength of Titanium Grade 7. The damage area is shown in brown.

Figure 6-77. Damage Areas and Maximum Stress Contours (Pa) in the Case of Rock Block 1 Impact into the Drip Shield Configuration with 15-mm-Thick Plates

6.5 WASTE PACKAGE ANALYSIS AFTER DRIP SHIELD FAILURE

6.5.1 Analysis for a Waste Package Surrounded by Rubble

6.5.1.1 Purpose

The kinematic calculations in Section 6.3 are appropriate when the drip shield is intact and the waste package can move freely beneath the drip shield. But at late times, when the degraded drip shield plates may fail from rockfall and seismic loads, the waste package will be surrounded by rubble. The direct loads from this rubble may cause damage to the waste package in response to vibratory ground motion. Rubble in the lithophysal zone is most relevant here because the small particle size of the lithophysal rubble means it can more easily slip or fall through gaps or tears in the plates of the drip shield and because the lithophysal zones encompass approximately 85% of the emplacement drifts in the repository. The effect of large rock blocks is discussed in Section 6.4.7.

The damage induced by the rubble surrounding the waste package is based on the two-dimensional coupled rockfall/structural response of the Alloy 22 outer barrier during vibratory ground motion. Damage is determined directly from the finite-difference output for the stress and strain state of the outer barrier; additional look-up tables are not required. The input data for the calculations of a single waste package surrounded by rubble include 17 ground-motion time histories at four PGV levels, elastic and plastic properties of the outer barrier, and the bulk properties of degraded waste package internals. The rock block pattern in the lithophysal rock is based on a new random seed for each realization.

Two thicknesses of the outer barrier are analyzed: 23 mm and 17 mm, both with degraded internals. These states represent the response of the waste package over very long time scales. These thicknesses are the average thickness of the outer barrier because average thickness is anticipated to be the key parameter for structural response. A future state with an outer barrier thickness less than 17 mm is not included here because preliminary results with corrosion parameters indicate that the spatially averaged thickness of the OCB thicknesses will not be significantly less than 17 mm (SNL 2007 [DIRS 176828], Section 6.5.2.2).

The damage model does not take credit for the stainless steel inner vessel, the TAD canister, or the basket assemblies as structural elements after the first seismic event that damages the outer barrier. This approach maximizes structural deformation and damaged area if the stainless steel elements do not degrade quickly in a dilute chemical environment. A case with intact internals is not included here. It is possible that the drip shield will fail before the internals become degraded from the first seismic event that damages the outer barrier. In other words, a waste package with intact internals could be surrounded by rubble. If this occurs in TSPA, then the damaged areas from the computational model with degraded internals will conservatively be used to estimate the damaged areas with intact internals. The intact configuration is expected to have less damage than the degraded configuration because the inner vessel provides internal support for the outer shell of Alloy 22. This internal support bears part of the load that is otherwise transferred completely to Alloy 22 with degraded internals. The concept that degraded internals experience greater damaged areas than intact internals is also confirmed by recent results with kinematic analyses for the TAD-bearing waste package.

Separate models are not developed for the TAD-bearing waste package and for the codisposal waste package surrounded by rubble because the results from the TAD-bearing waste package provide a reasonable estimate of damage for the codisposal waste package. With degraded internals, the computational model for the TAD-bearing waste package has a 23-mm-thick or 17-mm-thick outer barrier, and all internal components (inner vessel, TAD canister, fuel baskets, and fuel assemblies) are represented as material that is similar to sand, with no significant strength and with very limited cohesion. So the computational model for the TAD-bearing waste package with degraded internals would be quite similar to the corresponding model for the codisposal waste package because the load-bearing structural component, the circular ring (the two-dimensional waste package model configuration), will have the same thickness, although the outer diameter of the ring and the total weight of the degraded internals will be different.

The numerical calculations for the 23-mm-thick outer barriers are anticipated to show minimal deformation from a circular cross section, so a two-dimensional model provides a reasonable approximation for the deformation of the midsection of the waste package. The calculations for the 17-mm-thick outer barrier are anticipated to show more significant deformation from a circular cross section, so that the three-dimensional effects of the ends and lids of the waste package may be important. Fully coupled three-dimensional rockfall/structural response calculations are not computationally efficient for the long durations of the ground motions. In this situation, the effects of waste package three-dimensional geometry on potential modes of failure that are neglected in a two-dimensional approximation are investigated using a three-dimensional numerical representation with quasi-static loading. In these calculations, the three-dimensional waste package representation is loaded until deformation in the middle of the waste package resembles that observed in two-dimensional simulations. This approach directly includes the three-dimensional effects from the lids on the final structural deformation, providing an alternate representation of the structural response. Note that this decoupled approach is not intended to replace the two-dimensional calculations but provides a computationally efficient methodology for estimating the response of the waste package as a three-dimensional structure.

The uncertainty in the ground motions and in the rock block pattern is propagated into these calculations through sampled values for these input parameters. GoldSim (V. 8.02.500. STN: 10344-8.02-05 [DIRS 174650]) provides a Latin Hypercube sampling of the rock block pattern and the ground motion number (output DTN: MO0704SIPAWPSR.000). The rock block pattern and the ground motion number are defined by random integer seeds, selected from a discrete uniform distribution between 1 and 17. This sampling provides a list of input data in which a given time history is paired with a random seed for the rock block pattern. This listing is used as a basis for input data for the calculations at the 0.4 m/sec, 1.05 m/sec, 2.44 m/sec, and 4.07 m/sec PGV levels.

Elastic and plastic material properties are set to constant values at 60°C (Assumption 5.7, Section 5) based on data from handbooks or manufacturers' catalogs.

The residual stress threshold for initiation of stress corrosion cracking in the Alloy 22 outer barrier is defined as a range from 90% to 105% of the yield strength of Alloy 22. The uncertainty represented by this range is propagated into TSPA by abstracting damaged area at several representative values of the residual stress threshold. The TSPA model will interpolate

between the damaged areas for these representative values to capture the uncertainty in the residual stress threshold.

The fragility of the waste package surrounded and directly loaded by rubble is discussed in this section. This is important because a possible late stage in the evolution of the engineered barriers occurs when the drip shield plates have deteriorated completely, and the waste package is exposed directly to the accumulated load of rock rubble resulting from drift degradation. As discussed in the previous section, the drip shield plates may fail due to the combined effect of thinning due to corrosion, the static load of rock rubble accumulated on the drip shield and the dynamic amplification of that static load during seismic ground shaking. The block size of the rubble formed due to collapse of the emplacement drifts in the lithophysal rock mass will be of the order of 0.1 m (BSC 2004 [DIRS 166107], Section 6.1.4.1). If the drip shield plates fail as a result of tearing, these pieces of rubble would easily fall through the open gaps in the drip shield plates and accumulate around and on top of the waste package even if the drip shield frame were to remain stable.

The waste package will deform elastically due to the static load until the OCB loses at least 50% of its thickness due to uniform corrosion. However, the OCB of the waste package could undergo significant damage—and even rupture—during seismic ground motions as a result of interactions with the surrounding rubble. Seismic ground motion can either amplify the static rubble load or cause additional rockfall that would impact directly onto the waste package. If the waste package were not covered completely with rubble, seismic ground motion could increase the volume of rock surrounding and loading the waste package.

The potential for damage and rupture of the OCB of the waste package as a function of thickness of the OCB and intensity of the ground motion is analyzed and discussed in this section. Four different PGV levels were analyzed: 0.4 m/s, 1.05 m/s, 2.44 m/s, and 4.07 m/s. In addition, OCB thicknesses of 23 mm and 17 mm were considered in the analysis to account for uniform corrosion at different times. (The initial thickness of the OCB is 25.4 mm.) The potential for OCB rupture is assessed based on the maximum effective strain compared to the rupture strain. Damaged areas due to vibratory ground motion are estimated for both the inner and outer surfaces of the OCB. The results of the simulations were postprocessed for different stress thresholds for possible initiation of stress corrosion cracking.

These calculations were performed by the distinct element program UDEC (V. 3.1. STN: 10173-3.1-00 [DIRS 161949]), and output from these damage calculations provides the basis for new seismic damage abstractions and is documented in *Seismic Consequence Abstraction* (SNL 2007 [DIRS 176828]).

6.5.1.2 Numerical Representation

Dynamic analysis of interaction of the waste package with surrounding rubble has been analyzed using a two-dimensional approximation implemented in the numerical code UDEC (V. 3.1. STN: 10173-3.1-00 [DIRS 161949]). A geometrical representation of the emplacement drift similar to that used to analyze drift collapse in *Drift Degradation Analysis* (BSC 2004 [DIRS 166107], Sections 6.4.2.2 and 6.4.2.5) is applied here (see Figure 6-78). The rock mass is represented as an assembly of polygonal blocks, initially bonded together. The joints between

the blocks have finite shear and tensile strengths and can fail as dictated by stresses in the rock mass. Failing of the joints between the blocks represents fracturing of the rock mass and formation of blocks that fall under gravity to accumulate on the drift floor and around the waste package as rubble. Representation of different lithophysal rock mass qualities and analysis of rockfall using this approach is described in detail in *Drift Degradation Analysis* (BSC 2004 [DIRS 166107], Section 6.4). Because the objective of the analyses discussed here is an assessment of the integrity of the OCB of the waste package, the actual geometry and thickness of the OCB are included in the geometrical representation. The numerical representation of the geometry of the analyzed problem of the waste package surrounded by rubble at three different length scales is shown in Figure 6-78.

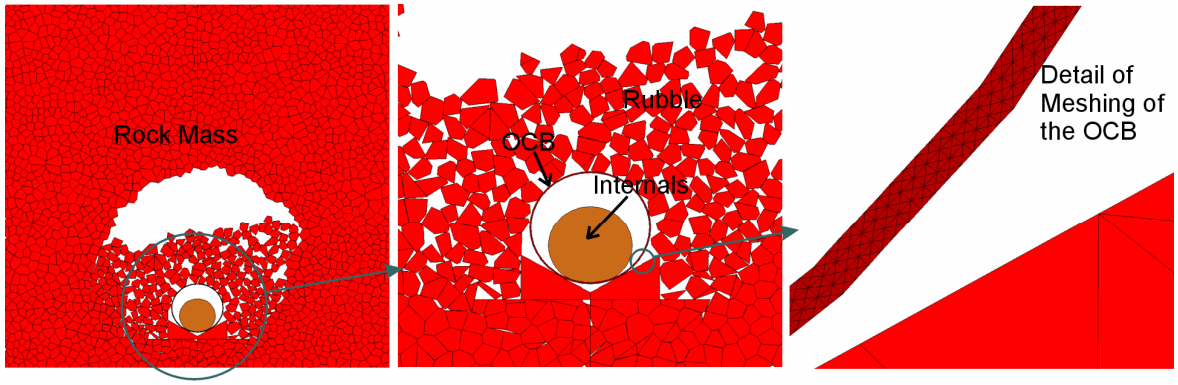

Source: Created for illustrative purposes only.

NOTE: WP = waste package.

Figure 6-78. Geometrical Representation Used in the Analysis of the Mechanical Interaction between the Waste Package and the Rubble During Seismic Ground Motions

The two-dimensional analysis is carried out in a plane perpendicular to the drift axis, and consequently the ground-motion component normal to the plane of analysis is not considered. The analysis was carried out for the vertical and one horizontal component (H1) of ground motion acting normal to the drift axis. The component of ground motion neglected in this analysis certainly affects interaction between different waste packages but has a second-order effect on rubble-waste package interaction. The two-dimensional, plane strain approximation also implies that the represented objects extend infinitely in the out-of-plane direction (i.e., normal to the plane of analysis). In reality, rubble block size in the out-of-plane direction is of the same order as in the plane of analysis. Thus, instead of line loads at contacts between rubble blocks and the OCB extending infinitely in the out-of-plane direction, the distribution and magnitude of the loads change along the waste package. The length scale over which the rubble load changes is equal to 0.1 m and is of the same order as the average block size, which is much smaller than the waste package length or diameter. Consequently, the effect of a randomly varying load on small scale is equivalent, with respect to the large-scale deformation of the waste package, to (relatively) uniformly distributed loading. The two-dimensional approximation overestimates the nonuniformity of the rubble load on the waste package, as well as the magnitude of the deformation and induced stresses. Finally, the waste package is a

three-dimensional structure of finite length with 25.4-mm-thick lids at the ends. The consequences of the two-dimensional approximation of deformation of the waste package deformation are discussed in Appendix D.

6.5.1.2.1 Geometrical and Mechanical Representation of Different Model Components

Rock Mass Representation—The lithophysal rock mass at the repository site is divided into Categories 1 through 5, based on lithophysal porosity (BSC 2004 [DIRS 166107], Section 6.4.1.2). Lithophysal rock-mass Category 3 is used in all calculations here. This category represents the average mechanical properties for much of the rock that will surround emplacement drifts. In this analysis the lithophysal rock mass is represented as an assembly of polygonal elastic blocks, as shown in Figure 6-78, initially bonded together along joints having finite tensile and shear strengths. The average block size of 0.3 m used in these simulations is consistent with the average block size of the rubble expected to form in the lithophysal rock mass based on lithophysae and joint spacing for Category 3 rock (BSC 2004 [DIRS 166107], Section 6.4.1.1).

The micro-mechanical properties for bonded joints and intact blocks, calibrated to the large-scale mechanical properties of the Category 3 lithophysal rock mass, are found in Table 4-4. Because of the random nature of the block geometry that occurs in nature, different realizations of block geometry, as controlled by random-number-generator seeds, were generated and analyzed. Seventeen different random-number generator seeds were used in the analyses: 1 through 15, 17 and 18. (The random-number-generator seed of 16 resulted in a relatively regular joint pattern and was replaced with 18.) Each block geometry realization was then paired with a vibratory ground motion time history for the analysis (see discussion in Section 6.5.1.3).

Outer Corrosion Barrier—The OCB is the only component of the waste package explicitly represented in the analysis. The inner OCB diameter is 1,830.7 mm (Table 4-2) in all analyses. The initial thickness of the Alloy 22 OCB is 25.4 mm. The analyses were carried out for 23-mm and 17-mm thicknesses of the OCB, assuming uniform thinning of the wall due to corrosion (Assumption 5.13, Section 5). The mechanical behavior of Alloy 22 is represented by the Tresca strain-hardening constitutive relation. The Tresca constitutive relation is a special case of the Mohr-Coulomb relation, in which the friction angle is zero, and the tensile failure cutoff is not used (i.e., the tensile strength is set to be infinitely large). The yield and strain-hardening parameters used in UDEC were set in such a way that the uniaxial stress-strain response of the material follows a bi-linear curve characterized by Young's modulus, yield strength and postyield tangent modulus. The list of UDEC input parameters used for representation of the mechanical behavior of Alloy 22 is provided in Table 6-158.

Table 6-158. UDEC Input Parameters Used for Representation of Mechanical Behavior of Alloy 22

Bulk modulus (K)	$K = \frac{E}{3(1-2\nu)}$	153.2 GPa
Shear modulus (G)	$G = \frac{E}{2(1+\nu)}$	79.8 GPa
Cohesion (c)	$c = \frac{\sigma_y}{2}$	175.8 MPa
Cohesion corresponding to 100% of strain (c_1)	$c_1 = \frac{\sigma_y + \left(1 - \frac{\sigma_y}{E}\right) E_t}{2}$	1146 MPa
Plastic shear strain corresponding to 100% of strain (ε_{p1})	$\varepsilon_{p1} = 1 - \frac{\sigma_y}{E}$	0.998

Source: Table 4-3.

NOTE: E is the Young's modulus; ν is the Poisson's ratio; σ_y is the yield strength; and E_t is postyield tangent modulus of Alloy 22 at 60°C. The formulas for K and G are taken from *Itasca Software–Cutting Edge Tools for Computational Mechanics* (Itasca Consulting Group 2002 [DIRS 160331], UDEC User's Guide, p. 2-34). The formulas for c and c_1 are taken from *Itasca Software–Cutting Edge Tools for Computational Mechanics* (Itasca Consulting Group 2002 [DIRS 160331], UDEC Theory and Background, Equation 2.37 with friction angle equal to zero). The plastic strain is calculated by subtracting elastic strain from the total strain.

Rupture Criterion—A bi-linear, continuously hardening stress-strain relation was specified for the OCB until 100% of rupture strain. This value is much greater than the 28.5% rupture strain of Alloy 22 (including knockdown factors). Assessment of the structural integrity of the OCB was conducted at the end of the calculation. If the maximum effective strain exceeded the rupture strain, the OCB was considered failed (ruptured). This approach was used, and rupture strain or stress was not specified in the numerical approximation of the mechanical behavior of Alloy 22.

Stainless steel components inside the OCB of the TAD-bearing waste package will corrode at a much faster rate than Alloy 22 components. However, there is much uncertainty regarding the evolution of strength and stiffness of stainless steel components, which have different thicknesses. It was assumed that, if the drip shield plates fail and the waste package is covered with rubble, OCB internals (including the internal vessel of the TAD-bearing waste package, the TAD canister shell, baskets and guides, and the SNF) will have degraded and will behave as a very weak continuum (Assumption 5.14, Section 5).

Porosity of Internals—The internals occupy 50% of the inner volume of the OCB (Assumption 5.10, Section 5).

Density of Internals—The bulk density of the degraded internals, ρ, is calculated based on the total mass of internals ($m = 64,038$ kg, obtained by subtracting the mass of the Alloy 22 components of 21,750 lbs in Table 4-7 from the nominal loaded weight for the TAD-bearing waste package of 163,000 lbs in Table 4-6), the radius of the volume occupied by internals, ($r = 647.2$ mm, obtained based on 50% porosity and the inside diameter of OCB in Table 4-2, $r = \sqrt{0.5}\, r_i$), and the length ($L = 5,629$ mm) of the OCB filled with degraded internals, as shown in Equation 6-5:

$$\rho = \frac{m}{\pi r^2 L} = 8644 \text{ kg/m}^3. \quad \text{(Eq. 6-5)}$$

The length, L, is calculated by subtracting the dimension of the overhang of the lower sleeve (101.6 mm), the thickness of the outer (2 × 25.4 mm) and middle (12.7 mm) lids, and the size of the gap between the middle and outer lids (30.2 mm) from the total length of the waste package (5,824.5 mm) (see Assumption 5.23, Section 5, and Table 4-7).

Mechanical Properties of Degraded Internals—The degraded internals are represented in the analyses as a relatively soft and weak, elastic-perfectly plastic Tresca material (Assumption 5.15, Section 5). The input parameters used to represent the mechanical behavior of degraded internals are listed in Table 5-1. The internals will degrade mechanically with time. However, it is very difficult to quantify the effect of degradation on the equivalent strength and stiffness of the internals.

Emplacement Geometry—In all the simulations, the waste package is considered to be resting on the emplacement pallet (Figure 6-78). It is not expected that the pallet will degrade completely by the time the OCB loses approximately 8 mm of thickness (for a 17-mm-thick OCB) due to uniform corrosion. The interactions between the waste package and the surrounding rubble are not affected significantly by the pallet. If the pallet completely degrades, the waste package will rest either on the invert or be completely surrounded by rubble. The blocks that represent the pallet in the numerical representation have the correct pallet mass. However, no attempt was made to represent the correct stiffness of the pallet. Instead, the numerical representation of the pallet was given a relatively large stiffness, so that it does not distort during the simulation (Assumption 5.21, Section 5).

6.5.1.2.2 Sequence of Analysis and Boundary Conditions

The analysis of the waste package surrounded by rubble was carried out in four stages, which included:

1. Establish equilibrium under gravitational load
2. Induce rockfall into the emplacement drift
3. Apply vibrational ground motion
4. Re-establish equilibrium.

The boundary conditions and modes of analysis (i.e., quasi-static and dynamic) were changed between different stages of analysis. Each of these stages is discussed in detail below.

Establish equilibrium under gravitational load—In the first stage of the calculations, carried out under quasi-static conditions, the initial equilibrium was calculated under the actions of gravity and in-situ stresses. (As discussed in *Drift Degradation Analysis* (BSC 2004 [DIRS 166107], Section 6.3.1.1), the principal stresses were considered to be vertical and horizontal. The magnitude of the vertical stress was taken to be 7 MPa; the horizontal stress was 3.5 MPa.) Rock strength was set to that of a Category 3 lithophysal rock. Equilibrium was achieved for a stable initial outline of the emplacement drift (i.e., no rockfall). In this stage of the calculations, the bottom and vertical boundaries of the calculation domain were fixed, and a constant vertical stress, equal to overburden weight, was applied on the top boundary.

Induce rockfall into the emplacement drift—Rockfall was induced in the second stage of the calculations, which were also carried out under quasi-static conditions. Because in situ rock stresses are insufficient to cause significant fracturing and subsequent rockfall in a Category 3 lithophysal rock mass, fracturing was induced by artificially reducing the cohesive and tensile strengths of the joints between the polygonal blocks to 0.1% of their initial values. The loose blocks fall under gravity and accumulate on the drift floor, around and on the top of the waste package. The OCB of the waste package is set to behave elastically during the rockfall by setting the yield strength of Alloy 22 to a sufficiently large value. The impacts of the block do not cause any plastic deformation of the OCB. After the rockfall stops, and a stable drift profile is achieved, elastic-plastic properties are assigned to the OCB and new equilibrium is calculated. In this step, inelastic deformation of the OCB could take place under static rubble load. The geometry of the numerical representation at the end of the second stage of calculation for block geometry realization 17 (random-number generator seed equal to 17) is shown at different scales in Figure 6-78.

Apply vibratory ground motion—During this stage of the simulation, incoming ground motions, propagating vertically upward, were applied at the base of the domain. This stage was carried out dynamically, and nonreflecting boundary conditions were applied at the top and bottom boundaries of the domain. (Nonreflecting boundary conditions dissipate incident P- and S-waves approximating their spatial divergence without their reflection back into the analyzed domain.) The free-field boundaries were applied on the vertical domain boundaries.[6] Although the ground motions were provided as displacement, velocity and acceleration histories, the boundary condition at the base of the model was applied as a stress history. The stress histories generated at the base of the domain are based on velocity histories.[7] Only the portions of the ground-motion time histories bracketed by the 15% and 85% points in energy buildup, as measured by the Arias Intensity, were simulated (Assumption 5.17, Section 5). The 15% and 85% points were determined for each component (H1, H2, and V); then, the earliest 15% point and the latest 85% point were used to define the duration for that set of ground motions. Time histories between the 15% and 85% thresholds were inspected visually, and thresholds were moved. The lower threshold always was decreased and the upper threshold always increased to ensure that the ground motions did not start or end with relatively large velocities.

[6] The free-field boundaries are nonreflecting boundaries that account for free-field motion. In other words, motion of the boundaries synchronous with free-field motion is not dissipated.

[7] Static and dynamic boundary conditions are discussed and validated in *Drift Degradation Analysis* (BSC 2004 [DIRS 166107], Section 6.4.2.1).

Re-establish equilibrium—Finally, the numerical representation was brought to static equilibrium after completion of the dynamic simulation of seismic ground motions. All outside boundaries were fixed, and this stage of the simulation was carried out quasi-statically.

6.5.1.2.3 Characterization of Damage

Effective Strain—The magnitude of damage (or plastic deformation) in the OCB is characterized by the effective strain parameter. In general, strain is a tensor that evolves during deformation. The effective strain is a convenient scalar measure of distortion that can be used to assess the potential for rupturing. This is accomplished by comparing effective strain with the failure strain determined from uniaxial stress tests for the same material. For a uniaxial tension test on a bar, the effective strain is equal to the ratio of the bar extension to its original length. The effective strain is defined (Dieter 1976 [DIRS 118647], p. 90) as:

$$\bar{\varepsilon} = \frac{\sqrt{2}}{3}\sqrt{(\varepsilon_1 - \varepsilon_2)^2 + (\varepsilon_2 - \varepsilon_3)^2 + (\varepsilon_3 - \varepsilon_1)^2} = \sqrt{\frac{4}{3}J_2} \qquad \text{(Eq. 6-6)}$$

where ε_1, ε_2 and ε_3 are principal strain magnitudes, and J_2 is the second invariant of deviatoric strain. Under conditions of large-strain deformation, the strain tensor and effective strain depend on the definition of the reference configuration. A possible approach to avoid ambiguity is to calculate the effective strain by integrating the effective strain rate with respect to time. In UDEC and FLAC3D, the plastic shear strain, $\bar{\varepsilon}_p$, which has an increment equal to the square root of the second invariant of the deviatoric plastic strain rate, is used as a softening-hardening parameter. Under plane-strain conditions, the increment (per computational time-step) of the plastic shear strain can be written (Equation 2.98 in the *Theory and Background* volume of the UDEC manual (Itasca Consulting Group 2005 [DIRS 174198])) as:

$$\Delta\bar{\varepsilon}_p = \sqrt{\frac{1}{2}\left(\Delta\varepsilon_1^{ps} - \Delta\varepsilon_m^{ps}\right)^2 + \frac{1}{2}\left(\Delta\varepsilon_m^{ps}\right)^2 + \frac{1}{2}\left(\Delta\varepsilon_3^{ps} - \Delta\varepsilon_m^{ps}\right)^2} \qquad \text{(Eq. 6-7)}$$

where

$$\Delta\varepsilon_m^{ps} = \frac{1}{3}\left(\Delta\varepsilon_1^{ps} + \Delta\varepsilon_3^{ps}\right) \qquad \text{(Eq. 6-8)}$$

and $\Delta\varepsilon_1^{ps}$ and $\Delta\varepsilon_3^{ps}$ are the principal plastic deviatoric strain increments. Because UDEC automatically keeps track of plastic shear strain for each zone throughout the simulation, the effective strain is approximated by plastic shear strain multiplied by $\sqrt{\frac{4}{3}}$ (hereafter referred to as effective plastic strain). This approximation is acceptable, because the maximum elastic effective strain for Alloy 22 of 0.17% (obtained by dividing the yield strength by Young's modulus) is relatively small compared to rupture strain of 28.5%. However, the maximum plastic shear strain, as obtained from UDEC analyses, accumulates the plastic deformation caused by both tensile and compressive stresses. In reality, only plastic strains associated with

tensile stress can cause rupture. Therefore, the effective plastic strain overestimates the potential for rupture of Alloy 22.

Damage Area—Another parameter used to estimate the potential for degradation of the OCB by accelerated subcritical cracking is the "damaged surface area." This is the OCB surface area with permanent, residual stresses greater than a given stress threshold above which stress-corrosion cracking is accelerated. The damaged surface area is determined from the final, equilibrium stress state achieved after the dynamic simulation of seismic ground motion. The effects of time-dependent creep, stress relaxation, and associated rubble load redistribution were not considered. Because the stresses in the OCB covered by the rubble are more a function of the rubble load than of the accumulated plastic strain, it is expected that large stresses and associated deformation of the OCB will cause additional arching of the load in the rubble with time and, consequently, a reduction of the load on the OCB. The damaged surface area is calculated by adding the lengths of the edges along the interior or the exterior OCB surface for the zones in which the major principal stress exceeds a threshold. The possible overlap of the damaged interior and exterior surfaces was not considered. Strictly speaking, overlapping portions of the interior and exterior damaged surfaces should not be counted twice. Therefore, the reported results overestimate the "damaged" surface area by less than 100%. The damaged surfaces were extracted from the UDEC results for the following stress thresholds: 80%, 90%, 100%, and 105% of the yield strength. These thresholds were taken to indicate the onset of accelerated stress-corrosion cracking. The 80% yield strength level is not used in *Seismic Consequence Abstraction* (SNL 2007 [DIRS 176828]).

6.5.1.3 Summary of the Simulations

In all, 136 simulations were carried out. Two different OCB thicknesses were analyzed, 17 mm and 23 mm. Each thickness was analyzed for 17 sets of ground motions at four PGV levels: 0.4 m/s, 1.05 m/s, 2.44 m/s, and 4.07 m/s. The ground motions at the 0.4 m/s and 4.07 m/s PGV levels were derived by rescaling the available ground motions at the 1.05 m/s and 5.35 m/s PGV levels, respectively (Assumption 5.16, Section 5). Each of 17 ground motions was simulated at each PGV level for different realizations of the rock block geometry. Latin Hypercube sampling was used to pair the ground-motion numbers with seeds for a random-number generator, which controlled the block geometry realization. The analyzed realizations are listed in Table 6-159. The UDEC input and output files from all 136 simulations are in DTN: MO0611WPRUBBLE.000. The output results presented in Section 6.5.1.4 are generated based on results in DTN: MO0611WPRUBBLE.000.

Table 6-159. Simulated Combinations of Ground-Motion Numbers and Random-Number Generator Seed Numbers

Realization (Case) Number	Ground Motion Number	Random-Number-Generator Seed for Joint Pattern
1	4	10
2	10	17
3	5	3
4	3	4
5	1	18[a]
6	17	6
7	6	12
8	11	8
9	8	1
10	12	13
11	7	9
12	15	7
13	13	14
14	14	11
15	2	5
16	16	15
17	9	2

[a] The random number-generator seed equal to 16 resulted in a relatively regular joint pattern. Therefore, 16 was replaced with the next available number, 18.

Output DTN: MO0704SIPAWPSR.000, file *udec_sampling_17_results.xls*.

6.5.1.4 Results

Figures 6-79 through 6-86 show deformed shapes of the OCB together with results of the maximum effective plastic strain and percentage of surface area with stresses greater than 80% of the yield strength, for all analyzed cases, including two OCB thicknesses and ground motions at four PGV levels.

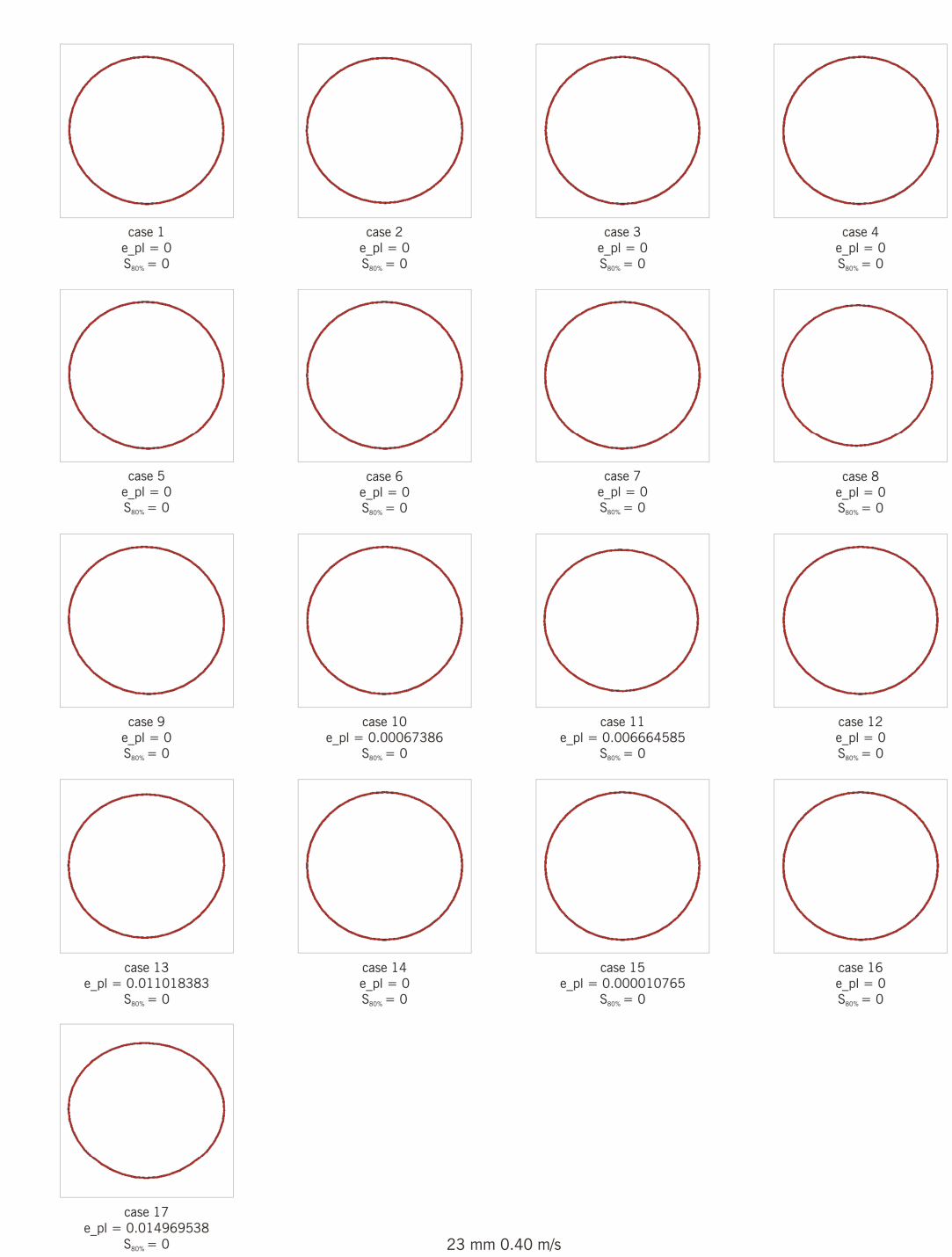

Output DTN: MO0704PUNCTURE.000, file *23mm040msC.pcx*.

Figure 6-79. Deformed Shapes, Maximum Effective Plastic Strains, and Percent of Surface Area with Residual Principal Tensile Stress Greater Than 80% of the Yield Strength for 23-mm-Thick OCB at the 0.40 m/s PGV Level

Output DTN: MO0704PUNCTURE.000, file *23mm105msC.pcx*.

Figure 6-80. Deformed Shapes, Maximum Effective Plastic Strains, and Percent of Surface Area with Residual Principal Tensile Stress Greater Than 80% of the Yield Strength for 23-mm-Thick OCB at the 1.05 m/s PGV Level

Output DTN: MO0704PUNCTURE.000, file *23mm244msC.pcx*.

Figure 6-81. Deformed Shapes, Maximum Effective Plastic Strains, and Percent of Surface Area with Residual Principal Tensile Stress Greater Than 80% of the Yield Strength for 23-mm-Thick OCB at the 2.44 m/s PGV Level

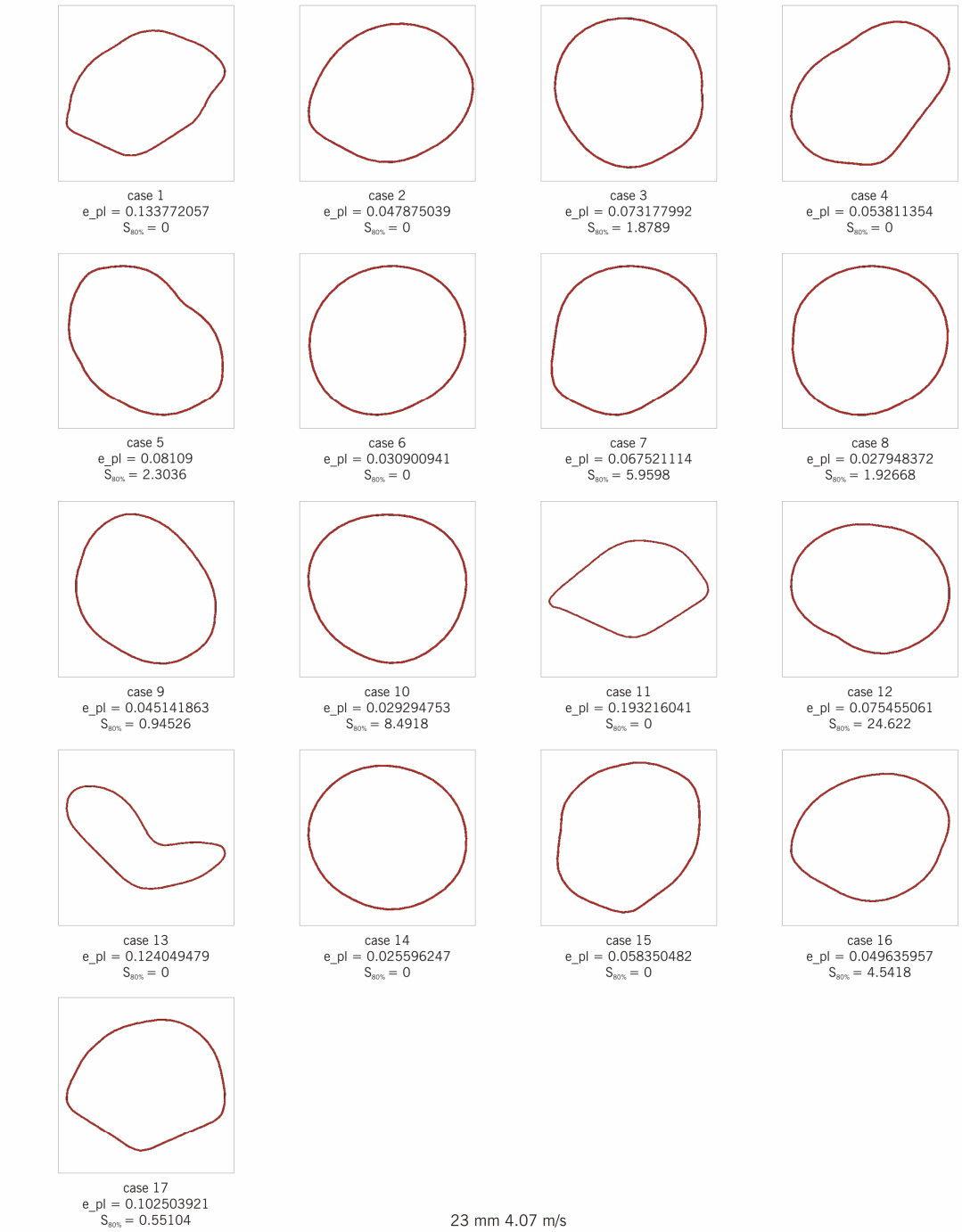

Output DTN: MO0704PUNCTURE.000, file *23mm407msC.pcx*.

Figure 6-82. Deformed Shapes, Maximum Effective Plastic Strains, and Percent of Surface Area with Residual Principal Tensile Stress Greater Than 80% of the Yield Strength for 23-mm-Thick OCB at the 4.07 m/s PGV Level

Output DTN: MO0704PUNCTURE.000, file *17mm040msC.pcx*.

Figure 6-83. Deformed Shapes, Maximum Effective Plastic Strains, and Percent of Surface Area with Residual Principal Tensile Stress Greater Than 80% of the Yield Strength for 17-mm-Thick OCB at the 0.40 m/s PGV Level

Output DTN: MO0704PUNCTURE.000, file *17mm040msC.pcx*.

Figure 6-84. Deformed Shapes, Maximum Effective Plastic Strains, and Percent of Surface Area with Residual Principal Tensile Stress Greater Than 80% of the Yield Strength for 17-mm-Thick OCB at the 1.05 m/s PGV Level

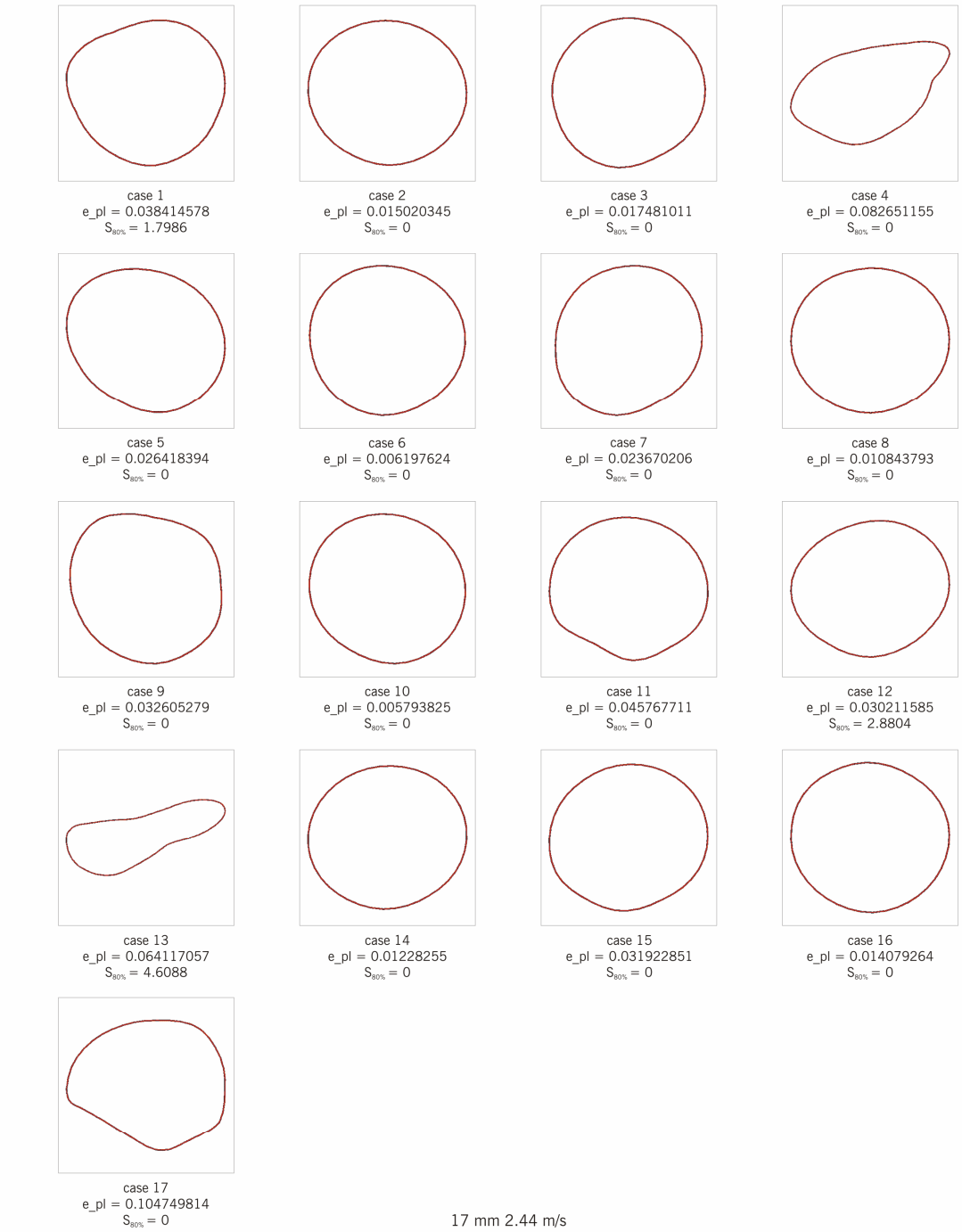

Output DTN: MO0704PUNCTURE.000, file *17mm040msC.pcx*.

Figure 6-85. Deformed Shapes, Maximum Effective Plastic Strains, and Percent of Surface Area with Residual Principal Tensile Stress Greater Than 80% of the Yield Strength for 17-mm-Thick OCB at the 2.44 m/s PGV Level

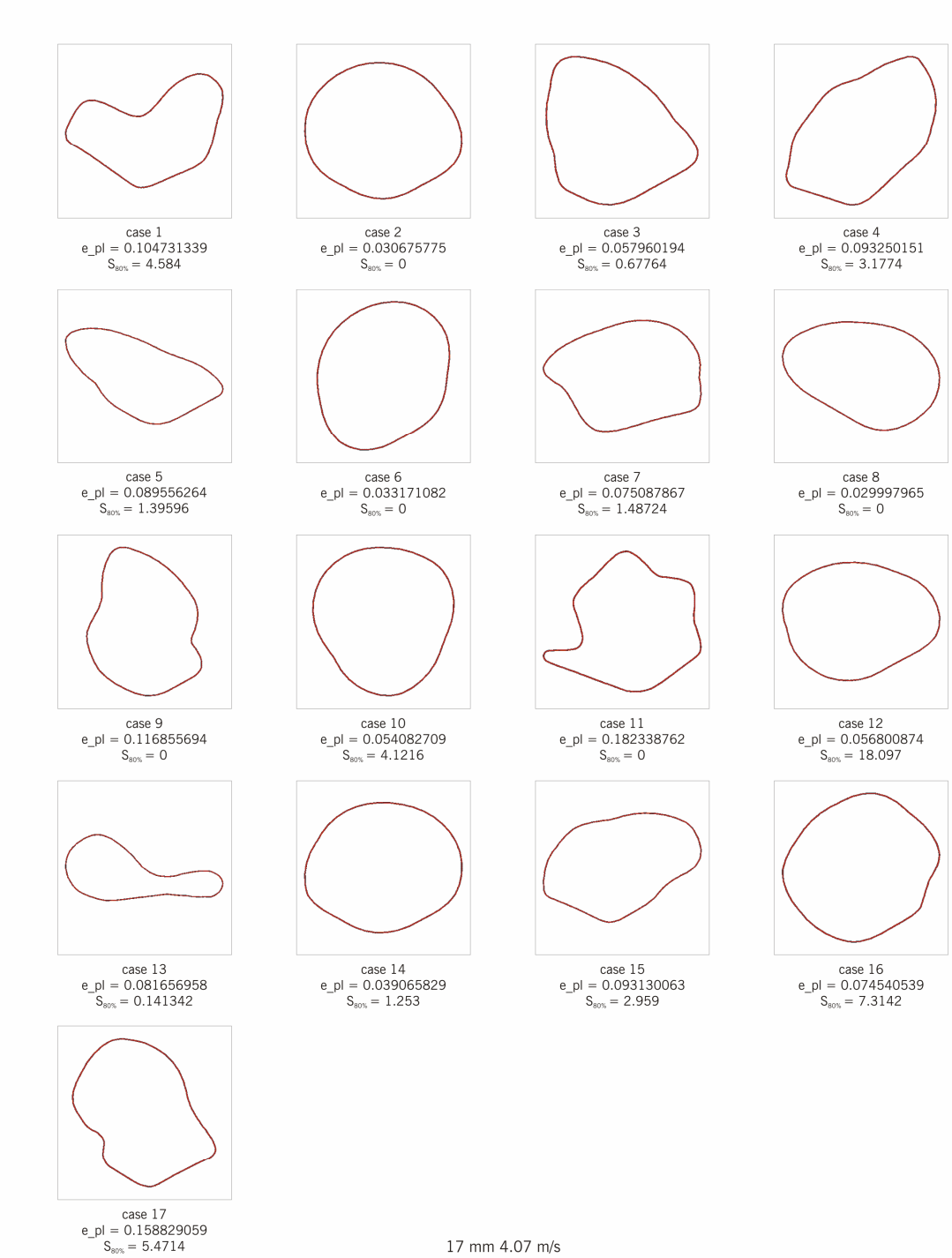

Output DTN: MO0704PUNCTURE.000, file *17mm407msC.pcx*.

Figure 6-86. Deformed Shapes, Maximum Effective Plastic Strains and Percent of Surface Area with Residual Principal Tensile Stress Greater Than 80% of the Yield Strength for 17-mm-Thick OCB at the 4.07 m/s PGV Level

Visual inspection of the results shown in Figures 6-79 through 6-86 indicates that the OCB deformation increases with PGV level and with the decrease in OCB thickness. The maximum effective plastic strains shown in the figures also correlate well with the visual impression of the OCB deformation. However, there is a weak correlation between the damaged surface area and distortion of the OCB or maximum effective plastic strain. Examples are Cases 12 and 13 for 23-mm-thick OCB (Figure 6-82), and Cases 12 and 13 for the 17-mm thick OCB at the 4.07 m/s PGV level (Figure 6-86). For Case 12 (23-mm thick OCB), residual stresses exceed 80% of the yield strength for 24.6% of the surface area, and the maximum effective plastic strain is 0.075. Case 13 (23-mm-thick OCB) with a completely distorted OCB shape, has no surface with residual stresses greater than 80% of the yield strength, while the maximum plastic strain is 0.124.

The analysis discussed in Section 6.5.2 indicates that deformed shapes in the middle of the OCB, as shown for Case 13 in Figures 6-82 and 6-86, are possible before the OCB fails at the connection with the lids or the lids can pop. There are few explanations for such a trend. The residual stresses are not only a function of inelastic deformation and distortion of the OCB, but they also are an even stronger function of the rubble load acting on the OCB. The rubble loads significantly fluctuate during seismic ground motions. Large dynamic loads that cause distortion of the OCB are transient and not necessarily correlated to the final static rubble loads. As the OCB undergoes a large deformation and distortion, particularly at the 4.07 m/s PGV level and 17-mm OCB thickness, it gradually closes the initial 50% porosity of the degraded internals inside the OCB. At one stage of deformation, the rubble load is transferred directly onto the internals. Although the internals have small values of stiffness and shear strength when confined by a deformed OCB, they can resist pressures comparable to or greater than the rubble loads. Consequently, some cases of 17-mm-thick OCB for ground motions at the 4.07 m/s PGV level, for which the OCB is distorted completely, have no surface with stresses greater than the 80% of the yield strength.

6.5.1.4.1 Potential for Rupture

The maximum effective plastic strain for two thicknesses of the OCB as a function of PGV level is shown in Figure 6-87 and listed in Table 6-160. The results, calculated for the 0.4 m/s, 1.05 m/s, 2.44 m/s and 4.07 m/s PGV levels, are averages of 17 realizations (cases). The plot shows that the maximum plastic strain is greater for the 17-mm than for the 23-mm OCB thickness for all velocities. For both thicknesses, the average plastic strain increases monotonically with velocity. Case 11 (Figures 6-82 and 6-86) produced the highest plastic strains of all cases analyzed. These strains occurred at the 4.07 m/s PGV level and were 0.193 for the 23-mm-thick and 0.182 for the 17-mm-thick OCB. The rupture strain of Alloy 22, reduced to account for the three-dimensionality of stresses, is 0.285 (see Section 6.2.2 and Appendix A). Therefore, none of the completed simulations indicates rupture of the Alloy 22 OCB.

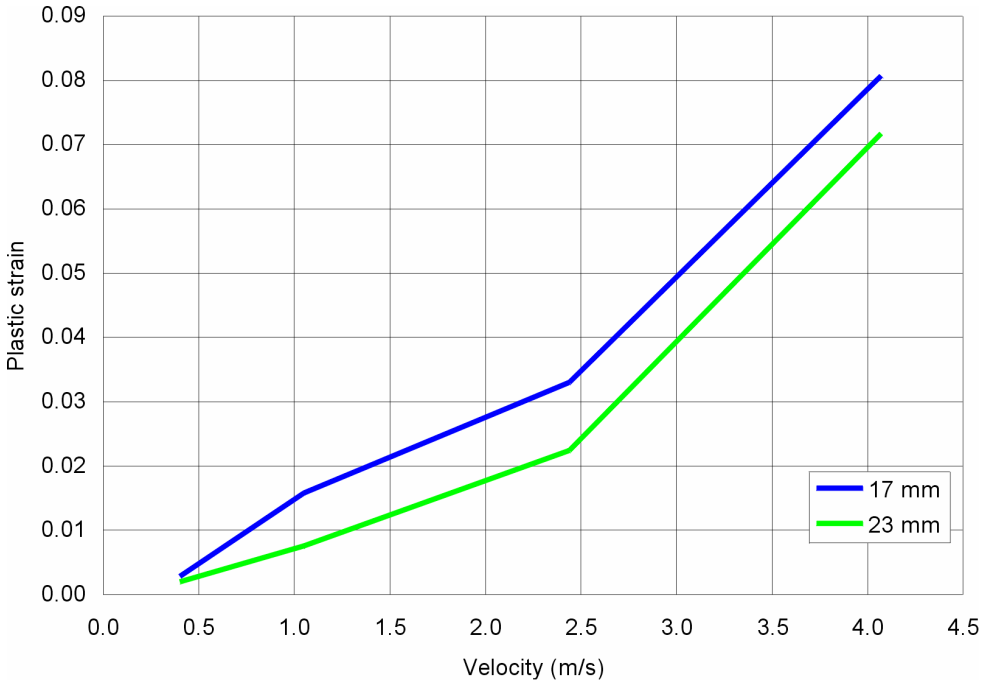

Output DTN: MO0702POSTRUBB.000, file *summary.xls*, chart "strain-velocity."

Figure 6-87. Average of the Maximum Effective Plastic Strains for Two OCB Thicknesses as Functions of the PGV Level

Table 6-160. Average of the Maximum Effective Plastic Strains for Two OCB Thicknesses as Functions of the PGV Level

Thickness (mm)	PGV Level (m/s)			
	0.4	**1.05**	**2.44**	**4.07**
17	2.83×10^{-3}	1.58×10^{-2}	3.31×10^{-2}	8.07×10^{-2}
23	1.96×10^{-3}	7.53×10^{-3}	2.25×10^{-2}	7.17×10^{-2}

Output DTN: MO0702POSTRUBB.000, file *\results production3\postprocessing \summary.xls,* sheet "sheet1."
NOTE: PGV = peak ground velocity.

In these simulations, the degraded internals are represented as continuous, homogeneous, and relatively soft and weak material (Section 6.5.1.2.2 and Assumption 5.15, Section 5). Such a representation of the degraded internals overestimates the deformability of the OCB because the internals (including the stainless steel inner vessel and TAD canister shell), at different stages of degradation, will provide some resistance to deformation of the OCB. The representation of the internals used in the analyses corresponds to the state when corrosion completely degrades all stainless steel components inside the OCB irrespective of geometry and thickness. Because of the different thicknesses of the stainless steel components and variable corrosion rates, there will be a state during the corrosion process when the stainless steel inner vessel and the TAD canister lose their structural integrity and become unable to provide resistance to OCB deformation, but degraded internals still contain relatively stiff and strong stainless steel pieces that are not degraded completely by corrosion. At such states, excessive OCB deformation, as illustrated in

Figures 6-85 and 6-86, poses an additional risk to the integrity of the OCB, which was not taken into consideration in the completed numerical simulations.

Although large deformation of the OCB does not result in strains sufficiently large to fail Alloy 22, the remaining potentially stiff and sharp pieces of stainless steel inside the OCB could puncture an OCB that has deformed sufficiently. A detailed and rigorous analysis of such a process would be difficult because of the wide range of possible degraded states, and the results (in terms of puncturing probability) would depend very much on assumptions of the state of the internals (e.g., number of stainless steel pieces, their sizes, shapes, stiffnesses, and strengths). Instead, the probability of puncturing is estimated using a simple analysis based on the results of OCB deformation (Figures 6-79 through 6-86). The puncturing probability of the OCB, p, is a function of the relative area, a, (i.e., the deformed cross-sectional area of the OCB interior scaled with the initial cross-sectional area), as expressed in the formula in Equation 6-9:

$$p = \frac{a_0 - a}{a_0 - a_1} \qquad \text{(Eq. 6-9)}$$

where a_0 is the largest relative area for which there is probability of puncture (i.e., a puncturing probability greater than zero), and a_1 is the relative area for which puncturing probability is 100%. Because the initial porosity of internals (inside the OCB) is 50%, a_1 is selected to be 0.5. In other words, the puncturing probability of the OCB by the sharp pieces of remaining stainless steel is 100% when the simulation indicates that the OCB completely closes on the internals. Selecting $a_0 = 1$ would lead to unrealistic predictions that there is probability of the OCB puncture for any OCB deformation. Considering the gaps between the OCB and the inner vessel, and between the inner vessel and the TAD canister, and considering the thicknesses of the inner vessel and the TAD canister shell, it is assumed that the puncturing probability is zero until deformation is such that one diameter reduces by four inches, while the other, perpendicular diameter remains unchanged—i.e.,

$$a_0 = \frac{\pi r(r - \Delta r)}{\pi r^2} = \frac{r - \Delta r}{r} = \frac{0.9153\,\text{m} - 2 \cdot 0.0254\,\text{m}}{0.9153\,\text{m}} = 0.944 \qquad \text{(Eq. 6-10)}$$

where $r = 0.9153\,\text{m}$ is the inner OCB radius (Table 4-2).

The puncturing probabilities of the OCB, calculated based on the cross-sectional areas of the OCB interior in the final deformed configurations (shown in Figures 6-79 through 6-86), are listed in Tables 6-161 and 6-162 for 17-mm- and 23-mm-thick OCB, respectively. The calculated puncturing probability shows reasonable trends: (a) it increases with increase in the PGV level (or intensity of the ground motion), and (b) it decreases with increase in the OCB thickness. The puncturing probability at 0.4 m/s is zero irrespective of the OCB thickness. That result is consistent with observations of the OCB deformed shapes in Figures 6-79 and 6-83, which do not indicate significant permanent deformation or distortion of the OCB. For the 23-mm-thick OCB, the puncturing probability is also zero at the 1.05 m/s PGV level. The greatest puncturing probability (0.20 on average, for 17 analyzed cases) is for the 4.07 m/s PGV level with 17-mm-thick OCB.

Table 6-161. Probabilities of Puncturing the 17-mm-Thick OCB Surrounded by Rubble

Realization (Case) No.	PGV level (m/s)			
	0.4	1.05	2.44	4.07
1	0.00	0.00	0.00	0.57
2	0.00	0.00	0.00	0.00
3	0.00	0.00	0.00	0.11
4	0.00	0.05	0.25	0.17
5	0.00	0.00	0.00	0.43
6	0.00	0.00	0.00	0.00
7	0.00	0.13	0.00	0.13
8	0.00	0.00	0.00	0.06
9	0.00	0.00	0.00	0.18
10	0.00	0.00	0.00	0.00
11	0.00	0.00	0.00	0.49
12	0.00	0.00	0.00	0.00
13	0.00	0.00	0.82	1.00
14	0.00	0.00	0.00	0.00
15	0.00	0.00	0.00	0.15
16	0.00	0.00	0.00	0.00
17	0.00	0.00	0.00	0.19
Average	0.00	0.01	0.06	0.20

Output DTN: MO0704PUNCTURE.000, file *Puncture Probability Data - WP Surrounded by Rubble.xls*, sheet "TAD Rubble Data."

Table 6-162. Probabilities of Puncturing the 23-mm-Thick OCB Surrounded by Rubble

Realization (Case) Number	PGV level (m/s)			
	0.4	1.05	2.44	4.07
1	0.00	0.00	0.00	0.07
2	0.00	0.00	0.00	0.00
3	0.00	0.00	0.00	0.00
4	0.00	0.00	0.02	0.05
5	0.00	0.00	0.00	0.01
6	0.00	0.00	0.00	0.00
7	0.00	0.00	0.00	0.00
8	0.00	0.00	0.00	0.00
9	0.00	0.00	0.00	0.00
10	0.00	0.00	0.00	0.00
11	0.00	0.00	0.00	0.24
12	0.00	0.00	0.00	0.00
13	0.00	0.00	0.00	0.82

Table 6-162. Probabilities of Puncturing the 23-mm-Thick OCB Surrounded by Rubble (Continued)

Realization (Case) Number	PGV level (m/s)			
	0.4	1.05	2.44	4.07
14	0.00	0.00	0.00	0.00
15	0.00	0.00	0.00	0.00
16	0.00	0.00	0.00	0.00
17	0.00	0.00	0.10	0.00
Average	0.00	0.00	0.01	0.07

Output DTN: MO0704PUNCTURE.000, file *Puncture Probability Data - WP Surrounded by Rubble.xls*, sheet TAD Rubble Data.

NOTE: PGV = peak ground velocity.

6.5.1.4.2 Damaged Areas

OCB surfaces with residual stresses greater than specified thresholds are characterized as damaged areas. Percentages of OCB surfaces characterized as damaged are shown in Figure 6-88 and listed in Table 6-163 for two OCB thicknesses as a function of PGV level. The results for all four PGV levels are averages of 17 realizations (cases). The damaged area percentages are shown for 80%, 90%, 100%, and 105% of the yield strength. This plot shows that the damaged areas are generally small. For 90% of the yield strength, or greater, the average damaged area is expected to be less than 2% of the total OCB surface area. These results show an increase in damaged area with an increase in peak ground velocity. The damaged area is greater for the 17-mm-thick than the 23-mm-thick OCB for PGV levels smaller than 4.07 m/s.

At the 4.07 m/s PGV level, a counter-intuitive result is observed. The average damaged area is greater for the thicker OCB. The reason for this apparent discrepancy, as discussed previously, is the nonlinear and nonmonotonic response of the OCB as it deforms sufficiently to close the initial open space around the degraded internals.

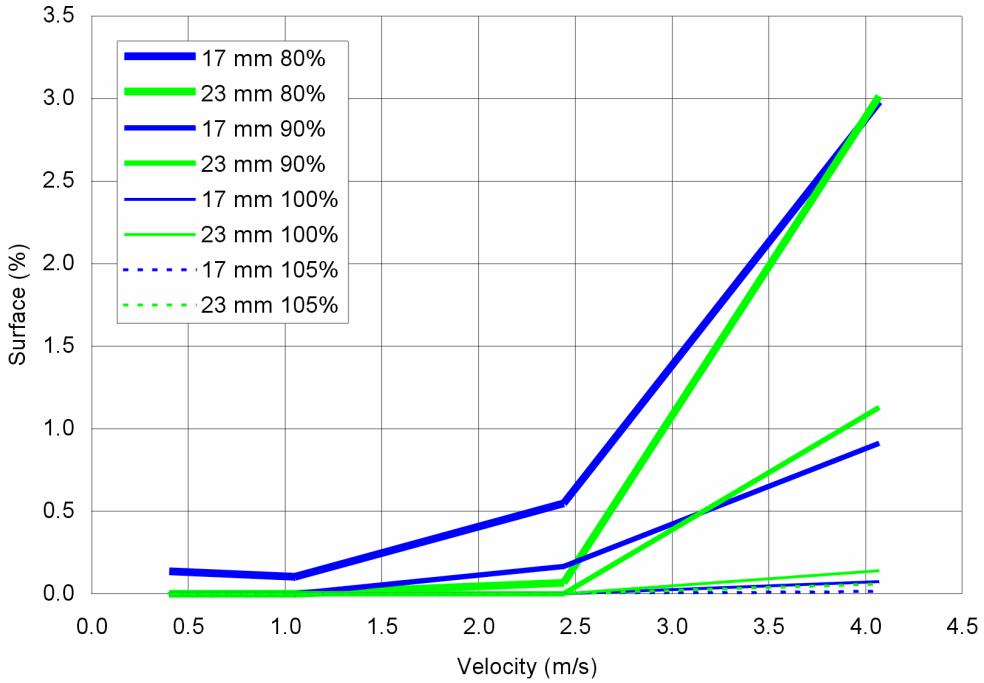

Output DTN: MO0702POSTRUBB.000, file *\results production3\postprocessing \summary.xls* chart *surface - velocity*.

Figure 6-88. Average Damaged Surface Area for Two OCB Thicknesses as a Function of PGV Level

Table 6-163. Average Damaged Surface Area (%) for Two OCB Thicknesses as a Function of PGV Level

		PGV Level (m/s)			
Stress Threshold	**Thickness (mm)**	**0.4**	**1.05**	**2.44**	**4.07**
80% σ_y	**17**	1.37×10^{-1}	1.04×10^{-1}	5.46×10^{-1}	2.98
	23	0.00	0.00	6.64×10^{-2}	3.01
90% σ_y	**17**	0.00	0.00	1.64×10^{-1}	9.12×10^{-1}
	23	0.00	0.00	0.00	1.13
100% σ_y	**17**	0.00	0.00	0.00	7.21×10^{-2}
	23	0.00	0.00	0.00	1.39×10^{-1}
105% σ_y	**17**	0.00	0.00	0.00	1.60×10^{-2}
	23	0.00	0.00	0.00	5.95×10^{-2}

Output DTN: MO0702POSTRUBB.000, file *\results production3\postprocessing \summary.xls*, sheet "sheet1."

NOTE: PGV = peak ground velocity.

6.5.2 Analyses for a Waste Package Loaded by the Drip Shield

6.5.2.1 Purpose

The analysis of drip shield failure modes documented in Section 6.4.4 demonstrates that the main failure mode is failure of the drip shield legs, either by buckling or by failure at the connection

with the crown. Subsequent to such failures, if the legs fail at sufficiently high location, the drip shield could come into contact with the waste package. Configurations of the drip shield and the waste package in the states that indicate drip shield failure for three analyzed realizations are shown in Figure 6-63. Because fracturing of the drip shield was not simulated, actual deformation of the drip shield and evolution of the configuration after the drip shield failure occurs are not simulated correctly. Therefore, the cases in which the drip shield crown is not in contact with the drip shield are not necessarily realistic representations of waste package and drip shield configurations. Under those circumstances, it is possible that the entire load of broken rubble, carried by the drip shield before its collapse, and the weight of the drip shield will be transferred to the waste package. However, if the drip shield plates in the crown do not fail before the framework, the load will not be distributed uniformly. The drip shield will rest on the waste package at the bulkhead flanges, and the entire load (i.e., the rubble load and the drip shield weight) will be transferred to the waste package through the contact surfaces between drip shield bulkhead flanges and the waste package. Structural integrity, stability, and damage in the OCB of the waste package as a function of static vertical load transferred to the waste package through the bulkhead flanges of the collapsed drip shield are investigated in this section.

6.5.2.2 Numerical Representation

The numerical code FLAC3D (V. 2.14. STN: 10502-2.14-00 [DIRS 172323]) was used in the analysis. The deformation and damage of the waste package loaded by the failed drip shield are analyzed for both intact and degraded waste package internals. Each case was analyzed for OCB thicknesses of 17 mm and 23 mm. Although the initial OCB thickness is 25.4 mm, reduced thicknesses were analyzed to account for the effect of uniform corrosion (Assumption 5.13, Section 5). In all simulations, the mechanical behaviors of Alloy 22 (OCB) and Stainless Steel Type 316 (internal vessel, TAD canister, internal plates) are approximated by the strain-hardening, Tresca elastic-plastic constitutive relation, which is discussed in more detail in Section 6.4.2.2.

6.5.2.2.1 Geometry and Mechanical Properties in Case of Intact Internals

For the case shown in Figure 6-89, the internals are considered to be intact. The structural components inside the OCB included in this numerical representation are the internal vessel, the TAD canister and the internal plates. Although the canister geometry is not symmetrical, symmetry is used in the calculations (Assumption 5.22, Section 5). The canister dimensions are given in Table 6-164. The TAD canister holds four horizontal plates and four vertical plates. The two plates nearest the center, at 139 mm, are 19 mm thick, and the two plates farthest from the center, at 413 mm, are 11 mm thick. The OCB and its lid were assigned the mechanical properties of Alloy 22 (Table 4-3). All other internal components of the OCB are assigned properties of Stainless Steel Type 316 (Table 6-165). Only the plates are included inside the TAD canister. However, the density of the plates was increased to account for the mass of the SNF and other components omitted in the numerical representation. The mass of internals (i.e., canister basket weight in Table 4-7) and SNF (21-PWR assemblies given in Table 4-1) inside the TAD canister is taken to be 30,571 lbs + 35,300 lbs = 65,871 lbs. Because the volume of the numerical representation of the plates is 0.22 m^3 (obtained as the output from the numerical representation of the plates), the plates are assigned a density of 33,222 kg/m^3.

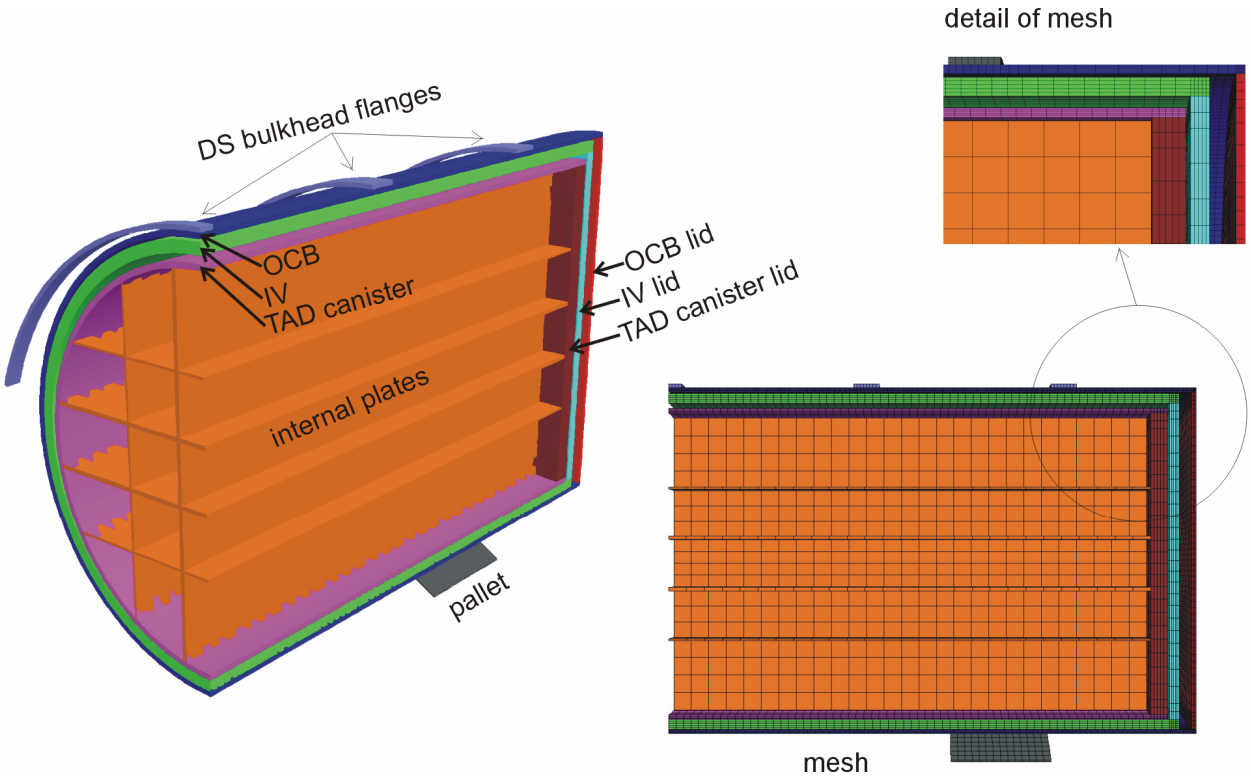

Source: Created for illustrative purposes only.

Figure 6-89. Geometrical Representation of the Waste Package Loaded by the Collapsed Drip Shield for the Case of Intact Internals

Table 6-164. Dimensions of the Canisters Used in the Analysis of the Waste Package Loaded by the Collapsed Drip Shield

	Inner Radius (mm)	Length (mm)	Wall Thickness (mm)	Lid Thickness (mm)
OCB	915.3	5723[a]	23 (17)[b]	23 (17)[b]
Internal vessel	859.8	5535.6	50.8	50.8
TAD canister	819.16	5408.6	25.4	88.9

[a] Because the sleeves are not included in the representation, the total waste package length is reduced by the length of the overhang of the lower sleeve.
[b] The initial OCB thickness is 25.4 mm. The analyses were carried out for two reduced thicknesses to account for uniform corrosion.

Source: Table 4-7.

NOTES: OCB = outer corrosion barrier; TAD = transportation, aging, and disposal (canister).

Table 6-165. FLAC3D Input Parameters Used to Represent the Mechanical Behavior of Stainless Steel Type 316

Property	Derivation	Value
Bulk modulus (K)	$K = \frac{E}{3(1-2\nu)}$	160 GPa
Shear modulus (G)	$G = \frac{E}{2(1+\nu)}$	74 GPa
Cohesion (c)	$c = \frac{\sigma_y}{2}$	96.5 MPa
Cohesion corresponding to 100% of strain (c_1)	$c_1 = \frac{\sigma_y + \left(1 - \frac{\sigma_y}{E}\right) E_t}{2}$	886 MPa
Plastic shear strain corresponding to 100% of strain (ε_{p1})	$\varepsilon_{p1} = 1 - \frac{\sigma_y}{E}$	0.999

Source: Table 4-3.

NOTE: E is the Young's modulus (modulus of elasticity); ν is the Poisson's ratio; σ_y is the yield strength; and E_t is the postyield tangent modulus (tangent hardening modulus) of Stainless Steel Type 316 at 60°C (Table 4-3).

6.5.2.2.2 Geometry and Mechanical Properties in Case of Degraded Internals

The geometrical representation of the waste package with degraded internals is shown in Figure 6-90. Dimensions of the OCB are listed in Table 6-164. The degraded internals inside the OCB have 50% porosity (Assumption 5.10, Section 5). The degraded internals are represented as a very weak, homogeneous, continuous material in the same way as the degraded internals in the analysis of the waste package surrounded by rubble (discussed in Section 6.5.1). The FLAC3D input parameters used in the representation of the mechanical behavior of degraded internals are listed in Table 5-1. The grain density of the internals in this numerical representation is given in Equation 6-11:

$$\rho = \frac{M}{V} = \frac{64038.2\,\text{kg}}{0.5\,\pi\,0.9153^2\,\text{m}^2\,(5.723\,\text{m} - 2\cdot 0.0254\,\text{m})} = 8579\,\text{kg/m}^3 \qquad \text{(Eq. 6-11)}$$

Lengths in the previous formula are taken from Table 6-164. The mass of degraded internals is taken from Section 6.5.1.2.1.

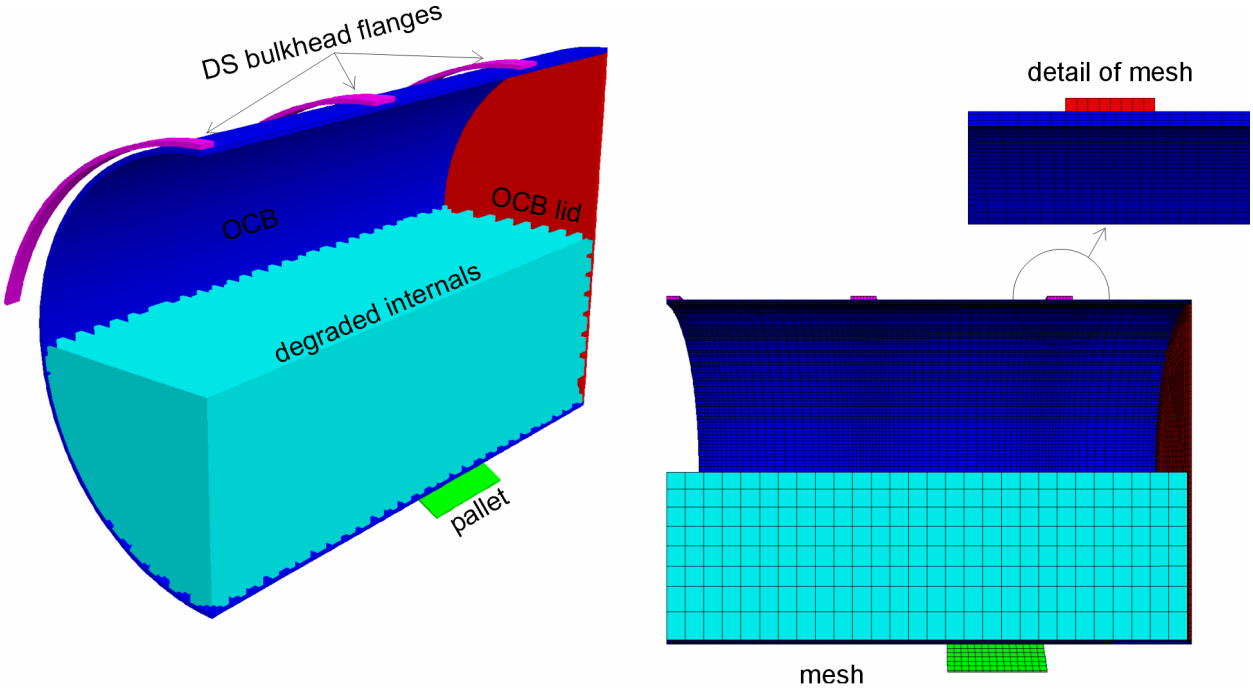

Source: Created for illustrative purposes only.

Figure 6-90. Geometrical Representation of the Waste Package Loaded by the Collapsed Drip Shield for the Case of Degraded Internals

6.5.2.2.3 Boundary Conditions

In this analysis, the pallet and the drip shield bulkhead flanges were considered infinitely rigid. Therefore, mechanical properties assigned to those components are inconsequential. The pallet is fixed. Three bulkheads move vertically downward at the same velocity. The velocity is sufficiently small to ensure quasi-static response of the loaded waste package representation (i.e., that the inertial forces are relatively small). The loads on the waste package are generated as a consequence of interaction between the bulkhead flanges and the OCB. Downward movement of the bulkheads causes the load on the waste package to increase. The velocity boundary conditions applied on the bulkhead flanges represent the scenario in which the drip shield structure is infinitely stiff, such that the rubble load and waste package–drip shield interaction do not cause the drip shield to deform. Under those circumstances, the forces between the bulkhead and the waste package vary from one bulkhead to another. The greatest force is at the bulkhead closest to the lid, because the stiffness of the waste package increases approaching the lid. At the other extreme, when the drip shield structure is relatively soft, three bulkheads move independently of each other, and the force between the bulkhead and the waste package is the same for all bulkheads. The main objective of the analyses discussed here was to determine the potential for subcritical cracking in the OCB, which is correlated with magnitude of the residual stresses and the area of the OCB with stresses greater than the subcritical cracking threshold. Because an uneven load distribution will cause higher stresses in the OCB, the analysis was conducted for all the drip shield bulkheads moving at the same velocity.

6.5.2.3 Results

The maximum stress contours and the "damage areas" (i.e., the interior and exterior surfaces of the OCB with maximum stresses greater than 90% of the Alloy 22 yield strength) are shown for two analyzed cases (with intact and degraded internals) in Figures 6-91 through 6-93. The results in the figures are for the cases with OCB thickness of 23 mm only. Qualitatively, the results for 17-mm-thick OCB are very similar. The damage area is indicated with brown. The plots include two views: one showing the outside surface of the OCB, and the other showing the inside surface of the OCB.

The results for the case with degraded internals are shown for two load levels, 486 kPa and 807 kPa, in Figures 6-91 and 6-92, respectively. (Here, the load is defined as the force between the bulkheads and the waste package, averaged over the surface of the waste package in plan view—i.e., the waste package diameter times the waste package length or, in this case, because of the symmetries used, the waste package radius times half of the waste package length.) The damage areas, which develop first (Figure 6-91) on the interior surface of the OCB in the crown along the symmetry plane half-way between the middle of the waste package and the waste package lid, are caused by bending stresses in the hoop direction. An additional increase in the load and deformation of the OCB does not cause a significant increase of the damage area in the crown on the interior surface. Instead, a large damage area develops on the outside surface along the springline (Figure 6-92).

The results for the case of intact internals, loaded by 1,483 kPa, are shown in Figure 6-93. The plot shows the OCB only, both the lid and the wall. All other structural components included in the numerical representation (indicated in Figure 6-89) are hidden. Although the contours of the maximum stress in the case of intact internals are qualitatively similar to those in the case of degraded internals (e.g., Figures 6-92 and 6-93), the internals make the response of the OCB significantly stiffer and stronger. The explanation for the effect of internals on deformation and damage of the OCB is illustrated in Figure 6-94. At a relatively small load (approximately 150 kPa), deformation of the OCB closes the initial gap in the crown between the OCB and the internal vessel. Because the thickness of the internal vessel wall (50.8 mm) is greater than the thickness of the OCB wall (23 mm or 17 mm), and the Young's moduli of Alloy 22 and Stainless Steel Type 316 are very similar, a greater proportion of the vertical load is carried by the internal vessel than by the OCB. Further load increase, beyond 1,483 kPa, will result in closure of the gap between the internal vessel and the TAD canister (Figure 6-94). At that stage, additional stiffness and strength of both the TAD canister and the internal plates will be mobilized, making the response of the waste package to outside loads even stiffer and stronger.

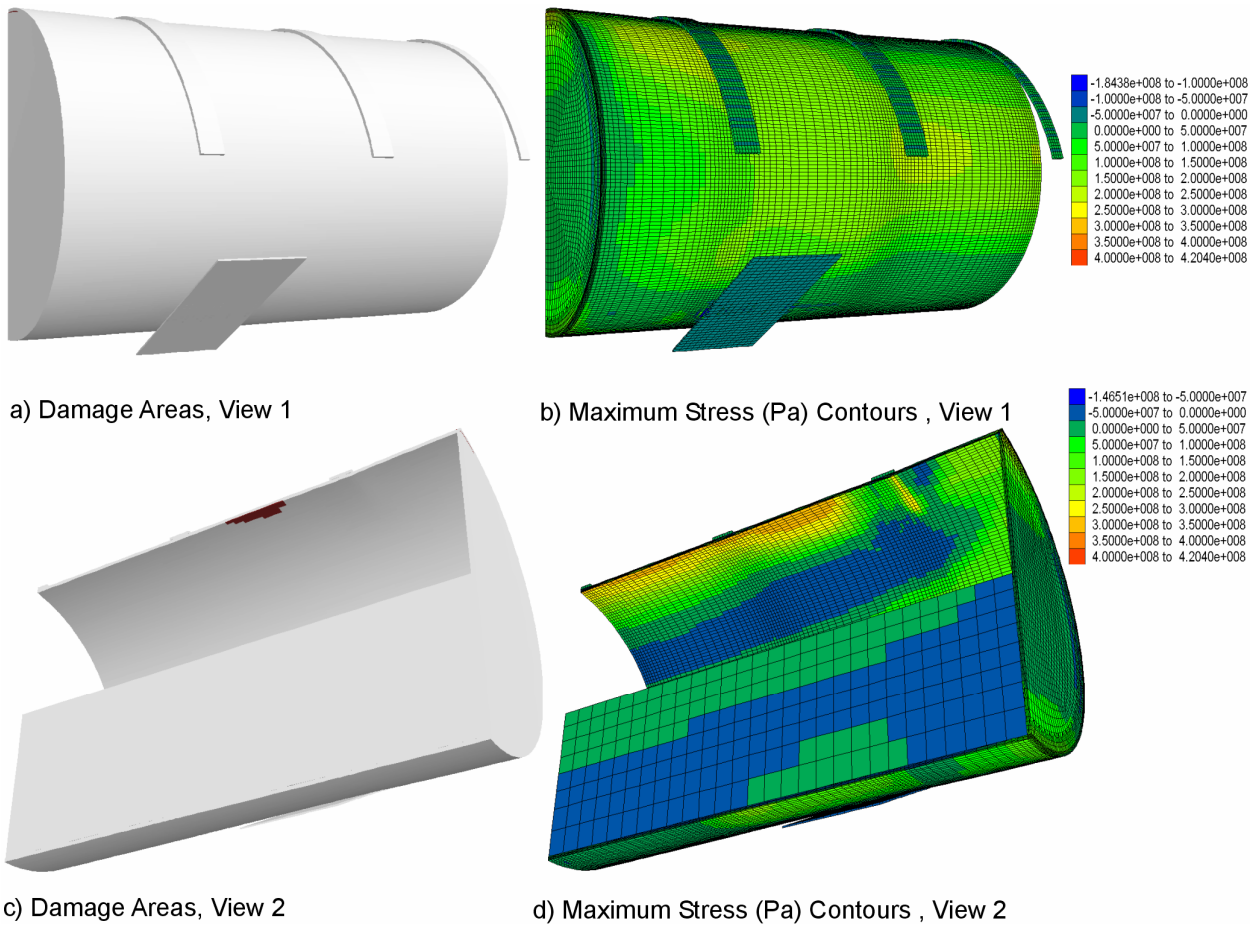

Output DTN: MO0705NDSSTATE.000, file *WPIDSdeg1.pcx*.

NOTE: The damage area is the inner or outer surface of the OCB with maximum stress greater than 90% of the yield strength of Alloy 22 (i.e., 316 MPa). The damage area is shown in brown.

Figure 6-91. Damage Areas and Maximum Stress Contours Shown in Two Views for a 23-mm-Thick OCB of the Waste Package with Degraded Internals Loaded by the Collapsed Drip Shield: 486 kPa Average Vertical Load

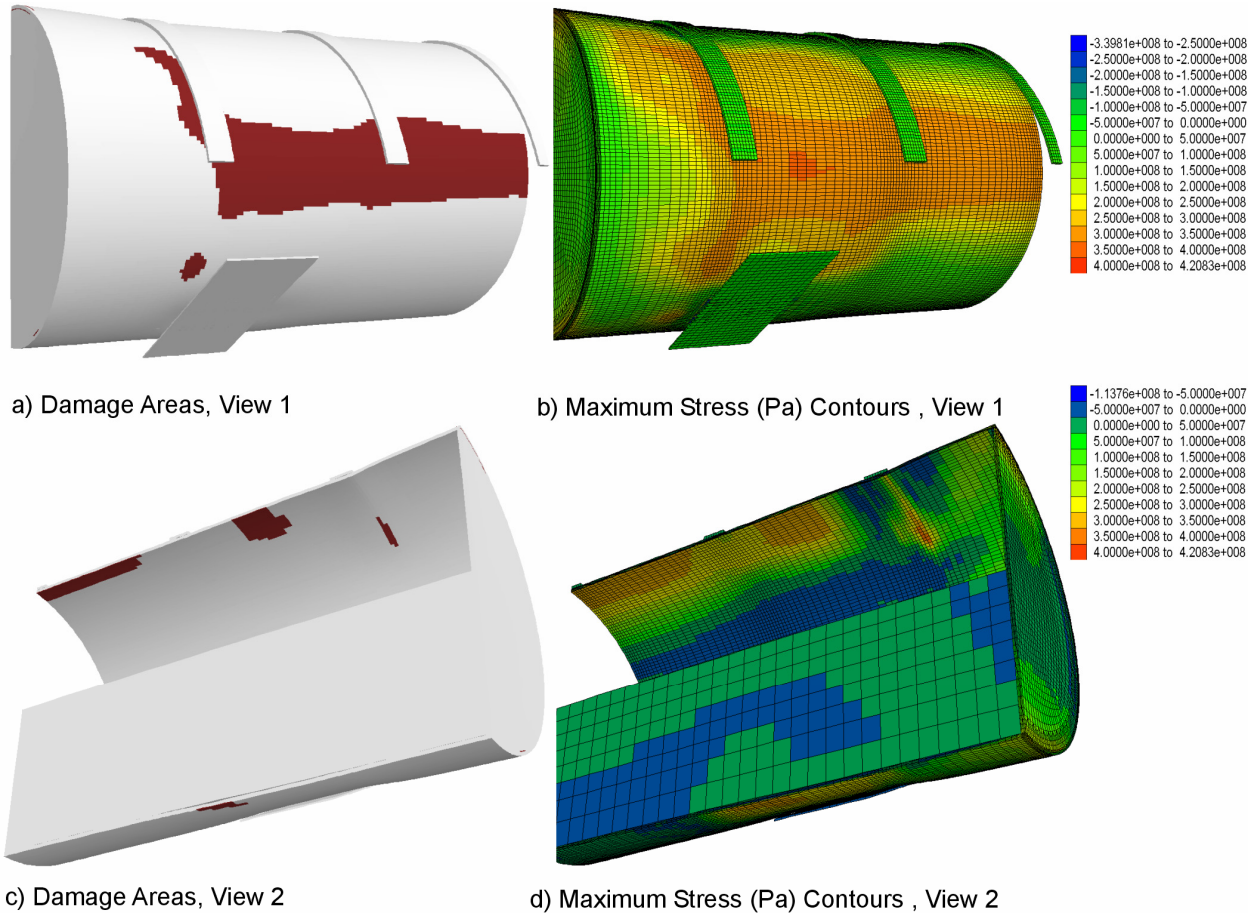

a) Damage Areas, View 1

b) Maximum Stress (Pa) Contours , View 1

c) Damage Areas, View 2

d) Maximum Stress (Pa) Contours , View 2

Output DTN: MO0701DRIPSHLD.000, file *\degraded internals\23mm\spPressure807kPa.sav*.

NOTE: The damage area is the inner or outer surface of the OCB with maximum stress greater than 90% of the yield strength of Alloy 22 (i.e., 316 MPa). The damage area is shown in brown.

Figure 6-92. Damage Areas and Maximum Stress Contours Shown in Two Views for a 23-mm-Thick OCB of the Waste Package with Degraded Internals Loaded by the Collapsed Drip Shield: 807 kPa Average Vertical Load

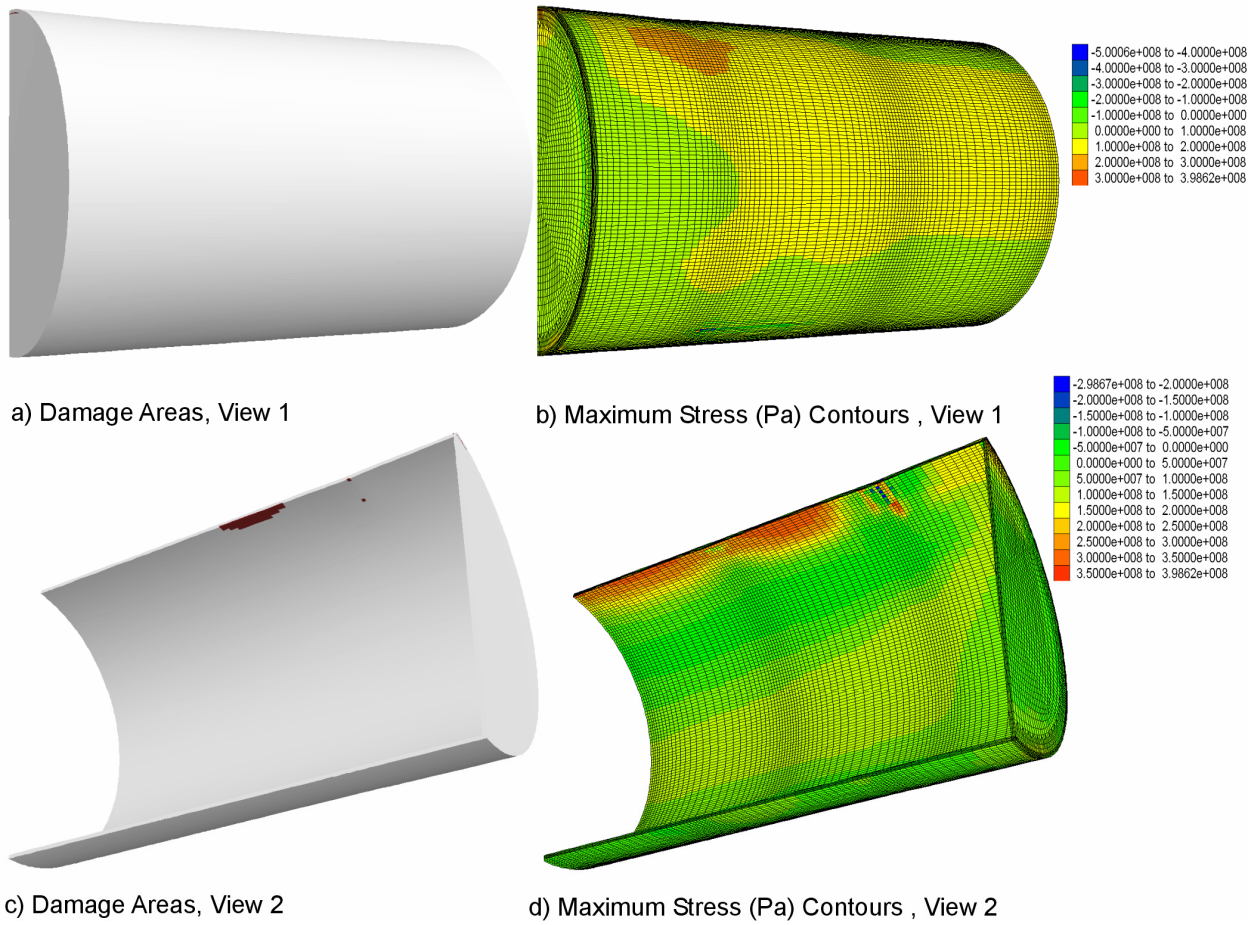

Output DTN: MO0701DRIPSHLD.000, file *\intact internals\23mm\wpPressure1483kPa.sav*.

NOTE: The damage area is the inner or outer surface of the OCB with maximum stress greater than 90% of the yield strength of Alloy 22 (i.e., 316 MPa). The damage area is shown in brown. The internals and pallet are not shown.

Figure 6-93. Damage Areas and Maximum Stress Contours Shown in Two Views for a 23-mm-Thick OCB of the Waste Package with Intact Internals Loaded by the Collapsed Drip Shield: 1,483 kPa Average Vertical Load

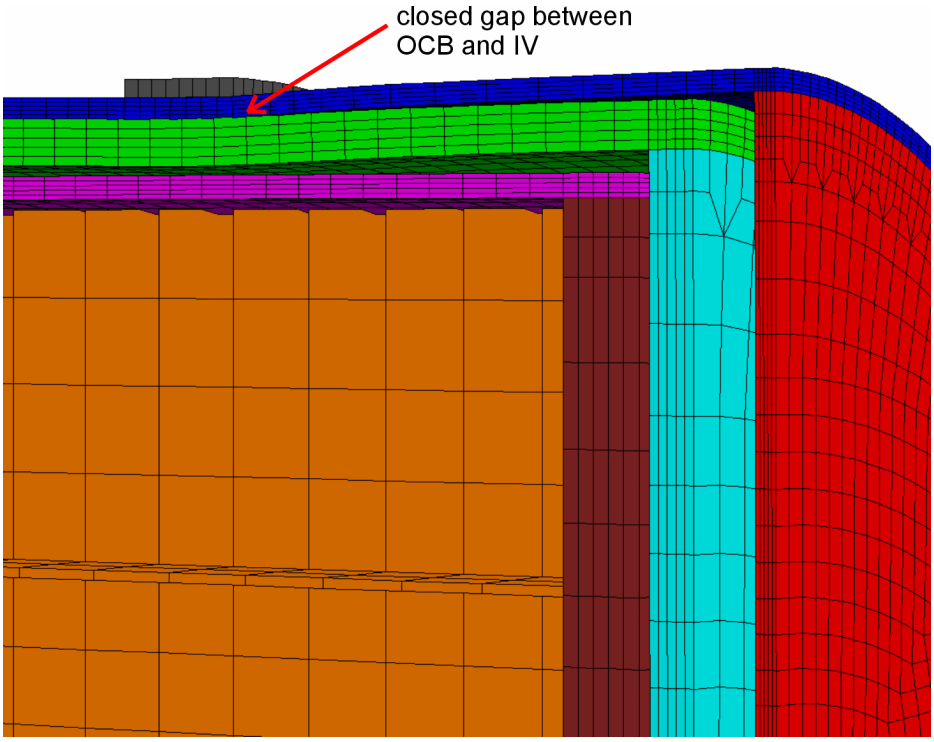

Output DTN: MO0701DRIPSHLD.000, file *\intact internals\23mm\wpPressure1483kPa.sav*.

Figure 6-94. Deformed Geometry of the Waste Package with Intact Internals When Loaded by the Collapsed Drip Shield at 1,483 kPa

The results of the calculations are summarized in terms of damage area as a function of the load (i.e., the average vertical pressure) in Figure 6-95 and Tables 6-166 through 6-169. The results are included for different OCB thicknesses and two extreme cases of the state of the internals (intact and degraded). A point on the OCB wall is considered damaged if the residual stresses on either inner or outer surface are greater than the stress threshold for onset of accelerated stress corrosion cracking. Some curves in Figure 6-95 (for example, 23-mm-thick OCB with intact internals) are not smooth over relatively small damage areas. In addition, in some instances, the damage area decreases with an increase in the load. Those effects are due to the following numerical errors: (a) the relatively large zone surface area compared to the initially small damage area; and (b) the fact that loading is applied by moving the bulkheads at small—but finite—velocities, with the consequence that the numerical simulation is not in perfect equilibrium. These relatively small numerical errors do not affect the main results and conclusion of the analyses. The results of the simulations for the case with intact internals indicate a larger damage surface in the thicker OCB (23 mm) than in the thinner OCB when the load exceeds 1,200 kPa. As the gap between the OCB and the internal vessel closes, the deformation is controlled predominantly, in both cases, by the 50.8-mm-thick internal vessel. Thus, OCB deformation for a given load is not affected by OCB thickness in the numerical representation. However, for the same displacement, the stresses in the thicker OCB are greater.

The average load on the waste package by the collapsed drip shield covered by rubble under static conditions is estimated in Equation 6-12 as

$$p = 127.9\ \text{kPa} + \frac{5\ \text{tons} \cdot 10\ \text{m/s}^2}{2 \cdot 5.723\ \text{m} \cdot (0.9153\ \text{m} + 0.023\ \text{m})} = 132.5\ \text{kPa} \qquad \text{(Eq. 6-12)}$$

where 127.9 kPa is the average static-rubble pressure (Table 6-136), the drip shield mass is 5 mT (Table 4-1), and the numbers in the denominator are dimensions of the waste package taken from Table 6-164. The results of the calculations indicate that, if the internals are degraded, the damage area of the OCB is less than 0.1% of the total area for loads less than or equal to 350 kPa. If the internals are intact, the proportion of the damage area does not exceed 0.1% until the load reaches 1,400 kPa.

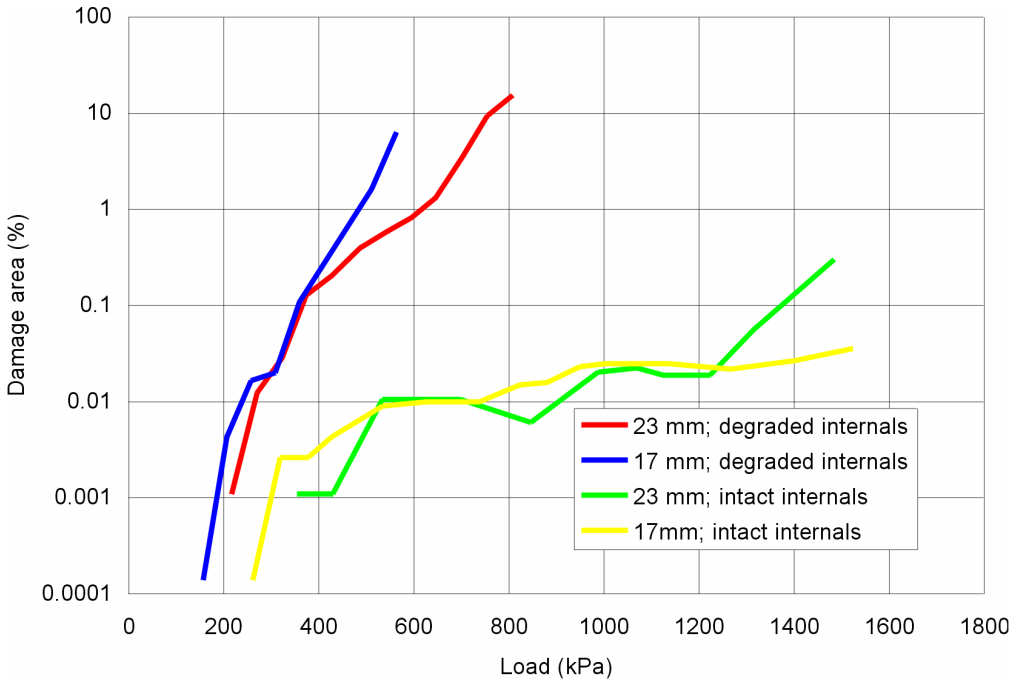

Output DTN: MO0701DRIPSHLD.000, file *summary WP loaded by DS.xls*.

Figure 6-95. Surface Areas with Residual Stresses Greater Than 90% of the Yield Strength of Alloy 22 ("Damage Area") as Function of Vertical Load for the Case of the Waste Package Loaded by the Collapsed Drip Shield for Two OCB Thicknesses

Table 6-166. Surface Areas with Residual Stresses Greater Than 90% of the Yield Strength of Alloy 22 ("Damage Area") as Function of Vertical Load for the Case of the Waste Package Loaded by the Collapsed Drip Shield for 23-mm-Thick OCB and Degraded Internals

Pressure (kPa)	Damage Area (%)	Damage Area (m^2)
0.00	0.00	0.00
50.41	0.00	0.00
112.72	0.00	0.00
164.03	0.00	0.00
216.54	0.00	0.00
270.34	0.01	0.00
322.18	0.03	0.01
372.99	0.13	0.04
426.70	0.20	0.07
486.88	0.40	0.13
545.27	0.60	0.20
595.49	0.81	0.27
646.19	1.33	0.44
702.43	3.48	1.15
753.90	9.36	3.10
807.66	15.30	5.07

Output DTN: MO0701DRIPSHLD.000, file *\waste package loaded by collapsed drip shield\summary\summary WP loaded by DS.xls*, sheet "data."

Table 6-167. Surface Areas with Residual Stresses Greater Than 90% of the Yield Strength of Alloy 22 ("Damage Area") as Function of Vertical Load for the Case of the Waste Package Loaded by the Collapsed Drip Shield for 17-mm-Thick OCB and Degraded Internals

Pressure (kPa)	Damage Area (%)	Damage Area (m^2)
0.00	0.00	0.00
50.92	0.00	0.00
103.36	0.00	0.00
156.30	0.00	0.00
206.86	0.00	0.00
256.96	0.02	0.01
307.80	0.02	0.01
359.34	0.11	0.04
510.60	1.62	0.53
563.33	6.37	2.10

Output DTN: MO0701DRIPSHLD.000, file *\waste package loaded by collapsed drip shield \summary\summary WP loaded by DS.xls*, sheet "data."

Table 6-168. Surface Areas with Residual Stresses Greater Than 90% of the Yield Strength of Alloy 22 ("Damage Area") as Function of Vertical Load for the Case of the Waste Package Loaded by the Collapsed Drip Shield for 23-mm-Thick OCB and Intact Internals

Pressure (kPa)	Damage Area (%)	Damage Area (m^2)
0.00	0.00	0.00
209.90	0.00	0.00
295.34	0.00	0.00
353.96	0.00	0.00
428.96	0.00	0.00
533.72	0.01	0.00
697.78	0.01	0.00
845.63	0.01	0.00
987.02	0.02	0.01
1,068.40	0.02	0.01
1,124.70	0.02	0.01
1,223.30	0.02	0.01
1,314.40	0.06	0.02
1,483.60	0.30	0.10

Output DTN: MO0701DRIPSHLD.000, file *\waste package loaded by collapsed drip shield\summary\summary WP loaded by DL.xls*, sheet "data."

Table 6-169. Surface Areas with Residual Stresses Greater Than 90% of the Yield Strength of Alloy 22 ("Damage Area") as Function of Vertical Load for the Case of the Waste Package Loaded by the Collapsed Drip Shield for 17-mm-Thick OCB and Intact Internals

Pressure (kPa)	Damage Area (%)	Damage Area (m^2)
0.00	0.00	0.00
51.80	0.00	0.00
103.40	0.00	0.00
175.56	0.00	0.00
261.61	0.00	0.00
317.92	0.00	0.00
376.89	0.00	0.00
426.93	0.00	0.00
533.35	0.01	0.00
627.37	0.01	0.00
737.59	0.01	0.00
822.38	0.01	0.00
880.32	0.02	0.01
949.15	0.02	0.01
1,003.10	0.02	0.01
1,080.50	0.02	0.01
1,136.60	0.02	0.01
1,266.70	0.02	0.01
1,401.50	0.03	0.01
1,524.20	0.04	0.01

Output DTN: MO0701DRIPSHLD.000, file *waste package loaded by collapsed drip shield\summary\summary WP loaded by DS.xls*, sheet "data."

6.6 FEATURES, EVENTS, AND PROCESSES

Table 6-170 provides a list of FEPs addressed in this report. The screening decision for FEP 1.2.03.02.0C, Seismic Induced Drift Collapse Damages EBS Components, was changed from "exclude" to "include" because the potential damage to the drip shield plates and drip shield framework from rockfall and ground motion is explicitly included in the seismic scenario class through drip shield fragility curves. FEP 1.2.03.02.0B, Seismic Induced Rockfall Damages EBS Components, remains excluded (a) because FEP 2.1.03.10.0B, Advection of Liquids and Solids Through Cracks in the Drip Shield, is screened out of TSPA; (b) because small amounts of rockfall and/or frictional forces prevent drip shield separation; and (c) because failure of the drip shield plates from rock block impacts has low consequence for dose.

Table 6-170. Features, Events, and Processes Addressed in this Report

FEP Number	FEP Name	Description	Other Reports/Calculations That Also Address This FEP
1.2.03.02.0A	Seismic ground motion damages EBS components	Seismic activity causes repeated vibration of the EBS components (drip shield, waste package, pallet, and invert). This could result in severe disruption of the drip shields and waste packages through vibration damage or contact between EBS components. Such damage mechanisms could lead to degraded performance.	*Seismic Consequence Abstraction* (SNL 2007 [DIRS 176828])
1.2.03.02.0C	Seismic induced drift collapse damages EBS components	Seismic activity could produce jointed-rock motion and/or changes in rock stress leading to enhanced drift collapse that could impact drip shields, waste packages, or other EBS components. Possible effects include both dynamic and static loading.	*Seismic Consequence Abstraction* (SNL 2007 [DIRS 176828])

6.7 UNCERTAINTY

Model uncertainty represents a limitation of any model to accurately represent the physical processes being considered. Models are simplified representations of reality and, as such, introduce inherent errors in estimated quantities due to the simplifications and abstractions necessary for formulating the model. In addition to the limitations in model predictions due to model uncertainty, parameter uncertainty introduces additional uncertainty. Measurement theory provides a useful analogy to compare model and parameter uncertainties. Model uncertainty is similar to measurement accuracy, while parameter uncertainty is similar to measurement precision. Both sources of uncertainty contribute to the final uncertainty in a model prediction or measurement quantity.

In the mechanical assessment of degraded waste packages and drip shields subject to vibratory ground motion, both sources of uncertainty are important and must be estimated. Most of the effort in these analyses has been focused on evaluating parameter uncertainty, and uncertainty in the input parameters for this report is described below.

Uncertainty in Input Parameters for Structural Response Analyses—The structural response analyses for the waste package and drip shield under vibratory ground motions include three major sources of uncertainty: (1) the ground motion time histories (aleatory uncertainty), (2) the metal-to-metal friction coefficient (epistemic uncertainty), and (3) the metal-to-rock friction coefficient (epistemic uncertainty).

Multiple three-component ground motion time histories are used to represent the uncertainty in the seismic forcing functions at PGV levels of 0.40 m/s, 1.05 m/s, 2.44 m/s, and 4.07 m/s. One horizontal component of each ground motion set is scaled to have the same horizontal PGV because its uncertainty has been incorporated into the hazard curves during the probabilistic seismic hazard analysis. The peak ground acceleration and the duration of the time histories span a wide range of response. For example, the PGA for the first horizontal ground motion component at the 2.44 m/s PGV level ranges from about 1.5 g to 7 g.

The metal-to-metal friction coefficient between the waste package, drip shield, and emplacement pallet varies from 0.2 to 0.8 to represent the uncertainty in its value. The friction coefficient affects the onset of sliding and dissipation of energy for the EBS components as a function of the amplitude of the ground motion. The static and dynamic friction coefficients are taken to be equal within the broad range (0.2 to 0.8) defined for this parameter. However, the importance of static friction is anticipated to diminish with increasing ground motion level because the EBS components begin to slide almost immediately for high-amplitude ground motions.

The metal-to-rock friction coefficient between the waste package and the invert, between the emplacement pallet and the invert, or between the drip shield and the invert varies from 0.2 to 0.8 to represent the uncertainty in its value. Again, the friction coefficient affects the onset of sliding and dissipation of energy for the unanchored EBS components as a function of the amplitude of the ground motion. However, the importance of friction is anticipated to diminish with increasing amplitude of the ground motions.

The selection of friction coefficients as major sources of uncertainty, in addition to the ground motions, is based on the potential for frictional forces to influence the kinematics of EBS components. Variability in ground motions is often the most significant uncertainty in structural response analyses for nuclear plant components. Variability of friction coefficients is important because impacts between adjacent components are affected by differences in friction values.

The variations of these uncertain input parameters are simultaneously included in the seventeen structural response analyses at each seismic hazard level. This is accomplished by a Latin Hypercube procedure that ensures robust sampling of the uncertain parameters over their full ranges (Sections 6.3.1, 6.4.4, and 6.5.1). The sampled values for the ground motion number and friction coefficients are documented in (BSC 2005 [DIRS 173172], Attachment X; DTN: MO0508SPAMECHA.000 [DIRS 181067], *AttachmentX.zip*, file *All_3_Sampling_Groups.txt*).

Propagation of Uncertainty—The results from the structural response analyses are postprocessed to determine the damaged areas on the drip shield or waste package. The seismic damage abstractions for the waste package and drip shield make use of a residual stress threshold as a failure criterion (Section 6.2). If the residual stress from mechanical damage exceeds the stress threshold for the barrier, then the affected area(s) are represented as a network of stress corrosion cracks. The residual stress threshold for the waste package is based on a uniform distribution between 90% and 105% of the yield strength for Alloy 22 (Sections 6.3.3, 6.3.4). Postprocessing of the output from waste package analyses determines the damaged areas corresponding to 90%, 100%, and 105% of the yield strength of Alloy 22 (Section 6.3.4.1). The residual stress threshold for titanium is conservatively set to a constant value of 80% of the yield strength of

Titanium Grade 7, so no uncertainty is propagated into TSPA-LA for damaged area on the drip shield from vibratory ground motion.

Uncertainty in Input Parameters for Rockfall Analyses—All rockfall analyses include the ground motion time histories as a major source of uncertainty (Sections 6.4 and 6.5). Seventeen ground motions represent the uncertainty in the seismic forcing functions at the 0.40 m/s, 1.05 m/s, 2.44 m/s, and 4.07 m/s PGV levels. The synthetic fracture pattern is an uncertain input parameter. The synthetic fracture pattern is a representation of the fracture system geometry in three dimensions. The variations in these uncertain parameters are simultaneously included in the rockfall analyses at each seismic hazard level.

Rockfall analyses for the nonlithophysal units predict a wide range of block sizes and velocities that can be ejected from the drift walls and impact the drip shield. More specifically, each rockfall analysis for the nonlithophysal unit predicts a complex, time-dependent sequence of rock blocks that impact the drip shield at varying locations and velocities. These impacts may cause damage to the drip shield if the block has enough mass and kinetic energy.

Conceptual Model Uncertainty—Conceptual model uncertainty for models used in this report results from sparse observational data and a lack of available information to corroborate or refute plausible alternative interpretations of the processes occurring. Alternative conceptual models have been considered for the analysis of rockfall (BSC 2004 [DIRS 166107], Table 6-52). In addition, model results have been validated by comparison to alternative numerical approaches and industry experience through external technical review (Appendix E). Comparison of results for the kinematic model for damage to the waste packages due to vibratory ground motion with other independent modeling techniques in Section 7.3.1 provides confidence that the uncertainty in the modeling method used in the kinematic model is similar to that found in other models. The model for waste package surrounded by rubble is formulated using the UDEC code and in Section 7.3.2 results from similar models formulated using UDEC are compared with results from other models developed for similar purposes. A corroboration of results from the UDEC model with data acquired from a 2-m scale experiment conducted on a rock block with artificial fractures is also presented. These results provide confidence that the uncertainty in the UDEC method is similar to that found in other models. Finally, comparison of the modeling of deformation and damage of the drip shield under static and dynamic conditions with predictions made using a model developed for similar purposes in Section 7.3.3 provides confidence that the uncertainty in this modeling method is similar to that found in other models used for similar purposes.

Output for the kinematic analysis with multiple waste packages (Section 6.3) is presented for two waste package types and as a function of several parameters that are major sources of uncertainty. These include seismic intensity, waste package thickness, and condition of internals. In addition, multiple threshold criteria are used for evaluation of rupture. These parameters are all considered sources of uncertainty in this analysis.

Output for analysis of drip shield damage mechanisms and damage area are presented as functions of drip shield thickness, seismic intensity and rockfall load (Sections 6.4.3 and 6.4.4). These parameters are considered sources of uncertainty for this analysis.

Output for kinematic analysis of waste package-to-drip shield impacts (Section 6.4.5) is presented as a function of seismic intensity, and impacts between five waste packages and the drip shield were analyzed. These parameters are considered sources of uncertainty for this analysis.

Results of the analysis of uneven settlement of the invert (Section 6.4.6) are provided for two different types of loading and for five different amounts of settlement. These parameters are considered sources of uncertainty for this analysis.

Analysis of drip shield damage due to impact by large rock blocks (Section 6.4.7) provides results as a function of seismic intensity, block energy and drip shield thickness. These parameters are considered sources of uncertainty for this analysis.

Output for the analysis of the waste package surrounded by rubble after drip shield failure (Section 6.5.1) is given for different failure criteria and as a function of seismic intensity, waste package thickness, and rock block pattern. These parameters are considered sources of uncertainty for this analysis.

Finally, the analysis of the waste package loaded by the drip shield and rockfall after drip shield failure (Section 6.5.2) presents results as a function of waste package thickness and the state of internals. These parameters are considered sources of uncertainty for this analysis.

The most significant uncertainties impacting the results of models of the mechanical assessment of waste packages and drip shields subject to vibratory ground motion are the uncertainties associated with the postclosure ground motions and with the time-dependent strength degradation of the EBS components. Some of the ground motions provided are larger than the largest ground motions observed and may not be physically realizable. Therefore, some of the cases analyzed in this report may be unrealistic. Given these challenges it is difficult to quantify model uncertainty. Moreover, given the complexity of the modeling, and uncertainty of the inputs, such uncertainty is not unprecedented. Finally, the amount of uncertainty in the models used in this report is acceptable given the complexity of the models and the built-in conservatisms.

6.8 LIMITATIONS

Major limitations of the mechanical assessment of degraded waste packages and drip shields subject to vibratory ground motion presented in this report are as follows:

- Analyses in this report are performed for representative TAD-bearing and codisposal waste packages. Detailed analyses of all the types of waste packages that will eventually be emplaced in the repository and their internals are beyond the scope of this report. However, it is important to note that the TAD-bearing and codisposal waste packages form the majority of waste packages that will be emplaced in the repository under the current design (DTN: MO0702PASTREAM.001 [DIRS 179925]).

- The kinematic analyses presented here use a limited series of waste packages to reasonably represent the mechanical response of waste packages in a complete emplacement drift. This representative sequence of waste packages in the simulated emplacement was developed using the approximate percentages of waste package types planned to occur in the inventory. However, a typical waste emplacement drift, 600 m in length, will contain roughly 100 waste packages of various types. Moreover, kinematic and associated damage analyses are based on the planned as-emplaced waste package configuration, and changes in the geometry of the waste packages over time as a function of previous seismic activity are neglected.

- Structural response calculations for the waste package are based on the average thickness of the outer barrier. Uniform thinning of waste package and drip shield is used to approximate uniform corrosion over time. It is unlikely that the waste package and drip shield components will corrode uniformly over their entire surface.

- Ground motions at 0.4 m/s and 4.07 m/s PGV levels have been created by linearly scaling the ground motions for the 1.05 m/s and 5.35 m/s PGV levels, respectively.

- The structural response calculations for the TAD-bearing and codisposal waste packages are based on two discrete values for the spatially averaged thickness of the OCB: 23 mm and 17 mm. The 23-mm-thick OCB provides a representation for an intact or almost intact waste package. The 17-mm-thick OCB provides a representation for a highly degraded waste package at late times after repository closure. The 17-mm-thick OCB provides a reasonable representation of degraded states of the OCB at approximately 1,000,000 years, as shown in (SNL 2007 [DIRS 176828], Section 6.5.2.2).

- Waste package internals are assumed to degrade as structural elements after the OCB is first damaged by a seismic event. More exactly, the internals degrade as a structural component by the time of the next seismic event after the first seismic event that breaches the waste package. This approach is conservative because a waste package with intact internals has significantly less deformation and no rupture relative to a waste package with degraded internals. However, this approach underestimates the structural capacity of stainless steel internal components, such as the 2-in-thick inner vessel or the TAD canister itself, for screening of criticality-related issues during a 10,000-year period.

- Structural response calculations for the waste package surrounded by rubble are based on the TAD-bearing waste package with degraded internals. Section 6.5.1.1 provides the rationale for using the results for the TAD-bearing waste package with degraded internals for the codisposal waste package with degraded internals.

- The internals of the waste package surrounded by rubble are always degraded. The use of degraded internals is consistent with the fact that the waste package becomes surrounded by rubble at late times, after the drip shield plates have failed and allowed rubble to contact the waste package. The use of degraded internals is conservative because damage to a waste package with degraded internals is observed to be

significantly greater than damage to a waste package with intact internals (see Sections 6.3.4 and 6.5.1.1).

- The carbon steel structural elements in the invert are not represented in the postclosure models because the carbon steel will degrade quickly in the postclosure timeframe. However, if the structural steel were present, either intact or in some intermediate state of corrosion, at the time of a seismic event, then there might be potential for waste packages to impact the invert steel and cause damage or puncture of the waste packages.

These limitations should be considered during use of these results in development of abstractions for TSPA.

7. MODEL VALIDATION

SCI-PRO-006, *Models,* requires that total system performance assessment (TSPA) model components be validated for their intended purpose and stated limitations, and to the level of confidence required by a component's relative importance to the performance of the repository. Section 1 of this report describes the intended purpose and limitations of the model components with regard to damage to Engineered Barrier System (EBS) components due to vibratory ground motion.

7.1 IDENTIFICATION OF CORROBORATING/SUPPORTING DATA, MODELS, OR INFORMATION USED TO COMPLETE MODEL VALIDATION ACTIVITIES

Sources containing corroborating/supporting information include journal articles and project reports and are identified in the subsection associated with each model validation discussion.

7.2 LEVEL OF MODEL IMPORTANCE, REQUIRED LEVEL OF CONFIDENCE, AND CONFIDENCE OBTAINED DURING MODEL DEVELOPMENT

7.2.1 Level of Model Importance

The governing technical work plan (SNL 2007 [DIRS 179869], Section 2.3.1) indicates that the level of confidence required for validation of the models for waste package damage during vibratory ground motion model is high (Level II) because damage to the waste package is a significant factor in determining the dose in TSPA calculations. Two postdevelopment validation methods are required to meet a Level II validation. The level of confidence required for damage calculations related to the drip shield during vibratory ground motion is also high (Level II). This is because the drip shield deflects seepage and rockfall away from the waste package, thereby reducing advective releases from the waste package, but it has no direct effect on the release through stress corrosion cracks in the waste package. The drip shield, therefore, has a lesser role than the waste package in radionuclide releases; however, it is categorized as Level II and two postdevelopment validation methods are required.

In accordance with the technical work plan (TWP) for this work (SNL 2007 [DIRS 179869]), three primary submodels are validated. These are: (1) a three-dimensional kinematic model for EBS damage due to vibratory ground motion appropriate for the postclosure period where relatively little EBS degradation occurs, (2) a model for deformation and damage of the drip shield under static and dynamic conditions appropriate for the postclosure period associated with an intermediate level of EBS degradation, and (3) a model for the waste package surrounded by rubble that is used to estimate damage at late times during the postclosure when there may be extensive degradation of the EBS.

Postdevelopment activities for the three dimensional kinematic model of EBS damage include corroboration of model results with results of other independent models developed for similar uses (Section 7.3.1.1), and a critical review of the model conducted by a technical specialist (Section 7.3.1.2). Postdevelopment activities for the model for the waste package surrounded by rubble include comparison of UDEC results to other numerical approaches (Section 7.3.2.1) and comparison of UDEC predictions with experimental results from an explosively loaded, scaled

tunnel in jointed rock (Section 7.3.2.2). Finally, postdevelopment activities for the model for drip shield damage under quasi-static and dynamic conditions includes a comparison of FLAC3D and LS-DYNA predictions for quasi-static drip shield deformations (Section 7.3.3.1) and for dynamic predictions of drip shield response to block impact (Section 7.3.3.2).

7.2.2 Decisions and Activities Implemented During the Model Development Process to Build Confidence in, Verify, and Justify an Adequate Technical Approach

In accordance with SCI-PRO-002, *Planning for Science Activities* (Attachment 3), Level I and II validations include a discussion of model development. In particular, this report documents decisions implemented during model development that build confidence and verify that an adequate technical approach, using scientific and engineering principles, was taken. The development of the models is documented in accordance with the requirements of Section 6.3.1 of SCI-PRO-006 and Attachment 3 of SCI-PRO-002. The development of the models for damage to EBS components during vibratory ground motion has been conducted according to these criteria, as follows:

1. *Evaluate and select input parameters and/or data that are adequate for the model's intended use (SCI-PRO-002, Attachment 3 Level I(1), and SCI-PRO-006, Section 6.3.1(b)).*

   The inputs to the models for damage to EBS components during vibratory ground motion have all been obtained from controlled sources. All data for the engineered and natural systems are from designs or studies specific to the site operations and postclosure conditions (Section 4). All design information is from Design TDIPs, and Section 4.1 discusses the selection of input and design parameters. The input data and their sources are summarized in Tables 4-1 to 4-8. Additional discussion of material properties, including rationale for use, is contained in Section 5.

2. *Formulate defensible assumptions and simplifications that are adequate for the model's intended use (SCI-PRO-002, Attachment 3 Level I(2)).*

   Discussion, including the rationale and justification of assumptions and simplifications for models used in this report, is provided in Section 5. Additional discussion of simplifications can be found in Appendix A.

3. *Consistency with physical principles, such as conservation of mass, energy, and momentum, is ensured to an appropriate degree commensurate with the model's intended use (SCI-PRO-002, Attachment 3 Level I(3)).*

   Consistency with physical principles for models used in this report is demonstrated by the conceptual, mathematical, and numerical formulations presented in Section 6 for the LS-DYNA, FLAC, FLAC3D, and UDEC codes based on those physical principles. It is not possible for the LS-DYNA, FLAC3D, and UDEC codes to complete a model simulation unless converged solutions are obtained for all calculation cycles (i.e., time steps).

4. *Represent important future state (aleatoric), parameter (epistemic) and alternative model uncertainties to an appropriate degree commensurate with the model's intended use (SCI-PRO-002, Attachment 3 Level I(4)).*

   The purpose of the models is to predict a reasonable range of damage to the EBS components due to vibratory ground motion, resulting from parametric uncertainty and variability. The aleatoric uncertainty is addressed throughout the analyses by the use of seventeen realizations of the seismic time histories, each at four different levels of peak ground velocity (PGV). Future states of the system are appropriately represented by modeling the evolutionary conditions and configurations of the EBS as outlined in Section 1.2. Discussion of the aleatoric and epistemic uncertainties associated with each model is presented in the subsection appropriate to each model.

   As explained in Section 1.2, the range of simulations has been structured to span the conditions predicted to exist in the EBS over the postclosure period. The full span of appropriate conditions is captured by, first, representing the drift with small amounts of rubble and corrosion, then evaluating the EBS with more rubble and with degraded drip shields, waste packages and waste package internals, and finally modeling the EBS with a collapsed or completely degraded drip shield, with waste packages surrounded by rubble.

5. *Ensure simulation conditions have been designed to span the range of intended use and avoid inconsistent outputs or that those inconsistencies can be adequately explained and demonstrated to have little impact on results (SCI-PRO-002, Attachment 3 Level I(5)).*

   Initial and boundary conditions for the models of damage to EBS components during vibratory ground motion are based on inputs from other project documents (Section 4). The assumptions used in the model formulation are documented in Section 5. Descriptions of design features are documented in information exchange documents. The seismic time histories are documented in *Development of Earthquake Ground Motion Input for Preclosure Seismic Design and Postclosure Performance Assessment of a Geologic Repository at Yucca Mountain, NV* (BSC 2004 [DIRS 170027], Section 6.3.2); rockfall estimates are documented in *Drift Degradation Analysis* (BSC 2004 [DIRS 166107], Section 6.4). These inputs are sufficient to define complete simulation conditions for the kinematic models.

   The models for damage to EBS components due to vibratory ground motion address variability in the magnitude of vibratory ground motion by using 17 unique time histories, each at four different PGV levels. Two predominant waste package types (transportation, aging, and disposal (TAD) canister and codisposal) are considered. Variability in the emplacement geometry of the waste packages is addressed in Section 6.3.2.

   The predictions of the models for EBS damage due to vibratory ground motion, as displayed in plots and tables throughout Sections 6.3 to 6.5, have been thoroughly inspected and thoroughly tested by way of sensitivity analyses documented in those sections to assure the reasonableness and appropriateness of the outputs and the avoidance of inconsistencies.

There were no calibration activities associated with the kinematic models for damage to EBS components during vibratory ground motion.

6. *Ensure that model predictions (performance parameters) adequately represent the range of possible outcomes, consistent with important uncertainties and modeling assumptions, conceptualizations, and implementation (SCI-PRO-002, Attachment 3 Level I(6)).*

   The range of possible outcomes for each of the models is discussed in the appropriate sections below and in the appropriate sections of Section 6.

7.3 POSTDEVELOPMENT MODEL VALIDATION ACTIVITIES AND RESULTS

Validation of Level II models must address at least two of the following criteria from Section 6.3.2 of SCI-PRO-006 (SCI-PRO-002, Attachment 3 Level II):

- Corroboration of model results with data acquired from laboratory, field experiments, analog studies, or other relevant observations, not previously used to develop or calibrate the model (peer review per SO-PRO-001, *Peer Review*).
- Corroboration of model results with results obtained from other independent mathematical models developed for similar purposes.
- Critical review conducted by a technical specialist(s).

Activities to address these criteria are presented below.

7.3.1 Validation Activities for Three-Dimensional Kinematic Model of EBS Damage Due to Vibratory Ground Motion

The three-dimensional kinematic model for EBS damage due to vibratory ground motion is validated by three postdevelopment activities as indicated in Table 2-1 of the TWP (SNL 2007 [DIRS 179869]). First, kinematic results obtained using LS-DYNA (a finite-element computer program) are compared to those obtained using two different numerical analyses. These include an alternative computational kinematic model in UDEC (a distinct element computer program), as discussed in Section 7.3.1.1.1, and detailed LS-DYNA analyses of single waste packages subjected to vibratory ground motion, as discussed in Section 7.3.1.1.2. Finally, an independent critical review conducted by a technical specialist is presented (see Section 7.3.4 and Appendix E).

7.3.1.1 Corroboration of Model Results with Results of Other Independent Models Developed for Similar Uses

7.3.1.1.1 Comparison to UDEC Results

In accordance with validation activities described in Table 2-1 of the TWP (SNL 2007 [DIRS 179869]), this section presents a comparison of results from the three-dimensional kinematic LS-DYNA model with results from an alternative computational technique. A previous study with a preliminary configuration of 13 waste packages was performed using this

model (Validation DTN: LL0705PA010SPC.027, file *LSDYNA_13WP_Validation_Analysis.tar.gz*). While the model is three-dimensional, there is a symmetry plane cut along the axis of the drift. Ground motions were applied horizontally, following the direction of the drift, and vertically. A similar analysis was also performed in two dimensions, using UDEC with the same configuration of 13 waste packages (Validation DTN: MO0705UDECMECH.000, file *UDEC_WP-WP.zip*). The models are compared in Figure 7-1 and Figure 7-2.

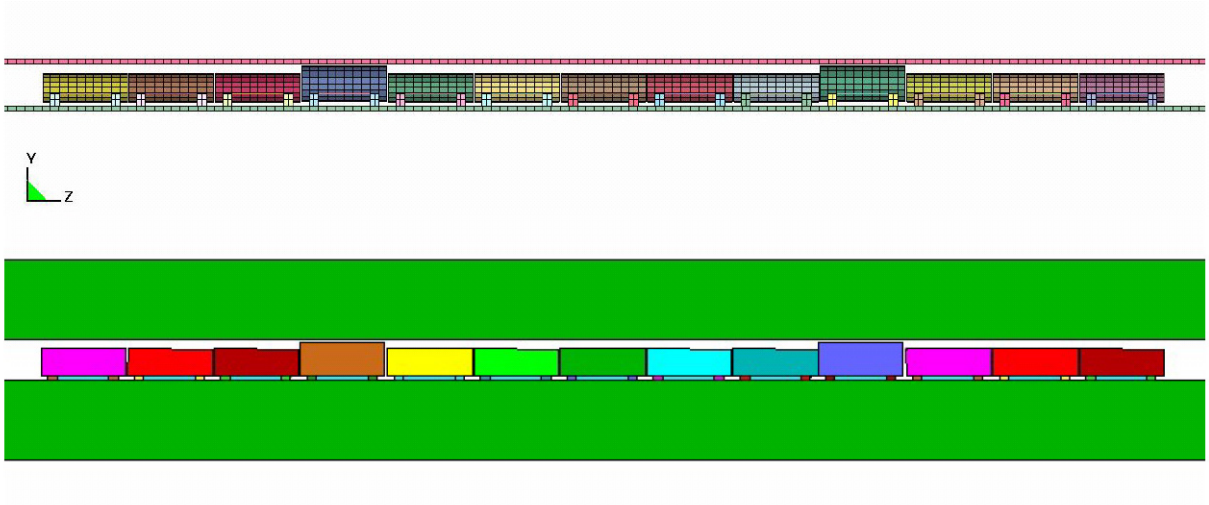

Output DTN: LL0704PA051SPC.026, file *Figures_Mech_Assessment_AMR.tar.gz.*

NOTES: The three-dimensional LS-DYNA model (top) has a vertical symmetry plane along the axis of the drift. The UDEC model (bottom) is two-dimensional along the same vertical plane.

Figure 7-1. LS-DYNA Model and UDEC Model of a Preliminary Configuration of 13 Waste Packages

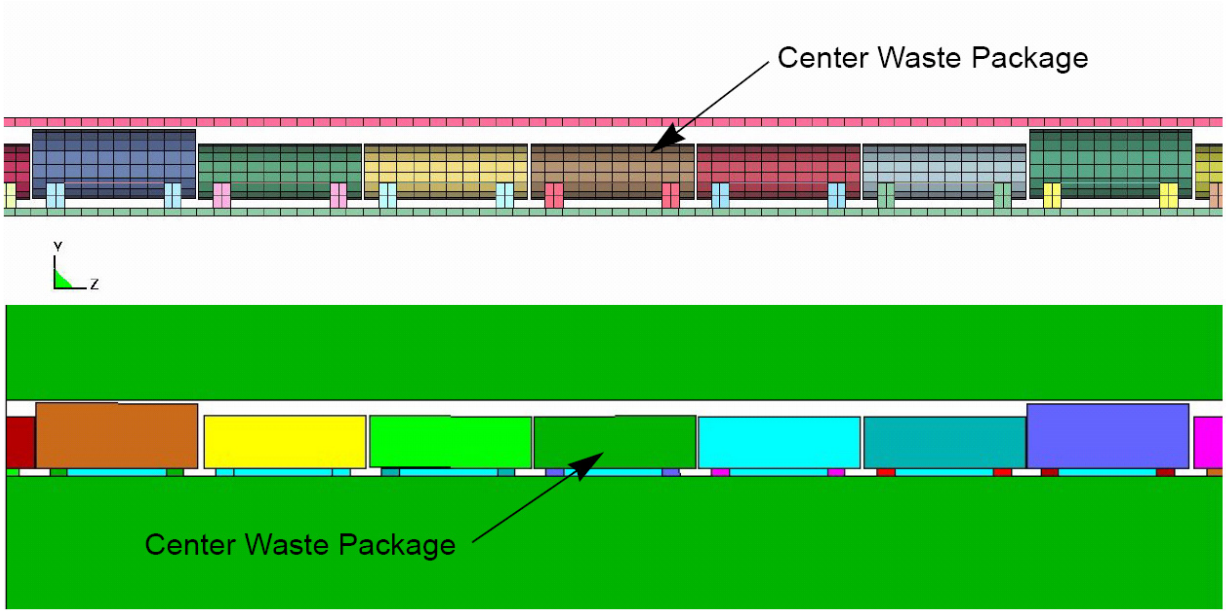

Output DTN: LL0704PA051SPC.026, file *Figures_Mech_Assessment_AMR.tar.gz*.

NOTES: The LS-DYNA model (top) has a vertical symmetry plane along the axis of the drift. The UDEC model (bottom) is two-dimensional.

Figure 7-2. Central Waste Packages of LS-DYNA Model and UDEC Model of a Preliminary Configuration of 13 Waste Packages

The vertical and H2 horizontal components of ground motion 1 at 5.35 m/s PGV (corresponding to realization 14) were applied to both models. The computed rigid-body velocity of the three central waste packages for the LS-DYNA and UDEC models is compared in Figures 7-3 to 7-5. The rigid-body motions computed for the two models are reasonable, agree well in terms of amplitude, show similar oscillatory behavior, and are appropriate for the intended use. Thus, these results meet the validation review criteria presented in the TWP (SNL 2007 [DIRS 179869], Table 2-1) and provide corroboration for the approach of using LS-DYNA to perform kinematic analyses of multiple waste packages subjected to seismic excitation, where the rigid-body behavior of the waste packages is of interest.

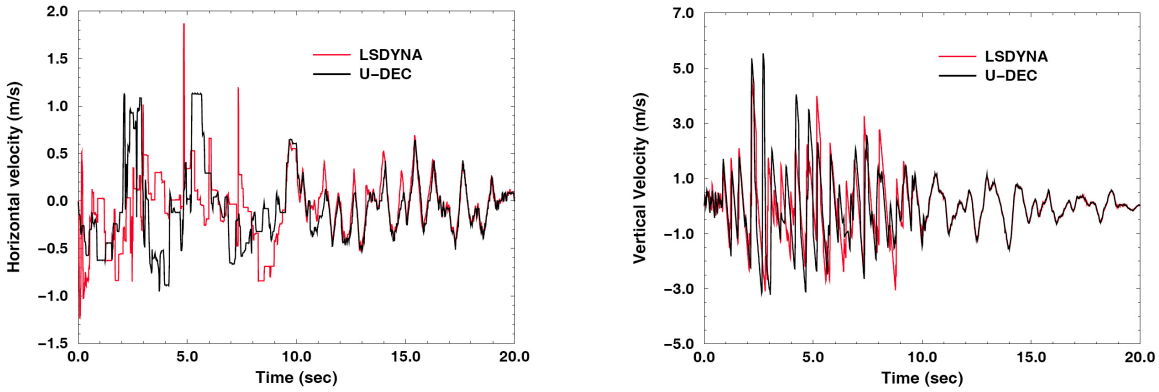

Output DTN: LL0704PA051SPC.026, file *Figures_Mech_Assessment_AMR.tar.gz.*

Figure 7-3. Horizontal (Along the Axis of the Drift) and Vertical Velocity Time Histories for the Center Waste Package Computed from the LS-DYNA and UDEC Models

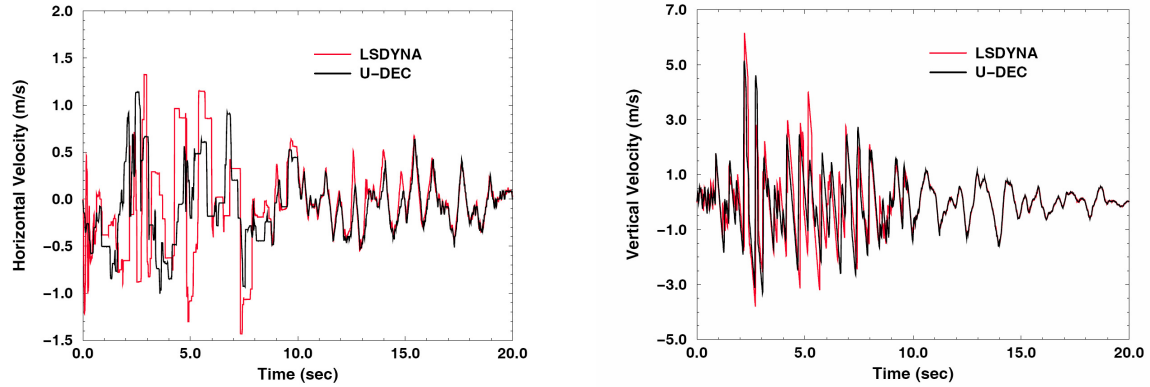

Output DTN: LL0704PA051SPC.026, file *Figures_Mech_Assessment_AMR.tar.gz.*

Figure 7-4. Horizontal (Along the Axis of the Drift) and Vertical Velocity Time Histories for the Left-of-Center Waste Package Computed from the LS-DYNA and UDEC Models

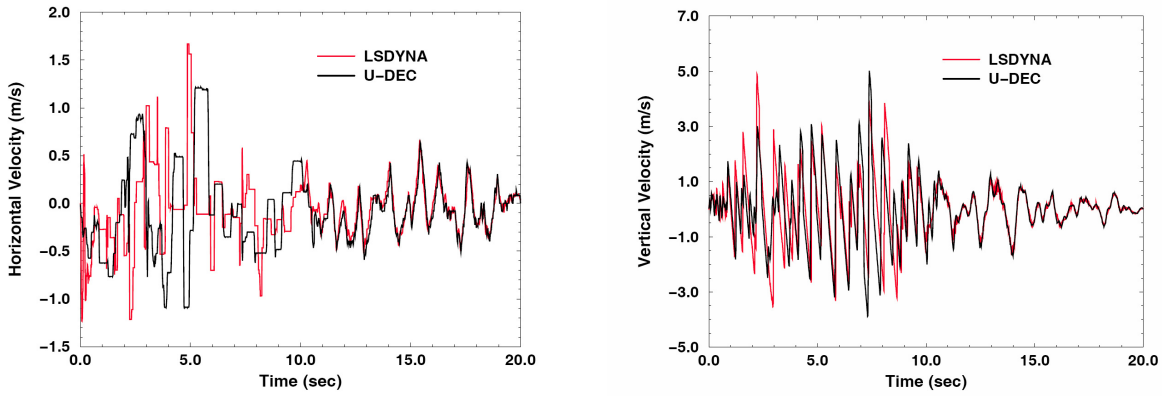

Output DTN: LL0704PA051SPC.026, file *Figures_Mech_Assessment_AMR.tar.gz.*

Figure 7-5. Horizontal (Along the Axis of the Drift) and Vertical Velocity Time Histories for the Right-of-Center Waste Package Computed from the LS-DYNA and UDEC Models

7.3.1.1.2 Comparison to Detailed LS-DYNA Analyses of Single Waste Packages

For TSPA, damage to the waste package has been estimated using a three-step process, as explained in Section 6.3. First, rigid-body kinematic simulations were performed to calculate and aggregate the number, magnitude, location, and relative angle for waste package-to-waste package and waste package-to-pallet impacts. Next, a series of representative impacts was simulated using detailed calculations to estimate damage to the waste packages due to individual impacts. Results from these detailed simulations were used to form a damage catalog. Finally, the damage catalog was used in conjunction with results from the rigid-body simulations to estimate damage to the waste packages due to the many impacts associated with the seismic time histories. In this manner, thousands of impacts and associated damage are used to develop a representative abstraction for TSPA (SNL 2007 [DIRS 176828]). Confidence in this method is obtained by comparing the results from Section 6.3 to high-resolution simulations of waste package and pallet response to seismic ground motion.

The detailed computational LS-DYNA models used for waste package-to-waste package and waste package-to-pallet damage lookup table analyses were subjected to selected seismic ground motion time histories. Analyses for both the TAD-bearing and codisposal waste packages were performed. Results of these simulations were then compared to damage estimates for the same time histories and PGV levels presented in Section 6.3. All analyses were performed for the model of the waste package with degraded internals and 17-mm-thick outer corrosion barrier (OCB). The waste package is situated on the pallet cradles, which are resting on the invert. Figures 7-6 and 7-7 show the initial configurations for the TAD-bearing and codisposal waste packages for the detailed analyses, respectively.

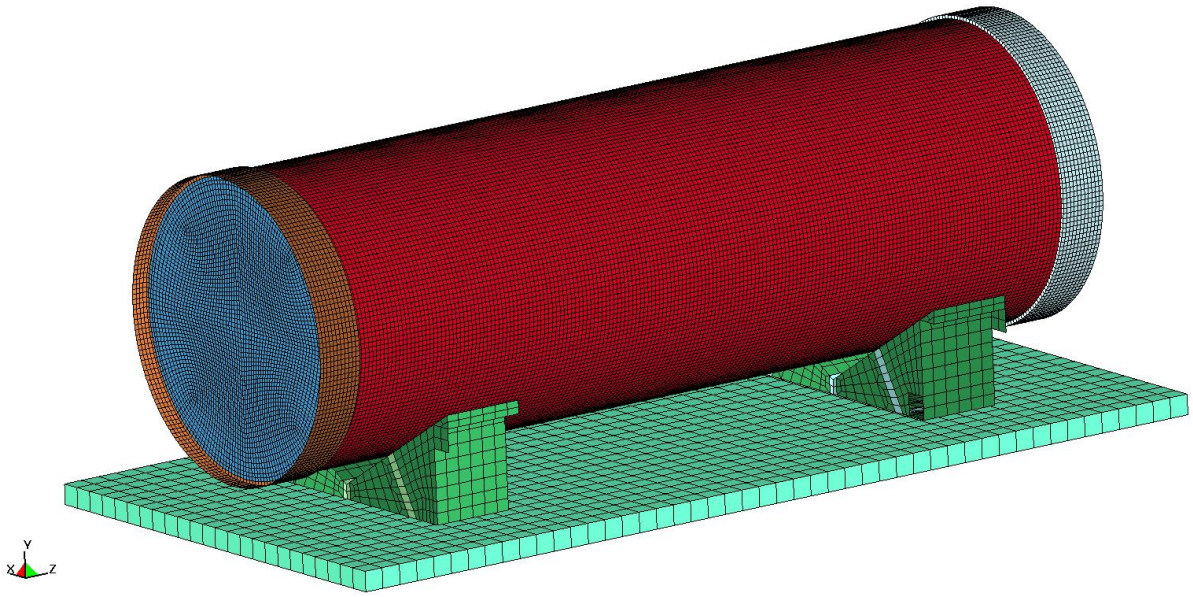

Output DTN: LL0704PA051SPC.026, file *Figures_Mech_Assessment_AMR.tar.gz*.

Figure 7-6. Single Detailed TAD-Bearing Waste Package Representation Subjected to Seismic Ground Motion

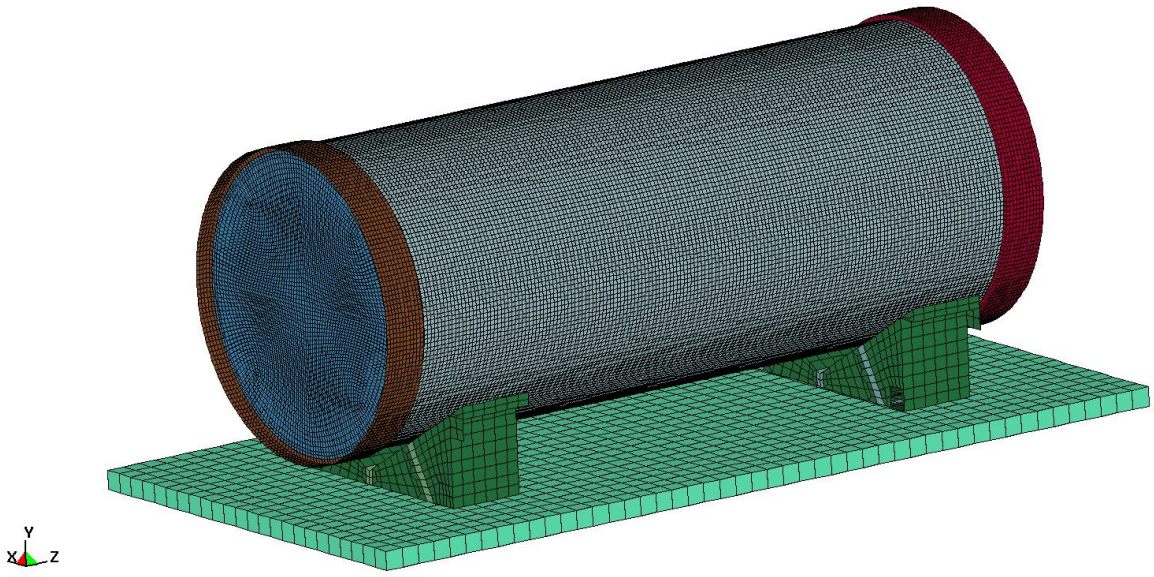

Output DTN: LL0704PA051SPC.026, file *Figures_Mech_Assessment_AMR.tar.gz*.

Figure 7-7. Single Detailed Codisposal Waste Package Representation Subjected to Seismic Ground Motion

One ground motion time history was used for detailed analysis of the TAD-bearing waste package, and three time histories were used for detailed analysis of the codisposal waste package. These time histories are listed in Tables 7-1 and 7-2 respectively. The realizations were chosen by observing which kinematic analyses included the maximum damaged areas but did not involve interaction with the drip shield or neighboring waste packages. Multiple waste packages in a single realization were modeled by modifying the friction parameters as in the kinematic analyses. For the TAD-bearing waste package, analyses were performed for the three central waste packages (I, J, K, see Figure 6-10) for realization 4 at 0.40 m/s PGV. For the codisposal waste package, analyses were performed for the two central codisposal packages (H and L) for realizations 3 and 4 at 0.40 m/s PGV, and for waste package H for realization 6 at 1.05 m/s PGV.

For these analyses, the simulation interval was chosen to include only the interval in which damaging impacts for the corresponding waste package had occurred in the kinematic analyses. At the end of this time, the ground motion was stopped, and the waste package stresses were allowed to relax for 0.5 second. The ground motion simulation times (not including the 0.5 second allotted for stress relaxation) for each analysis are given in Table 7-1 (for the TAD-bearing waste package) and Table 7-2 (for the codisposal waste package). Note that the simulation times do include 0.5 second at the beginning for gravity initialization. Input and output files for the TAD-bearing waste package can be found in validation DTN: LL0702PA055SPC.002, file *NavalLong_TAD_1WP_analyses.tar.gz*. Input and output files for the codisposal waste package can be found in validation DTN: LL0703PA007SPC.005, file *CDSP_1WP_analyses.tar.gz*.

Table 7-1. Ground Motion Simulation Times for the Detailed Single TAD-Bearing Waste Package Analyses

Ground Motion Level	Realization	Waste Package	Simulation Time (seconds)
0.40 m/s PGV	4	WP I	7.0
		WP J	9.5
		WP K	5.5

Validation DTN: LL0702PA055SPC.002, file *NavalLong_TAD_1WP_analyses.tar.gz.*

Table 7-2. Ground Motion Simulation Times for the Detailed Codisposal Waste Package Analyses

Ground Motion Level	Realization	Waste Package	Simulation Time (seconds)
0.40 m/s PGV	3	WP H	6.0
		WP L	6.0
	4	WP H	8.0
		WP L	8.0
1.05 m/s PGV	6	WP H	7.0

Validation DTN: LL0703PA007SPC.005, file *CDSP_1WP_analyses.tar.gz.*

The damaged areas (above 90%, 100%, and 105% of the yield strength) were computed from the detailed analyses and are given in Table 7-3 (for the TAD-bearing waste package) and Table 7-4 (for the codisposal waste package), with the damaged areas computed from the kinematic analyses for these same time histories and PGV levels included in parentheses for comparison.

A residual stress plot for a detailed analysis of a TAD-bearing waste package (for waste package K, 0.40 m/s PGV, realization 4) is shown in Figure 7-8, and Figure 7-9 shows damage levels for the same simulation. Similarly, a residual stress plot for a detailed analysis of a codisposal waste package (waste package H, 1.05 m/s PGV, realization 6) is shown in Figure 7-10, and Figure 7-11 presents damage levels for the same simulation.

Tables 7-3 and 7-4 show that, for both the TAD-bearing and codisposal waste packages, the detailed analyses show that the kinematic analyses presented in Section 6.3 overpredict the damaged area for these low PGV ground motions. For the TAD-bearing waste package, the detailed analyses predict essentially negligible damaged areas. For the codisposal waste package, the detailed analyses predicted damaged areas smaller than the corresponding kinematic analyses, with several of the detailed analyses predicting essentially negligible damaged areas.

This analysis shows that, while the kinematic approach to modeling waste packages subjected to seismic excitation does not yield damaged area estimates that match more detailed simulations; the kinematic approach does overestimate the potential for damage. Thus, the relatively efficient kinematic approach is a reasonable alternative to performing numerous detailed analyses that are extremely computation-intensive with multiple waste packages for multiple realizations and ground motion levels. Moreover, the kinematic approach meets the validation review criteria presented in the TWP (SNL 2007 [DIRS 179869], Table 2-1).

Table 7-3. Damaged Areas Computed for the Detailed Single TAD-Bearing Waste Package Analyses, Compared to Damaged Areas Computed from the Kinematic Analyses

Ground Motion Level	Realization	Waste Package	Damaged Area at 90% Yield Strength (m^2)	Damaged Area at 100% Yield Strength (m^2)	Damaged Area at 105% Yield Strength (m^2)
0.40 m/s PGV	4	I	0.0009 (0.3873)	0.0000 (0.1829)	0.0000 (0.0483)
		J	0.0000 (0.5083)	0.0000 (0.2358)	0.0000 (0.0619)
		K	0.0034 (0.4791)	0.0000 (0.2246)	0.0000 (0.0600)

Validation DTN: LL0702PA055SPC.002, file *NavalLong_TAD_1WP_analyses_DA_summary.xls*.

NOTE: Damaged areas computed from the kinematic analyses (Section 6.3) are shown in parentheses.

Table 7-4. Damaged Areas Computed for the Detailed Single Codisposal Waste Package Analyses, Compared to Damaged Areas Computed from the Kinematic Analyses

Ground Motion Level	Realization	Waste Package	Damaged Area at 90% Yield Strength (m^2)	Damaged Area at 100% Yield Strength (m^2)	Damaged Area at 105% Yield Strength (m^2)
0.40 m/s PGV	3	H	0.0222 (0.0588)	0.0000 (0.0299)	0.0000 (0.0000)
		L	0.0154 (0.0612)	0.0000 (0.0178)	0.0000 (0.0000)
	4	H	0.0000 (0.1923)	0.0000 (0.0569)	0.0000 (0.0025)
		L	0.0026 (0.0986)	0.0000 (0.0379)	0.0000 (0.0000)
1.05 m/s PGV	6	H	0.0342 (0.0958)	0.0043 (0.0458)	0.0000 (0.0000)

Validation DTN: LL0703PA007SPC.005, file *CDSP_1WP_analyses_DA_summary.xls.*

NOTE: Damaged areas computed from the kinematic analyses (Section 6.3) are shown in parentheses.

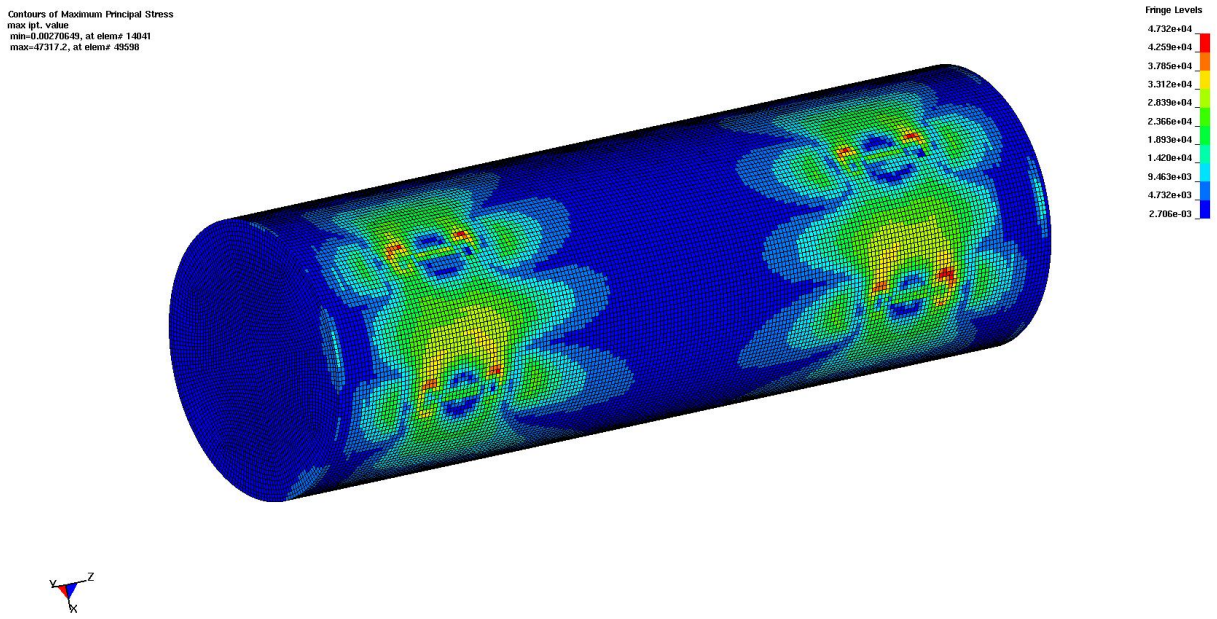

Output DTN: LL0704PA051SPC.026, file *Figures_Mech_Assessment_AMR.tar.gz.*

Figure 7-8. Residual Stress Contour Plot (psi) for Detailed LS-DYNA Simulation of TAD-Bearing Waste Package K Subjected to Seismic Ground Motion, Realization 4 at 0.40 m/s PGV

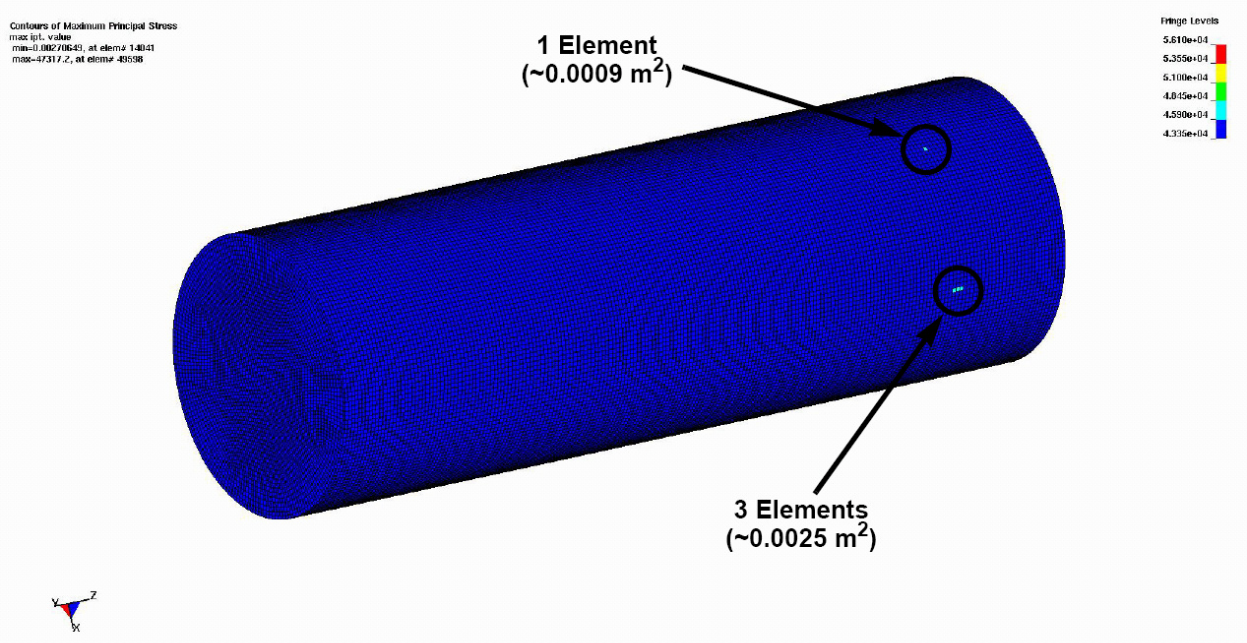

Output DTN: LL0704PA051SPC.026, file *Figures_Mech_Assessment_AMR.tar.gz.*

NOTE: This plot shows that only four elements have a residual stress level above 90% of yield strength.

Figure 7-9. Residual Stress Plot Showing Damage Levels (psi) for Detailed LS-DYNA Simulation for TAD-Bearing Waste Package K, Realization 4 at 0.40 m/s PGV

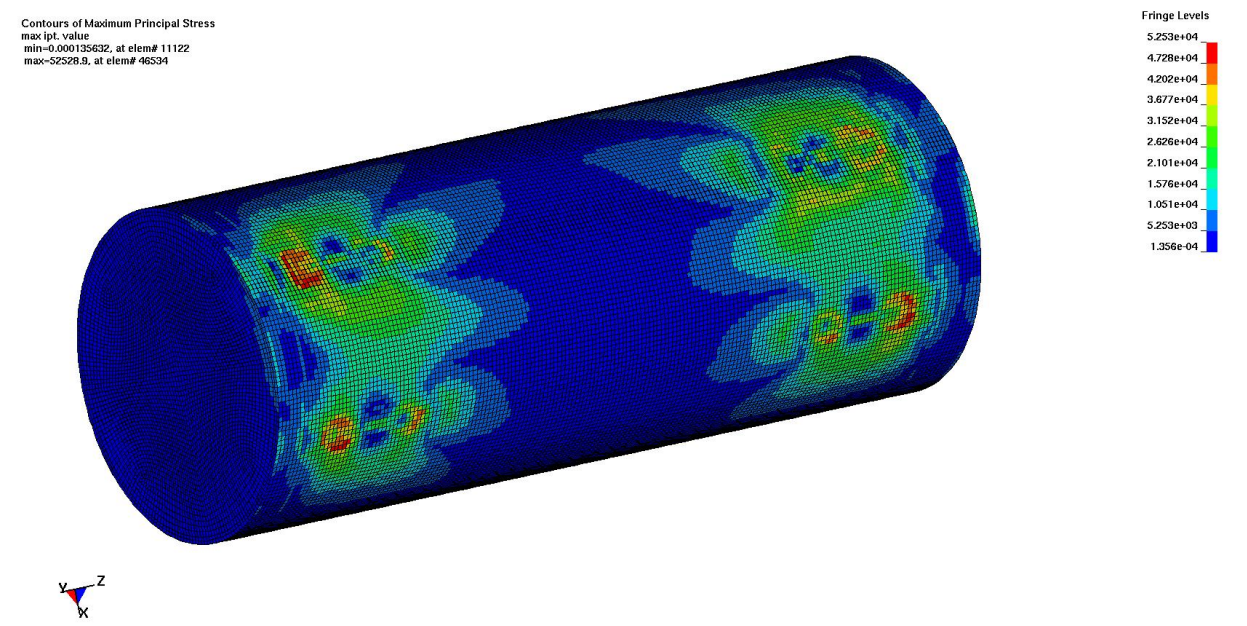

Output DTN: LL0704PA051SPC.026, file *Figures_Mech_Assessment_AMR.tar.gz.*

Figure 7-10. Residual Stress Contour Plot (psi) for Detailed LS-DYNA Simulation of Codisposal Waste Package H Subjected to Seismic Ground Motion, Realization 6 at 1.05 m/s PGV

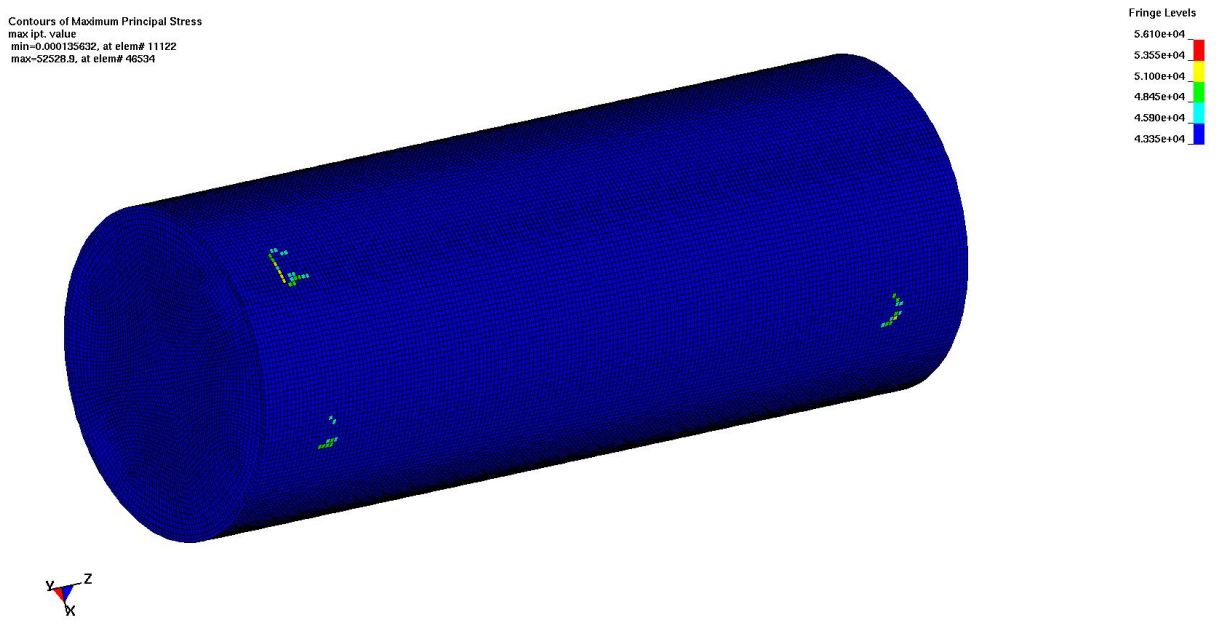

Output DTN: LL0704PA051SPC.026, file *Figures_Mech_Assessment_AMR.tar.gz*.

NOTE: Graphic uses the three-step damage abstraction process for TSPA feeds.

Figure 7-11. Residual Stress Plot Showing Damage Levels (psi) for Detailed LS-DYNA Simulations of Codisposal Waste Package H Subjected to Seismic Ground Motion, Realization 6 at 1.05 m/s PGV

While the kinematic results are expected to be conservative at higher PGV levels, the damaged area from the detailed model with multiple waste packages subjected to ground motion at high PGV would not be expected to yield the same very small damaged areas presented here for the lower PGV levels.

7.3.2 Validation of Model for Waste Package Surrounded by Rubble and Subjected to Vibratory Ground Motion

The model for damage to a waste package surrounded by rubble and subjected to vibratory ground motion is implemented using the UDEC numerical code. Validation activities for this model are indicated in Table 2-1 of the TWP (SNL 2007 [DIRS 179869]) and include: (1) corroboration of model results with results of other models developed for similar uses, (2) corroboration of model results with data acquired from a 2-m scale experiment conducted on a rock block containing artificial fractures, and (3) independent critical review by a technical specialist. This review is presented in Section 7.3.4 and Appendix E.

The following validation activities do not use the model for damage to a waste package surrounded by rubble and subjected to vibratory ground motion directly, but rather use models of dynamic deformation also formulated using the UDEC code. These models use many aspects of the UDEC code that are used in the waste package damage analysis and thus demonstrate that the UDEC code can be applied to evaluate such relevant rock mechanics problems successfully.

7.3.2.1 Comparison of UDEC Results to Other Numerical Approaches in Solving Dynamic Tunnel-Stability Problems in a Fractured Rock Mass

The Defense Nuclear Agency (DNA) conducted a comparison of a number of numerical modeling approaches to examine their utility in simulating the effects of dynamic stress-wave loading on tunnel stability in a fractured rock mass (Senseny 1993 [DIRS 162017], pp. 311 to 324). A series of five problems of increasing complexity were posed to five organizations, each of which used a different computer code (including UDEC) to conduct the simulations. The codes utilized different assumptions and solution procedures. All input parameters were given, along with boundary and initial conditions. The organizations were asked to provide results to an independent reviewer for analysis and comparison. This test, termed a "benchmark calculation exercise," provided a blind comparison of various methods for modeling a complex dynamic problem involving the highly non-linear response of a fractured material.

7.3.2.1.1 Description of the Benchmark Calculation Exercise

The ultimate problem to be solved was to predict the liner deformation in a lined tunnel in a jointed rock mass subjected to a spherically diverging wave initiated by a blast source (Figure 7-12). The intact rock was treated as a linearly elastic/perfectly plastic material, and the slip on joints was treated as a Coulomb frictional response. A 50-mm-thick tunnel liner was represented as an elastic-perfectly plastic von Mises material.

This problem has many aspects in common with the dynamic response of the waste package surrounded by rock rubble. In particular, the rock mass to be simulated was jointed, and a dynamic ground motion was applied to the system. The principal difference is that the dynamic source used in the benchmark exercise is a spherically diverging wave from a point source rather than shear- and compression-wave loading. However, both loading conditions give rise to many of the same mechanical effects.

The series of five problems of increasing complexity are listed in Table 7-5. Problems 1 to 3 have analytical solutions that can be used for comparison with the numerical output. The final two problems, which involve determination of dynamic wave propagation in a fractured rock mass and the dynamic stressing and yielding of a circular, steel-lined tunnel in a jointed rock mass, are complex and have no analytical solution.

These problems tested a number of aspects of the model for damage to a waste package surrounded by rubble and subjected to vibratory ground motion, including the following:

- Ability to represent wave transmission through intact and jointed rock
- Ability to represent the mechanical response of joints to normal and shear loading
- Ability to represent nonreflecting boundaries

- Ability to represent non-linear, joint-controlled rock mass deformation under dynamic loading
- Ability to represent the deformation and mechanical interaction of a relatively thin liner with a surrounding, discontinuous rock mass.

The five different numerical codes used to simulate the test problems are listed in Table 7-6. With the exception of the PRONTO code, the simulations were conducted by the organization that developed the codes; thus, the issue of having ill-informed users was removed from the benchmark study. The calculators used their own codes to solve the problems and submitted their solutions in a "blind" fashion.

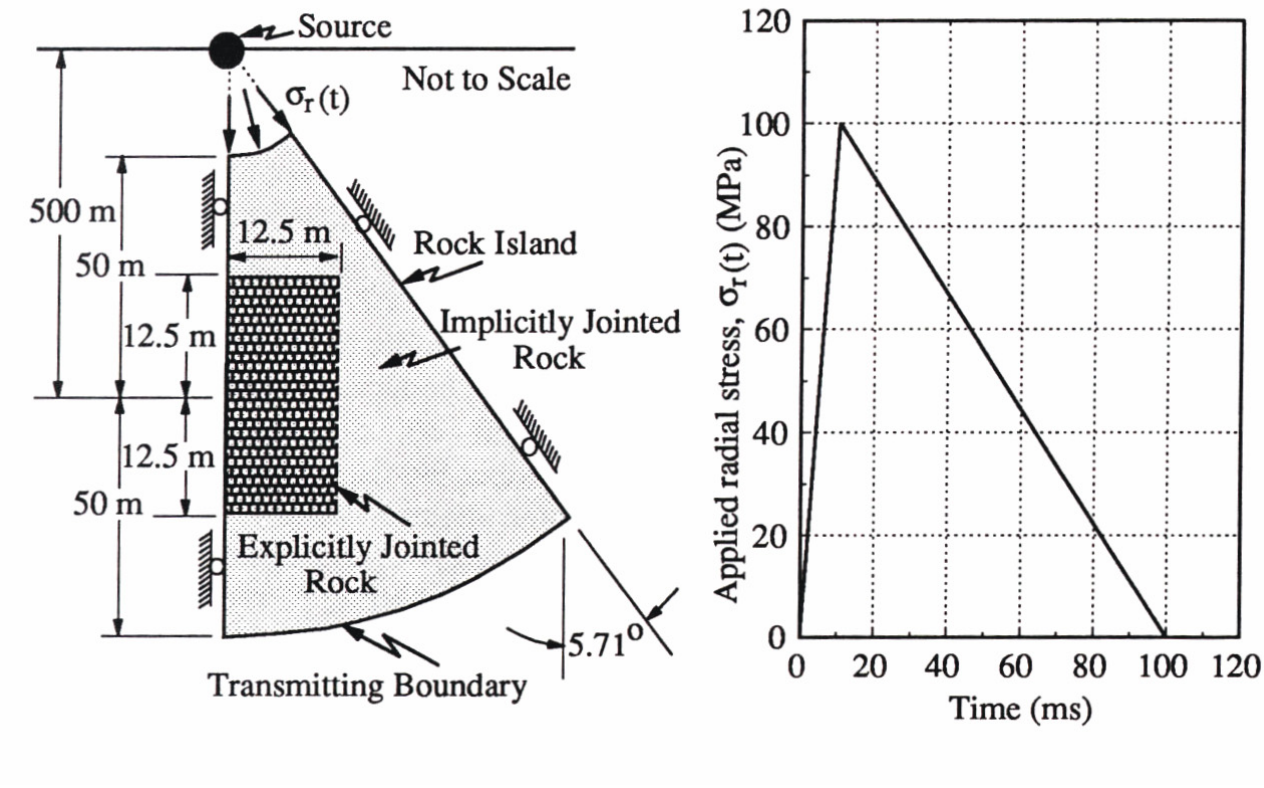

Source: Senseny 1993 [DIRS 162017], Figure 1.

NOTE: The stress characteristics of the source are shown at right.

Figure 7-12. Problem Geometry of the Mechanical Response of a 5-m-Diameter Tunnel in Jointed Rock Subjected to a Spherically Expanding Blast Source

Table 7-5. Benchmark Calculation Exercise Problems

Problem Number	Description	Comments
1	Testing of a spherically divergent strain path in intact rock.	Quasi-static strain path that simulates passage of a shock front in intact rock. Demonstrates that the model accounts properly for shock propagation in intact media.
2	One-dimensional compression of a 5-m by 4-m sample of jointed rock, exercising the joints in normal deformation.	Tests that the model is able to produce proper pressure versus volumetric strain response for jointed rock and intact rock components.
3	Compression of a jointed block, with joints in shear, while maintaining a homogenous strain rate in the intact rock.	Tests the ability of the model to produce proper deformations on a slipping joint in shear when subjected to a complex deformation path.
4	Deformation and stress changes in a wedge-shaped jointed rock mass subjected to a spherically divergent wave (same as Problem 5, but without tunnel present).	Ability to reproduce rock mass strains in the free field properly. No analytical solution—code-to-code comparison.
5	Deformation and yield of a tunnel liner in a jointed rock mass subjected to a spherically divergent blast wave. Prediction of stress in the rock mass around a tunnel.	Complex problem of a jointed rock mass subjected to a triangular blast wave. Highly non-linear response of tunnel as joints shear and large deformations of the tunnel liner occur. No analytical solution—code-to-code comparison.

Source: Senseny 1993 [DIRS 162017], pp. 311 to 324.

Table 7-6. Programs and Modeling Participants in the Benchmark Study

Organization	Abbreviation	Code
California Research and Technology Division, the Titan Corporation	CRT	EXCALIBUR (Finite element, joints modeled explicitly or via constitutive model)
Itasca Consulting Group	Itasca	UDEC (Distinct element/finite difference, joints modeled explicitly)
Lawrence Livermore National Laboratory	LLNL	DIBS (Distinct element, rigid block formulation)
RE/SPEC, Inc.	RE/SPEC	PRONTO (From Sandia National Laboratory, finite difference)
Weidlinger Associates	WA	FLEX (Finite element, joints modeled explicitly or via constitutive model)

Source: Senseny 1993 [DIRS 162017], Table 1.

7.3.2.1.2 Comparison of the Benchmark Calculation Exercise Results

The model formulated by Itasca using the UDEC code provided good agreement to analytical solutions for Problems 1 to 3. This result is described in detail in the study by Senseny (1993 [DIRS 162017], pp. 315 to 323), and further discussion of these problems can be found in that study.

Figure 7-13 presents radial stress and radial velocity results at the center of the tunnel (not yet excavated) for Problem 4, as simulated by all five models. Overall, the stress and velocity predictions are quite similar for the various models, primarily because there is little variation in the stresses or velocities over the computational grid—with the exception of temporal offsets in the input function, which is consistent with the wave speed. The UDEC model was found to compare favorably with the finite element approaches, which appear to account properly both for nonreflecting boundaries and for free-field deformation and energy dissipation due to plastic yield.

Problem 5, which involves tunnel deformation and stability under divergent wave loading, provides a significant numerical test for UDEC and the other codes. As stated in "Stress Wave Loading of a Tunnel: A Benchmark Study" (Senseny 1993 [DIRS 162017], p. 330), conventional wisdom assumes that, after peak stressing, the radial outward motion causes a rapid tangential unloading, resulting in greater loss of radial confinement and a reduced failure strength than would be assumed for uniaxial loading of the tunnel. The model formulated using the UDEC program was found to provide a reasonable match to crown-and-invert tunnel closures with other numerical approaches (Figure 7-14), with the exception of the RE/SPEC and LLNL models, which provided contrary results. The radial stresses for various radial lines around the tunnel at peak free-field stress arrival times are given in Figure 7-15.

All of the calculations are compared to the static analytical solution for an orthotropic elastic material. All of the models show that the effect of the tunnel is to relieve the radial stress component and greatly increase the tangential stresses in comparison to the equivalent free-field values. Radial stresses approaching about 8 MPa at the tunnel wall are the result of confinement provided by the steel tunnel liner. Comparison of tunnel deformation modes, shown in Figure 7-16, indicate that significant springline yield and closure (displacements exaggerated by a factor of 10), resulting from slip-on joints and intact rock plastic failure, occur in all models with the exception of the LLNL rigid-block model. This illustrates the importance of internal block deformability and yield for problems of this nature.

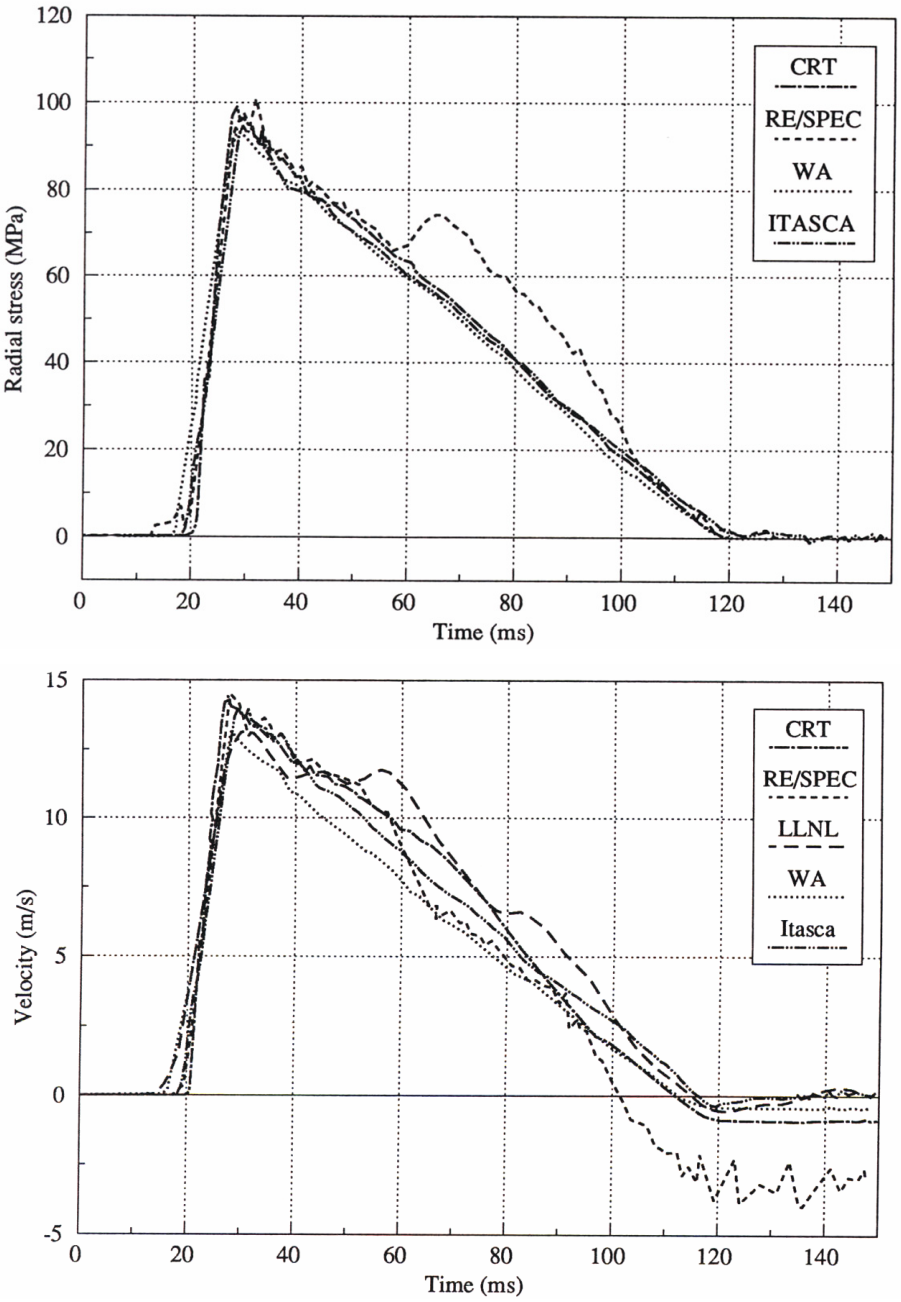

Source: Senseny 1993 [DIRS 162017], Figure 14.

NOTE: Radial stress is shown in the top figure; radial velocity is shown in the bottom figure.

Figure 7-13. Radial Stress and Radial Velocity at the Center of the Future Tunnel Location in Problem 4

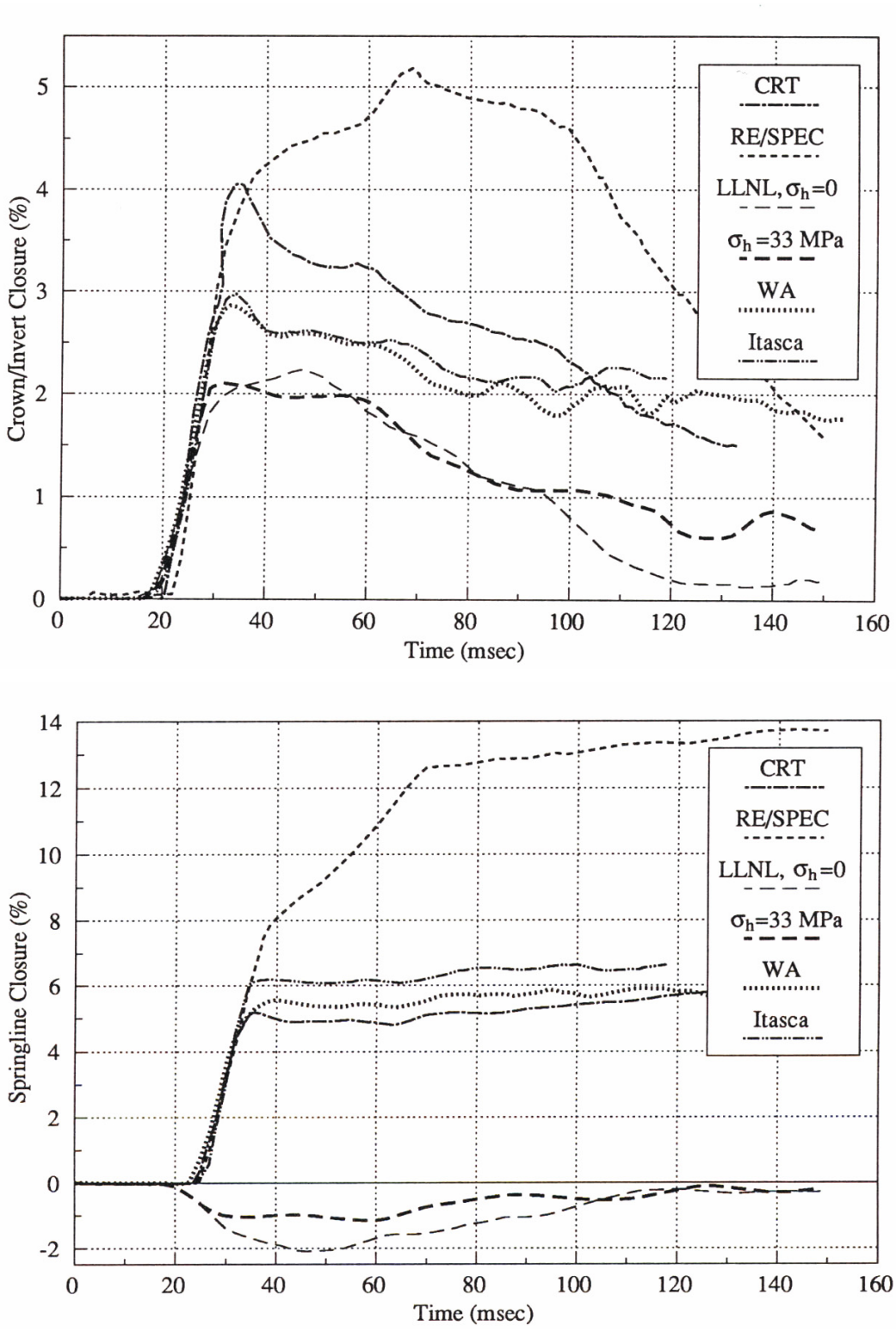

Source: Senseny 1993 [DIRS 162017], Figure 19.

NOTE: Closure for the tunnel invert/crown is shown in the top figure; closure for the springline is at the bottom.

Figure 7-14. Comparison of Predicted Tunnel Invert-Crown and Springline Closure for Problem 5

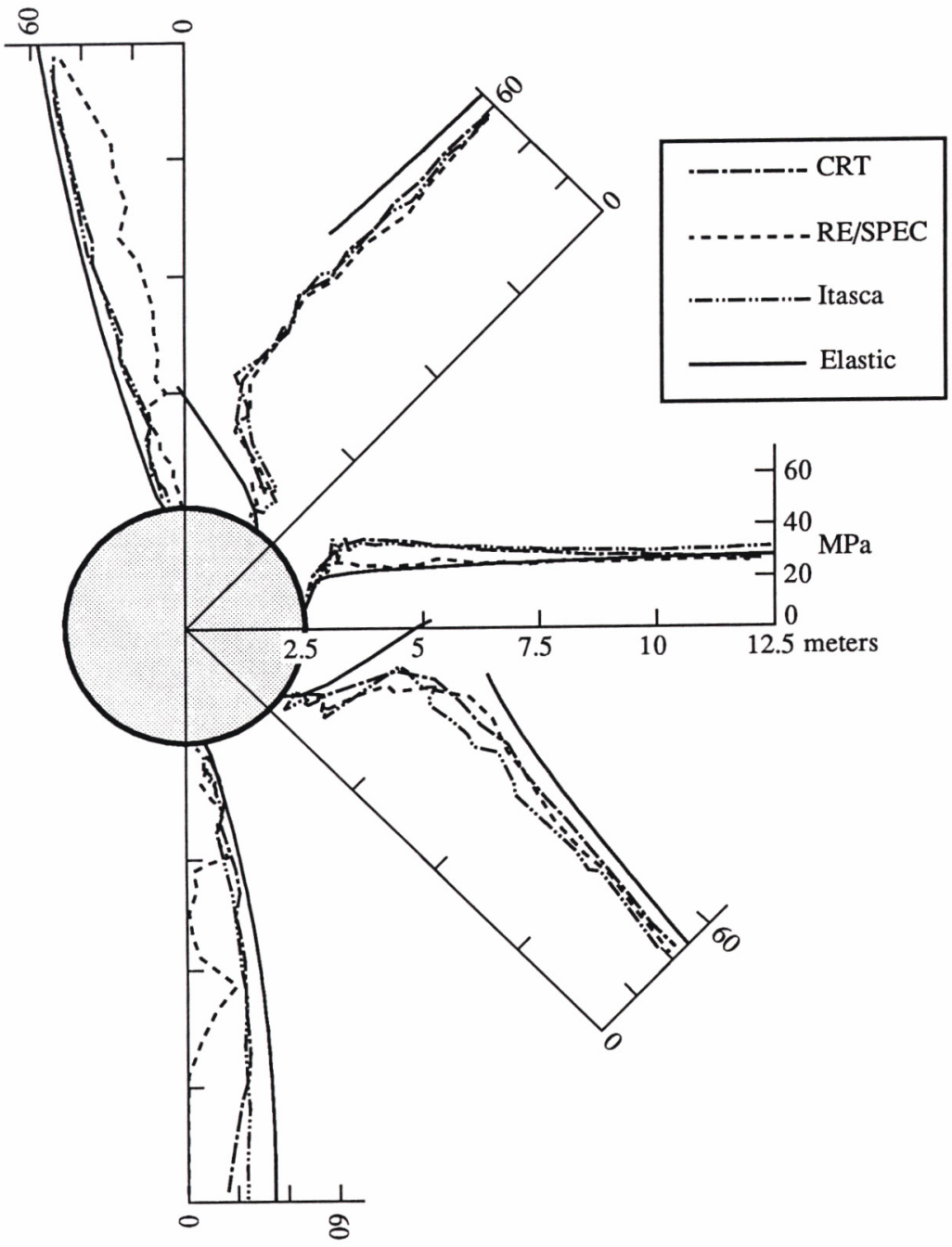

Source: Senseny 1993 [DIRS 162017], Figure 20.

Figure 7-15. Comparison of Radial Stress along Radial Lines at Peak Free-Field Stress Arrival Times, Problem 5

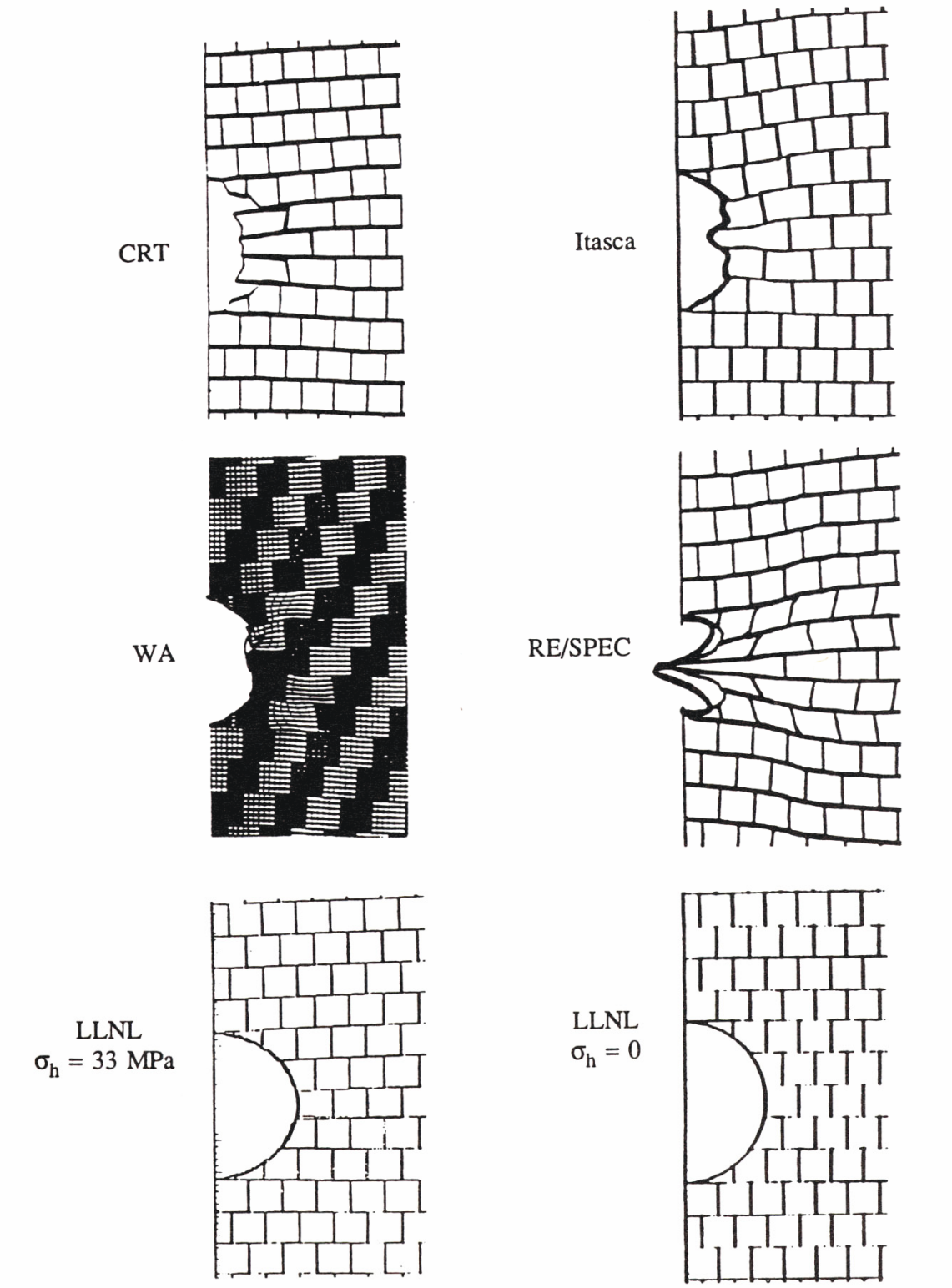

Source: Senseny 1993 [DIRS 162017], Figure 22.

Figure 7-16. Comparisons of Exaggerated Tunnel Shapes (× 10) at Equilibrium, Problem 5

As Senseny concludes (1993 [DIRS 162017], pp. 337 to 338), three of the five participants (CRT, WA, Itasca) obtained numerical solutions that—where comparisons were possible—agree with each other in most practical respects. All of these solutions appear credible, based on the significant body of evidence available:

1. Use of rational continuum models to represent the rock
2. Use of physically based models for the joints
3. Compatibility of results with basic understanding of wave propagation processes
4. Absence of obvious numerical artifacts such as spurious reflections
5. Comparison of stresses and strains with complete and partial analytic solutions in all the benchmark problems.

In summary, Section 7.3.2.1 presents the corroboration of the results from a UDEC-based model similar to the model for damage to a waste package surrounded by rubble and subject to vibratory ground motion, with other model results obtained from the implementation of other independent mathematical models developed for similar purposes. Results demonstrate the ability of the model to represent complex dynamic boundary conditions. In the validation exercise, comparisons were made between a model formulated using UDEC and models based on other numerical methods (Senseny 1993 [DIRS 162017], pp. 337 to 338). In this work, conducted for the DNA, a rigorous code-to-code comparison was conducted in which test problems of increasing complexity were analyzed in a "blind" calculation and comparison exercise. The UDEC-based model, as shown, compared very favorably with other numerical methods for all problems and demonstrated the ability of the code to reasonably represent the dynamic response of fractured media consistent with other models.

This result: (1) demonstrates that the output of the UDEC model is reasonable, and (2) is a corroboration of the results from a UDEC-based model similar to that used in Section 6.5 to estimate damage to a waste package surrounded by rubble and subjected to vibratory ground motion, with results obtained from other independent models developed for similar purposes and meets the validation review criteria presented in the TWP (SNL 2007 [DIRS 179869], Table 2-1).

7.3.2.2 Comparison of UDEC Predictions with Experimental Results from an Explosively Loaded, Scaled Tunnel in Jointed Rock

The DNA conducted a precise, well-instrumented, scaled tunnel-stability field experiment in a jointed rock mass subjected to explosive loading. The main objective of the program was to test the ability of sophisticated numerical software to predict deformation of a jointed rock mass, the interaction between the jointed rock mass and a tunnel liner, and the damage and deformation of the tunnel liner. Models formulated using UDEC and two other codes (FLEX and EXCALIBUR, Table 7-6) were part of this validation exercise. Moreover, the UDEC model utilized many of the UDEC functionalities that are used in the model for waste package damage due to vibratory ground motion. The numerical analysts did not know the results of the field measurements before they completed and reported the results of the numerical simulations

(i.e., "blind prediction"). Senseny and Pucik (1999 [DIRS 168479]) published a comparison of the predictions obtained by the three codes with the measurements from the experiment.

7.3.2.2.1 Description of Test and Validation Program

The test involved blast-induced dynamic loading of a scaled, lined cylindrical tunnel in jointed rock. The purpose of the test was to provide a well-instrumented experiment at a 2-m scale for validation and comparison of a number of numerical modeling codes capable of representing failure of a tunnel in a discontinuous rock mass under dynamic loading. Details of the physical experiment are described by Senseny and Pucik (1999 [DIRS 168479]) and summarized below.

The experimental sample consisted of an artificial rock mass composed of over 4,000 limestone bricks, each 51 mm square by 0.6 m or 1.2 m in length (Figure 7-17). The bricks were stacked into a nearly cubical specimen measuring 2.1 m square and 2.4 m in length, with a central 0.4-m-diameter cylindrical hole (representing the tunnel) lined with a thin aluminum tube. Instrumentation included 46 gauges to monitor velocity, stress, joint slip, and tunnel closure.

The entire sample was placed in a pit and covered with concrete. The midline of the concrete surface was formed in a half-cylinder to allow application of a cylindrically diverging blast wave generated by explosives. The resulting stress wave had the following components (Senseny and Pucik 1999 [DIRS 168479], p. 766):

- radius = 4.4 m
- rise time $\cong$ 500 μs
- peak stress $\cong$ 100 MPa
- peak particle velocity $\cong$ 14 m/sec
- total radial displacement $\cong$ 25 mm
- peak circumferential strain $\cong$ 0.6%.

This divergent dynamic environment was sufficient to cause joint slip, intact rock fracture, and permanent deformation of the lined opening.

This problem tests a number of UDEC functionalities that are used in the current model, including the following:

- Ability to represent wave transmission through intact and jointed rock
- Ability to represent the mechanical response of joints to normal and shear loading
- Ability to represent non-linear, joint-controlled rock mass deformation under dynamic loading
- Ability to represent deformation and mechanical interaction of a relatively thin liner with a surrounding discontinuous rock mass.

The numerical analysts were presented with the model boundary and initial conditions, the block geometry, and laboratory-measured rock and joint properties. A "blind" validation of three two-dimensional numerical programs (including UDEC), which used different methods to simulate joint surfaces, was then conducted. Analysts formulated the analysis methodology, conducted the numerical analyses, and submitted the results to Senseny and Pucik (1999 [DIRS 168479]), who performed the code-to-experiment and code-to-code comparisons.

The measured particle-velocity time histories induced by the input blast at its application point were used as a time-dependent boundary condition at the top of the model above the tunnel. The stresses and deformations induced in the stack of blocks were monitored during the test at the gauge locations shown in Figure 7-17. This figure shows that stress history was measured at two locations above the crown and at three locations laterally on each side of the tunnel, along the springlines. Deformation of the tunnel crown-invert and springline diameters was also measured. The model outputs are compared to the time histories of these measurements and to the deformed shape of the aluminum tunnel liner, as determined by measurement after the test was completed. Joint slip was not modeled in the numerical simulations, because the slip motions in the actual test were outside the resolution of the installed instrumentation.

7.3.2.2.2 Rock Properties Data

The rock chosen for this test was a porous limestone from the Salem Formation. Intact specimens were tested in triaxial compression and triaxial extension at three different testing laboratories. The reported data, shown in Figure 7-18, indicate very little variation among tests, and the results were consistent among the three testing laboratories. Figure 7-19 shows failure envelopes developed from the triaxial compression and triaxial extension tests.

Tests also were conducted on joints to determine their shear strength and stiffness. Special specimen-preparation procedures were employed to ensure that the joint surfaces in the laboratory tests were similar to those in the jointed rock test. The normal compressibility of the joint surfaces was determined by unconfined compression tests on specimens with a single joint oriented at 90° to the load axis. Each specimen was loaded to approximately 75% of its unconfined strength and then unloaded. Figure 7-20(a) shows typical joint normal-direction compressibility data. Under normal loading, the joints are closed fully after displacement of approximately 0.05 mm.

The shear strength of the joints was determined by a series of triaxial compression tests on cylindrical specimens, each containing a single joint oriented at 30° to the specimen axis. The confining pressure in these tests ranged from 1 MPa to 35 MPa. At confining pressures up to 30 MPa, the specimens failed by sliding of the joints at approximately constant stress. When loaded at a confining pressure of 35 MPa, the intact portion of the test specimen failed without sliding along the joint. Figure 7-20(b) plots peak shear stress as a function of normal stress on the joint for tests performed at confining pressures up to 30 MPa. The joint strength data are represented well by a straight line passing through the origin with a 38.3° friction angle.

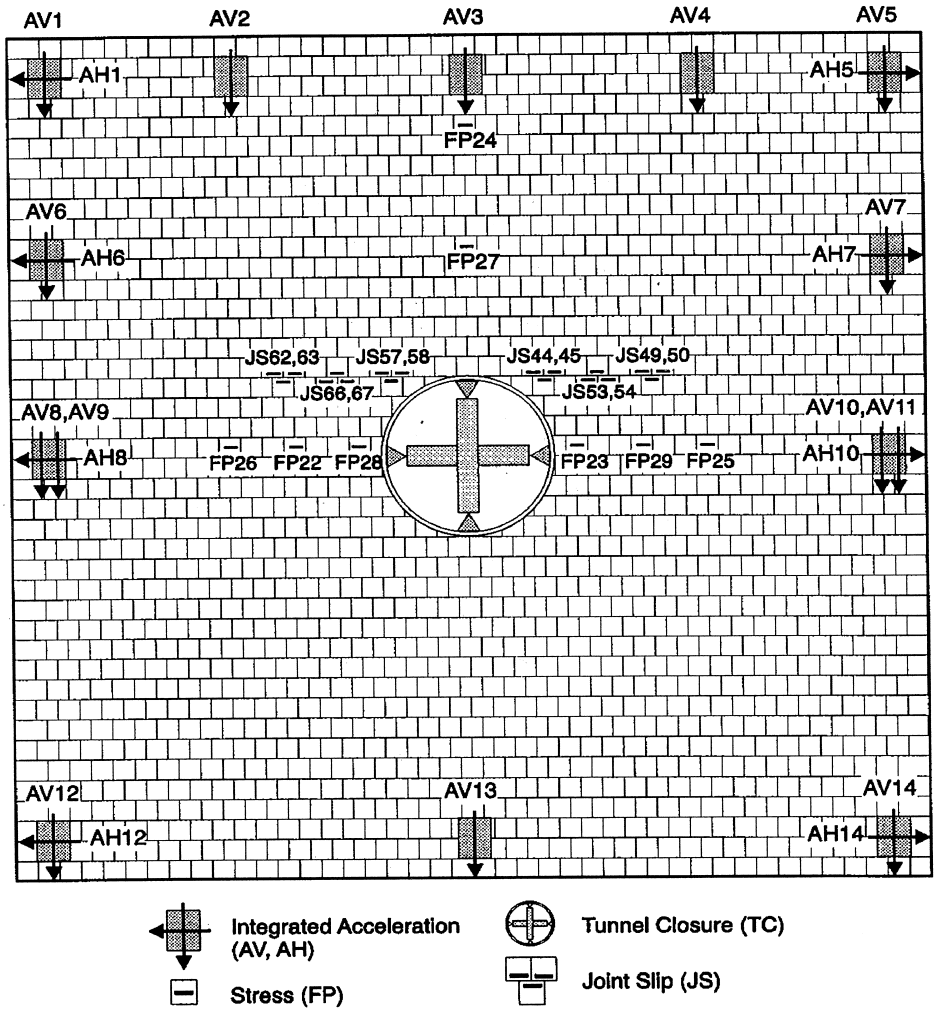

Source: Senseny and Pucik 1999 [DIRS 168479], Figure 14.

NOTE: The internal tunnel is 2.4 m long in the out-of-plane direction.

Figure 7-17. Geometry of the 2.1-m-Square Joint Rock Experiment Showing Internal Tunnel and Instrument Locations

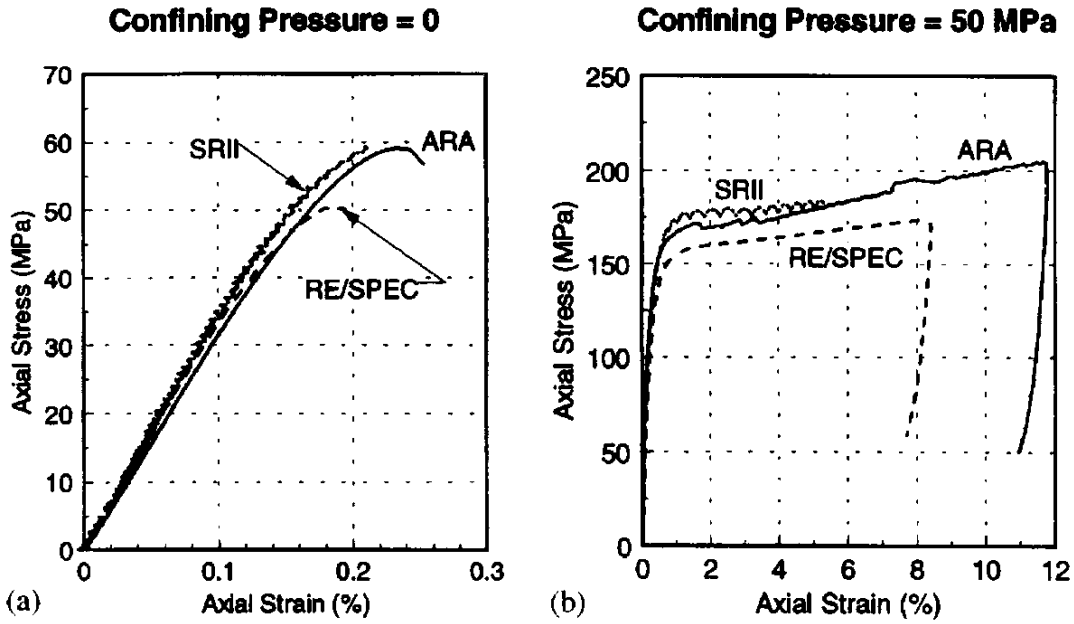

Source: Senseny and Pucik 1999 [DIRS 168479], Figure 3.

NOTE: Unconfined compression is shown in (a); triaxial compression is shown in (b).

Figure 7-18. Stress Strain Curves for Salem Limestone

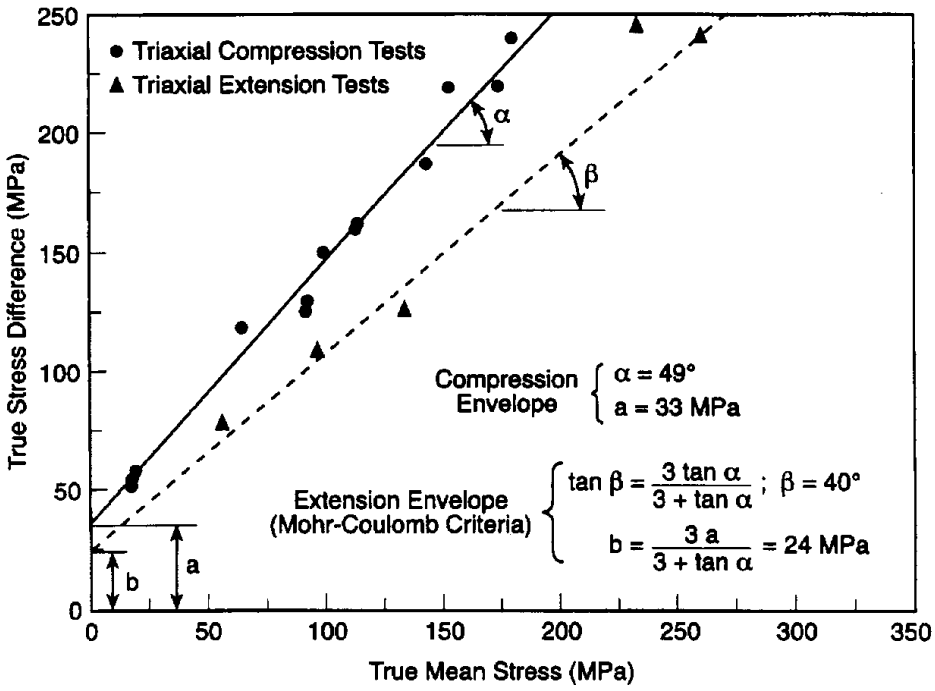

Source: Senseny and Pucik 1999 [DIRS 168479], Figure 4.

Figure 7-19. Comparison of Extension- and Compression-Strength Envelopes for Salem Limestone

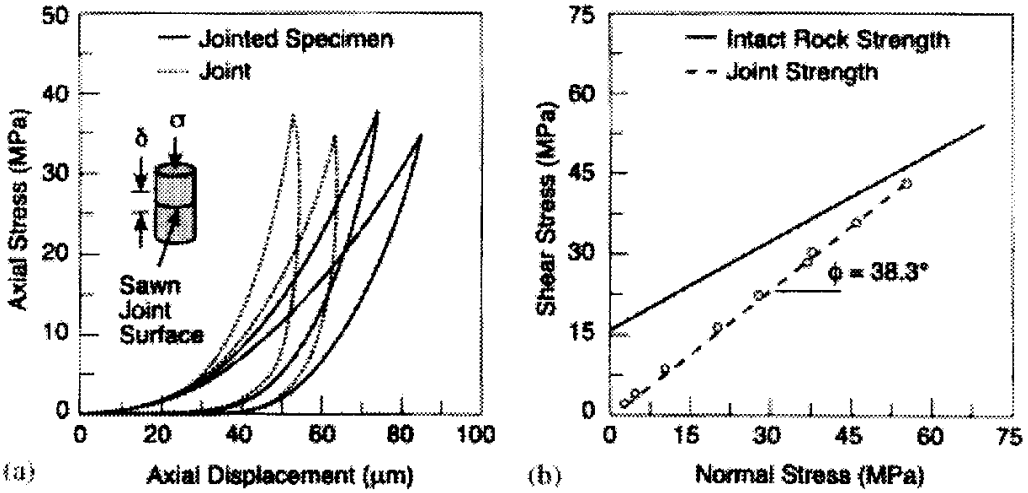

Source: Senseny and Pucik 1999 [DIRS 168479], Figure 5.

NOTE: Normal-load compressibility is shown in (a); the shear-strength envelope is shown in (b).

Figure 7-20. Compressibility and Strength in Salem Limestone

7.3.2.2.3 Numerical Approximation of Mechanical Behavior of Different Components of UDEC Representation

The constitutive relation used for intact limestone in the UDEC program is an elastic-plastic, strain-softening model (with no cap on the yield surface) using a Mohr-Coulomb shear failure surface with tension cutoff. The strains are subject to a nonassociated flow with zero dilatancy in shear and associated flow in tension. The strain softening is controlled via isotropic softening of the intact material cohesion and tensile strength. No rate dependence of material properties is assumed. The joint representation used a Coulomb-slip relation with constant shear stiffness and non-linear normal stiffness based on the data shown in Figure 7-20. The isotropic-hardening Tresca constitutive relation was used for the aluminum liner.

7.3.2.2.4 Gaps between Blocks

The UDEC model incorporated information about the effective vertical and horizontal gaps between the limestone bricks as measured in the actual experiment. The width of these gaps was determined using an indirect technique that relied on careful measurements of the overall dimensions of the stack of blocks in both directions. The contribution of the solid material to these measurements (i.e., the values that would be expected in the absence of gaps) was estimated by multiplying the number of bricks by the average brick thickness. The differences between these numbers and the actual measurements then provided an estimate of the total effective gap width. Dividing these differences by the number of joints provided an estimate of the average effective gap thickness in each direction.

7.3.2.2.5 Comparison of the Results

Figure 7-21 shows the predicted deformation of the thin tunnel liner. There is no time history of tunnel deformation available for model-test comparison, because the closure instrumentation used to measure the tunnel liner movements failed in the experiment. Therefore, Figure 7-21 shows only the final roof-to-floor and wall-to-wall closures of the liner (on the right edge of the figure) as measured after the test. Predictions from the model formulated using UDEC and actual final displacements of the crown and springline displacements show close agreement.

After the test, the tunnel liner was recovered and measured to determine more information than was obtained from the crown-invert and springline diameter changes alone. Figure 7-22 shows the magnified measured and predicted shape of the deformed aluminum liner. Over the entire perimeter, the liner displacements, as predicted by the UDEC model, lie within the variability of the actual measurements. The UDEC model accurately predicts the diametral closure along the centerline and the diametric expansion along the springline.

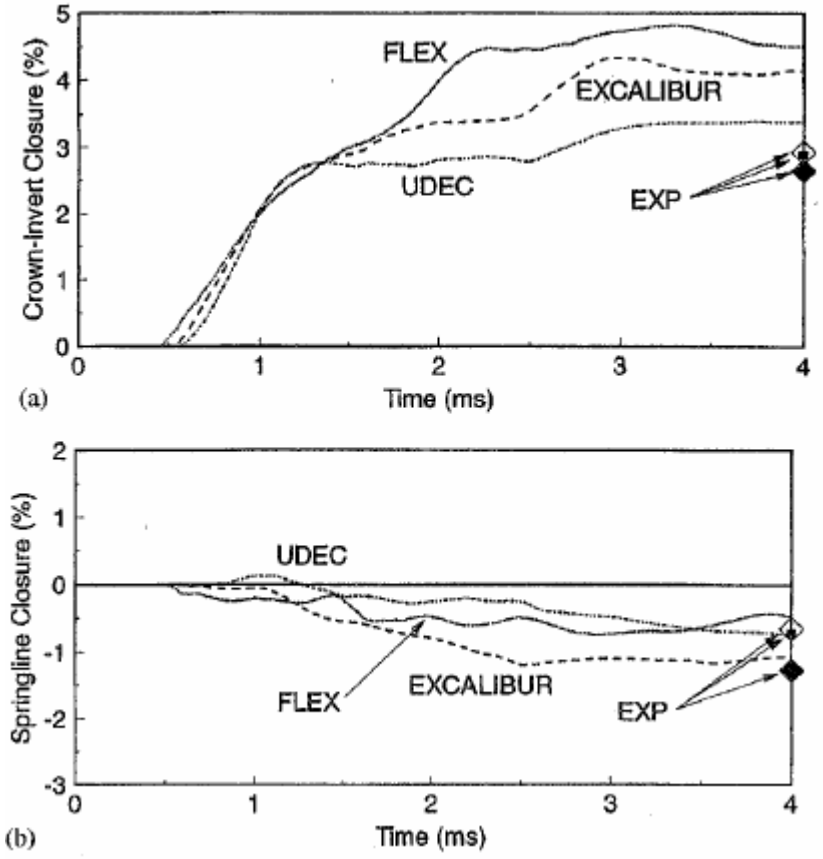

Source: Senseny and Pucik 1999 [DIRS 168479], Figure 17.

NOTE: Crown/invert closure is shown in (a); the springline closure in shown in (b).

Figure 7-21. Predicted Deformation of the Crown-Invert and Springline Tunnel Diameters

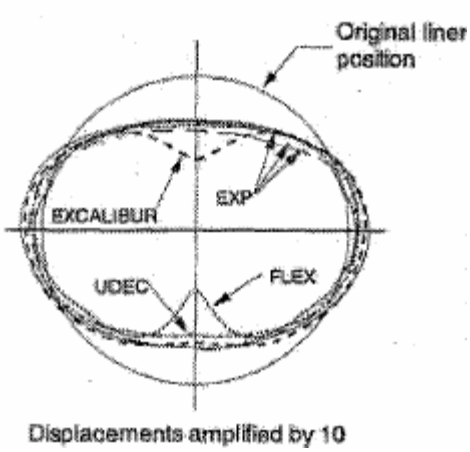

Source: Senseny and Pucik 1999 [DIRS 168479], Figure 18a.

Figure 7-22. Measured and Predicted Shape of the Deformed Aluminum Liner

Figure 7-23 shows the predicted and measured stresses at the two gauges (FPs 24 and 27) located on the specimen centerline above the tunnel crown. Because these gauges were located on the specimen centerline, it was not possible to make comparable measurements nor to ascertain the precision of the measurements. UDEC results are in very good agreement with test measurements. The only significant disagreement is in the magnitude of the peak stress at the lower gauge, FP 27: UDEC overpredicts the peak stress by approximately 50%.

This result represents corroboration of a UDEC-based model similar to the present with data acquired from field experiments not previously used to develop or calibrate the model.

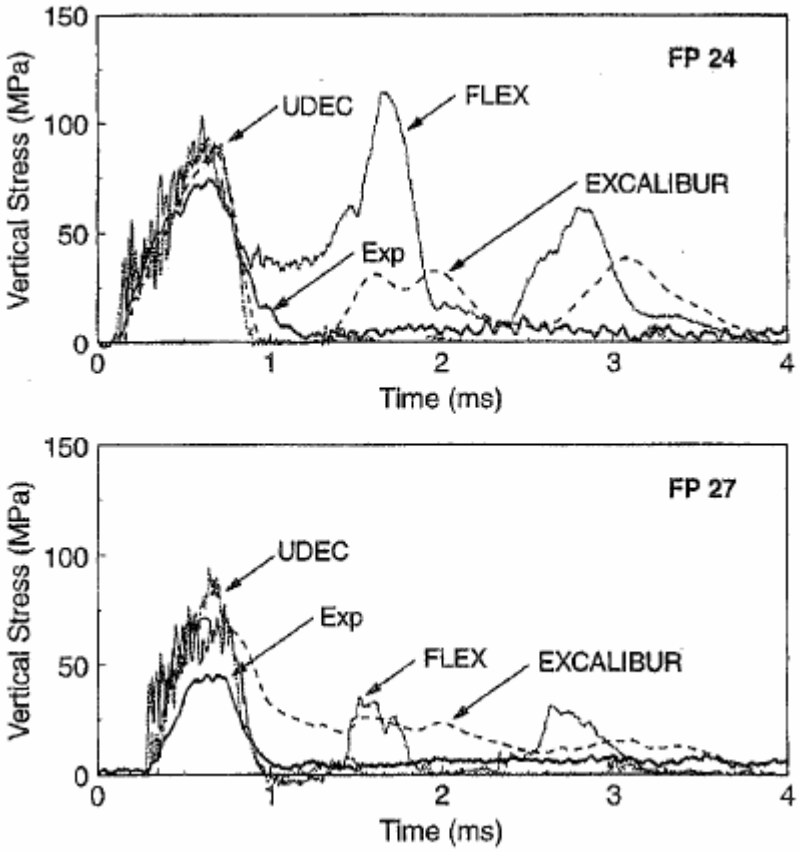

Source: Senseny and Pucik 1999 [DIRS 168479], Figure 15.

Figure 7-23. Predicted and Measured Stresses on the Specimen Centerline above the Tunnel Crown

Figure 7-24 shows the predicted and measured stresses at the six gauges located adjacent to the springlines (FPs 22, 23, 25, 26, 28, and 29). Because of symmetry in the experiment, the gauges on each side of the tunnel measure similar stress histories and, therefore, provide a measure of precision. As the figure shows, the precision in these stress measurements is very good. UDEC predicts the wave arrival times and the peak stresses accurately at all stations. Its predictions track the measurements quite well, with exception of a stress drop around 2 ms, which persists for about 0.5 ms. The stress drop is a result of a wave reflection from the bottom of the model. This could have been avoided by using nonreflecting boundaries. However, this simulation was performed using the same conditions as prescribed for the numerical experiments outlined in Senseny and Pucik (1999 [DIRS 168479], pp. 753-754).

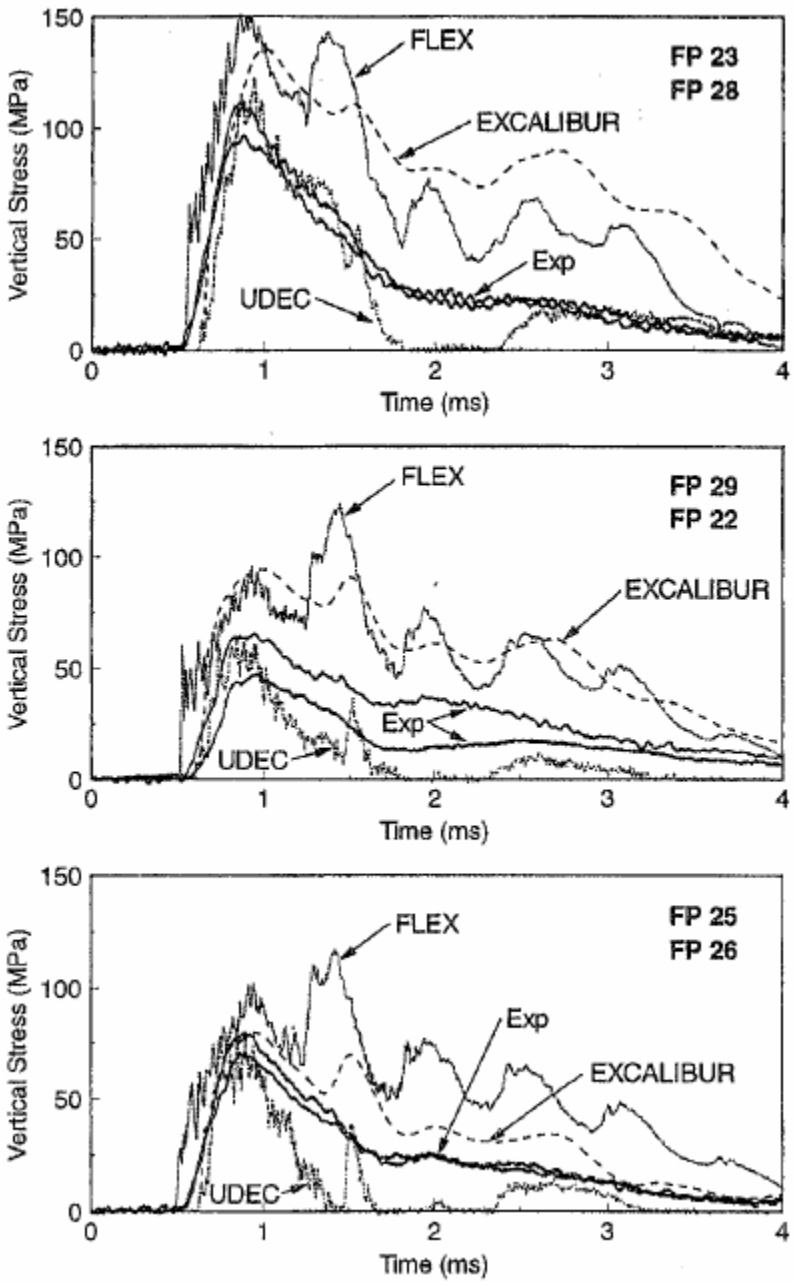

Source: Senseny and Pucik 1999 [DIRS 168479], Figure 16.

Figure 7-24. Predicted and Measured Stresses Adjacent to the Tunnel Springlines

This section has presented corroboration of data from a UDEC-based model, similar to the model for damage to a waste package surrounded by rubble and subjected to vibratory ground motion, with data acquired from field experiments not previously used to develop or calibrate the model, and meets the validation review criteria presented in the TWP (SNL 2007 [DIRS 179869], Table 2-1). In this work, comparison is made to results of a 2-m scale field experiment of a lined tunnel in a fractured rock mass subjected to dynamic loading sufficient to cause the material to fail and deform the tunnel lining. Of interest was that the results were not known in

advance—the predictions made were "blind" and the comparison of the results with various models was performed by an outside agency. The UDEC-based model results compared very favorably with the experimental results and demonstrated the ability of the program to reasonably represent the dynamic response of a fractured medium. The ability of the UDEC code to properly represent complex dynamic boundary conditions is also demonstrated in *UDEC User's Guide* (Itasca 2002 [DIRS 160331]).

7.3.3 Validation of Model for Deformation and Damage of Drip Shield under Static and Dynamic Conditions

The model for deformation and damage of drip shield under static and dynamic conditions is validated by three postdevelopment activities as indicated in Table 2-1 of the TWP (SNL 2007 [DIRS 179869]). First, results obtained using two different, completely independent codes (FLAC3D and LS-DYNA) based on different numerical formulations (finite differences and finite elements), different yield criteria (Tresca in FLAC3D, von Mises in LS-DYNA), and different discretizations (two brick layers in plates in FLAC3D versus shell elements in LS-DYNA) are compared here to provide validation of the FLAC3D model which is the model used for analysis of deformation and damage of structures. Next, FLAC3D results are compared to dynamic LS-DYNA predictions of drip shield response to block impact. (This analysis is in lieu of corroboration of the technical approach with analog studies per discussion in Section 1.5.) Finally, an independent critical review conducted by a technical specialist is presented in Section 7.3.4 and Appendix E.

The model for estimating damage to the drip shield from rockfall was developed to predict the deformation, damage, and fragility of the drip shield due to static and dynamic loads of rubble that could form as a result of the potential degradation of the emplacement drifts. The model was developed using the FLAC3D code, which is a general finite-difference, three-dimensional numerical code for analyzing the deformation of solids. It is widely used for geotechnical problems, but the basic formulation of FLAC3D is general enough that it can be applied to metals, provided that the proper material constitutive relation is used. In particular, the strain-hardening Tresca constitutive relation, available in FLAC3D, is used to represent the deformation and yield of metals. The model formulation utilizes brick elements, available in FLAC3D, to simulate the behavior of metals. The brick elements are effective, provided that the discretization of the thickness of the structural elements is sufficient to represent stress and strain gradients. The basic formulation of FLAC3D is dynamic, and there are many examples of dynamic analysis using FLAC3D. One advantage of using FLAC3D for this model is that both static and dynamic problems can be solved. The static problems are solved dynamically by using artificial damping to optimize calculation time.

7.3.3.1 Comparison of FLAC3D Results to Quasi-Static LS-DYNA Predictions of Drip Shield Deformation

The deformation and stability of the drip shield due to rockfall-induced rubble load in the lithophysal units were investigated using the LS-DYNA numerical code, and the results of the analyses were documented in *Structural Stability of a Drip Shield Under Quasi-Static Pressure* (BSC 2004 [DIRS 170791], Section 6). The analysis was conducted for six load realizations (i.e., nonuniform rubble load distribution around the drip shield profile in the vertical cross

section perpendicular to the drip shield longitudinal axis) under quasi-static conditions. The loads, listed in Table 6-136, were determined by the two-dimensional UDEC analyses (BSC 2004 [DIRS 166107], Section 6.4.2.5). The rubble load on the drip shield and its approximation in the analyses are discussed in more detail in Section 6.4.4. Due to the two-dimensional character of the load approximation, which does not vary along the drip shield, and the repetitive geometry of the drip shield, only one drip shield segment (as shown in Figure 6-49) was used in the geometrical representation. In the LS-DYNA finite-element representation, the plates were represented using shell elements, while the rest of the structure (e.g., the bulkheads, the support beams, and the longitudinal stiffeners) was represented using solid brick elements.

The same problem of drip shield deformation and stability was solved using FLAC3D, which is a finite-difference numerical code. Only solid brick elements (with constant-strain approximation) for both plates and other structural components were used in the FLAC3D analysis. Because LS-DYNA calculations did not indicate significant deformation of the plates between the framework and because the main objective was to compare the overall deformation of the framework, the plates were discretized with two layers of elements only. Both LS-DYNA and FLAC3D use a bi-linear stress-strain approximation for Titanium Grades 7 and 29 (i.e., the material of the plates and the framework). However, while the yield criterion used in LS-DYNA is the von Mises criterion, the Tresca yield criterion is used in FLAC3D simulations. The parameters for the two yield criteria were determined to match the same uniaxial tensile strength. In the case of the Tresca yield criterion, the strength under pure shear conditions is approximately 15% less than in the case of the von Mises criterion.

The results obtained using two different, completely independent codes (FLAC3D and LS-DYNA) based on different numerical formulations (finite differences and finite elements), different yield criteria (Tresca in FLAC3D, von Mises in LS-DYNA), and different discretizations (two brick layers in plates in FLAC3D versus shell elements in LS-DYNA) are compared here to provide additional validation of the FLAC3D model for analysis of deformation and damage of structures. This problem tested a number of aspects of the model for deformation and damage of the drip shield due to static load, including:

1. The ability to represent elastic and inelastic deformation of the drip shield structure

2. The ability to represent stresses in the drip shield structure.

As was determined previously (BSC 2004 [DIRS 170791], Section 6), the drip shield remains stable for all six load realizations under static conditions. The deformations of the drip shield in the vertical cross section through the bulkheads and the support beams predicted with FLAC3D are compared with the results obtained with LS-DYNA in Figures 7-25 through 7-30. The agreement between the results obtained with two different codes is excellent for five load realizations and meets the validation review criteria presented in the TWP (SNL 2007 [DIRS 179869], Table 2-1). There is only a fair agreement in the predicted short-term displacements for load realization 4, which is shown in Figure 7-28. The causes for the difference in the prediction for load realization 4 are the different yield criteria used in the calculations. The Tresca yield criterion, used in the FLAC3D calculations, predicts a lower pure-shear yielding stress than that predicted by the von Mises criterion, used in the LS-DYNA

calculations. FLAC3D predicts more plastic yielding of the plates in the area of connection between the bulkhead and the support beam on the right shoulder of the drip shield, resulting in different deformation of the drip shield in the crown and the left leg.

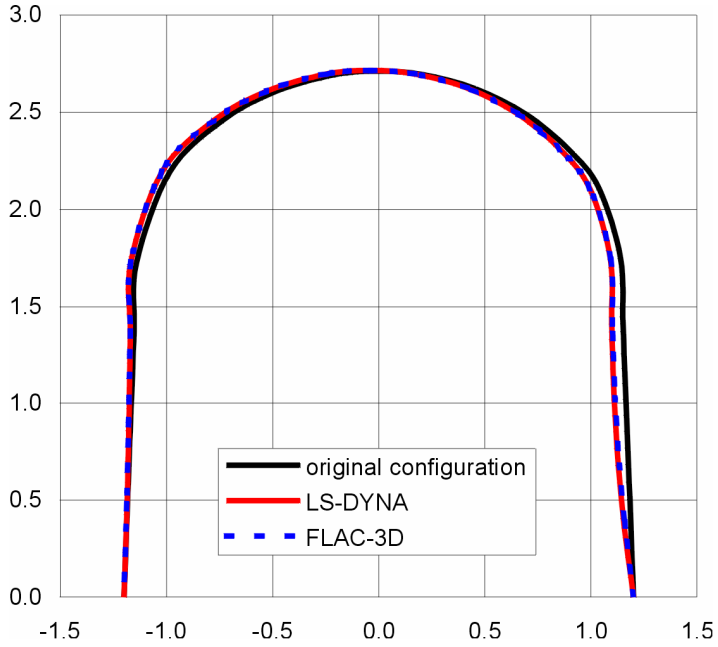

Validation DTN: MO0705DEFCONFG.000, file *deflection_allNR.xls.*

NOTE: Vertical and horizontal scales are in m.

Figure 7-25. Realization 1: Comparison of Deformed Drip Shield Based on LS-DYNA and FLAC3D Calculations

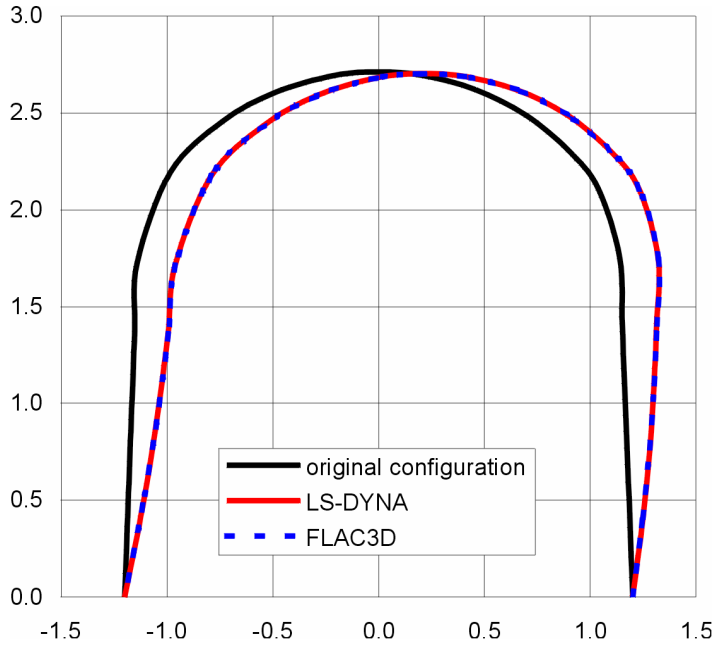

Validation DTN: MO0705DEFCONFG.000, file *deflection_allNR.xls.*

NOTE: Vertical and horizontal scales are in m.

Figure 7-26. Realization 2: Comparison of Deformed Drip Shield Based on LS-DYNA and FLAC3D Calculations

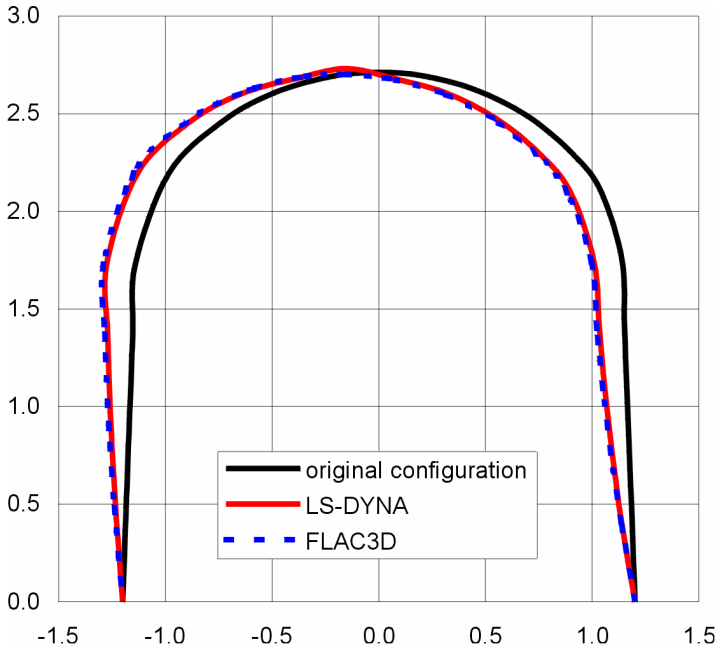

Validation DTN: MO0705DEFCONFG.000, file *deflection_allNR.xls.*

NOTE: Vertical and horizontal scales are in m.

Figure 7-27. Realization 3: Comparison of Deformed Drip Shield Based on LS-DYNA and FLAC3D Calculations

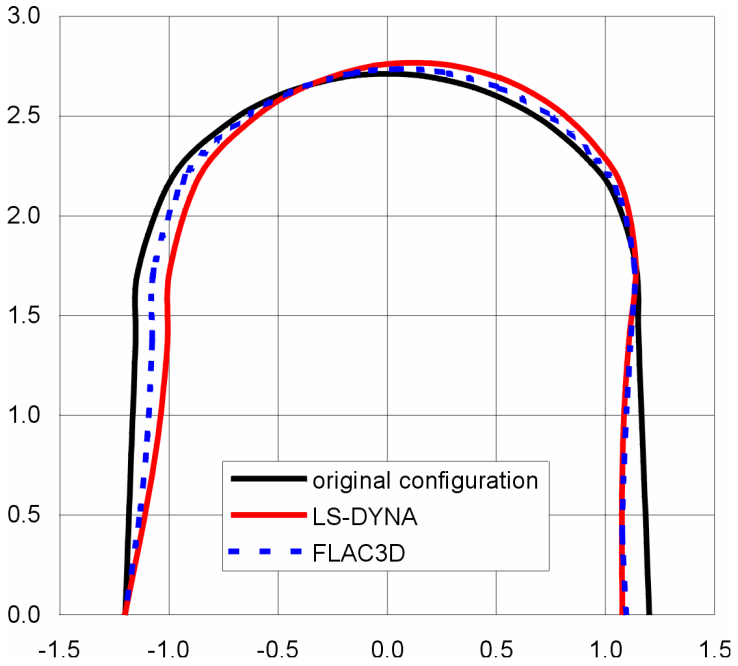

Validation DTN: MO0705DEFCONFG.000, file *deflection_allNR.xls.*

NOTE: Vertical and horizontal scales are in m.

Figure 7-28. Realization 4: Comparison of Deformed Drip Shield Based on LS-DYNA and FLAC3D Calculations

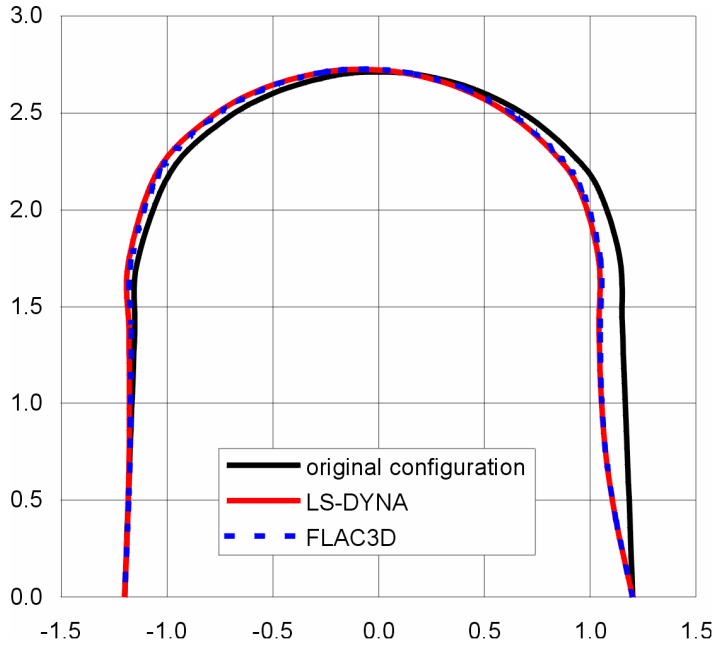

Validation DTN: MO0705DEFCONFG.000, file *deflection_allNR.xls.*

NOTE: Vertical and horizontal scales are in m.

Figure 7-29. Realization 5: Comparison of Deformed Drip Shield Based on LS-DYNA and FLAC3D Calculations

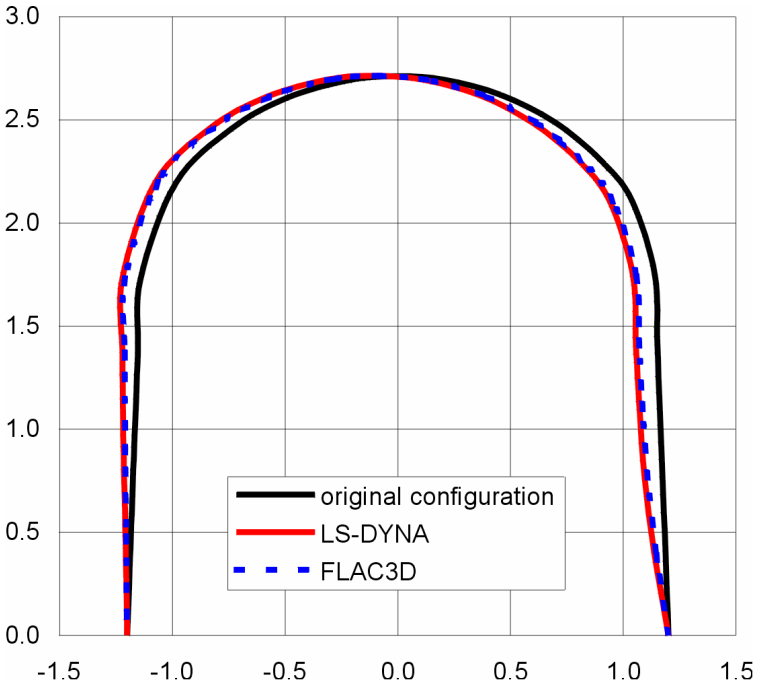

Validation DTN: MO0705DEFCONFG.000, file *deflection_allNR.xls.*

NOTE: Vertical and horizontal scales are in m.

Figure 7-30. Realization 6: Comparison of Deformed Drip Shield Based on LS-DYNA and FLAC3D Calculations

Stresses in the drip shield for load realization 3 (which has the greatest vertical load on the drip shield, as shown in Table 6-136), calculated using LS-DYNA and FLAC3D, are compared in Figures 7-31 through 7-33. Figure 7-31 shows the maximum shear stress contours on the scale of the entire drip shield on the vertical section plane perpendicular to the longitudinal axis of the drip shield, through the bulkhead and support beams. Figures 7-32 and 7-33 show the contours of the maximum shear stress in details 1 and 2, respectively, indicated in Figure 7-31. Considering the difference in the coloring schemes, the agreement between the stress fields is very good and meets the validation review criteria presented in the TWP (SNL 2007 [DIRS 179869], Table 2-1). The maximum stress at the base of the drip shield leg shown in Figure 7-32a (LS-DYNA) is greater than the maximum stress shown in Figure 7-32b (FLAC3D). The disagreement, which is localized to the corner point, is a result of the distribution of contact forces between the bottom of the leg and the invert. In the case of FLAC3D, the contact forces are distributed over a wider area, resulting in a smaller stress concentration.

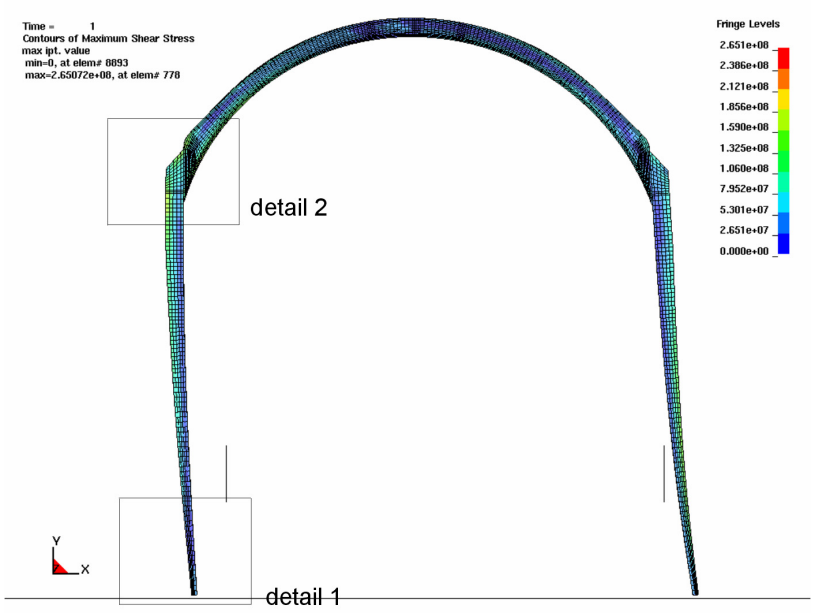

a) LS-DYNA results (Pa)

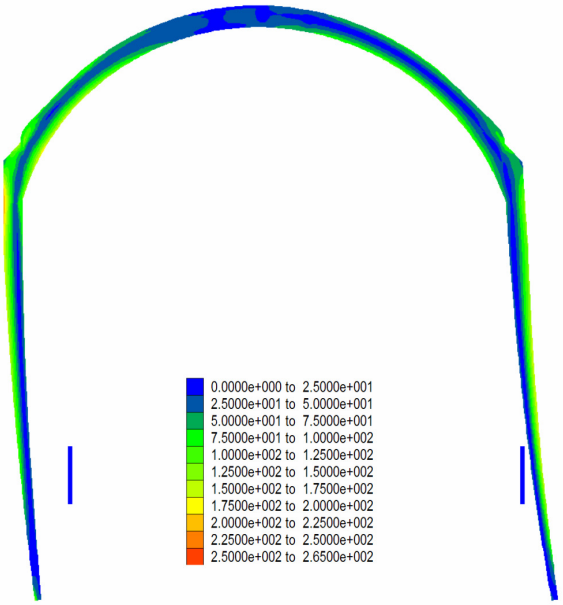

b) FLAC3D results (MPa)

Sources: LS-DYNA results taken from BSC 2004 [DIRS 170791], Figure III-1; FLAC3D results generated from DTN: MO0508SPACREEP.000 [DIRS 179984], file *\DS creep\coarse\no interaction\realization 3\initial.sav*.

NOTE: Values for rubble load realization 3 are taken from Table 6-136. Detail 1 and Detail 2 in a) are shown in Figure 7-32 and 7-33.

Figure 7-31. Comparison of Maximum Shear Stress Contours Obtained Using LS-DYNA and FLAC3D for Rubble Load Realization 3 Plotted on the Deformed Drip Shield Configurations

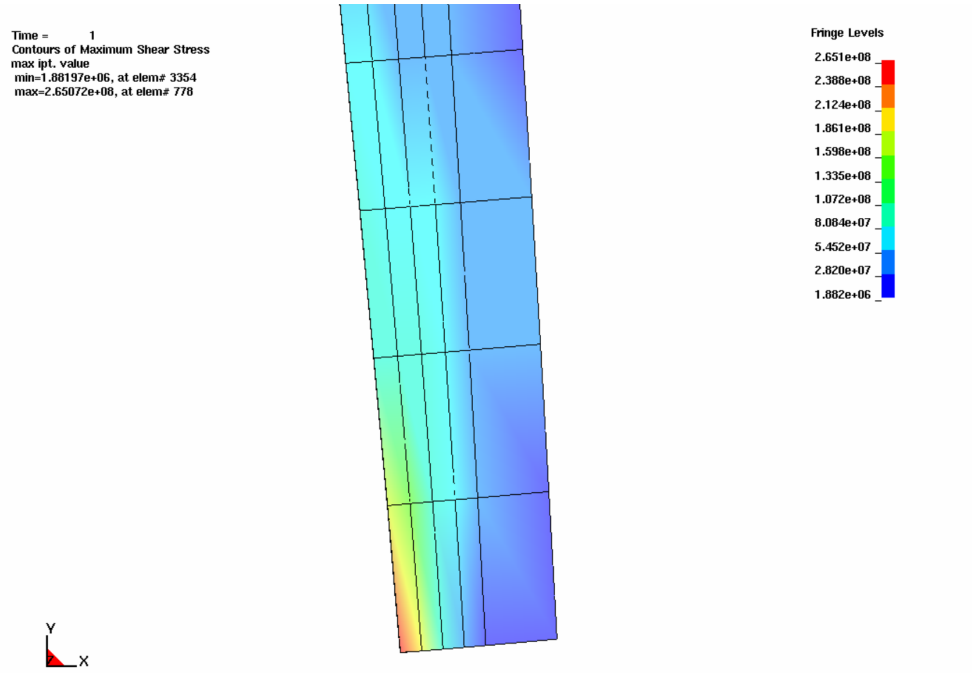

a) LS-DYNA results (Pa)

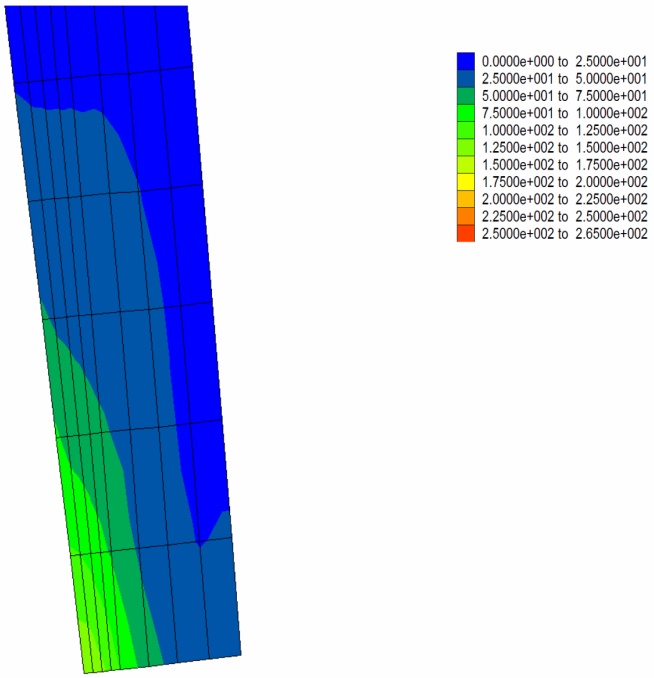

b) FLAC3D results (MPa)

Sources: LS-DYNA results taken from BSC 2004 [DIRS 170791], Figure III-2; FLAC3D results generated from DTN: MO0508SPACREEP.000 [DIRS 179984], file *\DS creep\coarse\no interaction\realization 3\initial.sav*.

Figure 7-32. Comparison of Maximum Shear Stress Contours Obtained Using LS-DYNA and FLAC3D for Rubble Load Realization 3 (Table 6-136) Plotted for Detail 1 Indicated in Figure 7-31

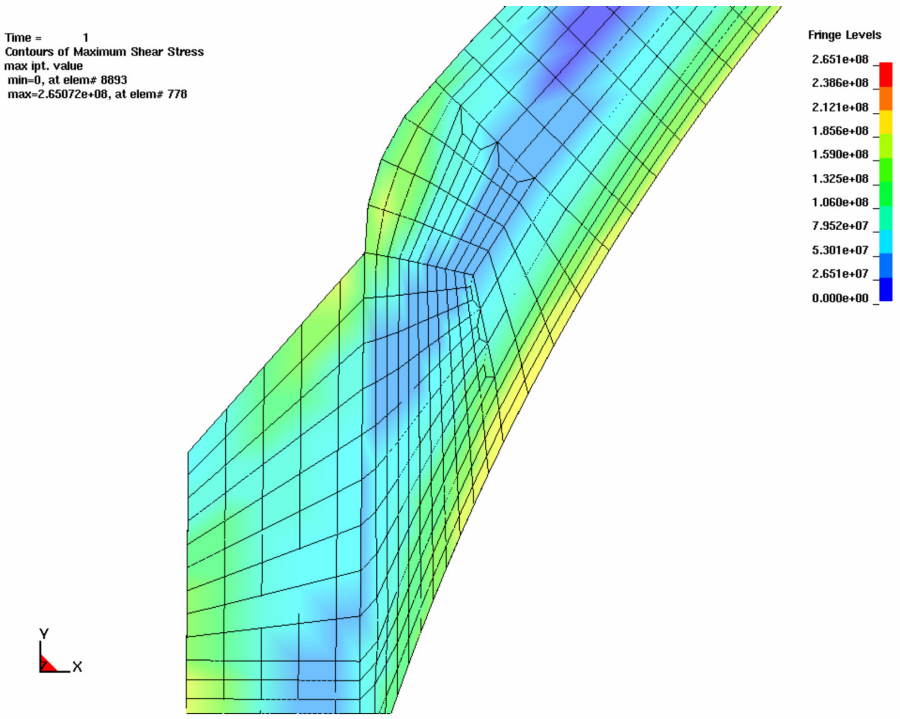

a) LS-DYNA results (Pa)

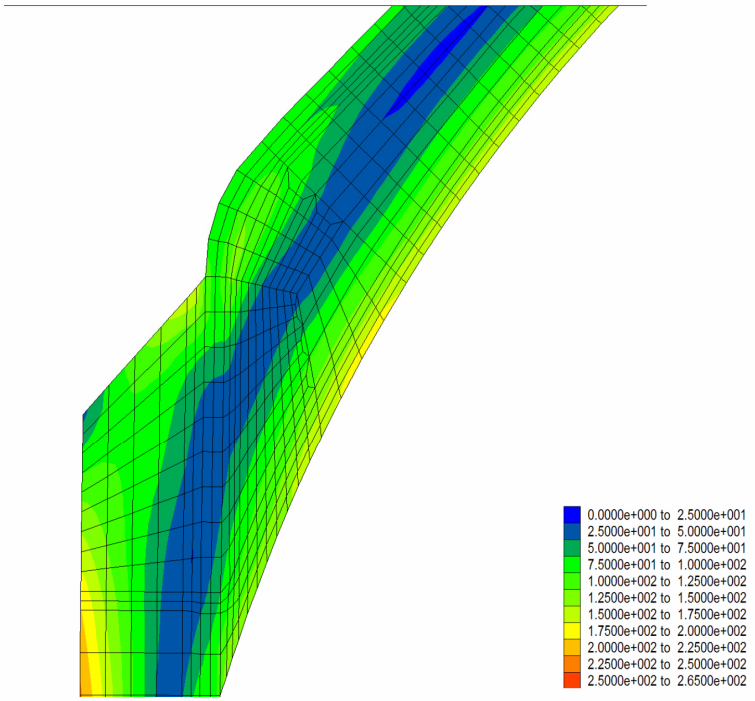

b) FLAC3D results (MPa)

Sources: LS-DYNA results taken from BSC 2004 [DIRS 170791], Figure III-4; FLAC3D results generated from DTN: MO0508SPACREEP.000 [DIRS 179984], file *\DS creep\coarse\no interaction\realization 3\initial.sav*.

Figure 7-33. Comparison of Maximum Shear Stress Contours Obtained Using LS-DYNA and FLAC3D for Rubble Load Realization 3 (Table 6-145) Plotted for Detail 2 Indicated in Figure 7-31

7.3.3.2 Comparison of FLAC3D Results to Dynamic LS-DYNA Predictions of Drip Shield Response to Block Impact

As prescribed in Section 1.5 of this report, a comparison of results from models formulated using FLAC3D and LS-DYNA to predict drip shield response to block impact can be used as part of the model validation. The LS-DYNA numerical code was used to investigate the deformation and stability of the drip shield structure due to single block impacts expected to occur in the nonlithophysal units, and the results were documented in *Drip Shield Structural Response to Rock Fall* (BSC 2004 [DIRS 168993], Sections 5 and 6). The analysis was carried out for six block geometries and impact velocities at the 2.44 m/s PGV level (10^{-6} annual exceedance probability in the case of unbounded seismic hazard) and one block geometry and impact velocity at the 5.35 m/s PGV level (10^{-7} annual exceedance probability in case of unbounded seismic hazard). The parallelepiped-shaped rock blocks are considered to impact the drip shield structure into the crown. Block velocity is vertical, and the impact location and the block center of mass are co-linear with the block velocity. Both the drip shield structure (the beams and the plates) and the rock blocks are represented with solid brick, eight-node, finite elements with a single Gaussian point. All five drip shield segments are included in the numerical representation. The symmetry of the geometry and boundary conditions with respect to the vertical plane along the drip shield axis is used to include only half of the geometry in the numerical analysis.

The impact analysis for a 3.3 mT block at 3.75 m/s impact velocity is carried out again using the FLAC3D numerical code in order to validate the FLAC3D model of rock block impact into the drip shield. Numerical discretizations (i.e., finite elements or finite difference zones) of the drip shield structure and plates in LS-DYNA and FLAC3D were almost identical. The difference is that only a quarter of the drip shield geometry was included in the FLAC3D numerical representation as a result of the use of symmetry conditions with respect to two vertical planes, one along the longitudinal drip shield axis (also used in LS-DYNA analysis) and the other perpendicular to the longitudinal drip shield axis in the middle of the drip shield at the impact location. Both the drip shield structure and the rock block were represented in the FLAC3D calculations using the solid brick elements, with constant-strain approximation similar to LS-DYNA brick elements with one Gaussian point. The main difference in the two numerical simulations is the representation of rock block geometry. In the LS-DYNA simulations, the rock block has the general shape of a parallelepiped with edges of different lengths. In the FLAC3D simulations, the block has a cubic shape. A result of this approximation is additional symmetry in the problem analyzed in the FLAC3D calculations. The codes used the same approximations of the material behavior of Titanium Grade 7 and Titanium Grade 24 as in the validations for quasi-static loading conditions discussed in Section 7.3.3.1. LS-DYNA used the von Mises yield criterion, and FLAC3D used the Tresca yield criterion.

The results obtained using two different, completely independent codes (FLAC3D and LS-DYNA) based on different numerical formulations (finite differences and finite elements) are compared here to validate the FLAC3D model for analysis of impact-induced deformation and damage to structures. This problem tested a number of aspects of the model for deformation and damage of the drip shield due to dynamic loading, including the ability to represent:

1. Interaction between the rock block and the drip shield
2. Momentum transfer from the rock block to the drip shield structure
3. Elastic and inelastic deformation of the drip shield structure for dynamic loading conditions
4. Dynamic stresses in the drip shield structure.

The results from the two calculations at the state of maximum drip shield deformation are shown in Figures 7-34 through 7-36. The maximum principal stresses in the entire drip shield structure (including the plates and the framework) are compared in Figure 7-34. Comparison of the contours of the maximum principal stresses in only the drip shield plates is shown in Figure 7-35. The contours of the vertical displacements are compared in Figure 7-36. Considering that the coloring schemes are not identical and that the figures from FLAC3D show only one quarter of the drip shield geometry, the figures illustrate very good qualitative and quantitative agreement between predictions obtained by the two different models and meet the validation review criteria prescribed in Section 1.5 and detailed in the TWP (SNL 2007 [DIRS 179869], Table 2-1). The maximum displacement predicted in LS-DYNA is 0.044 m compared to 0.035 m predicted in FLAC3D. The difference of 20% is acceptable and is a consequence of a different numerical formulation for the brick elements used in LS-DYNA and FLAC3D and different representation and discretization of rock blocks. Comparison between the maximum stresses shows similar trends. The maximum principal stress of 790 MPa predicted with LS-DYNA is greater than the 641-MPa maximum stress predicted with FLAC3D. Again, the difference of 19% between predictions is acceptable considering the complexity of the problem and the difference in numerical formulation and representation of block geometry. The above discussion adequately describes the limitations of the model, and shows that both the model and the results are reasonable and appropriate, and that, for the given inputs, the results are adequate for the intended use.

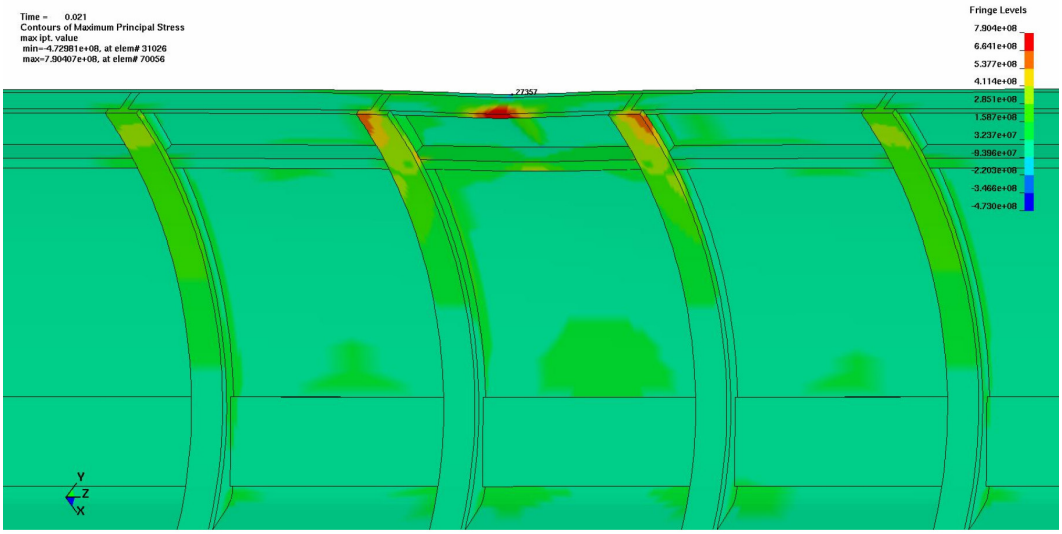

a) LS-DYNA results (Pa)

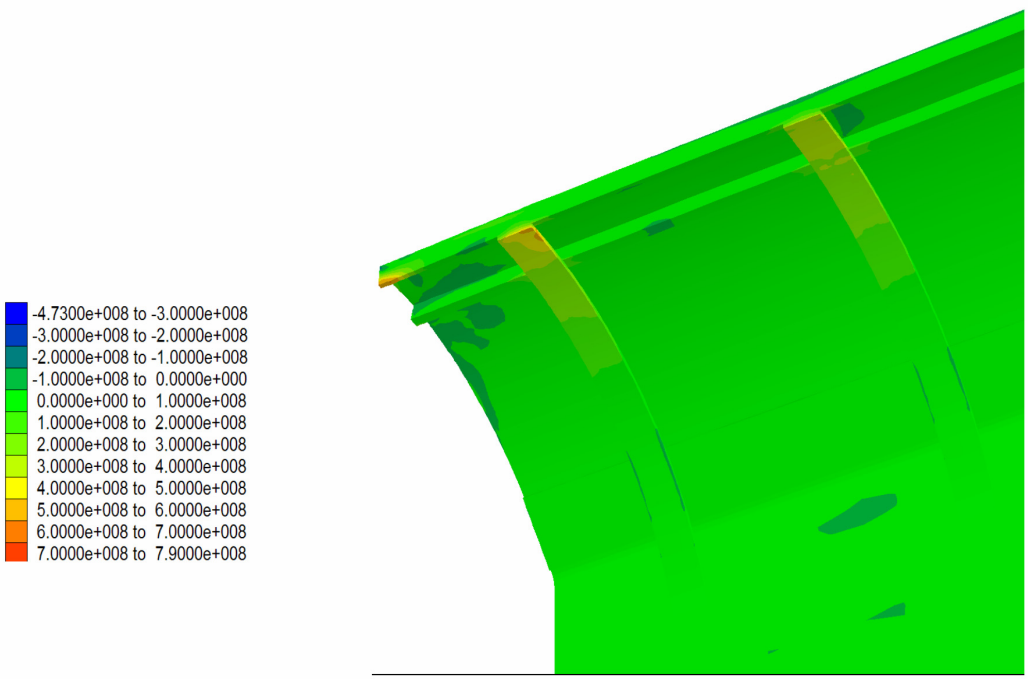

b) FLAC3D results (Pa)

Sources: Inputs for LS-DYNA simulation (Part a) in BSC 2004 [DIRS 168993], Table 8-1, c2; LS-DYNA output (Part a) in output DTN: LL0704PA051SPC.026, figure "Figures_Mech_Assessment_AMR/Cmpr_MaxPrinStrs_Drip_ Shield_part_a/c2_contour_stress1.jpg"; FLAC3D output (Part b) in Validation DTN: MO0705FLAC3DMT.000, file *structure stress.pcx*.

Figure 7-34. Comparison of Maximum Principal Stress Contours in the Drip Shield for 3.3 mT Block Impact Obtained Using LS-DYNA and FLAC3D

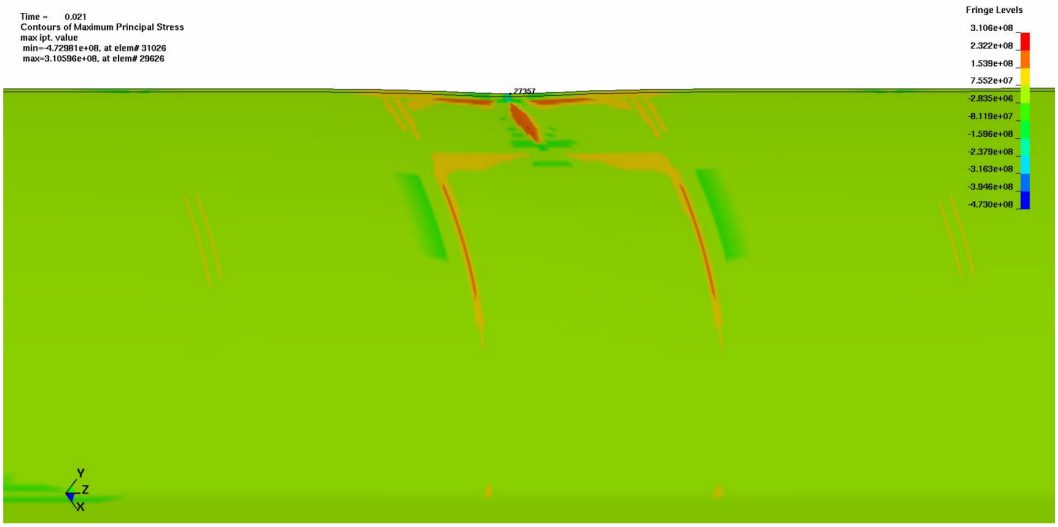

a) LS-DYNA results (Pa)

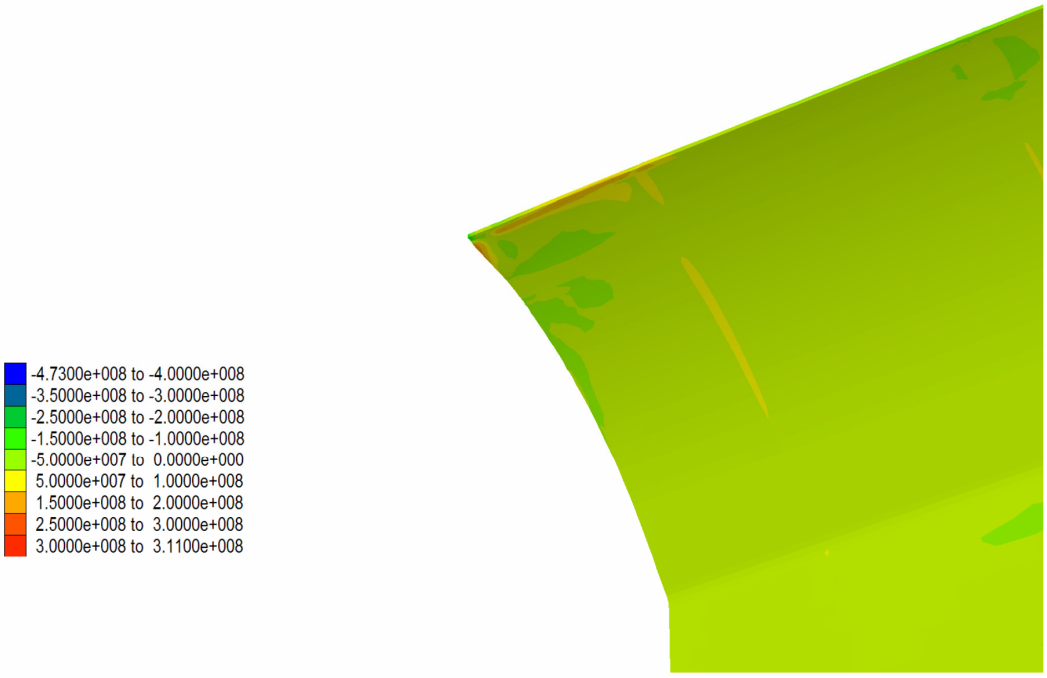

b) FLAC3D results (Pa)

Sources: Inputs for LS-DYNA simulation (Part a) in BSC 2004 [DIRS 168993], Table 8-1, c2, LS-DYNA output (Part a) in output DTN: LL0704PA051SPC.026, figure "Figures_Mech_Assessment_AMR/Cmpr_MaxPrinStrs_Drip_Shield_Plate_part_a/c2_ contour_stress_plate1.jpg"; FLAC3D output (Part b) in Validation DTN: MO0705FLAC3DMT.000, file *plate stress.pcx*.

Figure 7-35. Comparison of Maximum Principal Stress Contours in the Drip Shield Plate for 3.3 mT Block Impact Obtained Using LS-DYNA and FLAC3D

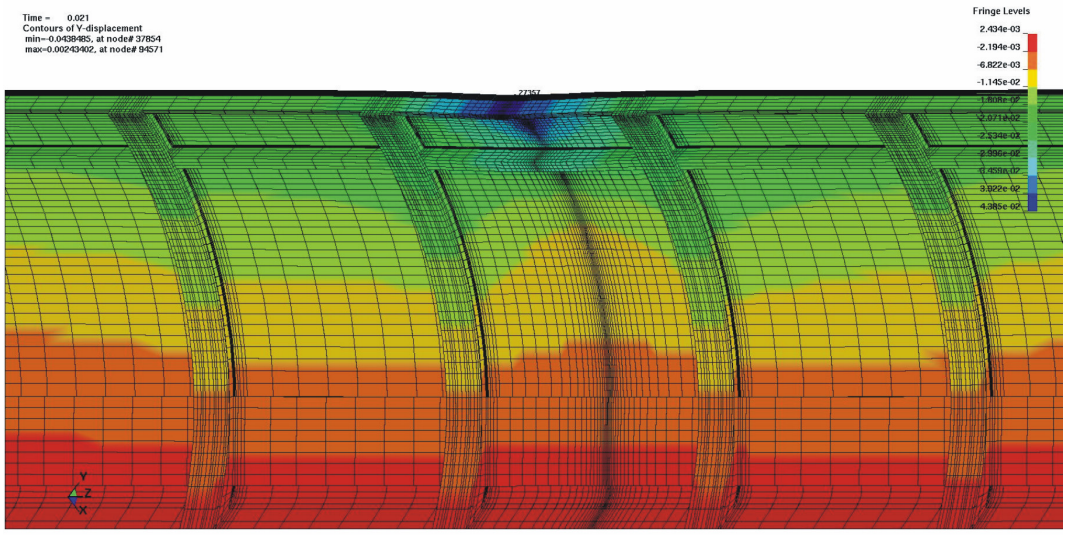

a) LS-DYNA results (m)

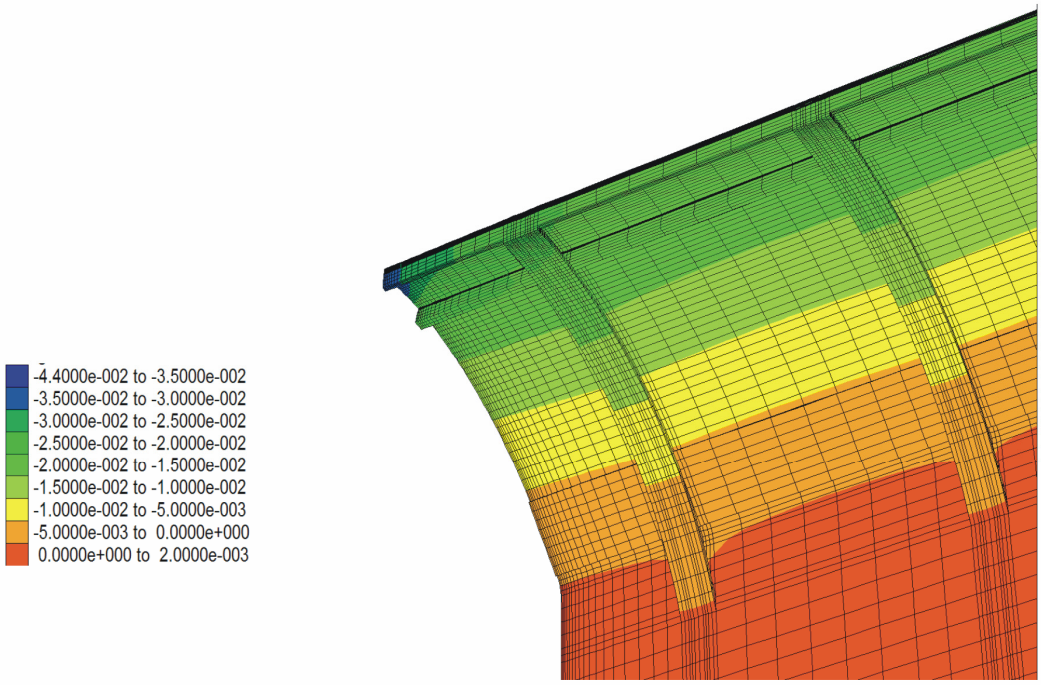

b) FLAC3D results (m)

Sources: Inputs for LS-DYNA simulation (Part a) in BSC 2004 [DIRS 168993], Table 8-1, c2; LS-DYNA output (Part a) in output DTN: LL0704PA051SPC.026, figure "Figures_Mech_Assessment_AMR/Cmpr_DispContour_Drip_Shield_part_a/c2_contour_ydisp_ mesh1.jpg"; FLAC3D output (Part b) in Validation DTN: MO0705FLAC3DMT.000, file *displacements.pcx*.

Figure 7-36. Comparison of Displacement Contours in the Drip Shield for 3.3 mT Block Impact Obtained Using LS-DYNA and FLAC3D

7.3.4 Critical Review of Three-Dimensional Kinematic Model for Waste Package Damage Due to Vibratory Ground Motion Conducted by a Technical Specialist

In accordance with the TWP for this work (SNL 2007 [DIRS 179869], Sections 2.3.2.1 and 2.3.2.3), a critical review has been performed by an independent technical specialist to assess the modeling approach for prediction of damage to waste packages and drip shield components of the EBS as they degrade with time due to corrosion and seismic activity. The required skill of the technical specialist for postdevelopment model validation is expertise in both structural engineering and structural response calculations.

A critical review was performed by Michael F. Hessheimer, P.E., Sandia National Laboratories. The reviewer found that the estimates of waste package performance are reasonable for the TSPA in support of the license application and that the limitations of the models used in the report are adequately described.

Moreover, the reviewer indicated that this report presents a comprehensive suite of analyses of the TAD-bearing and codisposal waste packages, emplacement pallets/invert, drip shield, and drift collapse that used seismic ground motions representing the full range of intensities anticipated for the repository. The reviewer also indicated that the outputs of the damage models, in terms of excessive residual stress or rupture of the waste package OCB, are reasonable and conservative.

The complete results of the review are presented along with explanatory notes and responses in Appendix E of this report.

7.4 VALIDATION SUMMARY

Model validation activities to meet the criteria presented in Section 6.3 of SCI-PRO-006 and the TWP (SNL 2007 [DIRS 179869], Section 2.3.2) have been conducted. These criteria address adequacy of the scientific basis and accuracy of the model consistent with intended use (Step 6.3.1B of SCI-PRO-006) and demonstrate that the appropriate level of confidence has been obtained for a given model. The validation activities documented in Sections 7.2 and 7.3 are satisfactory for the intended purpose of the three models, which is to determine EBS damage due to vibratory ground motion, and for achieving the required level of confidence.

The models documented in this report have been validated by applying acceptance criteria, which are based on evaluation of the relative importance of the model to the performance of the repository system. All validation requirements defined in the governing TWP (SNL 2007 [DIRS 179869], Section 2.3.2) have been fulfilled, including corroboration of model results with experimental data (Section 7.3.2.2), corroboration with an alternative mathematical model (Sections 7.3.1, 7.3.2.1, and 7.3.3), and critical review (Section 7.3.4). Based on the fulfillment of these requirements, each of the models is sufficiently accurate and adequate for the intended purpose, consistent with the level of confidence required by the relative importance of the model to the performance of the repository system.

The ability of the damage models to predict a reasonable range of damage for EBS components due to vibratory ground motion is supported in Section 7.3 by virtue of direct comparisons between stresses and deformations predicted by the damage models and those predicted by

corresponding models of a validation test case. Section 7.3.2.2 documents the comparison of displacements and deformations predicted by UDEC against those measured in a dynamic field test and supports the ability of the waste package rubble damage model and the drip shield damage model to predict reasonable behavior of a fractured rock mass subject to dynamic loading.

8. CONCLUSIONS

Work presented in this report provides detailed information on the damage that can be expected for several components of the EBS due to vibratory ground motion during the postclosure period. Analyses conducted include both two-dimensional and three-dimensional numerical simulations of the EBS response to several levels of vibratory ground motion.

The major results of this work are tables indicating damage at various levels of vibratory ground motion, which are used in damage abstractions presented in *Seismic Consequence Abstraction* (SNL 2007 [DIRS 176828]). In addition, the following conclusions can be drawn from the results presented in this report.

- Increasing the PGV level of the vibratory ground motion increases the amount of damage predicted for the waste package and drip shield components of the EBS.

- Uncertainty and variability of material properties of EBS components with respect to temperature have an insignificant influence on damage to the EBS components due to vibratory ground motion (Section 6.3.2.2.2).

- The TAD-bearing waste package with minor corrosion of the waste package OCB and intact internals is highly resistant to damage, even at PGV levels of 4.07 m/s (Section 6.3).

- The three-dimensional kinematic analysis of a string of waste packages indicates that most of the damage to waste packages from vibratory ground motion is caused by waste package-to-pallet impacts as opposed to waste package-to-waste package impacts (Section 6.3).

- Rupture associated with vibratory ground motion is predicted for only a small number of waste packages and only occurs at the higher levels of PGV and only with degraded internals (Sections 6.3 and 6.5.1).

- The analysis of drip shield damage indicates that vibratory ground motion may cause the drip shield framework to fail before the drip shield plates and that the failure by buckling will occur in the lower part of the legs of the drip shield (Sections 6.4.3 and 6.4.4).

- Analysis of waste package-to-drip shield collisions was performed to quantify the number and magnitude of impacts due to vibratory ground motion (Section 6.4.5). These calculations characterize the frequency and impact velocity between the TAD-bearing and codisposal waste packages and the internal ribs of the drip shield. This analysis supports an assessment of the importance of waste package-to-drip shield impacts for the seismic scenario class.

- Settlement of the drip shield in the invert during the postclosure period will not affect the stability of the drip shield (Section 6.4.6).

- Analysis of single-block impact on the drip shield indicates that impact of a block the size of block 1 (11.7 m^3 and 28.29 mT) considered in this simulation may cause the stiffeners in the drip shield to fail and potentially come into contact with the waste package (Section 6.4.7).

- Analysis of the waste package surrounded by rubble indicates that vibratory ground motion will cause little damage to the OCB (Section 6.5.1).

- The analysis of the waste package loaded by the collapsed drip shield shows that damage in the OCB is dependent on the state of the internals. For intact internals, most of the load is carried by the internals, resulting in a very small damage area in the OCB. Furthermore, the damage is almost independent of the OCB thickness. For degraded internals, the collapsed drip shield causes much more damage in the OCB (Section 6.5.2).

8.1 OUTPUT DATA AND USE IN TSPA

Output DTNs containing the work presented in this report are listed in Table 8-1. These DTNs provide input to *Seismic Consequence Abstraction* (SNL 2007 [DIRS 176828]), which in turn provides inputs to TSPA.

Table 8-1. Output DTNs for Results Presented in This Report

DTN	Title	Date Submitted
LL0703PA029SPC.014	Rupture Probability for the LS-DYNA Kinematic Analyses for the 5-DHLW/DOE SNF-Long Codisposal Waste Package and the TAD-Bearing Waste Package	03/14/2007
LL0703PA031SPC.015	LS-DYNA Waste Package-to-Pallet Temperature Sensitivity Analyses	04/19/2007
LL0704PA048SPC.023	LS-DYNA Kinematic Damaged Area Analyses for the TAD-Bearing Waste Package April 2007	05/01/2007
LL0704PA049SPC.024	LS-DYNA Kinematic Damaged Area Analyses for the 5-DHLW/DOE SNF-Long Co-Disposal Waste Package April 2007	05/01/2007
LL0704PA050SPC.025	LS-DYNA Kinematic Waste Package-to-Drip Shield Analyses	05/01/2007
LL0704PA051SPC.026	Figures for 2007 Seismic Post-Closure Mechanical Assessment AMR	05/01/2007
LL0706MG004SPC.001	Peak Acceleration of Waste Package Internals from Impacts with Waste Packages and Pallets	06/06/2007
MO0611ROCKFALL.000	Seismic Rockfall Analysis for Emplacement Drifts in Lithophysal Rock Mass Subject to Various Vibratory Ground Motion Levels	11/28/2006
MO0611WPRUBBLE.000	Input and Output Files for Analysis of the Waste Package Surrounded by Rubble Subjected to Seismic Ground Motion	11/27/2006

Table 8-1. Output DTNs for Results Presented in this Report (Continued)

DTN	Title	Date Submitted
MO0701DRIPSHLD.000	The Input Data and Results of Analysis of the Drip Shield Plate and Framework Fragility, Drip Shield Failure Modes, Effects of Uneven Invert Settlement on Drip Shield Stability, and Deformation and Damage of the Waste Package Loaded by Collapsed Drip Shield	01/15/2007
MO0702POSTRUBB.000	Post-Processing Results for Analysis of the Waste Package Surrounded by Rubble Subjected to Seismic Ground Motion	02/20/2007
MO0703PADSBLOC.000	Drip Shield Damage Due to Block Impact and Distributed Loading	03/09/2007
MO07043DWPFAIL.000	Three-Dimensional Effects on Waste Package Failure Modes and Loads	04/25/2007
MO0704DSFLAC3D.000	FLAC3D Input and Output Files from Analysis of Vertical Rock Block Impact into the Drip Shield	04/09/2007
MO0704PUNCTURE.000	Puncture Probability for the Outer Corrosion Barrier of the TAD-Bearing Waste Package When the Package Surrounded with Rubble and with Degraded Internals is Subjected to Strong Seismic Ground Motions	04/25/2007
MO0704SIPAWPSR.000	Sampling of Input Parameters for the Analysis of Waste Package Surrounded by Rubble	04/18/2007
MO0705IMPACTST.000	State During Impact of 7.49-mT Rock Block at 4.81 m/s into Drip Shield Configuration with 15-mm-Thick Plates	05/08/2007
MO0705NDSSTATE.000	State of the Naval Long Waste Package with Degraded Internals Loaded by Collapsed Drip Shield at Average Pressure of 486 kPa	05/08/2007
Output DTNs Used for Validation Purposes Only		
LL0702PA055SPC.002[a]	LS-DYNA Single Waste Package Damaged Area Analyses for the TAD-Bearing Waste Package	02/21/2007
LL0703PA007SPC.005[a]	LS-DYNA Single Waste Package Damaged Area Analyses for the 5-DHLW/DOE SNF-Long Co-Disposal Waste Package	03/06/2007
LL0705PA010SPC.027[b]	LS-DYNA 13 Waste Package Validation Analysis	05/07/2007
MO0705DEFCONFG.000[b]	Comparison of Predicted Deformed Drip Shield Configurations Obtained Using LS-DYNA and FLAC3D	05/04/2007
MO0705FLAC3DMT.000[b]	Input and Output Data from FLAC3D Analysis of 3.3 mT Block Impact into the Drip Shield	05/04/2007
MO0705UDECMECH.000[b]	UDEC Results of Mechanical Interaction of 13 Waste Packages Subject to Ground Motion at 5.35 m/s PGV	05/03/2007

[a] These DTNs are considered qualified because they were produced from qualified inputs, using qualified processes.

[b] These unqualified DTNs are for use in validation activities only and if used for direct input in a document, must be qualified for intended use.

8.2 LIMITATIONS AND RESTRICTIONS

Limitations of the analyses are presented in Section 6.8 and are summarized below:

- Analyses in this report are performed for representative TAD-bearing and codisposal waste packages. Detailed analyses of all the types of waste packages that will eventually be emplaced in the repository and their internals are beyond the scope of this report.

- The kinematic analyses presented here use a limited series of waste packages to reasonably represent the mechanical response of waste packages in a complete emplacement drift. Changes in the geometry of the waste packages over time as a function of previous seismic activity are neglected.

- Structural response calculations for the waste package are based on the average thickness of the outer barrier. Uniform thinning of waste package and drip shield is used to approximate uniform corrosion over time. It is unlikely that the waste package and drip shield components will corrode uniformly over their entire surface.

- Ground motions at 0.4 m/s and 4.07 m/s PGV levels have been created by linearly scaling the ground motions for the 1.05 m/s and 5.35 m/s PGV levels, respectively. While it is an approximation, the difference between linear scaling and other more sophisticated methods is negligible relative to other uncertainties in the calculations.

- The structural response calculations for the TAD-bearing and codisposal waste packages are based on two discrete values for the spatially averaged thickness of the OCB: 23 mm and 17 mm. The 17-mm-thick OCB provides a reasonable representation of degraded states of the OCB at approximately 1,000,000 years, as shown in (SNL 2007 [DIRS 176828], Section 6.5.2.2).

- Waste package internals are assumed to degrade as structural elements after the OCB is first damaged by a seismic event. However, this approach underestimates the structural capacity of stainless steel internal components, such as the 2-in-thick inner vessel or the TAD canister itself, for screening of criticality-related issues during a 10,000-year period.

- Structural response calculations for the waste package surrounded by rubble are based on the TAD-bearing waste package with degraded internals. Section 6.5.1.1 provides the rationale for using the results for the TAD-bearing waste package with degraded internals for the codisposal waste package with degraded internals.

- The internals of the waste package surrounded by rubble are always degraded. The use of degraded internals is consistent with the fact that the waste package becomes surrounded by rubble at late times, after the drip shield plates have failed and allowed rubble to contact the waste package. The use of degraded internals is conservative because damage to a waste package is observed to be significantly greater with degraded internals than with intact internals (see Sections 6.3.4 and 6.5.1.1).

- The carbon steel structural elements in the invert are not represented in the postclosure models because the carbon steel will degrade quickly in the postclosure timeframe. However, if the structural steel were present, either intact or in some intermediate state of corrosion, at the time of a seismic event, then there might be potential for waste packages to impact the invert steel and cause damage or puncture of the waste packages.

These limitations should be considered in using these results to develop abstractions for TSPA.

The analyses presented here are expected to overestimate damage to the EBS components due to vibratory ground motion as follows:

- The two-dimensional waste package representation underestimates the strength and stiffness of the true three-dimensional waste package structure (Section 6.5.1). This is because, in the two dimensional analysis, a cylinder with infinite length is assumed, while the actual waste package has a finite length of approximately 5.8 m, a diameter of 1.9 m, and lids on both ends. The shorter length and endcaps will add strength to the cylinder cross section.

- Elastic and plastic material properties are set to constant values at 60°C based on data from handbooks or manufacturers' catalogs. This temperature provides conservative values for material properties over the long duration of the seismic scenario class. Material properties at 60°C show less strength than at the lower temperatures that occur after 10,000 years (Assumption 5.7, Section 5).

- Accelerated stress corrosion cracking (SCC) from high residual stress is assumed to be the cause of waste package failure from impact processes under vibratory ground motion. A criterion for initiation of SCC of Alloy 22 based on residual stress thresholds is utilized (SNL 2007 [DIRS 177417], Section 6.2.2). The use of an SCC initiation criterion is appropriate for seismic analysis because regions where the residual stress from mechanical damage exceeds the tensile failure criterion are expected to be severely cold-worked and, hence, potentially subject to enhanced SCC. Moreover, a residual stress threshold failure criterion predicts failure at an earlier time than does a detailed corrosion model, which typically will have a delay time until failure. Finally, using this approach, the time of failure is immediate (i.e., failure occurs at the same time as when the seismic shaking occurs). However, in reality, if cracking were to occur as a result of specific environmental conditions coincident with the mechanical deformation, cracks would take time to develop after the shaking event causes a change in loading. Also, the specific environmental conditions necessary for crack growth may not always be present, and furthermore, SCC will not be sustained if the residual stress in the crack growth direction drops below the stress threshold.

- A threshold value of effective strain is used to determine whether rupture has occurred. Alternatively, effective plastic strain can be used in place of effective strain as the metric to compare to a threshold value. As is explained in Appendix A, using the effective plastic strain predicts rupture at lower strains than the effective strain. Also, this analysis does not account for increases in static yield strength resulting from high strain rate dynamic loading.

- The residual stress threshold for failure of the waste package via SCC is represented by a uniform distribution with a lower bound of 90% and an upper bound of 105% of the yield strength of Alloy 22. The upper bound is based on experimental data and conservatively incorporates a safety factor of 2.0 because of the very long lifetime of the waste package. The lower bound is introduced to evaluate the sensitivity of damaged area to potential uncertainty in the residual stress threshold (SNL 2007 [DIRS 177417], Section 6.2.2). This residual stress criterion (90% to 105% of the yield strength) is also consistent with the failure criterion for initiation of SCC in other waste package analyses.

- For codisposal waste packages, the waste package-to-waste package lookup table analyses were performed for the orientation providing the worst-case damaged area, and that damaged area was prescribed regardless of the waste package orientation in the kinematic analysis.

- The estimated area of damage is assumed as the area susceptible to cracking in the waste package.

- Total damage from multiple seismic events is based on the sum of the damaged areas from individual events without accounting for possible overlap of damaged areas in sequential events.

- Drip shield plates, as simulated in Section 6.4.3, do not overlap, whereas overlapping drip shields will be used in the actual repository; also, to account for variability in the loads on the drip shield, the pressure in a particular segment was applied along the entire length of the segment in the three-dimensional model.

- The static friction coefficient is set equal to the dynamic friction coefficient. The effect of relative velocity of the surfaces in contact is not considered in the analyses. This maximizes the relative motion of the drip shield with respect to the invert by minimizing the friction coefficient**.**

Restrictions in use of the analysis are included in Section 6.8 and are summarized below.

- No restrictions on subsequent use of the results presented in this report have been identified.

8.3 HOW THE YUCCA MOUNTAIN REVIEW PLAN ACCEPTANCE CRITERIA ARE ADDRESSED

This section identifies how the results in this report address the various review criteria identified as relevant in *Yucca Mountain Review Plan, Final Report* (NRC 2003 [DIRS 163274], Section 2.2.1.3.2).

Acceptance Criterion 1: System Description and Model Integration Are Adequate.

1. *Total system performance assessment adequately incorporates important design features, physical phenomena, and couplings, and uses consistent and appropriate assumptions throughout the mechanical disruption of engineered barrier abstraction process.*

   Response: Section 6 explains how design features, physical phenomena, and couplings are incorporated into the analysis of the EBS response to vibratory ground motion. The structural response analyses in Sections 6.3 and 6.4 include the mechanical coupling between the EBS components in defining damaged areas on the drip shield and waste package. Sections 6.4 and 6.5 consider the potential damage to the EBS components from rockfall induced by vibratory ground motion. These sections collectively address the methodology for incorporating design features, seismic response, and mechanical/thermal coupling for input into the seismic abstractions. Specific aspects of the methodology are as follows:

   - The estimates for damaged areas on the waste package are based on a statistically robust sampling of uncertain parameters, including the ground motion time histories, rock fracture patterns, and friction coefficients (Sections 6.3 and 6.5). The rockfall analyses and structural response analyses use consistent assumptions and consistent material properties.

   - Degradation of the drip shield and waste package is addressed for different periods after repository closure by reducing the thickness of the outer barrier of the waste package and the thickness of the drip shield plates (Sections 6.3, 6.4, and 6.5).

   - Material properties for structural response analyses are based on a temperature of 60°C, resulting in a bounding temperature after the first 10,000 years postclosure, as discussed in Assumption 5.7, Section 5. Sensitivity analyses with material properties at elevated temperatures (Section 6.3.2.2.2) demonstrate that the damaged area of the OCB is relatively insensitive to elevated temperatures that occur during the first 10,000 years.

   - Drip shield damage from rockfall induced by vibratory ground motion in the lithophysal and nonlithophysal zones is analyzed (Section 6.4). Rockfall is analyzed with state-of-the-art computer codes that are used for other drift-degradation analyses.

2. *The description of geological and engineering aspects of design features, physical phenomena, and couplings that may affect mechanical disruption of engineered barriers is adequate. For example, the description may include materials used in the construction of engineered barrier components, environmental effects (e.g., temperature, water chemistry, humidity, radiation, etc.) on these materials, and mechanical-failure processes and concomitant failure criteria used to assess the performance capabilities of these materials. Conditions and assumptions in the abstraction of mechanical disruption of engineered barriers are readily identified and consistent with the body of data presented in the description.*

Response: The structural response analyses and kinematic analyses in Sections 6.3 to 6.5 include the mechanical coupling between the EBS components in defining damaged areas on the drip shield and waste package. Sections 6.4 and 6.5 consider the potential damage to the EBS components from rockfall induced by vibratory ground motion. These sections collectively address the methodology for incorporating design features, physical phenomena, and the mechanical/thermal coupling between these phenomena for use in the damage abstractions for the seismic scenario class. Specific aspects of the methodology are as follows:

- Degradation of the drip shield and waste package is addressed for the first 10,000 years to 20,000 years after repository closure by reducing the thickness of the outer barrier of the waste package and the thickness of the drip shield plates by 2 mm.

- Material properties for structural response analyses are based on a temperature of 60°C, resulting in a bounding temperature after the first 10,000 years postclosure, as discussed in Assumption 5.7, Section 5. Sensitivity analyses with material properties at elevated temperatures (Section 6.3.2.2.2) demonstrate that damaged area of the OCB is relatively insensitive to elevated temperatures that occur during the first 10,000 years.

- The failure criteria for Alloy 22 and Titanium Grade 7 are based on a residual stress threshold for initiation of SCC, as explained in Section 6.2.

4. *Boundary and initial conditions used in the total system performance assessment abstraction of mechanical disruption of engineered barriers are propagated throughout its abstraction approaches.*

   Response: The rockfall analyses and structural response analyses use the same sets of ground motions at the four PGV levels, 0.40 m/s, 1.05 m/s, 2.44 m/s, and 4.07 m/s. Other boundary and initial conditions that ensure consistency are as follows:

   - The rockfall analyses and structural response analyses presented here use consistent boundary conditions and initial conditions. Results from these analyses are then passed to the abstractions.

   - Degradation of the drip shield and waste package is addressed for the first 10,000 years to 20,000 years after repository closure by reducing the thickness of the outer barrier of the waste package and the thickness of the drip shield plates by 2 mm.

   - Material properties for structural response analyses are based on a temperature of 60°C, resulting in a bounding temperature after the first 10,000 years postclosure, as discussed in Assumption 5.7, Section 5. Sensitivity analyses with material properties at elevated temperatures (Section 6.3.2.2.2) demonstrate that damaged area of the OCB is relatively insensitive to elevated temperatures that occur during the first 10,000 years.

Acceptance Criterion 2: Data Are Sufficient for Model Justification.

1. *Geological and engineering values, used in the license application to evaluate mechanical disruption of engineered barriers, are adequately justified. Adequate descriptions of how the data were used, interpreted, and appropriately synthesized into the parameters are provided.*

   Response: The underlying data for geologic properties and for engineering material properties are generally not directly used in the development of the seismic damage models and were not used in developing the model under discussion in this report, with the exception of the residual stress failure criteria for Alloy 22 and for Titanium Grade 7. Justification of the appropriate values is provided through external references. These justifications are based on experimental data for SCC, on handbook values and manufacturer's literature for the elastic and inelastic properties of EBS component materials, and on expert elicitation. Specific source documents that support development of the seismic scenario class are as follows:

   - The residual stress failure criteria are based on experimental data for the initiation of SCC in Alloy 22 and Titanium Grade 7 (SNL 2007 [DIRS 177417], Sections 6.2.2 and 6.8.3.1.3).

   - The constitutive relationships for Alloy 22 and for Titanium Grade 7 are based on material properties in the published literature. More specifically, the Young's modulus, Poisson's ratio, yield strength, and friction factors are based on data in the published literature (see Section 4).

   - The ground motion time histories for the rockfall and structural response analyses have been developed in a manner that is consistent with and builds upon the results of an expert elicitation (CRWMS M&O 1998 [DIRS 103731], Sections 5 and 6).

3. *Data on geology of the natural system, engineering materials, and initial manufacturing defects, used in the total system performance assessment abstraction, are based on appropriate techniques. These techniques may include laboratory experiments, site-specific field measurements, natural analog research, and process-level modeling studies. As appropriate, sensitivity or uncertainty analyses used to support the U.S. Department of Energy total system performance assessment abstraction are adequate to determine the possible need for additional data.*

   Response: As with the response to subcriterion 1 above, the underlying data for the simulations in this report in support of the seismic scenario class are based on experimental data for SCC, on handbook values and manufacturers' literature for the elastic and inelastic properties of EBS component materials, and on expert elicitation. Specific sources that support development of the seismic scenario class are as follows:

   - The residual stress failure criteria are based on experimental data for the initiation of SCC in Alloy 22 and Titanium Grade 7 (SNL 2007 [DIRS 177417], Sections 6.2.2 and 6.8.3.1.3).

- The constitutive relationships for Alloy 22 and Titanium Grade 7 are based on material properties in the published literature. More specifically, the Young's modulus, Poisson's ratio, yield strength, and friction factors are based on data in the published literature (see Section 4).

- The ground motion time histories for the rockfall and structural response analyses have been developed in a manner that is consistent with and builds upon the results of an expert elicitation (CRWMS M&O 1998 [DIRS 103731], Sections 5 and 6).

4. *Engineered barrier mechanical failure models for disruptive events are adequate. For example, these models may consider the effects of prolonged exposure to the expected emplacement drift environment, material test results not specifically designed or performed for the Yucca Mountain site, and engineered barrier component fabrication flaws.*

   Response: The potential failure modes of EBS components are analyzed in Section 6.2. Based on this discussion, accelerated SCC is the expected failure mechanism for EBS components resulting from a seismic event, rather than puncture or tearing at the ultimate tensile strain. The constitutive relationships for Alloy 22 and Titanium Grade 7 are based on material properties in the published literature. More specifically, the Young's modulus, Poisson's ratio, yield strength, and friction factors are based on data in the published literature (see Section 4).

Acceptance Criterion 3: Data Uncertainty Is Characterized and Propagated Through the Model Abstraction.

Data uncertainty is explicitly included in the mechanical assessment of degraded waste packages and drip shields subject to vibratory ground motion. Parameter uncertainty is included in the ground motion time histories that are direct inputs to the structural response analyses that provide the basis for the damage abstractions presented in *Seismic Consequence Abstraction* (SNL 2007 [DIRS 176828]). Uncertainty in the input parameters for the structural response calculations and rockfall analyses is described next, followed by information on subcriteria (1), (2), and (3) for this acceptance criterion.

Uncertainty in Input Parameters for Structural Response Analyses—The structural response analyses for the waste package and drip shield under vibratory ground motions include three major sources of uncertainty: (1) the ground motion time histories (aleatory uncertainty), (2) the metal-to-metal friction coefficient (epistemic uncertainty), and (3) the metal-to-rock friction coefficient (epistemic uncertainty).

Multiple three-component ground motion time histories are used to represent the uncertainty in the seismic forcing functions at PGV levels of 0.40 m/s, 1.05 m/s, 2.44 m/s, and 4.07 m/s. One horizontal component of each ground motion set is scaled to have the same horizontal PGV because its uncertainty has been incorporated into the hazard curves during the probabilistic seismic hazard analysis. The peak ground acceleration and the duration of the time histories span a wide range of response. For example, the peak ground acceleration for the first horizontal ground motion component at the 2.44 m/s PGV level ranges from about 1.5 g to 7 g.

The metal-to-metal friction coefficient between the waste package, drip shield, and emplacement pallet varies from 0.2 to 0.8 to represent the uncertainty in its value. The friction coefficient affects the onset of sliding and dissipation of energy for the EBS components as a function of the amplitude of the ground motion. The static and dynamic friction coefficients are taken to be equal within the broad range (0.2 to 0.8) defined for this parameter. However, the importance of static friction is anticipated to diminish with increasing ground motion level because the EBS components begin to slide almost immediately for high amplitude ground motions.

The metal-to-rock friction coefficient between the waste package and the invert, between the emplacement pallet and the invert, or between the drip shield and the invert varies from 0.2 to 0.8 to represent the uncertainty in its value. Again, the friction coefficient affects the onset of sliding and dissipation of energy for the unanchored EBS components as a function of the amplitude of the ground motion. However, the importance of friction is anticipated to diminish with increasing amplitude of the ground motions.

The selection of friction coefficients as major sources of uncertainty, in addition to the ground motions, is based on the potential for frictional forces to influence the kinematics of EBS components. Variability in ground motions is often the most significant uncertainty in structural response analyses for nuclear plant components. Variability of friction coefficients is important because impacts between adjacent components are affected by differences in friction values.

The variations of these uncertain input parameters are simultaneously included in the seventeen structural response analyses at each seismic hazard level. This is accomplished by a Latin Hypercube procedure that ensures robust sampling of the uncertain parameters over their full ranges (Sections 6.3.1, 6.4.4, and 6.5.1). The sampled values for the ground motion number and friction coefficients are documented in (BSC 2005 [DIRS 173172], Attachment X; DTN: MO0508SPAMECHA.000 [DIRS 181067], *AttachmentX.zip*, file *All_3_Sampling_Groups.txt*).

The results from the structural response analyses are postprocessed to determine the damaged areas on the drip shield or waste package. The seismic damage abstractions for the waste package and drip shield make use of a residual stress threshold as a failure criterion (Section 6.2). If the residual stress from mechanical damage exceeds the stress threshold for the barrier, then the affected area(s) are represented as a network of stress corrosion cracks. The residual stress threshold for the waste package is based on a uniform distribution between 90% and 105% of the yield strength for Alloy 22 (Sections 6.3.3 and 6.3.4). Postprocessing of the output from waste package analyses determines the damaged areas corresponding to 90%, 100%, and 105% of the yield strength of Alloy 22 (Section 6.3.4.1). The residual stress threshold for titanium is conservatively set to a constant value of 80% of the yield strength of Titanium Grade 7, so no uncertainty is propagated into TSPA-LA for damaged area on the drip shield from vibratory ground motion.

Uncertainty in Input Parameters for Rockfall Analyses—All rockfall analyses include the ground motion time histories as a major source of uncertainty (Sections 6.4 and 6.5). Seventeen ground motions represent the uncertainty in the seismic forcing functions at the 0.40 m/s, 1.05 m/s, 2.44 m/s, and 4.07 m/s PGV levels. The synthetic fracture pattern is an uncertain input parameter. The synthetic fracture pattern is a representation of the fracture system geometry in

three dimensions. The variations in these uncertain parameters are simultaneously included in the rockfall analyses at each seismic hazard level.

Rockfall analyses for the nonlithophysal units predict a wide range of block sizes and velocities that can be ejected from the drift walls and impact the drip shield. More specifically, each rockfall analysis for the nonlithophysal unit predicts a complex, time-dependent sequence of rock blocks that impact the drip shield at varying locations and velocities. These impacts can cause damage to the drip shield if the block has enough mass and kinetic energy.

Discussion for Subcriteria (1), (2), and (3)

1. *Models use parameter values, assumed ranges, probability distributions, and bounding assumptions that are technically defensible, reasonably account for uncertainties and variabilities, and do not result in an under-representation of the risk estimate.*

   Response: The above discussion directly addresses the technical defensibility, uncertainty, and variabilities in parameter values. Specific examples include:

   - Rockfall models and structural response analyses use parameter values and parameter ranges that are defensible and account for variabilities in rock properties and fracture patterns and uncertainties in ground motion time histories and friction coefficients.

   - A major uncertainty in the response of the lithophysal zone is the rock compressive strength. This parameter is sampled from five levels for the rockfall analyses.

   - Material properties for structural response analyses are based on a temperature of 60°C, resulting in a bounding temperature after the first 10,000 years postclosure, as discussed in Assumption 5.7, Section 5. Sensitivity analyses with material properties at elevated temperatures (Section 6.3.2.2.2) demonstrate that the damaged area of the OCB is relatively insensitive to elevated temperatures that occur during the first 10,000 years.

2. *Process-level models, used to represent mechanically disruptive events within the emplacement drifts at the proposed Yucca Mountain repository, are adequate. Parameter values are adequately constrained by Yucca Mountain site data, such that the effects of mechanically disruptive events on engineered barrier integrity are not underestimated. Parameters within conceptual models for mechanically disruptive events are consistent with the range of characteristics observed at Yucca Mountain.*

   Response: The LS-DYNA, FLAC3D, and UDEC codes are used to determine the mechanical response of EBS components to vibratory ground motion. LS-DYNA is used for the structural response analyses for the seismic scenario class (Sections 6.3.3 and 6.4.5). The analysis of rockfall for the seismic scenario class and for the nominal scenario class is based on state-of-the-art computer codes, including FLAC3D and UDEC, that can represent continuum and discontinuous response of rock in the lithophysal and nonlithophysal units of the repository (Sections 6.4 and 6.5). The appropriateness of the parameters within LS-DYNA and for the rockfall analyses with FLAC3D and UDEC are discussed in

underlying documents, such as *Drift Degradation Analysis* (BSC 2004 [DIRS 166107], Section 6.4.2) and are beyond the scope of this document.

3. *Uncertainty is adequately represented in parameter development for conceptual models, process-level models, and alternative conceptual models considered in developing the assessment abstraction of mechanical disruption of engineered barriers. This may be done either through sensitivity analyses or use of conservative limits.*

   Response: The discussion preceding subcriterion 1 directly addresses the incorporation of parameter uncertainty into the abstraction process. Specific examples include:

   - Material properties for structural response analyses are based on a temperature of 60°C, resulting in a bounding temperature after the first 10,000 years postclosure, as discussed in Assumption 5.7, Section 5. Sensitivity analyses with material properties at elevated temperatures (Section 6.3.2.2.2) demonstrate that the damaged area of the OCB is relatively insensitive to elevated temperatures that occur during the first 10,000 years.

   - Thicknesses of the waste package outer barrier and drip shield plates have been reduced by 2 mm to account for general corrosion over the first 10,000 years to 20,000 years after closure.

Acceptance Criterion 4: Model Uncertainty Is Characterized and Propagated Through the Model Abstraction.

2. *Consideration of conceptual model uncertainty is consistent with available site characterization data, laboratory experiments, field measurements, natural analog information and process-level modeling studies; and the treatment of conceptual model uncertainty does not result in an under-representation of the risk estimate.*

   Response: Conceptual model uncertainty has been incorporated into the models used in this report as discussed in Section 6.7. Conceptual model uncertainty for these models is due in large part to sparse observational data and a lack of available information to corroborate or refute plausible alternative interpretations of the processes occurring.

   The most significant uncertainties impacting the results of models of the mechanical assessment of waste packages and drip shields subject to vibratory ground motion are the uncertainties associated with the postclosure ground motions and with the time-dependent strength degradation of the EBS components. Some of the ground motions provided are larger than the largest ground motions observed and may not be physically realizable. Moreover, given the complexity of the modeling, and uncertainty of the inputs, such uncertainty is not unprecedented. Additional actions to assure that the treatment of conceptual model uncertainty does not result in an under-representation of risk in the results presented are as follows.

   - Model results have been validated by comparison to alternative numerical approaches (Sections 7.3.1, 7.3.2, and 7.3.3) and industry experience through external technical

review (Section 7.3.4 and Appendix E). These comparisons provide confidence that the uncertainty in the methods used in each of the models is similar to that found in alternative models appropriate for each analysis.

- Results for the kinematic analysis with multiple waste packages (Section 6.3) are presented for two waste package types and as a function of several parameters that are major sources of uncertainty. These include seismic intensity, waste package thickness, and condition of internals. In addition, multiple threshold criteria are used for evaluation of rupture. These parameters are all considered sources of uncertainty in this analysis.

- Results for the analysis of drip shield damage mechanisms and damage areas are presented as functions of drip shield thickness, seismic intensity and rockfall load (Sections 6.4.3 and 6.4.4). These parameters are considered sources of uncertainty for this analysis, and inputs have been chosen so that the risk estimate is not under-represented.

- Results for the kinematic analysis of waste package-to-drip shield impacts (Section 6.4.5) include analysis of impacts between five waste packages and the drip shield and are presented as a function of seismic intensity. These parameters are considered sources of uncertainty for this analysis, and inputs have been chosen so that the risk estimate is not under-represented.

- Results of the analysis of uneven settlement of the invert (Section 6.4.6) are provided for two different types of loading and for five different amounts of settlement. These parameters are considered sources of uncertainty for this analysis, and inputs have been chosen so that the risk estimate is not under-represented.

- Analysis of drip shield damage due to impact by large rock blocks (Section 6.4.7) provides results as a function of seismic intensity, block energy, and drip shield thickness. These parameters are considered sources of uncertainty for this analysis, and inputs have been chosen so that the risk estimate is not under-represented.

- Results for the analysis of the waste package surrounded by rubble after drip shield failure (Section 6.5.1) are given for different failure criteria and as a function of seismic intensity, waste package thickness, and rock-block pattern. These parameters are considered sources of uncertainty for this analysis, and inputs have been chosen so that the risk estimate is not under-represented.

- The analysis of the waste package loaded by the drip shield and rockfall after drip shield failure (Section 6.5.2) presents results as a function of waste package thickness and the state of internals. These parameters are considered sources of uncertainty for this analysis, and inputs have been chosen so that the risk estimate is not under-represented.

3. *Appropriate alternative modeling approaches* [are] *investigated that are consistent with available data and current scientific knowledge, and appropriately consider their results and limitations using tests and analyses that are sensitive to the processes modeled.*

   Response: Model results presented in this report have been validated by comparison to alternative numerical approaches (Sections 7.3.1, 7.3.2, and 7.3.3) and industry experience through external technical review (Section 7.3.4 and Appendix E). The alternative models used in these comparisons comprise appropriate alternative modeling approaches for the processes modeled in this report.

   - Comparison of results for the kinematic model for damage to the waste packages due to vibratory ground motion is made with two alternative modeling techniques in Section 7.3.1. Both alternative models used appropriate material properties and boundary conditions (including ground motion inputs) and showed sensitivity to the processes modeled. Results of the comparisons provide confidence that the uncertainty method used in this report is similar to that found in other models.

   - The model for waste package surrounded by rubble is formulated using the UDEC code, and in Section 7.3.2 results from similar models formulated using UDEC are compared with results from alternative models developed for similar purposes. A corroboration of results from the UDEC model with data acquired from a 2-m scale experiment conducted on a rock block with artificial fractures is also presented. These results provide confidence that the uncertainty in the UDEC method used in this report is similar to that found in other models.

   - Comparison of the modeling of deformation and damage of the drip shield under static and dynamic conditions with predictions made using two alternative models developed for similar purposes is presented in Section 7.3.3. These alternative models utilize two independent numerical formulations. Both alternative models used appropriate material properties and boundary conditions (including ground motion inputs) and showed sensitivity to the processes modeled. Results of the comparisons provide confidence that the uncertainty in the modeling method is similar to that found in other models used for similar purposes.

   - Alternative modeling approaches have been evaluated for the conceptual and computational models of lithophysal and nonlithophysal rock (BSC 2004 [DIRS 166107], Section 7.6.5 and 7.7.5), but discussion of these models is beyond the scope of this document.

Acceptance Criterion 5: Model Abstraction Output is Supported by Objective Comparisons.

(3) Well-documented procedures, that have been accepted by the scientific community to construct and test the mathematical and numerical models, are used to simulate mechanical disruption of engineered barriers.

Response: The damage models presented in Sections 6.3, 6.4 and 6.5, and verified in Section 7.3, are based on finite-element or distinct-element representations. These representations are standard engineering approaches for simulation of mechanical response to seismic events within the emplacement drifts. An independent technical review for model validation has been performed (Appendix E) for the damage models to ensure acceptance by the scientific and engineering community.

9. INPUTS AND REFERENCES

9.1 DOCUMENTS CITED

114107 AISC (American Institute of Steel Construction) 1995. *Manual of Steel Construction, Allowable Stress Design*. 9th Edition, 2nd Revision. Chicago, Illinois: American Institute of Steel Construction. TIC: 232994.

104317 ASM (American Society for Metals) 1980. *Properties and Selection: Stainless Steels, Tool Materials and Special-Purpose Metals*. Volume 3 of *Metals Handbook*. 9th Edition. Benjamin, D., ed. Metals Park, Ohio: American Society for Metals. TIC: 209801.

141615 ASM International 1990. *Properties and Selection: Nonferrous Alloys and Special-Purpose Materials*. Volume 2 of *ASM Handbook*. Formerly Tenth Edition, Metals Handbook. 5th Printing 1998. Materials Park, Ohio: ASM International. TIC: 241059.

158115 ASME (American Society of Mechanical Engineers) 2001. *2001 ASME Boiler and Pressure Vessel Code (includes 2002 addenda)*. New York, New York: American Society of Mechanical Engineers. TIC: 251425.

176967 ASME (American Society of Mechanical Engineers) 2005. "Materials." Section II of *2004 ASME Boiler and Pressure Vessel Code (includes 2005 Addenda)*. New York, New York: American Society of Mechanical Engineers. TIC: 256479.

103508 Avallone, E.A. and Baumeister, T., III, eds. 1987. *Marks' Standard Handbook for Mechanical Engineers*. 9th Edition. New York, New York: McGraw-Hill. TIC: 206891.

158781 Beavers, J.A.; Devine, T.M., Jr.; Frankel, G.S.; Jones, R.H.; Kelly, R.G.; Latanision, R.M.; and Payer, J.H. 2002. *Final Report, Waste Package Materials Performance Peer Review Panel, February 28, 2002*. Las Vegas, Nevada: Waste Package Materials Performance Peer Review Panel. ACC: MOL.20020614.0035.

168820 BSC (Bechtel SAIC Company) 2002. *Software Implementation Report for FLAC Version 4.0*. Document Number: 10167-SIR-4.0-00. Las Vegas, Nevada: Bechtel SAIC Company. ACC: MOL.20020925.0376.

168821 BSC 2002. *Software Implementation Report for FLAC3D Version 2.1*. Document Number: 10502-SIR-2.1-00. Las Vegas, Nevada: Bechtel SAIC Company. ACC: MOL.20020730.0346.

172041 BSC 2002. *Software Implementation Report for UDEC Version 3.1*. Document Number: 10173-SIR-3.1-00. Las Vegas, Nevada: Bechtel SAIC Company. ACC: MOL.20021105.0245.

166183 BSC 2003. *Scoping Analysis on Sensitivity and Uncertainty of Emplacement Drift Stability*. 800-K0C-TEG0-00600-000-000. Las Vegas, Nevada: Bechtel SAIC Company. ACC: ENG.20031125.0002.

170027 BSC 2004. *Development of Earthquake Ground Motion Input for Preclosure Seismic Design and Postclosure Performance Assessment of a Geologic Repository at Yucca Mountain, NV*. MDL-MGR-GS-000003 REV 01. Las Vegas, Nevada: Bechtel SAIC Company. ACC: DOC.20041111.0006; DOC.20051130.0003.

166107 BSC 2004. *Drift Degradation Analysis*. ANL-EBS-MD-000027 REV 03. Las Vegas, Nevada: Bechtel SAIC Company. ACC: DOC.20040915.0010; DOC.20050419.0001; DOC.20051130.0002; DOC.20060731.0005.

168993 BSC 2004. *Drip Shield Structural Response to Rock Fall*. 000-00C-SSE0-00300-000-00A. Las Vegas, Nevada: Bechtel SAIC Company. ACC: ENG.20040405.0019; ENG.20050817.0026.

169753 BSC 2004. *Mechanical Assessment of the Drip Shield Subject to Vibratory Motion and Dynamic and Static Rock Loading*. CAL-WIS-AC-000002 REV 00A. Las Vegas, Nevada: Bechtel SAIC Company. ACC: DOC.20041028.0004; DOC.20050830.0003.

170791 BSC 2004. *Structural Stability of a Drip Shield Under Quasi-Static Pressure*. 000-00C-SSE0-00500-000-00A. Las Vegas, Nevada: Bechtel SAIC Company. ACC: ENG.20040830.0032.

174715 BSC 2005. *Creep Deformation of the Drip Shield*. CAL-WIS-AC-000004 REV 0A. Las Vegas, Nevada: Bechtel SAIC Company. ACC: DOC.20050830.0007.

173433 BSC 2005. *EBS Radionuclide Transport Abstraction*. ANL-WIS-PA-000001 REV 02. Las Vegas, Nevada: Bechtel SAIC Company. ACC: DOC.20050825.0008.

173172 BSC 2005. *Mechanical Assessment of the Waste Package Subject to Vibratory Ground Motion*. CAL-WIS-AC-000001 REV 0B. Las Vegas, Nevada: Bechtel SAIC Company. ACC: DOC.20050823.0001; DOC.20050830.0005.

173247 BSC 2005. *Seismic Consequence Abstraction*. MDL-WIS-PA-000003 REV 02. Las Vegas, Nevada: Bechtel SAIC Company. ACC: DOC.20050829.0005.

177536 BSC 2006. *Technical Work Plan for Postclosure Waste Package Modeling and Testing.* TWP-WIS-MD-000017 REV 01. Las Vegas, Nevada: Bechtel SAIC Company. ACC: DOC.20060815.0001.

178693 BSC 2007. *Subsurface Geotechnical Parameters Report*. ANL-SSD-GE-000001 REV 00. Las Vegas, Nevada: Bechtel SAIC Company. ACC: ENG.20070115.0006.

103731 CRWMS M&O (Civilian Radioactive Waste Management System Management and Operating Contractor) 1998. *Probabilistic Seismic Hazard Analyses for Fault Displacement and Vibratory Ground Motion at Yucca Mountain, Nevada*. Milestone SP32IM3, September 23, 1998. Three volumes. Las Vegas, Nevada: CRWMS M&O. ACC: MOL.19981207.0393.

172418 Das, B.M. 1990. *Principles of Geotechnical Engineering*. 2nd Edition. Boston, Massachusetts: PWS-KENT Publishing Company. TIC: 256726.

178495 Davis, E.A. and Connelly, F.M. 1959. "Stress Distribution and Plastic Deformation in Rotating Cylinders of Strain-Hardening Material." *Journal of Applied Mechanics*, *26*, (1), 25-30. New York, New York: American Society of Mechanical Engineers. TIC: 258873.

161539 DeGrassi, G. 1992. *Review of the Technical Basis and Verification of Current Analysis Methods Used to Predict Seismic Response of Spent Fuel Storage Racks*. NUREG/CR-5912. Washington, D.C.: U.S. Nuclear Regulatory Commission. TIC: 253724.

118647 Dieter, G.E. 1976. *Mechanical Metallurgy*. 2nd Edition. Materials Science and Engineering Series. New York, New York: McGraw-Hill Book Company. TIC: 247879.

181350 DOE (U.S. Department of Energy) 2004. *Software Validation Report for: FLAC3D Version 2.14*. Document ID: 10502-SVR-2.14-00. Las Vegas, Nevada: U.S. Department of Energy, Office of Repository Development. ACC: MOL.20041108.0413.

174541 DOE 2005. *Software Validation Report (SVR) for: LS-DYNA SMP D V970.3858*. Document ID: 10300-SVR-970.3858-01-SGI-IRIX64 6.5. Las Vegas, Nevada: U.S. Department of Energy, Office of Repository Development. ACC: MOL.20050207.0007.

182051 DOE 2007. *Quality Assurance Requirements and Description*. DOE/RW-0333P, Rev. 19. Washington, D. C.: U.S. Department of Energy, Office of Civilian Radioactive Waste Management. ACC: DOC.20070717.0006.

178852 DOE 2007. *Software Validation Report (SVR) for: LS-DYNA 971.7600.398-00*. Document ID: 10300-SVR-971.7600.398-00 Intel Itanium2 Redhat Linux 4. Las Vegas, Nevada: U.S. Department of Energy, Office of Repository Development. ACC: MOL.20070122.0233.

178854 DOE 2007. *Software Validation Report for: km_impacts_pp 1.0*. Document ID: 11235-SVR-1.0-00 AMD Opteron Redhat Linux 4. Las Vegas, Nevada: U.S. Department of Energy, Office of Repository Development. ACC: MOL.20070118.0298.

178855 DOE 2007. *Software Validation Report for: km_impacts_pp 1.0*. Document ID: 11235-SVR-1.0-00 Intel Itanium2 Redhat Linux 4. Las Vegas, Nevada: U.S. Department of Energy, Office of Repository Development. ACC: MOL.20070118.0296.

178853 DOE 2007. *Software Validation Report for: LS-DYNA 971.7600.398-00*. Document ID: 10300-SVR-971.7600.398-00 AMD Opteron Redhat Linux 4. Las Vegas, Nevada: U.S. Department of Energy, Office of Repository Development. ACC: MOL.20070122.0235.

174693 DOE 2005. *Software Validation Report for GoldSim V8.02.500, Verification Copy*. Document ID: 10344-SVR-8.02-05-WIN2000. Las Vegas, Nevada: U.S. Department of Energy, Office of Repository Development. ACC: MOL.20050611.0048.

161776 Duncan, J.M.; Byrne, P.; Wong, K.S.; and Mabry, P. 1980. *Strength, Stress-Strain and Bulk Modulus Parameters for Finite Element Analyses of Stresses and Movements in Soil Masses*. UCB/GT/80-01. Berkeley, California: University of California, College of Engineering, Office of Research Services. TIC: 253873.

155373 Hallquist, J.O. 1998. *LS-DYNA, Theoretical Manual*. Livermore, California: Livermore Software Technology Corporation. TIC: 238997.

174198 Itasca Consulting Group 2005. *Itasca Software-Cutting Edge Tools for Computational Mechanics*. Minneapolis, Minnesota: Itasca Consulting Group. TIC: 257396.

160331 Itasca Consulting Group 2002. *Itasca Software–Cutting Edge Tools for Computational Mechanics*. Minneapolis, Minnesota: Itasca Consulting Group. TIC: 252592.

177025 Kokajko, L.E. 2005. "Pre-Licensing Evaluation of Key Technical Issue Agreements: Total System Performance Assessment and Integration 2.01, 2.02, 2.03, 2.04, and 2.07." Letter from L.E. Kokajko (NRC) to J.D. Ziegler (DOE/ORD), April 21, 2005, 0427055409, with enclosure. ACC: MOL.20050427.0113.

103337 Kramer, S.L. 1996. *Geotechnical Earthquake Engineering. Prentice-Hall International Series in Civil Engineering and Engineering Mechanics*. Hall, W.J., ed. Upper Saddle River, New Jersey: Prentice-Hall. TIC: 243891.

166841 Livermore Software Technology Corporation. 2003. *LS-DYNA Keyword User's Manual*. Version 970. Livermore, California: Livermore Software Technology Corporation. TIC: 254203.

178496 Manjoine, M.J. 1983. "Damage and Failure at Elevated Temperature." *Transactions of the ASME*, *105*, 58-62. New York, New York: American Society of Mechanical Engineers. TIC: 258853.

157883 Marachi, N.D.; Chan, C.K.; and Seed, H.B. 1972. "Evaluation of Properties of Rockfill Materials." *Journal of the Soil Mechanics and Foundations Division, Proceedings of the American Society of Civil Engineers*, *98*, (SM1), 95-114. New York, New York: American Society of Civil Engineers. TIC: 252235.

157510 McGuire, R.K.; Silva, W.J.; and Costantino, C.J. 2001. *Technical Basis for Revision of Regulatory Guidance on Design Ground Motions: Hazard- and Risk-Consistent Ground Motion Spectra Guidelines*. NUREG/CR-6728. Washington, D.C.: U.S. Nuclear Regulatory Commission. TIC: 251294.

178497 NNSA (National Nuclear Security Administration) 2005. *Design and Development Guide for NNSA Type B Packages*. SG1-00, Rev. 2. Albuquerque, New Mexico: U.S. Department of Energy, National Nuclear Security Administration. ACC: MOL.20070220.0128.

159538 NRC (U.S. Nuclear Regulatory Commission) 2002. *Integrated Issue Resolution Status Report*. NUREG-1762. Washington, D.C.: U.S. Nuclear Regulatory Commission, Office of Nuclear Material Safety and Safeguards. TIC: 253064.

163274 NRC (U.S. Nuclear Regulatory Commission) 2003. *Yucca Mountain Review Plan, Final Report*. NUREG-1804, Rev. 2. Washington, D.C.: U.S. Nuclear Regulatory Commission, Office of Nuclear Material Safety and Safeguards. TIC: 254568.

181340 Popov, E.P. 1968. *Introduction to Mechanics of Solids*. Civil Engineering and Engineering Mechanics Series. Englewood Cliffs, New Jersey: Prentice-Hall. TIC: 244870.

178492 Rebak, R.B.; Summers, T.S.E.; and Carranza, R.M. 1999. *Mechanical Properties, Microstructure and Corrosion Performance of C-22 Alloy Aged at 260°C to 800°C*. UCRL-ID-136425. Livermore, California: Lawrence Livermore National Laboratory. ACC: MOL.20010529.0185.

162017 Senseny, P.E. 1993. "Stress Wave Loading of a Tunnel: A Benchmark Study." *Dynamic Analysis and Design Considerations for High-Level Nuclear Waste Repositories, Proceedings of the Symposium Sponsored by the Nuclear Dynamic Analysis Committee of the Structural Division of the American Society of Civil Engineers and Co-sponsored by the U.S. Department of Energy, Office of Civilian Radioactive Waste Management, San Francisco, California, August 19-20, 1992*. Hossain, Q.A., ed. Pages 311-338. New York, New York: American Society of Civil Engineers. TIC: 206451.

168479 Senseny, P.E. and Pucik, T.A. 1999. "Development and Validation of Computer Models for Structures in Jointed Rock." *International Journal for Numerical and Analytical Methods in Geomechanics*, *23*, (8), 751-778. New York, New York: John Wiley & Sons. TIC: 253795.

181383 SNL (Sandia National Laboratories) 2007. *Multiscale Thermohydrologic Model*. ANL-EBS-MD-000049 REV 03 AD01. Las Vegas, Nevada: Sandia National Laboratories. ACC: DOC.20050711.0001.

176828 SNL 2007. *Seismic Consequence Abstraction*. MDL-WIS-PA-000003 REV 03. Las Vegas, Nevada: Sandia National Laboratories.

177417 SNL 2007. *Stress Corrosion Cracking of Waste Package Outer Barrier and Drip Shield Materials*. ANL-EBS-MD-000005 REV 03. Las Vegas, Nevada: Sandia National Laboratories. ACC: DOC.20070530.0012.

179869 SNL 2007. *Technical Work Plan for: Calculation of Waste Package and Drip Shield Response to Vibratory Ground Motion and Revision of the Seismic Consequence Abstraction*. TWP-MGR-GS-000004 REV 01 ICN 02. Las Vegas, Nevada: Sandia National Laboratories. ACC: DOC.20070416.0003.

179354 SNL 2007. *Total System Performance Assessment Data Input Package for Requirements Analysis for EBS In-Drift Configuration*. TDR-TDIP-ES-000010 REV 00. Las Vegas, Nevada: Sandia National Laboratories.

179466 SNL 2007. *Total System Performance Assessment Data Input Package for Requirements Analysis for Subsurface Facilities*. TDR-TDIP-PA-000001 REV 00. Las Vegas, Nevada: Sandia National Laboratories.

179394 SNL 2007. *Total System Performance Assessment Data Input Package for Requirements Analysis for TAD Canister and Related Waste Package Overpack Physical Attributes Basis for Performance Assessment*. TDR-TDIP-ES-000006 REV 00. Las Vegas, Nevada: Sandia National Laboratories.

179567 SNL 2007. *Total System Performance Assessment Data Input Package for Requirements Analysis for DOE SNF/HLW and Navy SNF Waste Package Overpack Physical Attributes Basis for Performance Assessment*. TDR-TDIP-ES-000009 REV 00. Las Vegas, Nevada: Sandia National Laboratories.

157726 TIMET 1993. First in Titanium Worldwide, Quality Products and Services. Denver, Colorado: Titanium Metals Corporation. TIC: 242692.

160688 TIMET. 2000. "Timetal 6-4, 6-4 ELI, 6-4-.1Ru Medium to High Strength General-Purpose Alloys." Denver, Colorado: Titanium Metals Corporation. Accessed August 26, 2002. TIC: 253102. http://www.timet.com/pdfs/6-4.pdf

178494 Zabotkin, K.; O'Toole, B.; and Trabia, M. 2003. "Identification of the Dynamic Tensile Properties of Metals Under Moderate Strain Rates." *16th ASCE Engineering Mechanics Conference, July 16-18, 2003, University of Washington, Seattle, Washington*. New York, New York: American Society of Civil Engineers. TIC: 259107.

9.2 CODES, STANDARDS, REGULATIONS, AND PROCEDURES

180319 10 CFR 63. 2007. Energy: Disposal of High-Level Radioactive Wastes in a Geologic Repository at Yucca Mountain, Nevada. Internet Accessible.

162726 ASTM B 265-02. 2002. *Standard Specification for Titanium and Titanium Alloy Strip, Sheet, and Plate.* West Conshohocken, Pennsylvania: American Society for Testing and Materials. TIC: 254000.

103515 ASTM G 1-90 (Reapproved 1999). 1999. *Standard Practice for Preparing, Cleaning, and Evaluating Corrosion Test Specimens.* West Conshohocken, Pennsylvania: American Society for Testing and Materials. TIC: 238771.

IM-PRO-002. *Control of the Electronic Management of Information.*

IM-PRO-003, *Software Management.*

SCI-PRO-002, *Planning for Science Activities.*

SCI-PRO-003, *Document Review.*

SCI-PRO-004, *Managing Technical Product Inputs.*

SCI-PRO-006, *Models*.

SO-PRO-001, *Peer Review.*

9.3 SOURCE DATA, LISTED BY DATA TRACKING NUMBER

148850 MO0003RIB00071.000. Physical and Chemical Characteristics of Alloy 22. Submittal date: 03/13/2000.

152926 MO0003RIB00073.000. Physical and Chemical Characteristics of Ti Grades 7 and 16. Submittal date: 03/13/2000.

168891 MO0403AVDSC106.001. Acceleration, Velocity, and Displacement Time Histories for the Repository Level at 10-6 Annual Exceedance Frequency. Submittal date: 03/09/2004.

168892 MO0403AVTMH107.003. Acceleration, Velocity, and Displacement Time Histories for the Repository Level at 10-7 Annual Exceedance Frequency. Submittal date: 03/22/2004.

170873 MO0407MWDDSLCR.000. Drip Shield Load in Collapsed Lithophysal Rock. Submittal date: 07/21/2004.

171483 MO0408MWDDDMIO.002. Drift Degradation Model Inputs and Outputs. Submittal date: 08/31/2004.

179984 MO0508SPACREEP.000. Inputs and Outputs for the Creep Deformation of the Drip Shield. Submittal date: 08/26/2005.

181067 MO0508SPAMECHA.000. Inputs and Outputs for the Mechanical Assessment of the Waste Package Subject to Vibratory Motions. Submittal date: 08/16/2005.

178664 MO0610AVDTM105.002. Acceleration, Velocity, and Displacement Time Histories for the Repository Level at 10-5 Annual Exceedance Frequency. Submittal date: 10/10/2006.

179925 MO0702PASTREAM.001. Waste Stream Composition and Thermal Decay Histories for LA. Submittal date: 02/15/2007.

180514 MO0702PASTRESS.002. Output DTN of Model Report, "Stress Corrosion Cracking of Waste Package Outer Barrier and Drip Shield Materials," ANL-EBS-MD-000005. Submittal date: 04/24/2007.

182878 MO0703PASDSTAT.001. Statistical Analyses for Seismic Damage Abstractions. Submittal date: 09/05/2007.

182188 SN0704PADSGCMT.002. Drip Shield General Corrosion Rate Multiplier for Titanium Grade 29. Submittal date: 07/27/2007.

9.4 OUTPUT DATA, LISTED BY DATA TRACKING NUMBERS

LL0702PA055SPC.002. LS-DYNA Single Waste Package Damaged Area Analyses for the TAD-Bearing Waste Package. Submittal date: 02/21/2007.

LL0703PA007SPC.005. LS-DYNA Single Waste Package Damaged Area Analyses for the 5-DHLW/DOE SNF-Long Co-Disposal Waste Package. Submittal date: 03/06/2007.

LL0703PA029SPC.014. Rupture Probability for the LS-DYNA Kinematic Analyses for the 5-DHLW/DOE SNF-Long Codisposal Waste Package and the TAD-Bearing Waste Package. Submittal date: 03/14/2007.

LL0703PA031SPC.015. LS-DYNA Waste Package-to-Pallet Temperature Sensitivity Analyses. Submittal date: 04/19/2007.

LL0704PA048SPC.023. LS-DYNA Kinetic Damaged Area Analyses for the TAD-Bearing Waste Package April 2007. Submittal date: 05/01/2007.

LL0704PA049SPC.024. LS-DYNA Kinetic Damaged Area Analyses for the 5-DHLW/DOE SNF-Long Co-Disposal Waste Package April 2007. Submittal date: 05/01/2007.

LL0704PA050SPC.025. LS-DYNA Kinematic Waste Package-to-Drip Shield Analyses. Submittal date: 05/01/2007.

LL0704PA051SPC.026. Figures for 2007 Seismic Post-Closure Mechanical Assessment AMR. Submittal date: 05/01/2007.

LL0705PA010SPC.027. LS-DYNA 13 Waste Package Validation Analysis. Submittal date: 05/07/2007.

LL0706MG004SPC.001. Peak Acceleration of Waste Package Internals from Impacts with Waste Packages and Pallets. Submittal date: 06/06/2007.

MO0611ROCKFALL.000. Seismic Rockfall Analysis for Emplacement Drifts in Lithophysal Rock Mass Subject to Various Vibratory Ground Motion Levels. Submittal date: 11/28/2006.

MO0611WPRUBBLE.000. Input and Output Files for Analysis of the Waste Package Surrounded by Rubble Subjected to Seismic Ground Motion. Submittal date: 11/27/2006.

MO0701DRIPSHLD.000. The Input Data and Results of Analysis of the Drip Shield Plate and Framework Fragility, Drip Shield Failure Modes, Effects of Uneven Invert Settlement on Drip Shield Stability, and Deformation and Damage of the Waste Package Loaded by Collapsed Drip Shield. Submittal date: 01/15/2007.

MO0702POSTRUBB.000. Post-Processing Results for Analysis of the Waste Package Surrounded by Rubble Subjected to Seismic Ground Motion. Submittal date: 02/20/2007.

MO0703PADSBLOC.000. Drip Shield Damage Due to Block Impact and Distributed Loading. Submittal date: 03/09/2007.

MO07043DWPFAIL.000. Three-Dimensional Effects on Waste Package Failure Modes and Loads. Submittal date: 04/25/2007.

MO0704DSFLAC3D.000. FLAC3D Input and Output Files from Analysis of Vertical Rock Block Impact into the Drip Shield. Submittal date: 04/09/2007.

MO0704PUNCTURE.000. Puncture Probability for the Outer Corrosion Barrier of the TAD-Bearing Waste Package When the Package Surrounded with Rubble and with Degraded Internals is Subjected to Strong Seismic Ground Motions. Submittal date: 04/25/2007.

MO0704SIPAWPSR.000. Sampling of Input Parameters for the Analysis of Waste Package Surrounded by Rubble. Submittal date: 04/18/2007.

MO0705DEFCONFG.000. Comparison of Predicted Deformed Drip Shield Configurations Obtained Using LS-DYNA and FLAC3D. Submittal date: 05/04/2007.

MO0705FLAC3DMT.000. Input and Output Data from FLAC3D Analysis of 3.3 mT Block Impact into the Drip Shield. Submittal date: 05/04/2007.

MO0705IMPACTST.000. State During Impact of 7.49-mT Rock Block at 4.81 m/s into Drip Shield Configuration with 15-mm-Thick Plates. Submittal date: 05/08/2007.

MO0705NDSSTATE.000. State of the Naval Long Waste Package with Degraded Internals Loaded by Collapsed Drip Shield at Average Pressure of 486 kPa. Submittal date: 05/08/2007.

MO0705UDECMECH.000. UDEC Results of Mechanical Interaction of 13 Waste Packages Subject to Ground Motion at 5.35 m/s PGV. Submittal date: 05/03/2007.

9.5 SOFTWARE CODES

161953 FLAC V. 4.0. 2002. WINDOWS 2000/NT 4.0. STN: 10167-4.0-00.

161947 FLAC3D V. 2.1 Sub Release 2.10.196. 2002. WINDOWS 2000/NT 4.0. STN: 10502-2.1-00.

172323 FLAC3D V. 2.14. 2004. WINDOWS 2000. STN: 10502-2.14-00.

174650 GoldSim V. 8.02.500. 2005. WINDOWS 2000. STN: 10344-8.02-05.

178489 km_impacts_pp V1.0. 2007. RedHat Linux 4. STN: 11235-1.0-00.

172925 LS-DYNA SMP D V. 970.3858. 2005. OSF1 V5.1. STN: 10300-970.3858-02.

178801 LS-DYNA V971.7600.398-00. 2007. RedHat Linux Chaos 3.0. STN 10300-971.7600.398-00.

161949 UDEC V. 3.1 Sub-Release 3.10.109. 2002. WINDOWS 2000/NT 4.0. STN: 10173-3.1-00.

INTENTIONALLY LEFT BLANK

APPENDIX A
MATERIAL PROPERTIES OF TITANIUM GRADES 7 AND 24, ALLOY 22, AND STAINLESS STEEL TYPE 316 AT 60°C AND USE OF A KNOCKDOWN FACTOR TO REPRESENT THE EFFECTS OF TRIAXIALITY AND STRAIN RATE ON ULTIMATE TENSILE FAILURE OF ALLOY 22

APPENDIX A – MATERIAL PROPERTIES OF TITANIUM GRADES 7 AND 24, ALLOY 22, AND STAINLESS STEEL TYPE 316 AT 60°C AND USE OF A KNOCKDOWN FACTOR TO REPRESENT THE EFFECTS OF TRIAXIALITY AND STRAIN RATE ON ULTIMATE TENSILE FAILURE OF ALLOY 22

A1. TITANIUM PROPERTIES AT 60°C

Temperature-dependent mechanical properties of Titanium Grade 7 and Titanium Grade 24 have been derived at 60°C by linear interpolation. The material property data and temperatures used in the interpolations are given in Tables A-1 and A-2 below. The tables also give the data sources and additional equations used to calculate certain properties. Room temperature values of density and Poisson's ratio, used in the UDEC calculations, are also given in the tables. The properties calculated for 60°C include:

For Titanium Grade 7:

Modulus of elasticity E = 105 GPa
Ultimate tensile strength σ_u = 396 MPa
Yield strength σ_y = 316 MPa
Ultimate true elongation ε_u = 22%.

For Titanium Grade 24:

Modulus of elasticity E = 112 GPa
Ultimate tensile strength σ_u = 1,121 MPa
Yield strength σ_y = 862 MPa
Elongation in two inches e_u = 18%.

Table A-1. Mechanical Properties of Titanium Grade 7 (SB-265 R52400) Used in the UDEC Calculations

Properties	Temperatures (°C/°F)				Source
	21/70	60/140	93/200	204/400	
Density ρ (kg/m^3)	4,520	–	–	–	DTN: MO0003RIB00073.000 [DIRS 152926], p. 2
Poisson's ratio ν	0.32	–	–	–	DTN: MO0003RIB00073.000 [DIRS 152926], p. 3
Young's modulus E (MPa)	106,870	105,001 (interpolated)	103,420	96,530	DTN: MO0003RIB00073.000 [DIRS 152926], p. 3
Yield strength σ_y (MPa)	363	316 (interpolated)	–	145	DTN: MO0003RIB00073.000 [DIRS 152926], p. 2
Ultimate engineering elongation e_u	0.20	0.25 (interpolated)	–	0.42	DTN: MO0003RIB00073.000 [DIRS 152926], p. 2
Ultimate true elongation ε_u [a]	0.18	0.22	–	0.35	$\varepsilon_u = \ln(1+e_u)$ Dieter 1976 [DIRS 118647], p. 337

Table A-1. Mechanical Properties of Titanium Grade 7 (SB-265 R52400) Used in the UDEC Calculations (Continued)

Properties	Temperatures (°C/°F)				Source
	21/70	60/140	93/200	204/400	
Engineering tensile strength s_u (MPa)	345	318 (interpolated)	–	218	DTN: MO0003RIB00073.000 [DIRS 152926], p. 2
True tensile strength σ_u (MPa)[a]	414	396	–	308	$\sigma_u = s_u(1+e_u)$ Dieter 1976 [DIRS 118647], p. 339
Tangent modulus E_t (MPa)[a]	288	368	–	471	$E_t = \frac{\sigma_u - \sigma_y}{\varepsilon_u - \sigma_y / E}$

[a] Values are not interpolated but are calculated using the formulas in "Source" column and available properties at 60°C.

NOTE: Interpolation conducted between two closest available temperatures. When range is provided in the source, the average value is used. Dieter (1976 [DIRS 118647], pp. 337 to 339) is the source of the equations rather than a data source.

Table A-2. Mechanical Properties of Titanium Grade 24 (SB-265 R56405) Used in the UDEC Calculations

Properties	Temperatures (°C/°F)				Source
	21/70	60/140	93/200	204/400	
Density ρ (kg/m^3)	4,430	–	–	–	ASM 1990 [DIRS 141615], p. 620
Poisson's ratio ν	0.34	–	–	–	ASM 1990 [DIRS 141615], p. 621
Young's modulus E (MPa)	114,500	112,377 (interpolated)	–	103,000	TIMET 2000 [DIRS 160688], Table 2
Yield strength σ_y (MPa)	910	862 (interpolated)	683	–	TIMET 1993 [DIRS 157726], p. 11
Ultimate engineering elongation e_u	0.180	0.178 (interpolated)	0.17	–	TIMET 1993 [DIRS 157726], p. 11
Ultimate true elongation ε_u [a]	0.166	0.164	0.16	–	$\varepsilon_u = \ln(1+e_u)$ Dieter 1976 [DIRS 118647]
Engineering tensile strength s_u (MPa)	1,000	951 (interpolated)	772	–	TIMET 1993 [DIRS 157726], p. 11
True tensile strength σ_u (MPa)[a]	1,180	1,121	903	–	$\sigma_u = s_u(1+e_u)$ Dieter 1976 [DIRS 118647]
Tangent modulus E_t (MPa)[a]	1,714	1,660	–	–	$E_t = \frac{\sigma_u - \sigma_y}{\varepsilon_u - \sigma_y / E}$

[a] Values are not interpolated but are calculated using the formulas in "Source" column and available properties at 60°C.

NOTE: Interpolation conducted between two closest available temperatures. When range is provided in the source, the average value is used. Dieter (1976 [DIRS 118647], pp. 337 to 339) is the source of the equations rather than a data source.

A2. ALLOY 22 PROPERTIES AT 60°C

Mechanical properties of Alloy 22 at 60°C have been derived for temperature-dependent properties (DTN: MO0003RIB00071.000 [DIRS 148850], Table S04196_001) by linear interpolation. The properties for ¼-in to ¾-in plate are used for yield strength, ultimate tensile strength, and elongation in 2 in. The properties at room temperature (assumed to be 24°C) are:

Modulus of elasticity E = 29.9x10^6 psi (206 GPa)
Ultimate tensile strength s_u = 114 ksi (786 MPa)
Yield strength σ_y = 54 ksi (372 MPa)
Elongation in two inches e_u = 62%.

The properties at 93°C are:

Modulus of elasticity E = 29.4x10^6 psi (203 GPa)
Ultimate tensile strength s_u = 107 ksi (738 MPa)
Yield strength σ_y = 49 ksi (338 MPa)
Elongation in two inches e_u = 65%.

The properties computed for 60°C by interpolation are:

Modulus of elasticity E = 29.6x10^6 psi (204 GPa)
Ultimate tensile strength s_u = 110 ksi (758 MPa)
Yield strength σ_y = 51 ksi (350 MPa)
Elongation in two inches e_u = 64%.

After accounting for knockdowns in effective strain at failure, as discussed below, a tangent modulus of 282 ksi (1.94 GPa) was chosen to approximate the behavior of Alloy 22 in the plastic region. This tangent modulus reasonably approximates the true stress-strain relationship in the range of strain that encompasses the effective strain at failure after reduction.

Factors Affecting Material Properties of Alloy 22

Factors that can affect material properties and material response are: temperature, welding, cold work, residual stress, aging, radiation damage, and strain rate.

The material properties are determined for 60°C, so temperature effects are accounted for.

Solution heat treatment of the outer corrosion barrier will eliminate precipitates formed during welding and stress-relieve the shell. It is expected that the finished shell will have uniform material properties (i.e., welding, cold work) and that residual stresses will not affect the material properties.

If Alloy 22 is subjected to elevated temperatures (over 600°C) for times on the order of 1,000 hours, a molybdenum-rich precipitate will form. This aging process is accompanied by loss of toughness and reduced corrosion resistance. The waste packages are not expected to experience temperatures above 300°C. However, the aging process is active even at room temperature—the process just requires considerable time. When aged at temperatures of about 260°C for about 1,000 hours, Alloy 22 is observed to undergo long-range ordering. The long-range ordering was found (Rebak et al. 1999 [DIRS 178492]) not to adversely affect chemical resistance in laboratory tests, and Arrhenius extrapolations suggest that the alloy will be thermally stable when exposed to temperatures around 300°C for 10,000 years. Aging will not affect material properties.

Radiation damage is not expected to alter the mechanical properties of Alloy 22 (*Final Report, Waste Package Materials Performance Peer Review Panel, February 28, 2002* (Beavers et al. 2002 [DIRS 158781], Section 3.10)).

During extreme seismic events, the waste packages are predicted by finite-element representations to impact other waste packages, pallets, and drip shields. The finite-element representations indicate that strain rates up to 150 s^{-1} are possible during impacts. Zabotkin et al. (2003 [DIRS 178494]) discuss the dependence of Alloy 22 material properties on strain rates up to 200 s^{-1}. As the strain rate increases from 10^{-4} s^{-1} to 200 s^{-1}, the changes in material properties are:

Yield strength: +50%
Ultimate tensile strength: +14.5%
Elongation in two inches: −11%.

It is conservative to assume the quasi-static values of yield strength and ultimate tensile strength, as those values increase with strain rate.

Predicting Ultimate Tensile Failure of Alloy 22

Davis and Connelly (1959 [DIRS 178495], p. 29) proposed a triaxiality factor to measure the ductility of a material, given in Equation A-1:

$$TF = \sqrt{2}\ \frac{(Octahedral\ Normal\ Stress)}{(Octahedral\ Shear\ Stress)} = \frac{\sqrt{2}(\sigma_1 + \sigma_2 + \sigma_3)}{\sqrt{[(\sigma_1 - \sigma_2)^2 + (\sigma_2 - \sigma_3)^2 + (\sigma_3 - \sigma_1)^2]}} \quad \text{(Eq. A-1)}$$

Manjoine (1983 [DIRS 178496], pp. 58 to 62) found that the elongation measured in a tensile test could be adjusted to predict failure under multi-axial stress states using the relation shown in Equation A-2:

$$\varepsilon_f/e_t = (2^{1-TF}) \text{ for } TF > 0, \text{ and } \varepsilon_f/e_t = 2 \text{ for } TF < 0 \quad \text{(Eq. A-2)}$$

where:

ε_f/e_t is the ductility ratio
ε_f is the effective strain at failure
e_t is the tensile elongation measured in tensile tests
TF is the triaxiality factor.

The effective strain is defined as:

$$\bar{\varepsilon} = \frac{\sqrt{2}}{3}\sqrt{[(\varepsilon_1 - \varepsilon_2)^2 + (\varepsilon_2 - \varepsilon_3)^2 + (\varepsilon_3 - \varepsilon_1)^2]}\,.$$

"Development of Alternate Structural Acceptance Criteria Guidance" (NNSA 2005 [DIRS 178497], Appendix M) discusses the use of Manjoine's method in analyzing containment boundaries. Figure A-1 illustrates the variation of triaxiality factor with ductility ratio.

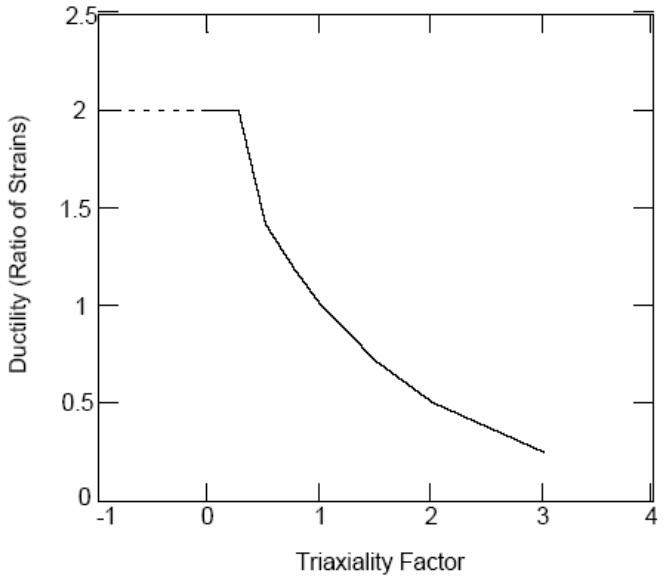

Source: NNSA 2005 [DIRS 178497], Figure M-1, Appendix M.

Figure A-1. Ductility Ratio vs. Triaxiality Factor

A triaxiality factor of 1.0, which corresponds to uniaxial tension, has a ductility ratio of 1.0. Negative values of triaxiality correspond to compressive stress states and have ductility ratio equal to 2.0. Stress states that have hydrostatic tension components have ductility ratios less than 1.0 and triaxiality factors greater than 1.0. For a case of biaxial tension (equal or unequal tension in two principal directions and zero stress in the third), the triaxiality factor can be as high as 2.0 and the ductility ratio can be as low as 0.5.

Manjoine's method can be adapted for use in predicting failure with seismic impact analyses. Two approaches are discussed: the first is a direct application of Manjoine's method; the second is a simplified approach, developed from Manjoine's method that takes advantage of the specific geometry being considered for the EBS components.

Postprocessing databases of most structural analysis codes include the information required to calculate the triaxiality factor and effective strain. It is often possible, using either a commercial postprocessing code or a special-purpose routine written by the user, to evaluate Equation A-2 for all elements and times in the database. Equation A-2 defines the boundary between "failed" material and "intact" material. The postprocessing method should make note of any excursion into the "failed" region.

A simplified failure criterion can be developed from Manjoine's method if one can assert that an upper bound on the triaxiality factor exists for the type of problem being investigated. Waste packages may be thought of as closed cylindrical shells. The lid and bottom of the waste packages are fairly stiff; impacts in these regions tend to cause a large compressive stress normal to the surface of the waste package. The surrounding material will provide confinement and produce compressive stress in the other two directions. This stress state corresponds to a very low triaxiality factor. When the impact is past, the surface of the waste package will be traction-free. Residual tensile stresses are possible in the other two directions. This will, at worst, correspond to a biaxial state of stress with triaxiality factor of 2.0. Impacts at less stiff regions such as shell walls or the center of a lid will tend to cause geometric changes that cause large shell or plate stresses to develop. These cases will also, at worst, correspond to a biaxial state of stress with triaxiality factor of 2.0. Therefore, a conservative estimate for the maximum value of the triaxiality factor is 2.0 for the seismic impact analyses. Manjoine's method, then, suggests that failure occurs when the effective strain predicted by the finite element codes reaches one-half the tensile elongation.

Recall that finite-element representations indicate that strain rates up to 150 s^{-1} are possible during impacts, and that Zabotkin et al. (2003 [DIRS 178494]) have indicated that the tensile elongation of Alloy 22 decreases by 11% as strain rate increases from 10^{-4} s^{-1} to 200 s^{-1}. In order to account for strain-rate effects, the tensile elongation is estimated to be 57% (64% elongation for quasi-static tensile tests reduced 11% for strain rates up to 200 s^{-1}). This value should be used with Equation A-1 for assessing failure. If the simplified approach is used, failure can be assumed to occur when the effective strain predicted by the finite element codes reaches 0.285.

As a practical matter, it is easier to look at effective plastic strain than effective strain. Effective plastic strain is a scalar that is stored as a history variable in most post-processing databases. Effective plastic strain *can* be slightly lower than effective strain by an amount roughly corresponding to the elastic strain. For a ductile material like Alloy 22, this difference is not significant. At times, the effective plastic strain can be much larger than the effective strain. This is because the effective plastic strain is a sum of all increments of plastic strain, including strain reversals. Effective strain is a function of the current strain state. Given that the effective plastic strain is approximately equal to, or greater than, the effective strain, a value of 28.5% is determined for the effective strain threshold for Alloy 22. This analysis provides a conservative

threshold for the effective strain to determine whether rupture has occurred. This is because using the effective plastic strain is conservative compared to the effective strain.

It must be pointed out that analyses using the methods outlined above cannot be used to infer postfailure behavior of waste packages.

A3. STAINLESS STEEL TYPE 316 PROPERTIES

Mechanical properties of Stainless Steel Type 316 at 60°C have been derived from temperature-dependent properties provided in *2004 ASME Boiler and Pressure Vessel Code* (ASME 2005 [DIRS 176967], Section II, Materials). This manual provides the modulus of elasticity (Part D, Subpart 2, Table TM-1), ultimate tensile strength (Part D, Subpart 1, Table U) and yield strength (Part D, Subpart 1, Table Y-1) with temperature dependence, so the values at 60°C are computed by linear interpolation. The elongation in 2 in (Part A, SA-240/SA-240M, Table 2) is only provided at room temperature. These properties are the minimum allowable properties for Stainless Steel Type 316. Thus, it is conservative to use these properties. The temperature-dependent elastic moduli are:

Modulus of elasticity E at 21°C = 28.3 x10^6 psi (195 GPa)
Modulus of elasticity E at 93°C = 27.5 x10^6 psi (190 GPa).

The temperature-dependent ultimate tensile strengths are:

Ultimate tensile strength s_u at 38°C = 75.0 ksi (517 MPa)
Ultimate tensile strength s_u at 93°C = 75.0 ksi (517 MPa).

The temperature-dependent yield strengths are:

Yield strength σ_y at 38°C = 30.0 ksi (207 MPa)
Yield strength σ_y at 66°C = 27.4 ksi (189 MPa).

The properties computed for 60°C by interpolation are:

Modulus of elasticity E = 27.9 x10^6 psi (192 GPa)
Ultimate tensile strength s_u = 75.0 ksi (517 MPa)
Yield strength σ_y = 28.0 ksi (193 MPa).

The elongation in 2 inches e_u at room temperature is 40%.

The effective strain at failure of Stainless Steel Type 316 is not directly used in the analyses, and, as noted, the reported elongation is actually the minimum allowable value for Stainless Steel Type 316, so it is not necessary to consider knockdowns for temperature, strain rate, and triaxiality in order to determine a reasonable tangent modulus. A tangent modulus of 229 ksi (1.58 GPa) was chosen to approximate the behavior of Stainless Steel Type 316 in the plastic region. This is based on the yield strength, ultimate strength and elongation. The slope between the yield strength and the true ultimate strength at the true ultimate strain is the tangent modulus.

INTENTIONALLY LEFT BLANK

APPENDIX B
TWO-DIMENSIONAL REPRESENTATIONS OF THE DRIP SHIELD AND WASTE PACKAGE IN ANALYSIS OF DRIP-SHIELD FAILURE MODES

APPENDIX B – TWO-DIMENSIONAL REPRESENTATIONS OF THE DRIP SHIELD AND WASTE PACKAGE IN ANALYSIS OF DRIP-SHIELD FAILURE MODES

B1. INTRODUCTION

Cross sections of structures in two-dimensional analyses are implicitly rectangular. Although longitudinal cross sections of the drip shield are not rectangular, the analysis of deformation and collapse of the drip shield (Section 6.4.3.2) indicates that the drip shield deforms as a two-dimensional structure. Therefore, drip shield deformation and collapse can be analyzed in a two-dimensional approximation. Geometrical and mechanical characteristics of two-dimensional approximations of the drip shield cross sections (used in the analysis documented in Section 6.4.4) are determined from the condition that the two-dimensional approximation has a bending moment equal to or smaller than the bending moment of the approximated cross section for the given curvature. The same criterion was used to calculate mechanical properties of the numerical representation of the waste package with increased OCB wall thickness. The OCB wall thickness in the numerical representation was increased compared to the actual thickness in the analysis of the drip shield failure modes, documented in Section 6.4.4, in order to increase the calculation critical time step.

B2. GENERAL APPROACH

The first step in approximating an arbitrarily shaped cross section using a rectangular, two-dimensional cross section is to develop moment-curvature diagrams for the original cross section. Both the moment and the curvature can be expressed in terms of the maximum strain in the cross section. If the maximum strain in the cross section, $\varepsilon_{\max}$, is at the distance from the neutral axis, y_0, the curvature is:

$$\rho = \frac{1}{r} = \frac{\varepsilon_{\max}}{y_0}$$

where r is the radius of curvature. For a given maximum strain, the positions of the neutral axis and the corresponding bending moment are functions of the geometry of the cross section and the stress profile. It is assumed that the strains vary linearly over the height of the cross section. The line in the cross section where the strains are zero is called the neutral axis. For a given strain profile, the stress profile can be determined from the stress-strain relations of the materials in the cross section. In case of the drip shield, the plate is constructed of Titanium Grade 7, and the other components are constructed of Titanium Grade 24. The waste package OCB is Alloy 22. A bi-linear approximation of the stress-strain relation shown in Figure B-1 is used for Titanium Grades 7 and 24 and Alloy 22. The relation is defined by Young's modulus, E, yield strength, σ_y, tangent modulus, E_t, and ultimate strength, σ_u (or, equivalently, yield strain, ε_y, ultimate strain, ε_u, yield strength, σ_y, and ultimate strength, σ_u). The properties, which are different for different materials, are listed in Tables 4-3, 4-6, A-1, and A-2, or can be calculated from data in those tables.

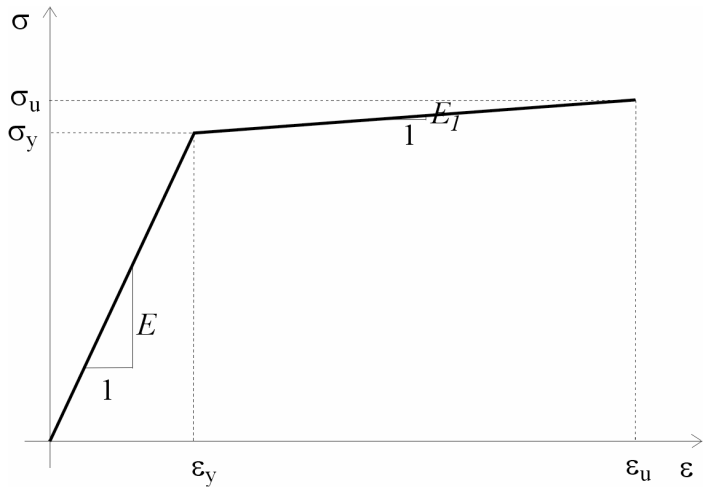

Source: Created for illustrative purposes only.

Figure B-1. Stress-Strain Relation Used for Mechanical Representation of Alloy 22, Stainless Steel Type 316, Titanium Grades 7 and 24

If the strain at a certain distance from the neutral axis is less than the yield strain, ε_y, then the stress is calculated based on the following relation:

$$\sigma = E\varepsilon = \frac{\sigma_y}{\varepsilon_y}\varepsilon .$$

Similarly, if the strain is greater than the yield strain, the stress is calculated based on the following relation:

$$\sigma = \sigma_y + \frac{\sigma_u - \sigma_y}{\varepsilon_u - \varepsilon_y}\left(\varepsilon - \varepsilon_y\right).$$

The position of the neutral axis (i.e., distance from the bottom edge of the cross section), y_0, as indicated, for example, in Figure B-2, is determined from the equilibrium of the stresses in the cross section, as shown in Equation B-1:

$$\int_A \sigma(x,y)\,dA = 0 . \qquad \text{(Eq. B-1)}$$

Once the position of the neutral axis is determined, the moment is calculated from Equation B-2:

$$M = \int_A \sigma(x,y)(y - y_0)\,dA . \qquad \text{(Eq. B-2)}$$

Initially, for relatively small moments, the entire cross section is elastic. The first yielding in the cross section occurs in the fiber farthest from the neutral axis. As the moment in the cross section increases, the limits between the elastic and plastic regions (elastic–plastic boundaries) of

the cross section move toward the neutral axis. The neutral axis is inside the elastic region. The plastic regions (or region) are between the elastic-plastic boundaries and the outside fibers of the cross section (i.e., the fibers farthest from the neutral axis). The distribution of stresses and strains in the cross section representative of the bulkhead and top of the support beam, if the dimensions of flanges are set to zero, is shown in Figures B-2 through B-4.

Three figures represent the states corresponding to three levels of maximum strain ($\varepsilon_{1\max}$, $\varepsilon_{2\max}$, and $\varepsilon_{3\max}$) as the elastic-plastic boundaries move closer to the neutral axis. Three stress distributions are shown because the forms of Equations B-1 and B-2 change as the elastic-plastic boundary moves from one region of the cross section to another (i.e., from the flanges into the rib of the bulkhead). The same stress profiles could not be used for the cross section at the bottom of the support beam. The main reason is that the analysis has shown that for the geometry of that cross section, because of the relatively low height of the support beam, the neutral axis falls inside the plate. Three stress profiles for the cross section at the bottom of the support beam are shown in Figures B-5 through B-7.

Nonlinear Equation B-1 is solved, using Mathcad V. 7.0 software, for each stress profile indicated in Figures B-2 through B-7, knowing that each profile is valid for a range of maximum strains until the elastic-plastic boundary moves from one region of the cross section into another. (The Mathcad files used in the analysis are included in output DTN: MO0701DRIPSHLD.000, folder "\drip shield failure modes\2D approximation\.") For each value of maximum strain and determined location of the neutral axis, the curvature and moment are calculated. Piecing together sections of the moment-curvature curve determined from different cross section stress profiles, it is possible to reconstruct the entire moment-curvature relation for the given cross section. In Figures B-2 through B-7, L_1 is the bulkhead or support beam spacing, d_1 is the plate thickness, h_2 is the bulkhead or support beam height, d_2 is the bulkhead or support beam thickness, and L_3 and d_3 are dimensions of the bulkhead flange. The support beam has no flange.

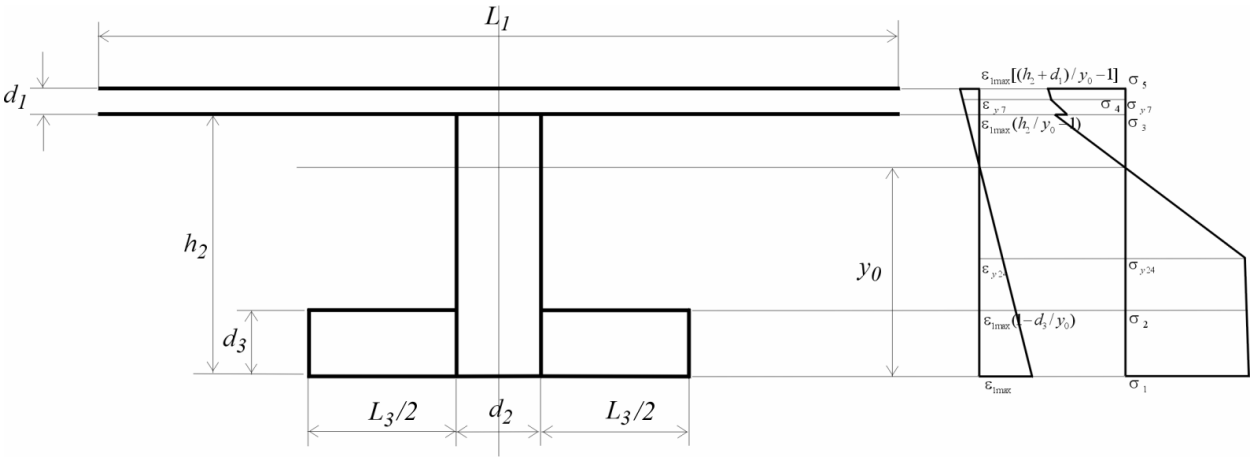

Source: Created for illustrative purposes only

NOTE: Definition of variables as functions of maximum strain, $\varepsilon_{1\max}$, and material properties of two materials (Titanium Grade 7 in plate and Titanium Grade 24 in other components): yield strength, $\sigma_{y7(24)}$, yield strain, $\varepsilon_{y7(24)}$, ultimate strength, $\sigma_{u7(24)}$ and ultimate strain, $\varepsilon_{u7(24)}$.

$$\sigma_1 = \sigma_{y24} + \frac{\sigma_{u24} - \sigma_{y24}}{\varepsilon_{u24} - \varepsilon_{y24}} \left(\varepsilon_{1\max} - \varepsilon_{y24} \right)$$

$$\sigma_2 = \sigma_{y24} + \frac{\sigma_{u24} - \sigma_{y24}}{\varepsilon_{u24} - \varepsilon_{y24}} \left[\varepsilon_{1\max} \left(1 - d_3 / y_0 \right) - \varepsilon_{y24} \right]$$

$$\sigma_3 = \frac{\varepsilon_{1\max} (h_2 / y_0 - 1)}{\varepsilon_{y24}} \sigma_{y24}$$

$$\sigma_4 = \frac{\varepsilon_{1\max} (h_2 / y_0 - 1)}{\varepsilon_{y7}} \sigma_{y7}$$

$$\sigma_5 = \sigma_{y7} + \frac{\sigma_{u7} - \sigma_{y7}}{\varepsilon_{u7} - \varepsilon_{y7}} \left\{ \varepsilon_{1\max} \left[\left(h_2 + d_1 \right) / y_0 - 1 \right] - \varepsilon_{y7} \right\}$$

Figure B-2. Distribution of Bending Strains and Stresses in the Drip-Shield Bulkhead Cross Section (including the plate): State 1

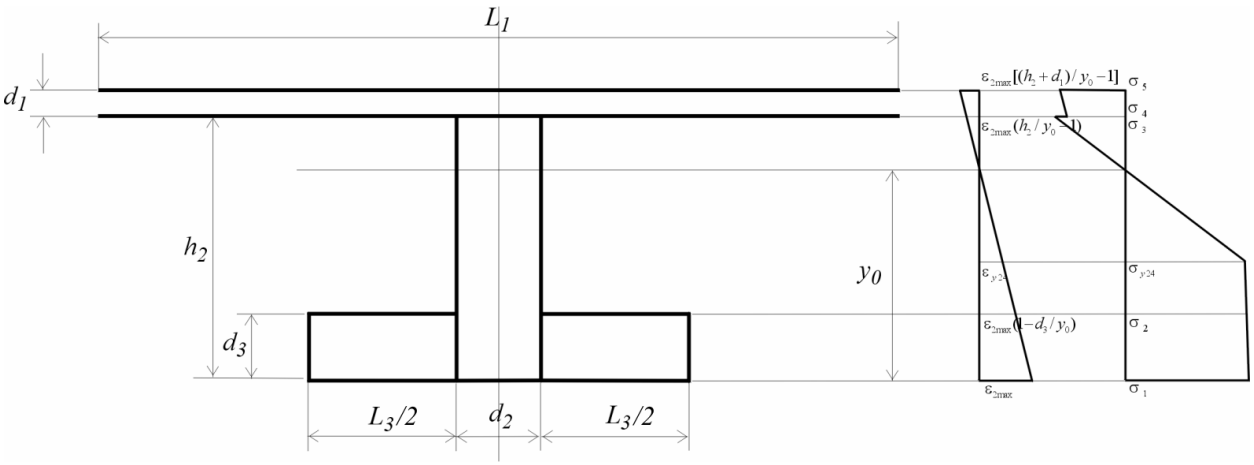

Source: Created for illustrative purposes only

NOTE: Definition of variables as functions of maximum strain, $\varepsilon_{2\max}$, and material properties of two materials (Titanium Grade 7 in plate and Titanium Grade 24 in other components): yield strength, $\sigma_{y7(24)}$, yield strain, $\varepsilon_{y7(24)}$, ultimate strength, $\sigma_{u7(24)}$ and ultimate strain, $\varepsilon_{u7(24)}$.

$$\sigma_1 = \sigma_{y24} + \frac{\sigma_{u24} - \sigma_{y24}}{\varepsilon_{u24} - \varepsilon_{y24}}\left(\varepsilon_{2\max} - \varepsilon_{y24}\right)$$

$$\sigma_2 = \sigma_{y24} + \frac{\sigma_{u24} - \sigma_{y24}}{\varepsilon_{u24} - \varepsilon_{y24}}\left[\varepsilon_{2\max}\left(1 - d_3 / y_0\right) - \varepsilon_{y24}\right]$$

$$\sigma_3 = \frac{\varepsilon_{2\max}(h_2 / y_0 - 1)}{\varepsilon_{y24}}\sigma_{y24}$$

$$\sigma_4 = \sigma_{y7} + \frac{\sigma_{u7} - \sigma_{y7}}{\varepsilon_{u7} - \varepsilon_{y7}}\left[\varepsilon_{2\max}\left(h_2 / y_0 - 1\right) - \varepsilon_{y7}\right]$$

$$\sigma_5 = \sigma_{y7} + \frac{\sigma_{u7} - \sigma_{y7}}{\varepsilon_{u7} - \varepsilon_{y7}}\left\{\varepsilon_{2\max}\left[\left(h_2 + d_1\right) / y_0 - 1\right] - \varepsilon_{y7}\right\}$$

Figure B-3. Distribution of Bending Strains and Stresses in the Drip-Shield Bulkhead Cross Section (including the plate): State 2

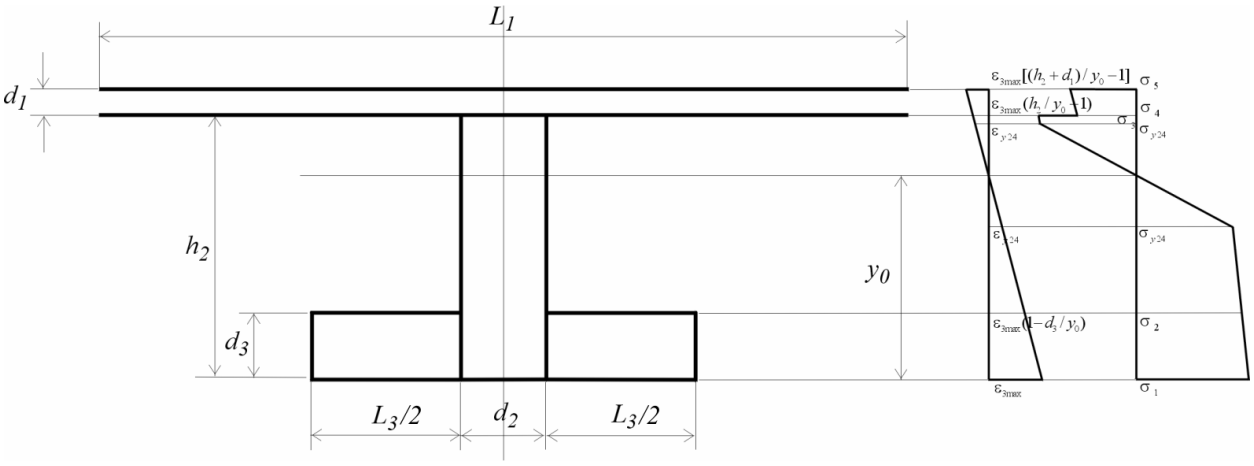

Source: Created for illustrative purposes only

NOTE: Definition of variables as functions of maximum strain, $\varepsilon_{3\max}$, and material properties of two materials (Titanium Grade 7 in plate and Titanium Grade 24 in other components): yield strength, $\sigma_{y7(24)}$, yield strain, $\varepsilon_{y7(24)}$, ultimate strength, $\sigma_{u7(24)}$ and ultimate strain, $\varepsilon_{u7(24)}$.

$$\sigma_1 = \sigma_{y24} + \frac{\sigma_{u24} - \sigma_{y24}}{\varepsilon_{u24} - \varepsilon_{y24}}\left(\varepsilon_{3\max} - \varepsilon_{y24}\right)$$

$$\sigma_2 = \sigma_{y24} + \frac{\sigma_{u24} - \sigma_{y24}}{\varepsilon_{u24} - \varepsilon_{y24}}\left[\varepsilon_{3\max}\left(1 - d_3 / y_0\right) - \varepsilon_{y24}\right]$$

$$\sigma_3 = \sigma_{y24} + \frac{\sigma_{u24} - \sigma_{y24}}{\varepsilon_{u24} - \varepsilon_{y24}}\left[\varepsilon_{3\max}\left(h_2 / y_0 - 1\right) - \varepsilon_{y24}\right]$$

$$\sigma_4 = \sigma_{y7} + \frac{\sigma_{u7} - \sigma_{y7}}{\varepsilon_{u7} - \varepsilon_{y7}}\left[\varepsilon_{3\max}\left(h_2 / y_0 - 1\right) - \varepsilon_{y7}\right]$$

$$\sigma_5 = \sigma_{y7} + \frac{\sigma_{u7} - \sigma_{y7}}{\varepsilon_{u7} - \varepsilon_{y7}}\left\{\varepsilon_{3\max}\left[\left(h_2 + d_1\right) / y_0 - 1\right] - \varepsilon_{y7}\right\}$$

Figure B-4. Distribution of Bending Strains and Stresses in the Drip-Shield Bulkhead Cross Section (including the plate): State 3

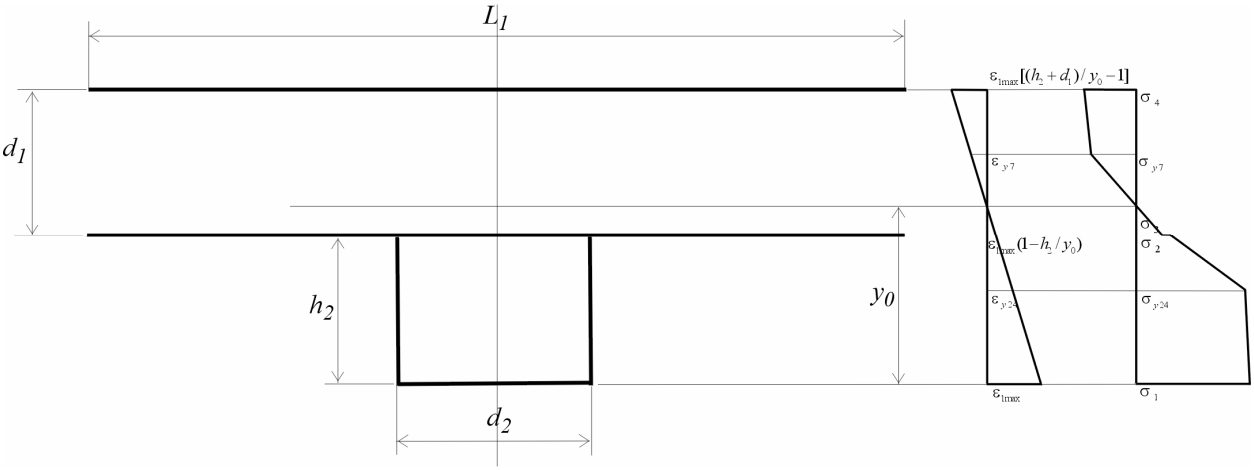

Source: Created for illustrative purposes only.

NOTE: Definition of variables as functions of maximum strain, $\varepsilon_{1\max}$, and material properties of two materials (Titanium Grade 7 in plate and Titanium Grade 24 in other components): yield strength, $\sigma_{y7(24)}$, yield strain, $\varepsilon_{y7(24)}$, ultimate strength, $\sigma_{u7(24)}$ and ultimate strain, $\varepsilon_{u7(24)}$.

$$\sigma_1 = \sigma_{y24} + \frac{\sigma_{u24} - \sigma_{y24}}{\varepsilon_{u24} - \varepsilon_{y24}}\left(\varepsilon_{1\max} - \varepsilon_{y24}\right)$$

$$\sigma_2 = \frac{\varepsilon_{1\max}(1 - h_2 / y_0)}{\varepsilon_{y24}}\sigma_{y24}$$

$$\sigma_3 = \frac{\varepsilon_{1\max}(1 - h_2 / y_0)}{\varepsilon_{y7}}\sigma_{y7}$$

$$\sigma_4 = \sigma_{y7} + \frac{\sigma_{u7} - \sigma_{y7}}{\varepsilon_{u7} - \varepsilon_{y7}}\left\{\varepsilon_{1\max}\left[(h_2 + d_1)/y_0 - 1\right] - \varepsilon_{y7}\right\}$$

Figure B-5. Distribution of Bending Strains and Stresses in the Drip-Shield Support Beam (including the plate): State 1

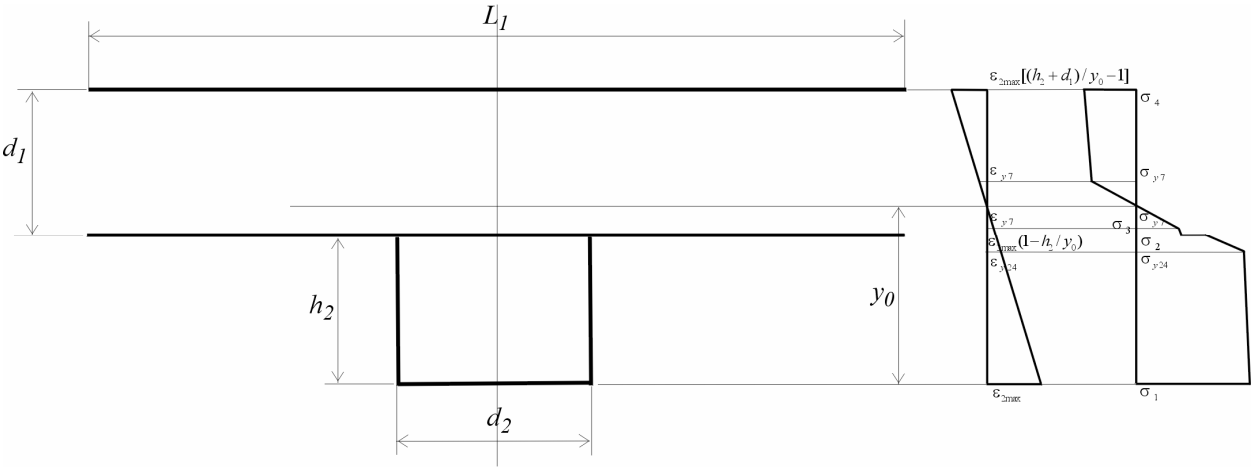

Source: Created for illustrative purposes only.

NOTE: Definition of variables as functions of maximum strain, $\varepsilon_{2\max}$, and material properties of two materials (Titanium Grade 7 in plate and Titanium Grade 24 in other components): yield strength, $\sigma_{y7(24)}$, yield strain, $\varepsilon_{y7(24)}$, ultimate strength, $\sigma_{u7(24)}$ and ultimate strain, $\varepsilon_{u7(24)}$.

$$\sigma_1 = \sigma_{y24} + \frac{\sigma_{u24} - \sigma_{y24}}{\varepsilon_{u24} - \varepsilon_{y24}}\left(\varepsilon_{2\max} - \varepsilon_{y24}\right)$$

$$\sigma_2 = \frac{\varepsilon_{2\max}(1 - h_2 / y_0)}{\varepsilon_{y24}}\sigma_{y24}$$

$$\sigma_3 = \sigma_{y7} + \frac{\sigma_{u7} - \sigma_{y7}}{\varepsilon_{u7} - \varepsilon_{y7}}\left[\varepsilon_{2\max}\left(1 - h_2 / y_0\right) - \varepsilon_{y7}\right]$$

$$\sigma_4 = \sigma_{y7} + \frac{\sigma_{u7} - \sigma_{y7}}{\varepsilon_{u7} - \varepsilon_{y7}}\left\{\varepsilon_{2\max}\left[\left(h_2 + d_1\right)/ y_0 - 1\right] - \varepsilon_{y7}\right\}$$

Figure B-6. Distribution of Bending Strains and Stresses in the Drip-Shield Support Beam (including the plate): State 2

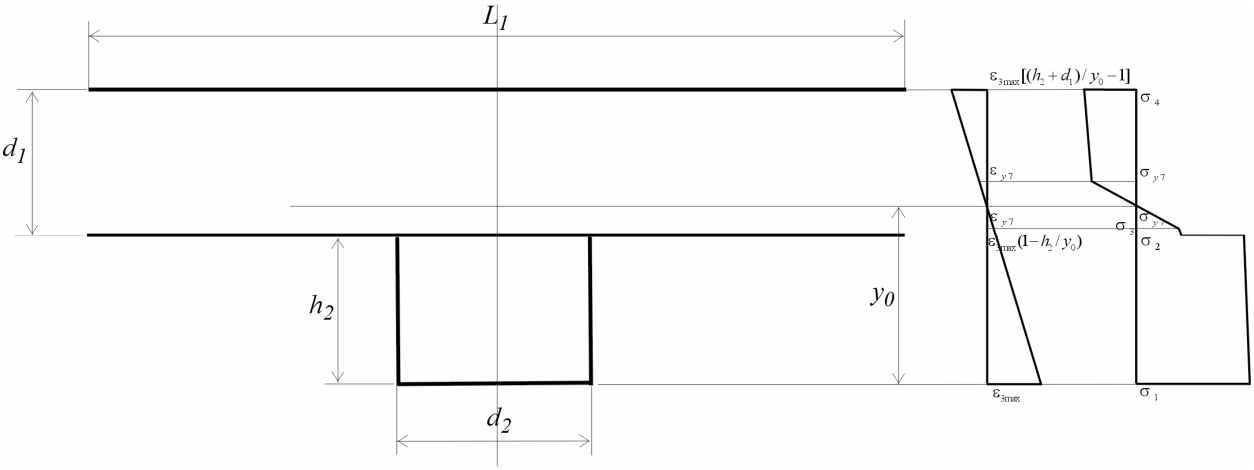

Source: Created for illustrative purposes only.

NOTE: Definition of variables as functions of maximum strain, $\varepsilon_{3\max}$, and material properties of two materials (Titanium Grade 7 in plate and Titanium Grade 24 in other components): yield strength, $\sigma_{y7(24)}$, yield strain, $\varepsilon_{y7(24)}$, ultimate strength, $\sigma_{u7(24)}$ and ultimate strain, $\varepsilon_{u7(24)}$.

$$\sigma_1 = \sigma_{y24} + \frac{\sigma_{u24} - \sigma_{y24}}{\varepsilon_{u24} - \varepsilon_{y24}}\left(\varepsilon_{3\max} - \varepsilon_{y24}\right)$$

$$\sigma_2 = \sigma_{y24} + \frac{\sigma_{u24} - \sigma_{y24}}{\varepsilon_{u24} - \varepsilon_{y24}}\left[\varepsilon_{3\max}\left(1 - h_2 / y_0\right) - \varepsilon_{y24}\right]$$

$$\sigma_3 = \sigma_{y7} + \frac{\sigma_{u7} - \sigma_{y7}}{\varepsilon_{u7} - \varepsilon_{y7}}\left[\varepsilon_{3\max}\left(1 - h_2 / y_0\right) - \varepsilon_{y7}\right]$$

$$\sigma_4 = \sigma_{y7} + \frac{\sigma_{u7} - \sigma_{y7}}{\varepsilon_{u7} - \varepsilon_{y7}}\left\{\varepsilon_{3\max}\left[\left(h_2 + d_1\right)/ y_0 - 1\right] - \varepsilon_{y7}\right\}$$

Figure B-7. Distribution of Bending Strains and Stresses in the Drip-Shield Support Beam (including the plate): State 3

B3. DIMENSIONS AND PROPERTIES OF APPROXIMATING CROSS SECTIONS OF THE DRIP SHIELD

Three cross sections of the drip shield structure were approximated by two-dimensional cross sections: (1) the cross section perpendicular to the bulkhead in the middle of the drip shield crown, (2) the cross section perpendicular to the support beam at the top of the drip shield leg, and (3) the cross section perpendicular to the support beam at the bottom of the drip shield leg. The cross section in the middle of the bulkhead is considered to be representative of the entire drip shield span. The approximation is adequate because bulkhead rib height is constant for most of the span and increases only close to the connection with the support beam. Because the support-beam height varies approximately linearly from the top to the bottom of the drip shield

leg, approximations of the support beam at the top and the bottom are sufficient to characterize geometry of the support beam.

Three cross sections (one in the bulkhead and two in the support beams) are approximated by the rectangular cross section for three configurations of the drip shield: (1) the initial configuration, (2) the 5-mm thinned configuration, and (3) the 10-mm thinned configuration. The dimensions indicated in Figures B-2 through B-7 for different cross sections in different configurations, as used in the analysis, are listed in Table B-1.

Table B-1. Dimensions of Drip Shield Cross-Sections in Different Configurations Indicated in Figures B-2 through B-7

Configuration	Cross Section	L_1 (m)	d_1 (m)	h_2 (m)	d_2 (m)	L_3 (m)	d_3 (m)
Initial	Bulkhead	1.071	0.015	0.090	0.038	0.100	0.020
	Support beam top	1.071	0.015	0.086	0.076	0	0
	Support beam bottom	1.071	0.015	0.028	0.076	0	0
5-mm thinned	Bulkhead	1.071	0.010	0.090	0.033	0.100	0.015
	Support beam top	1.071	0.010	0.081	0.071	0	0
	Support beam bottom	1.071	0.010	0.023	0.071	0	0
10-mm thinned	Bulkhead	1.071	0.005	0.090	0.028	0.100	0.010
	Support beam top	1.071	0.005	0.076	0.066	0	0
	Support beam bottom	1.071	0.005	0.018	0.066	0	0

Sources: The initial configuration for framework spacing, (L_1), bulkhead dimensions, support beam, and plate thickness, (d_1), are from Table 4-1.

NOTES: Difference between 1.071 m and 1.0716 m in Table 4-1 is insignificant.

Dimensions of the other configurations are derived by thinning the components by the indicated magnitudes. For the support beam, both thickness, d_2 , and height, h_2 , are thinned.

Because the support beam does not have a flange, d_3 and L_3 are 0. (L_3 is not set to 0 in the Mathcad files, but this is irrelevant, because L_3 is always multiplied by d_3).

Instead of going through the formalism described by Equations B-1 and B-2, the height and the Young's modulus of the approximating rectangular cross section are determined first from the condition resulting from matching the bending (Equation B-3) and axial stiffness (Equation B-4):

$$E' \frac{bh^3}{12} = EI \qquad \text{(Eq. B-3)}$$

$$E' bh = EA \quad \text{(Eq. B-4)}$$

where E' is the Young's modulus of the approximating cross section, $b = 1.071\,\text{m}$ is the bulkhead spacing, and h is the height of the approximating cross section. Equations B-3 and B-4 uniquely define two unknowns, E' and h. However, if E' and h are determined from these equations, the height of the cross section, h, can be relatively low, imposing difficulties for numerical solution of the problem, and correlation of the strains between the approximating and actual cross sections is not straightforward. For that reason, E' and h are determined from Equation B-3 and the condition that the height of the approximation is greater (but not significantly) than twice the distance of the neutral axis from the bottom fiber of the cross section (e.g., Figure B-2). The second condition ensures that there is a sufficient height of the numerical approximation that will not impose severe limitation on the calculation time step and that the calculated maximum strains in two-dimensional approximation are approximately equal but overpredict the strain in the true cross section (for the same curvature). In the approach adopted, Equation B-4 is not satisfied: axial stiffness of the rectangular approximation significantly underestimates that of the actual cross section. However, axial forces and stiffness have a secondary effect, compared to the bending forces and stiffness, on overall deformation of the drip shield structure. Thus, underestimating the axial stiffness in the two-dimensional representation has a relatively small effect on the quality of the approximation.

The calculation was carried out using Mathcad software. The Mathcad files used in the analysis are included in output DTN: MO0701DRIPSHLD.000, folder "\drip shield failure modes\2D approximation\," file *elastic properties.mcd* in different subfolders corresponding to the three configurations and the three cross sections. The subfolder names for different configurations are based on the plate thickness (i.e., "15 mm", "10 mm" and "5 mm" corresponding to the initial 5-mm thinned and 10-mm thinned configurations, respectively). The same Young's modulus, $E' = 3.3\,\text{GPa}$, was used for all cross sections and configurations. The position of the neutral axis, y_0, and moment of inertia, I, of the cross sections bent elastically are calculated using the following formulas:

$$A = L_1 d_1 + h_2 d_2 + L_3 d_3$$

$$y_0 = \frac{L_1 d_1 (h_2 + 0.5 d_1) + 0.5 d_2 h_2^2 + 0.5 L_3 d_3^2}{A}$$

$$I = \frac{L_1 d_1^3}{12} + L_1 d_1 (h_2 + 0.5 d_3 - y_0)^2 + \frac{L_3 d_3^3}{12} + L_3 d_3 (0.5 d_3 - y_0)^2 + \frac{d_2 h_2^3}{12} + h_2 d_2 (0.5 h_2 - y_0)^2 .$$

(The dimensions are illustrated in Figures B-2 through B-7.) The calculated heights of the cross sections are listed in Table 6-139.

The nonlinear portion of the moment-curvature relation was matched by adjusting the yield strength, σ_y', and the ultimate strength, σ_u', or tangent stiffness, E_t', of the approximation. The prime symbols indicate that the values pertain to the rectangular approximations. The moment-curvature curves for three original cross sections and their approximations in the three analyzed configurations are shown in Figures B-8 through B-10. Those approximations are achieved

using the values of σ_y' and σ_u' (or σ_y and σ_u) listed in Table 6-139. One pair of values for σ_y' and σ_u' is assigned to the bulkhead (crown); the other pair is assigned to the support beams (legs). Figures B-8 through B-10 illustrate that the moment curves of approximating cross sections closely follow those of the original cross sections in the range of curvatures (and strains) of interest (between 2 m^{-1} and 2.5 m^{-1}). The only exception is the bulkhead approximation for 10-mm thinned configuration (red lines in Figure B-10), which overestimates the moment of the three-dimensional cross section by approximately 20% for the maximum curvature of interest. However, validation of the approximation, discussed in Section B4, demonstrates that the two-dimensional approximation underestimates fragility of the drip shield for all configurations.

The calculation of moment-curvature diagrams for both original and approximating cross sections was carried out using Mathcad software. The Mathcad files used in the analysis of the moment-curvature diagrams for the original cross sections are included in output DTN: MO0701DRIPSHLD.000, folder "\drip shield failure modes\2D approximation\." The files *neutral true1.mcd*, *neutral true2.mcd* and *neutral true3.mcd* are stored in different subfolders corresponding to the three configurations and the three cross sections. The Mathcad files used in the analysis of the moment-curvature diagrams for the approximating cross sections are included in output DTN: MO0701DRIPSHLD.000, folder "\drip shield failure modes\2D approximation\," file *neutral rectangular.mcd*, stored in different subfolders corresponding to the three configurations and the three cross sections. The subfolders for different configurations are named based on the plate thickness (i.e., "15 mm," "10 mm," and "5 mm" corresponding to the initial, 5-mm thinned and 10-mm thinned configurations, respectively).

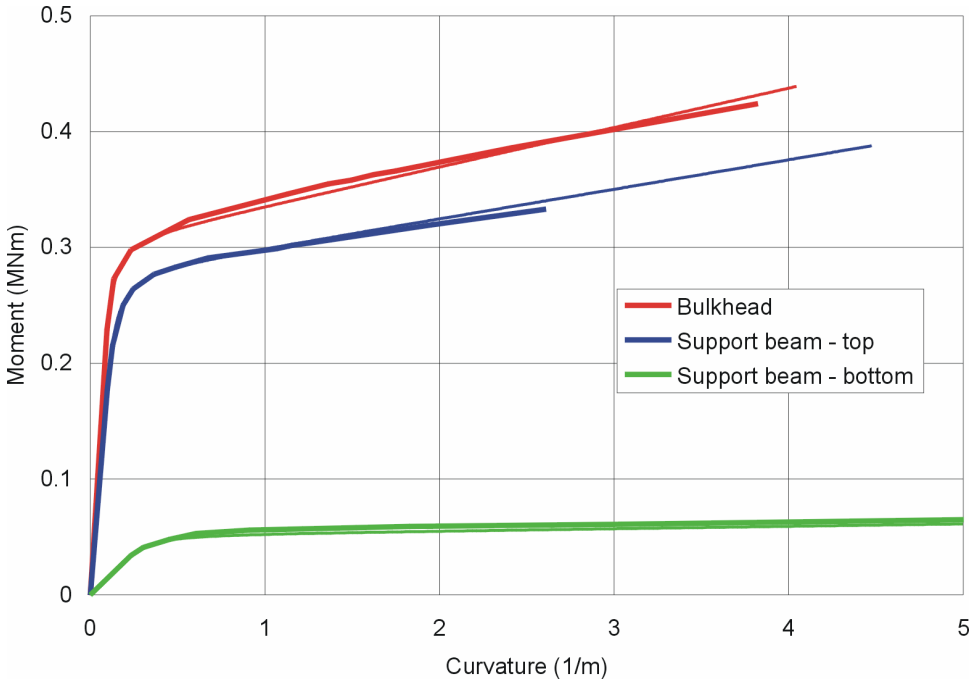

Output DTN: MO0701DRIPSHLD.000, file *\drip shield failure modes\2D approximation\inital\comparison.xls*, worksheet "chart 1."

NOTE: Thicker lines are for the original geometry; thinner lines are for the rectangular approximations.

Figure B-8. Moments as Functions of Curvature for Three Cross Sections and Their Rectangular Approximations in the Initial Configuration

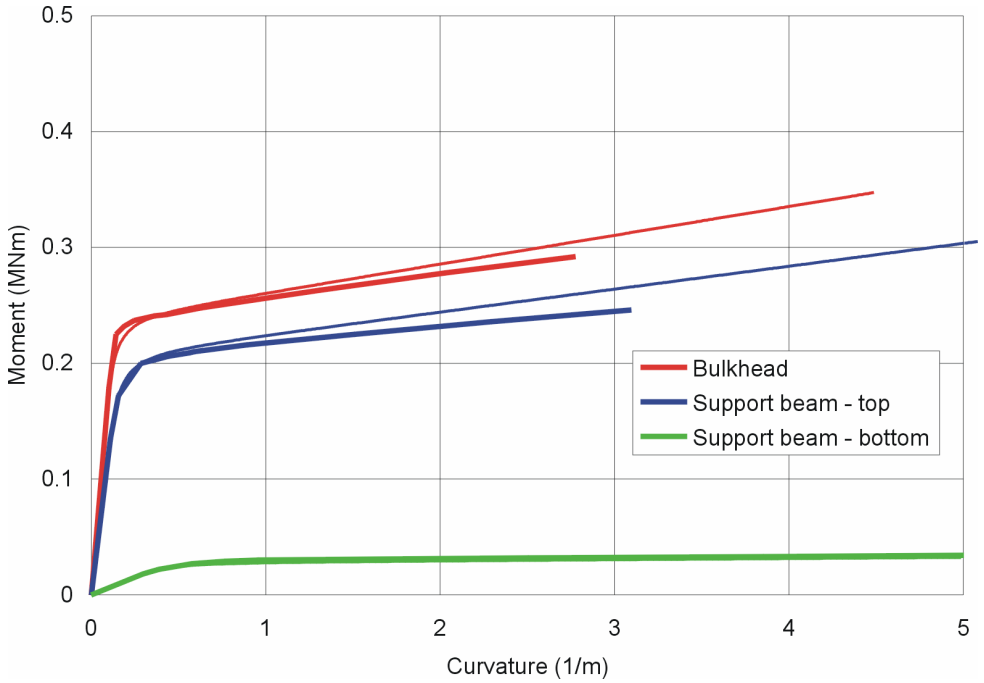

Output DTN: MO0701DRIPSHLD.000, file *\drip shield failure modes\2D approximation\5mm\comparison.xls*, worksheet "chart 1."

NOTE: Thicker lines are for the original geometry; thinner lines are for the rectangular approximations.

Figure B-9. Moments as Functions of Curvature for Three Cross Sections and Their Rectangular Approximations in the 5-mm Thinned Configuration

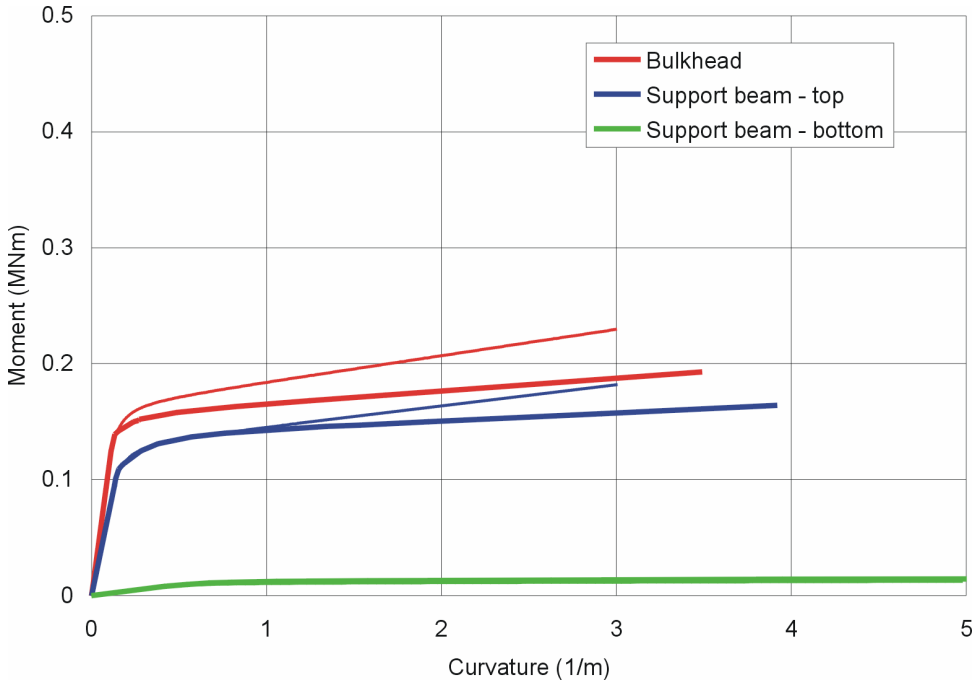

Output DTN: MO0701DRIPSHLD.000, file *\drip shield failure modes\2D approximation\10mm\comparison.xls*, worksheet "chart 1."

NOTE: Thicker lines are for the original geometry; thinner lines are for the rectangular approximations.

Figure B-10. Moments as Functions of Curvature for Three Cross Sections and Their Rectangular Approximations in the 10-mm Thinned Configuration

Table B-2. Densities of the Drip Shield Two-Dimensional Representations

Configuration	Mass of 1.071-m-Long Segment (kg)	Area of Two-Dimensional Drip Shield Representation (m^2)	Density of Two-Dimensional Drip Shield Representation (kg/m^3)
Initial	829	1.146	675
5-mm thinned	588	1.002	548
10-mm thinned	348	0.841	386

Sources: Obtained from output DTN: MO0701DRIPSHLD.000, folder "DS failure modes/DS 2D quasi-static fragility/load realization 3/," FLAC3D save files *initial/case4seed4-initial_ini.sav* (initial configuration), *5mm/case4seed4-5mm_ini.sav* (5-mm thinned configuration) and *10mm/case4seed4-10mm_ini.sav* (10-mm thinned configuration).

Area obtained from output DTN MO0701DRIPSHLD.000, folder "DS framework fragility/average load/," UDEC save files *15mm/eq_lf132.sav* (initial configuration), *10mm/eq_lf83.sav* (5-mm thinned configuration) and *5mm/eq_lf38.sav* (10-mm thinned configuration).

NOTES: Total mass, M, of a single drip shield segment (associated with bulkheads, spaced at distance L = 1.07 m) is obtained from the drip shield three-dimensional numerical representation. Total area, A, of the drip shield is obtained from the drip shield two-dimensional representation. The density, ρ, is calculated using the following relation: $\rho = M/(AL)$.

Densities of the two-dimensional drip shield approximations are calculated by (a) dividing the total mass of the three-dimensional drip shield representation, which includes one drip shield segment, with the drip shield area in the two-dimensional representation, and (b) spacing the bulkheads along the drip shield. A uniform density is assigned to the two-dimensional drip shield representation. The total mass of the single drip shield segment, for each of the three configurations, is obtained from the three-dimensional representations used for analysis of drip shield framework fragility (Section 6.4.3.2).

B4. VALIDATION OF THE TWO-DIMENSIONAL APPROXIMATION OF THE DRIP SHIELD

In order to validate the two-dimensional approximation of the drip shield deformation and failure, the drip shield framework fragility analysis, completed using a three-dimensional geometrical representation (documented in Section 6.4.3.2), is carried out again with a two-dimensional approximation. The boundary conditions, loads, and interaction of the drip shield with the surrounding rubble are implemented in the two-dimensional analysis in the same way as in the three-dimensional analysis (described in Section 6.4.3.2.2). One inconsequential difference is that the two-dimensional approximation includes a representation of the waste package and the waste package internals, which is omitted completely in the three-dimensional representation. The geometry and the mechanical properties of the two-dimensional representation, derived following the approach described in this appendix, are listed in Tables 6-138 through 6-142.

The calculations were conducted for two load distributions corresponding to load realization 3 and an average load from Table 6-136. (Rubble loads on the drip shield are discussed in Section 6.4.3.2.2.2.) Three different configurations of the drip shield were analyzed: (1) the initial configuration, (2) the 5-mm thinned configuration, and (3) the 10-mm thinned configuration. The vertical load on the drip shield crown was increased in increments equal to 50% of the initial load until the drip shield collapsed. The average vertical loads (pressures) when the drip shield fails are compared in Figure B-11 (for different load distributions) as functions of the drip shield plate thickness, for both two- and three-dimensional approximations. The figure indicates that: (a) the two-dimensional approximation closely follows the trends predicted from the three-dimensional analyses, and (b) the two-dimensional approximation always underpredicts the failure loads compared to the three-dimensional analyses.

The failure modes predicted from the two- and three-dimensional calculations are compared in Figure B-12. Two different approximations predict identical failure modes for different configurations of the drip shield. The bulkhead buckles in the middle of the span in the initial configuration. (The analyses were carried out for increasing vertical load under quasi-static conditions.) As the drip shield components are thinned, buckling of the drip shield legs becomes the dominant mode of failure. Comparison of the strain magnitudes is not relevant here, as, in all three-dimensional cases, states of active failure, not equilibrium, are shown. It is very difficult, if not impossible, to stop different calculations at identically the same state of failure.

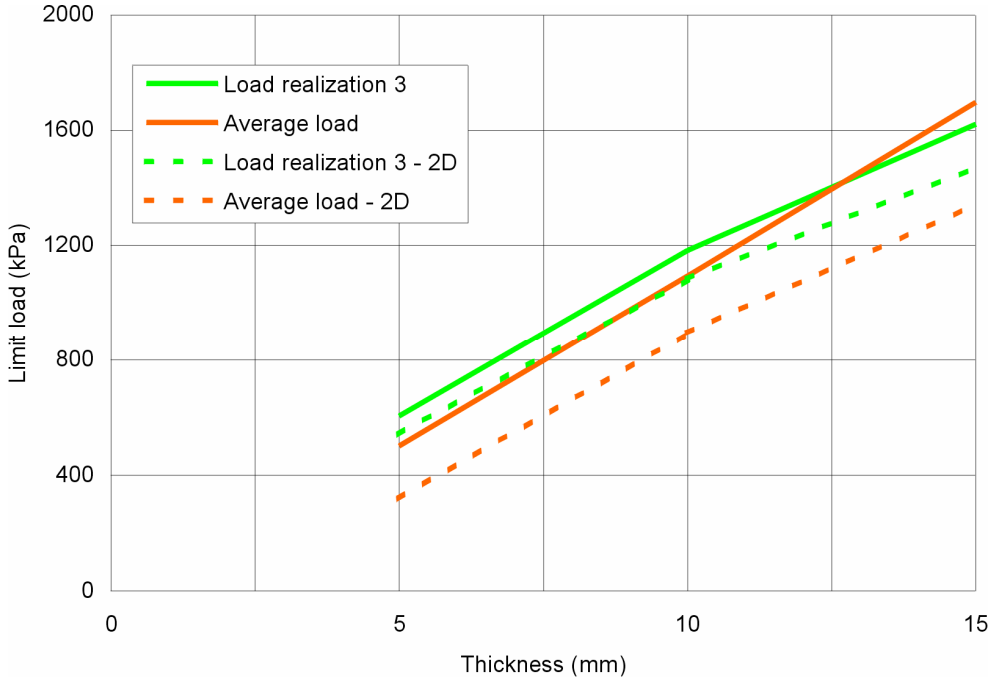

Output DTN: MO0701DRIPSHLD.000, file *\drip shield failure modes\2D approximation\ 2D vs 3D DS framework fragility.xls*, chart "ch limit load."

Figure B-11. Comparison of Drip-Shield Framework Limit Loads Obtained Using Two- and Three-Dimensional Representations

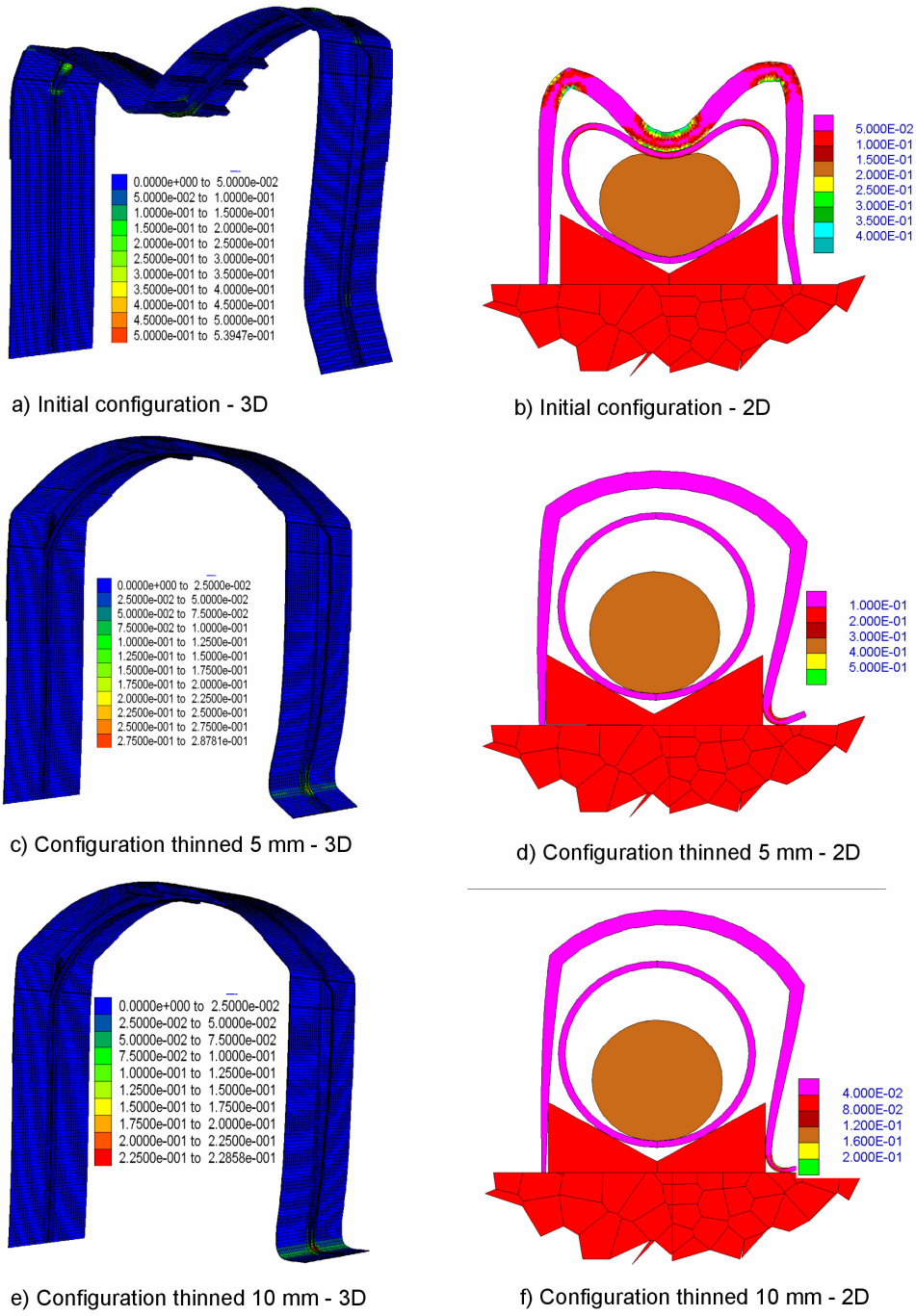

a) Initial configuration - 3D

b) Initial configuration - 2D

c) Configuration thinned 5 mm - 3D

d) Configuration thinned 5 mm - 2D

e) Configuration thinned 10 mm - 3D

f) Configuration thinned 10 mm - 2D

Output DTN: MO0701DRIPSHLD.000. Three-dimensional results from folder "\drip shield framework fragility\average load\ FLAC3D save," files *\15mm\eq_lf134.sav*, *\10mm\eq_lf86.sav*, and *\5mm\eq_lf40.sav*; two-dimensional results from folder "\drip shield failure modes\2D quasi-static fragility\ UDEC save," files *\initial\case4seed4_95_eq.sav*, *\5mm\case4seed4_70_eq.sav*, and *\10mm\case4seed4_35_eq.sav.*

NOTE: In the two-dimensional simulations, contours of plastic shear strain are shown for the drip shield and the waste package only. Coloring of the invert, pallet and waste package internals does **not** indicate magnitude of plastic shear strain.

Figure B-12. Comparison of Drip-Shield Framework Failure Modes and Plastic Strains Obtained Using Two- and Three-Dimensional Representations

B5. DIMENSIONS AND PROPERTIES OF APPROXIMATING CROSS SECTION OF THE WASTE PACKAGE

The thickness of the OCB, which was included in the dynamic analysis of drip shield failure modes in Section 6.4.4, was increased in order to avoid having it be a limiting factor for the critical calculation time step. Although, in this case, the rectangular cross section was approximated with the rectangular cross section, the approximation was carried out using the same methodology as that described and used in Sections B-2 and B-3. The geometrical and mechanical properties of the approximating cross section, listed in Table B-3, were derived using the Mathcad software. The Mathcad files used in the analysis are included in output DTN: MO0701DRIPSHLD.000. Comparison of the moment-curvature diagrams for the original and approximating cross sections is shown in Figure B-13. The density of the approximation is calculated by rescaling the original density by the ratio of thicknesses:

$$\rho' = \rho(d/d') = 8690\,\mathrm{kg/m^3}\,(0.0694\,\mathrm{m}/0.0254\,\mathrm{m}) = 3180\,\mathrm{kg/m^3}.$$

Table B-3. Geometrical and Mechanical Properties of the Approximating Cross Section of the OCB in the Analysis of Drip Shield Failure Modes

Property	Original	Approximation
Thickness (*d*)	0.0254 m	0.0694 m
Young's modulus (E)	204.1 GPa	10 GPa
Yield strength (σ_y)	351.6 MPa	47.1 MPa
Stress corresponding to 100% of strain (σ_1)	2,293 MPa	307 MPa

Source: Table 4-3.

NOTE: The original values of E and σ_y are taken from Table 4-3. Stress corresponding to 100% of strain is derived from the relation $\sigma_1 = \sigma_y + \left(1 - \sigma_y / E\right) E_t$, where E_t is taken from Table 4-3.

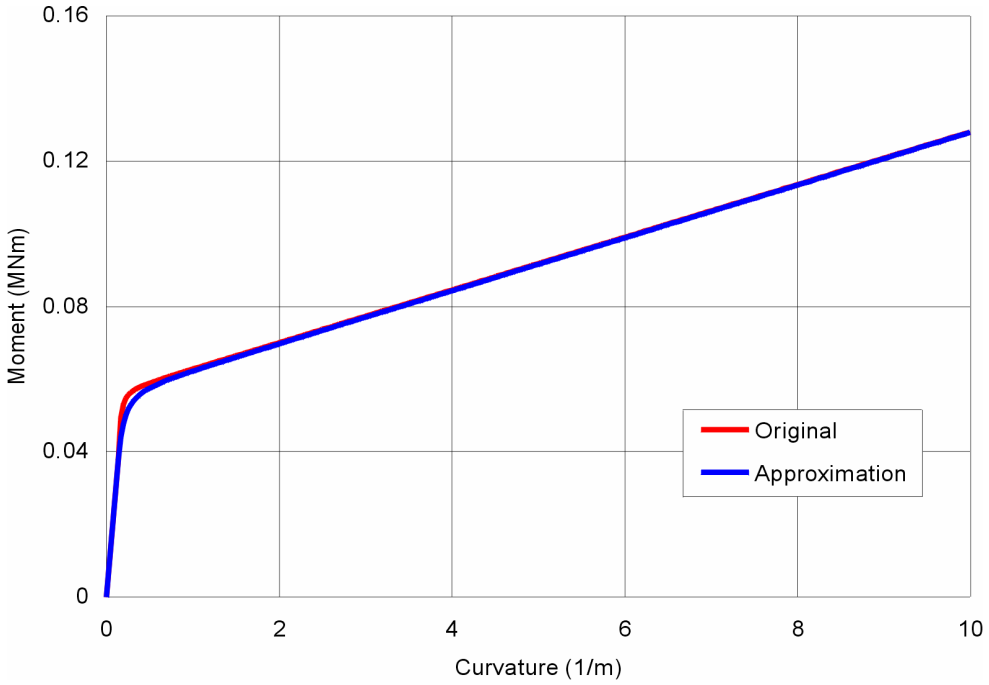

Output DTN: MO0701DRIPSHLD.000, file *\drip shield failure modes\2D approximation\WP\comparison.xls*, worksheet "chart 1."

Figure B-13. Moments as Functions of Curvature for OCB and Its Approximations to Increased Thickness

APPENDIX C
SEISMICALLY INDUCED ROCKFALL AND STABLE DRIFT PROFILES IN LITHOPHYSAL UNITS

APPENDIX C – SEISMICALLY INDUCED ROCKFALL AND STABLE DRIFT PROFILES IN LITHOPHYSAL UNITS

C1. INTRODUCTION

Stability of the emplacement drifts in lithophysal units during seismic ground motions has been analyzed previously and is documented in Sections 6.4.2.2.1 (preclosure ground motions) and 6.4.2.2.2 (postclosure ground motions) of the *Drift Degradation Analysis* (BSC 2004 [DIRS 166107]). The analyses were carried out for two pre-closure levels of annual probability of exceedance, 5×10^{-4} (the 0.19 m/s PGV level)[1] and 1×10^{-4} (the 0.384 m/s PGV level), and two postclosure levels of annual probability of exceedance, 1×10^{-5} (the 1.05 m/s PGV level) and 1×10^{-6} (the 2.44 m/s PGV level). For preclosure ground motion levels, there was only one set of three time histories (i.e., three components of motion) provided and analyzed for each level. Fifteen sets of three time histories from 17 sets were analyzed for each postclosure PGV level. Because the results for the 2.44 m/s PGV level show complete drift collapse, the emplacement drift stability for the ground motions at greater PGV levels was not analyzed. Detailed postprocessing of rockfall analysis results was conducted for the 1.05 m/s PGV level. The reported results include rockfall volume for each analyzed case. However, for the 2.44 m/s PGV level, only the qualitative assessment that the drifts completely collapse is provided.

Quantitative characterization of the rockfall volume and evolution of stable drift profiles for the PGV levels starting with 0.4 m/s are needed for seismic-consequence abstraction and seepage analysis. Therefore, additional rockfall analysis is carried out for 15 ground motions at the 0.4 m/s PGV level, and the rockfall volumes and stable drift profiles are extracted from the existing results for the 2.44 m/s PGV level.

C2. DESCRIPTION OF THE ANALYSIS

The existing UDEC model, described in Sections 6.4.2.1 and 6.4.2.2 of the *Drift Degradation Analysis* (BSC 2004 [DIRS 166107]), is used again to estimate seismically induced rockfall at the 0.4 m/s PGV level. An assembly of polygonal, elastic blocks, joined together along the interfaces, represents the rock mass. The average block size of 0.3 m used in the calculations corresponds to the average size of blocks expected to form in the lithophysal rock mass, as dictated by the spacing of joints and lithophysae mapped underground. The mechanical properties (both stiffness and strength) of the blocks and the joints are calibrated using the existing laboratory and in situ testing data, such that large-scale behavior of the assembly matches the deformability and strength of the rock mass. As stresses cause the joints between

[1] In case of unbounded seismic hazard, assumed in *Drift Degradation Analysis* (BSC 2004 [DIRS 166107], Tables X-1 to X-5), the following is the correspondence between the values of annual exceedance frequency at the repository level and the values of PGV:

- PGV of 0.19 m/s corresponds to the 5×10^{-4} per year exceedance frequency
- PGV of 0.384 m/s corresponds to the 10^{-4} per year exceedance frequency
- PGV of 1.05 m/s corresponds to the 10^{-5} per year exceedance frequency
- PGV of 2.44 m/s corresponds to the 10^{-6} per year exceedance frequency
- PGV of 5.35 m/s corresponds to the 10^{-7} per year exceedance frequency.

the blocks to open or slip, equivalent to fracturing of the rock mass, loose blocks form and fall on the drift floor or drip shield under the action of gravity.

Only one ground motion (set of three time histories) was provided for the 0.384 m/s PGV level. In order to capture the effect of spectral content and the duration of time histories on rockfall prediction, the analyses were conducted for 15 ground motions generated by rescaling the ground motions from the 1.05 m/s PGV level by the factor $0.4/1.05 \approx 0.381$. Fifteen realizations of combinations between ground motion number and rock-mass category number (listed in Table 6-44 of *Drift Degradation Analysis* (BSC 2004 [DIRS 166107])) were analyzed at the 0.4 m/s PGV level.

C3. RESULTS OF THE ANALYSIS

At the end of the analysis for each realization in the equilibrium state after dynamic simulation, the volume of rockfall is calculated and the stable drift profile determined. Because the analysis is two-dimensional, rockfall area (or rockfall volume per unit length of the drift) is calculated. The rockfall is determined based on displacements of the blocks. If the average block displacement relative to the free-field elastic displacement in both the x- and y-coordinate directions is equal to or greater than the specified threshold, the block is classified to be part of the rockfall. The displacement threshold of 0.1 m was used in all calculations. This threshold seems reasonable and does not affect the estimated rockfall results significantly. The drift height is 5.5 m, and most loose blocks fall a meter or more before they come to rest on top of accumulated rubble.

The results of the calculations are summarized in Figures C-1 through C-3. The figures show stable outlines of the drifts for the different realizations listed in *Drift Degradation Analysis* (BSC 2004 [DIRS 166107], Table 6-44). The loose blocks that form rockfall (or rubble) are not shown in the figures. (Realizations 4 and 12 in Figure C-3 show a few "floating" blocks inside the stable outline.) These blocks were not classified as rockfall because of a deficient criterion that is based on the magnitude of final displacements. In reality, a loose block can undergo large displacement that is reversible, returning the block to a position within the specified threshold from the original position. Again, this criterion deficiency has an insignificant effect on the total predicted rockfall volume. The rectangular shape in the middle of the drift represents the drip shield. The initial, stable outline of the drift is also indicated in the plots, as is the rockfall volume per unit length of the drift. The results in Figures C-2 and C-3 are obtained by post-processing calculations carried out as part of the work documented in *Drift Degradation Analysis* (BSC 2004 [DIRS 166107], Section 6.4.2.2.2) for 1.05 m/s and 2.44 m/s PGV levels, respectively. Although the 1.05 m/s PGV level was investigated for more than 15 realizations, only the 15 realizations listed in *Drift Degradation Analysis* (BSC 2004 [DIRS 166107], Table 6-44) are presented here to be consistent with results for the 0.4 m/s and 2.44 m/s PGV levels.

Most of the cases (realizations) at the 0.4 m/s PGV level show no rockfall at all. If rockfall occurs (realizations 4, 6, 11 and 12 in Figure C-1), it is in the weakest, relatively sparse, Category 1 lithophysal rock mass. The maximum rockfall area is 7.16 m^2. In contrast, the minimum rockfall area for the 2.44 m/s PGV level (Figure C-3) is greater than 60 m^2, indicating total drift collapse. Different ground motions or rock mass quality do not have significant effects

on drift stability. Clearly, the 1.05 m/s PGV level is within the transition between the PGV levels that do not cause significant rockfall and those that completely collapse the drift. (The results for the 1.05 m/s PGV level are shown in Figure C-2.) The rockfall results at the 1.05 m/s PGV level are documented and analyzed in detail in *Drift Degradation Analysis* (BSC 2004 [DIRS 166107], Section 6.4.2.2.2.1).

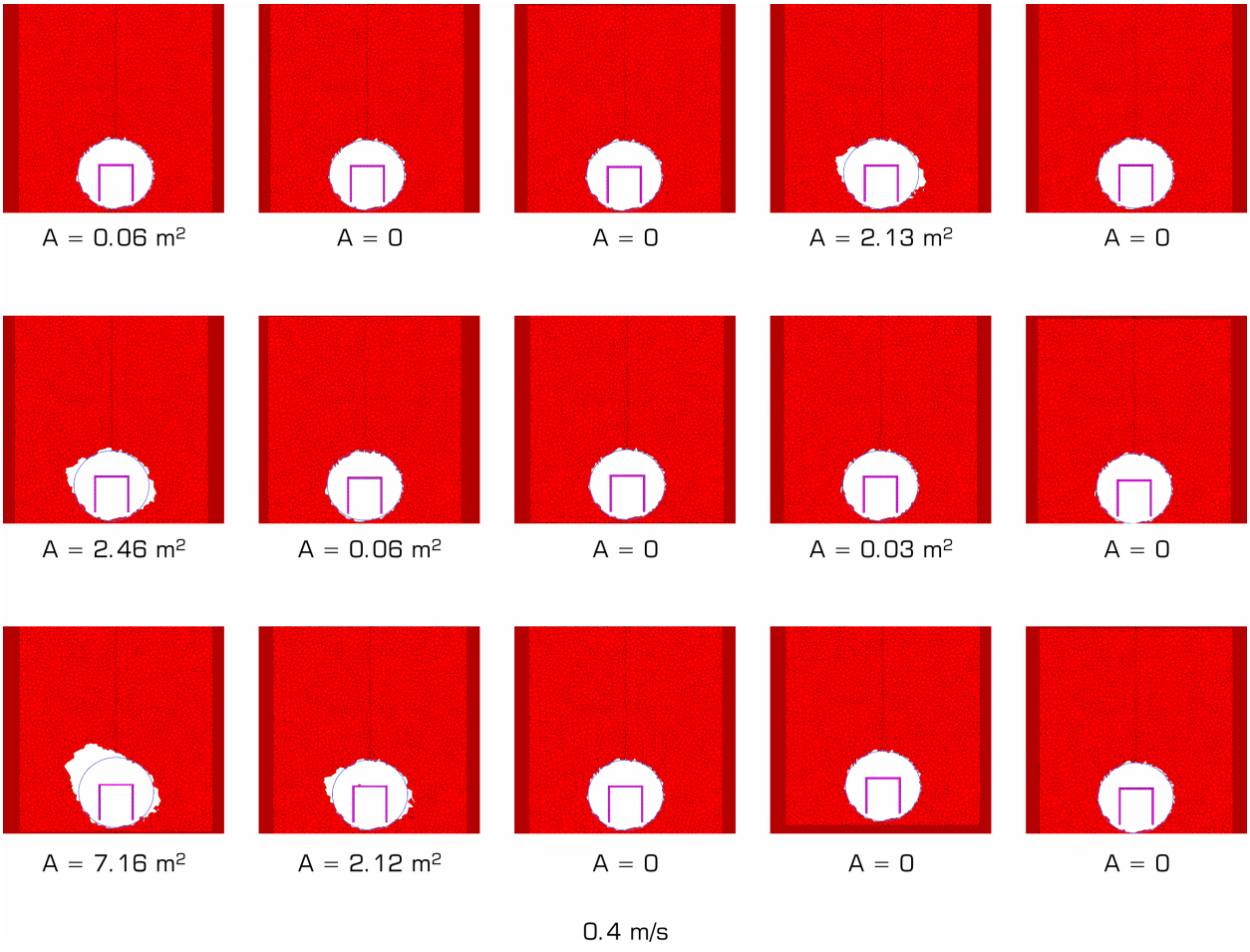

Output DTN: MO0611ROCKFALL.000, file *\results rockfall\summary\004ms.pcx*.

NOTES: Realizations 1 through 5 are in the first row, from left to right; realizations 6 through 10 are in the second row, from left to right; and realizations 11 through 15 are in the third row, from left to right. The realization numbers correspond to Table 6-44 in *Drift Degradation Analysis* (BSC 2004 [DIRS 166107]).

The loose blocks that are part of rockfall are not shown.

The rectangular shape inside the drift represents the drip shield. The initial drift outline is shown by blue lines.

Figure C-1. Stable Drift Profiles and Rockfall Volumes per Unit Length (Areas) for 15 Realizations at the 0.4 m/s PGV Level

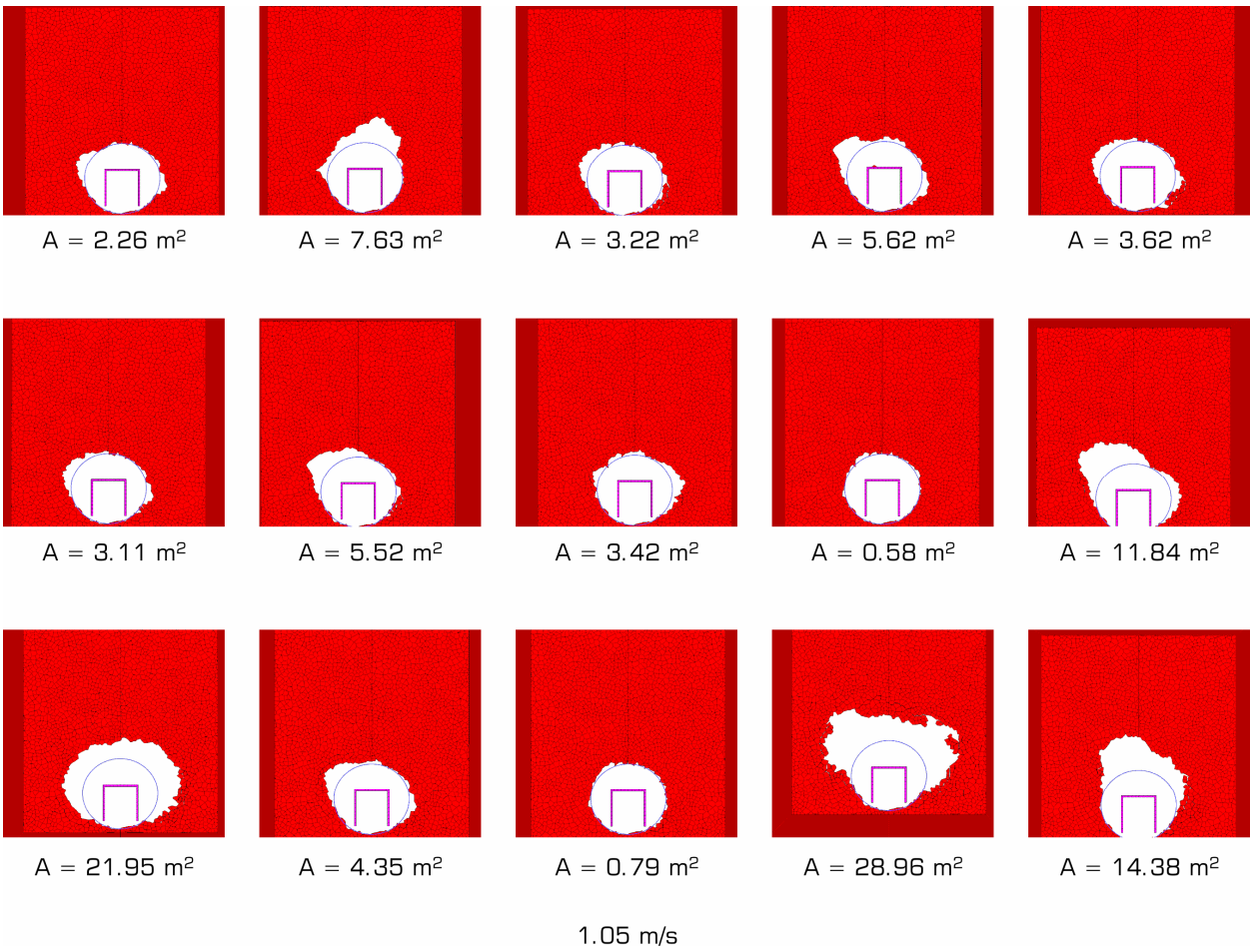

Output DTN: MO0611ROCKFALL.000, file *\results rockfall\summary\105ms.pcx*.

NOTES: Realizations 1 through 5 are in the first row, from left to right; realizations 6 through 10 are in the second row, from left to right; and realizations 11 through 15 are in the third row, from left to right. The realization numbers correspond to Table 6-44 in *Drift Degradation Analysis* (BSC 2004 [DIRS 166107]).

The loose blocks that are part of rockfall are not shown.

The rectangular shape inside the drift represents the drip shield. The initial drift outline is shown by blue lines.

Figure C-2. Stable Drift Profiles and Rockfall Volumes per Unit Length (Areas) for 15 Realizations at the 1.05 m/s PGV Level

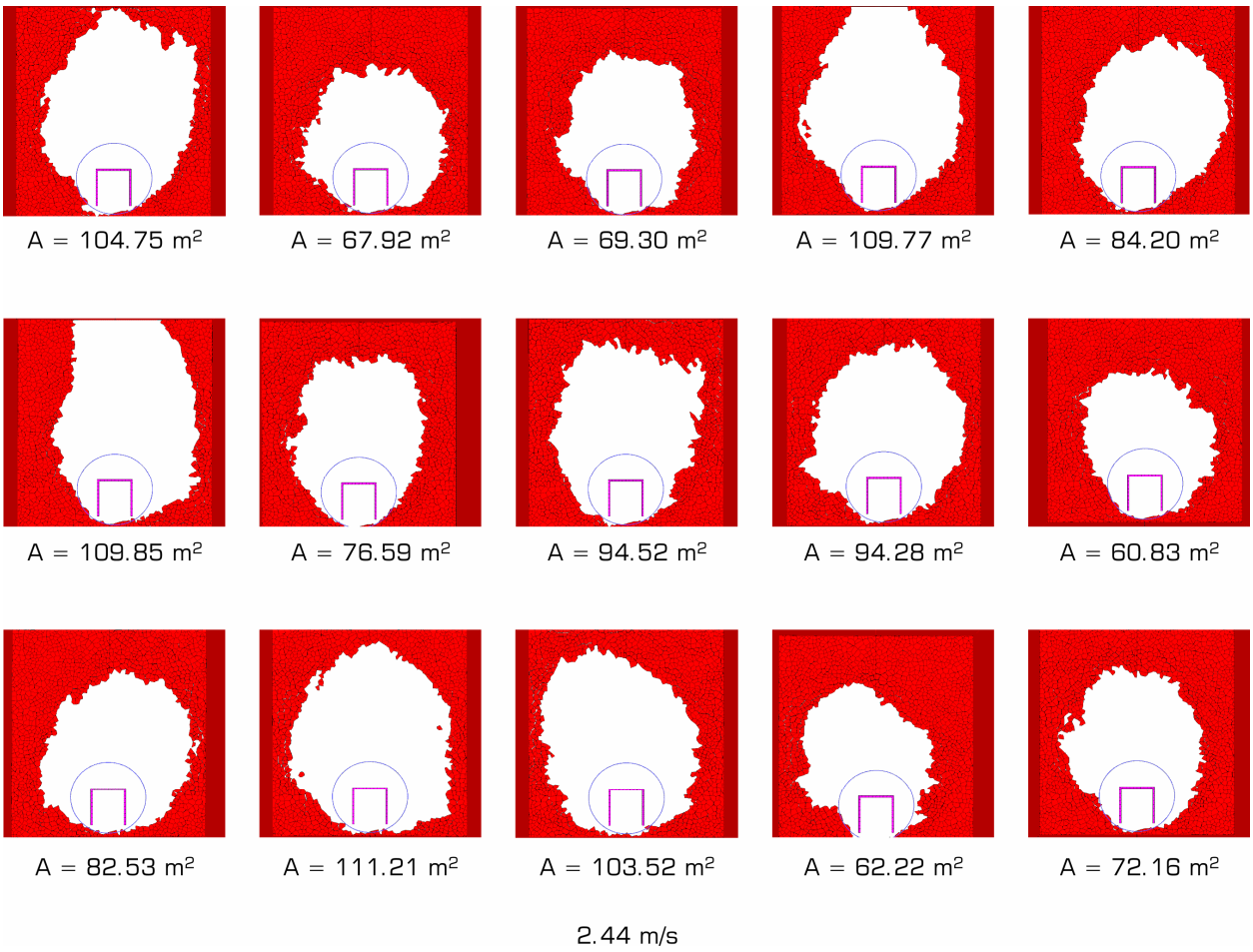

Output DTN: MO0611ROCKFALL.000, file *\results rockfall\summary\244ms.pcx*.

NOTES: Realizations 1 through 5 are in the first row, from left to right; realizations 6 through 10 are in the second row, from left to right; and realizations 11 through 15 are in the third row, from left to right. The realization numbers correspond to Table 6-44 in *Drift Degradation Analysis* (BSC 2004 [DIRS 166107]).

The loose blocks that are part of rockfall are not shown.

The rectangular shape inside the drift represents the drip shield. The initial drift outline is shown by blue lines.

Figure C-3. Stable Drift Profiles and Rockfall Volumes per Unit Length (Areas) for 15 Realizations at the 2.44 m/s PGV Level

INTENTIONALLY LEFT BLANK

APPENDIX D
MODEL CONSERVATISM—COMPARISON BETWEEN TWO-DIMENSIONAL AND THREE-DIMENSIONAL REPRESENTATIONS

APPENDIX D – MODEL CONSERVATISM—COMPARISON BETWEEN TWO-DIMENSIONAL AND THREE-DIMENSIONAL REPRESENTATIONS

The two-dimensional waste package representation underestimates the strength and stiffness of the true three-dimensional waste package structure. This is because the three-dimensional structure has a finite length and diameter (approximately 5.8 m and 1.9 m respectively), and lids on both ends. Although there are modes of failure in the lids and the connections between the lids and the wall that can occur before failure of the outer corrosion barrier (OCB) in the middle cross section, these are ignored in the two-dimensional representation of the OCB. Further, some states of deformation in the middle of the OCB, which do not exceed the rupture strain and stress, could result in failure of the OCB at the connections between the wall and the lids and/or failure (or popping) of the lids. Results presented below explore these other modes of failure and show that the two-dimensional representation is weaker than the three-dimensional representation.

Three-Dimensional Analysis—To investigate the potential for failure of a lid or the connections between the lids and the wall, deformation and collapse of the OCB were analyzed in a three-dimensional representation. The geometry of the problem analyzed here is illustrated in Figure D-1. Only the portion of the waste package geometry on the right (in Figure D-1) was analyzed using symmetries of the geometry and loading and by applying proper boundary conditions. The internals were not included in these simulations.

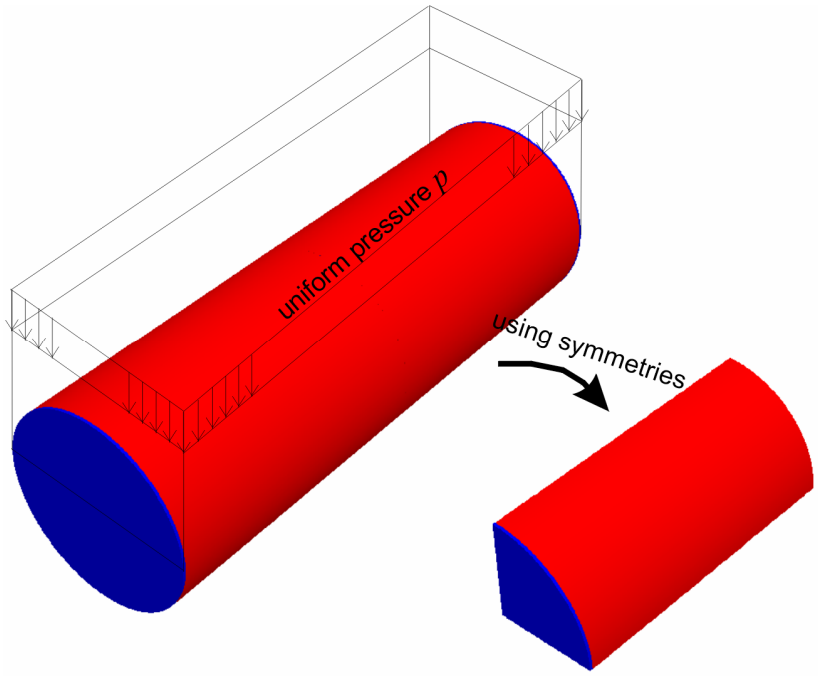

Source: Created for illustrative purposes only.

Figure D-1. Analyzed Geometry and Boundary Conditions in Investigation of Three-Dimensional Effects on Deformation and Collapse of the Waste Package

In the analysis, uniform pressure, p, was increased gradually in increments of 100 kPa. If possible, the equilibrium of the numerical representation was calculated for each load increase. At certain pressure levels, the OCB collapses, and equilibrium was not achievable. The analysis was conducted for two OCB thicknesses: 12 mm, and 18 mm. The analysis was performed for the 21-PWR waste package OCB geometry, but the conclusions are applicable to the interpretation of the mechanical behavior of the TAD-bearing waste package OCB. For evaluating the effects of a three-dimensional OCB geometry on deformation, strains, and failure, the same problem was analyzed in a two-dimensional representation.

Results show that the OCB collapses as a result of wall buckling, which begins when strains and stresses in the structure are much smaller than the rupture strains and stresses. Estimates of the collapse loads from the two- and three-dimensional analyses are listed in Table D-1. The collapse load estimates from the three-dimensional analyses are between 3.5 and 6.0 times greater than those from two-dimensional analyses.

It is important to note that incorporation of a pallet into the simulation would decrease the difference between the two estimates of collapse load. This is because the loading in these simulations is symmetrical relative to the horizontal plane through the center of the waste package. Consequently, there is no confinement to restrain horizontal deformation of the waste package. Pallet shape provides a more effective confinement with a greater effect on the two-dimensional than on the three-dimensional representation of the waste package for the following two reasons: (1) in the two-dimensional representation, the waste package rests on the pallet along its entire length; and (2) the effect of confinement is greater for more compliant and weaker structures. The two-dimensional representation of the waste package is more compliant and weaker than the actual structure, which is strengthened by the lids.

Table D-1. Approximate Estimates of the OCB Collapse Loads from Two-Dimensional and Three-Dimensional Analyses

Geometry/Thickness	12 mm	18 mm
Two-dimensional	102 kPa	198 kPa
Three-dimensional	500-600 kPa	700-800 kPa

Output DTN: MO07043DWPFAIL.000, *summary.xls*, worksheet “sheet 2.”

NOTE: Precision of the OCB collapse load estimated from two-dimensional analyses is 2 kPa. Load increment in three-dimensional analyses is 100 kPa. Therefore, the collapse load is estimated with a precision of 100 kPa. For the purpose of this investigation, 100-kPa precision is satisfactory.

The OCB geometries, including contours of plastic shear strain and the major principal stresses are shown in Figures D-2 and D-3 for the 18-mm-thick OCB at two states during collapse. Three different views are provided for each case. In state 1, shown in Figure D-2, there is significant deformation, and the maximum plastic shear strain is approximately 0.07 in the middle cross section of the OCB. The strains in the lid and at the connections between the lid and the walls are much smaller, less than 0.035. The more-advanced collapse state of the OCB, shown in Figure D-3, is not realistic because a portion of the OCB wall has deformed so much that it has

crossed the horizontal plane of symmetry, which is not possible. However, these results are instructive for investigating the evolution of deformation and strain in different portions of the OCB. At this state of OCB collapse, the lid deforms significantly by bending outward, but the greatest strains are still in the OCB wall, away from the lid. It appears from these results that significant deformation of the OCB in the middle cross section will not be preceded by failure or popping of the lids. It is interesting that despite excessive deformation, the OCB barely ruptures in the state shown in Figure D-3. The maximum plastic shear strains of 0.41 are associated with compressive stress state and, therefore, will not rupture Alloy 22. The maximum plastic shear strain associated with tensile stresses is 0.3648 (again away from the lid) in element (zone) number (ID) 33930. The corresponding effective plastic strain (see discussion in Section 6.5.1.2.3) is 0.42. Using the principal stresses in zone 33930 ($\sigma_1 = 890.12\,\text{MPa}$; $\sigma_2 = 788.67\,\text{MPa}$; $\sigma_3 = -60.85\,\text{MPa}$) and the formula (Equation A-1) from Appendix A, Section A.2, the triaxiality factor is calculated to be 1.789. Consequently, the ductility ratio, as given by Equation A-2, is 0.579, and the ultimate strain accounting for triaxiality of stresses is 0.37. (The elongation of Alloy 22 is 0.64, as listed in Appendix A, Section A.2.) Thus, the analysis shows that the OCB barely fails even in the extreme state of deformation illustrated in Figure D-3.

Two-Dimensional Analysis—Strains and stresses at two states during OCB collapse were calculated using a two-dimensional representation and are shown in Figures D-4 and D-5. The two states correspond approximately (comparing magnitude of deformation in the middle cross section) to the states shown in Figures D-2 and D-3. Two views are shown for each state: one showing the geometry of the entire representation, and one showing details, with maximum strains and stresses.

Results—These analyses indicate that the two-dimensional representation of the waste package underpredicts OCB stiffness and strength. As the OCB collapses, the greatest deformation and effective strains are in the middle cross section, away from the lids. Even for extremely large deformation of the middle cross section (the state shown in Figure D-3), there is no indication of lid failure. Another interesting observation is the large ductility of the OCB structure. Even for the very large deformation and distortion of the structure, the maximum strains do not reach the rupture strain. The results are presented here for the 18-mm-thick OCB, but trends and qualitative responses are the same for the 12-mm-thick OCB.

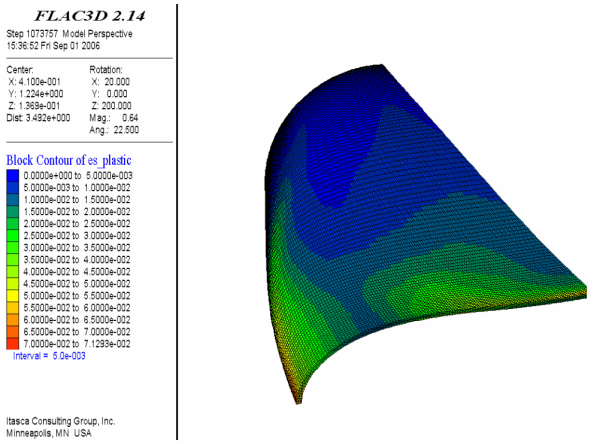

a) Strain, View 1

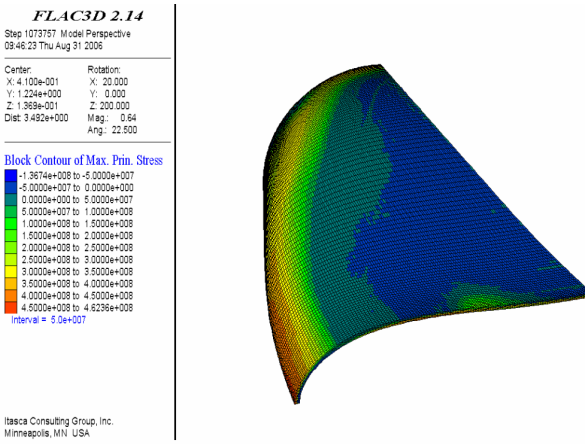

b) Stress (Pa), View 1

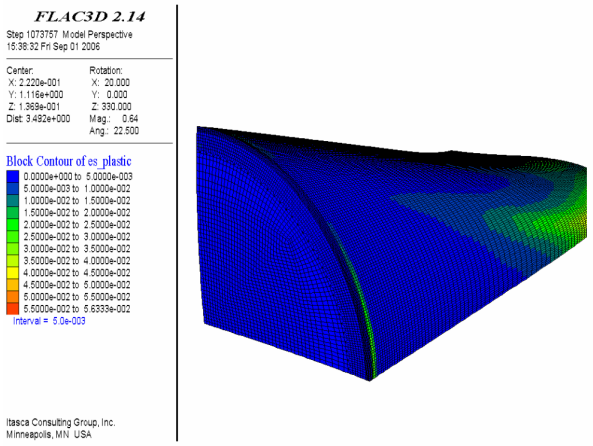

c) Strain, View 2

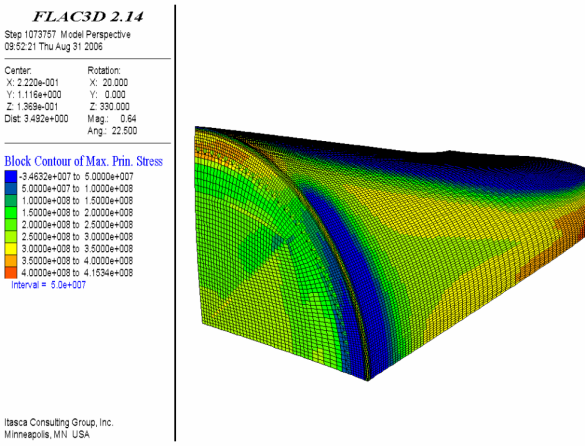

d) Stress (Pa), View 2

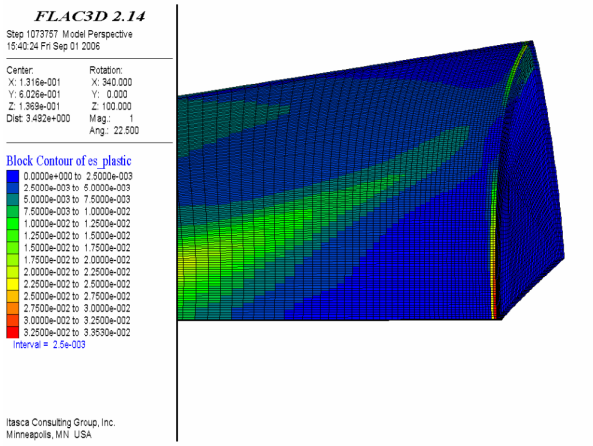

e) Strain, View 3

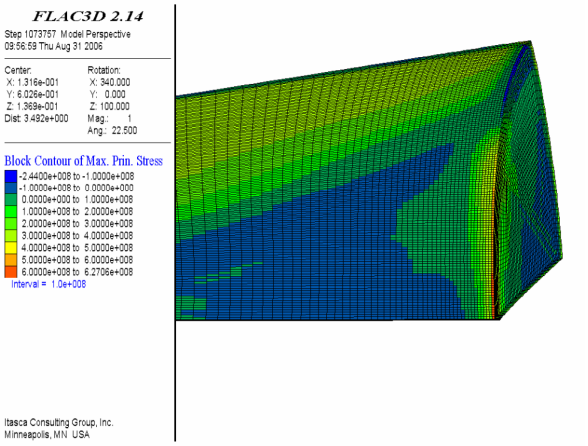

f) Stress (Pa), View 3

Output DTN: MO07043DWPFAIL.000, file *3D/18mm/wp3dstate1.pcx*.

Figure D-2. Different Views of Strain and Stress Contours Due to Uniformly Distributed Load in a Three-Dimensional Representation of the Waste Package: State 1 During Collapse

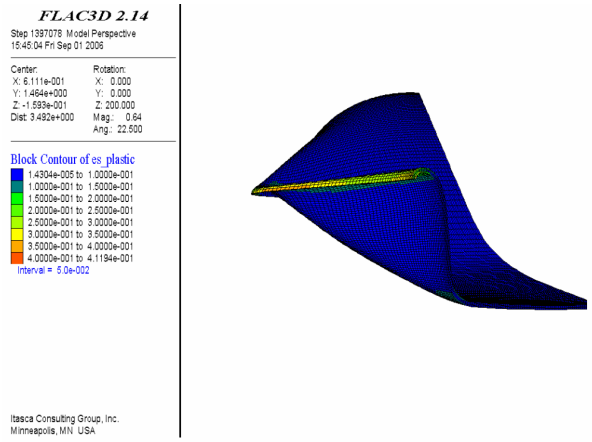

a) Strain, View 1

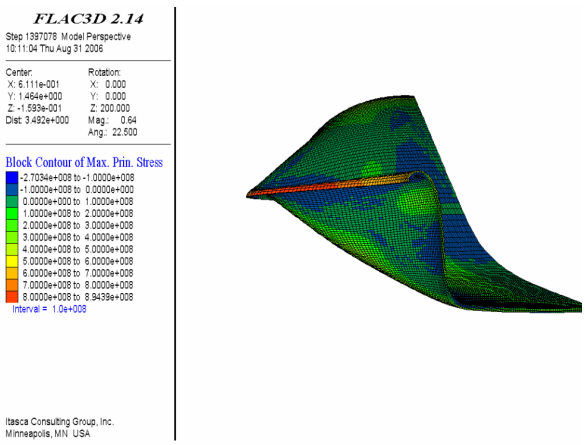

b) Stress (Pa), View 1

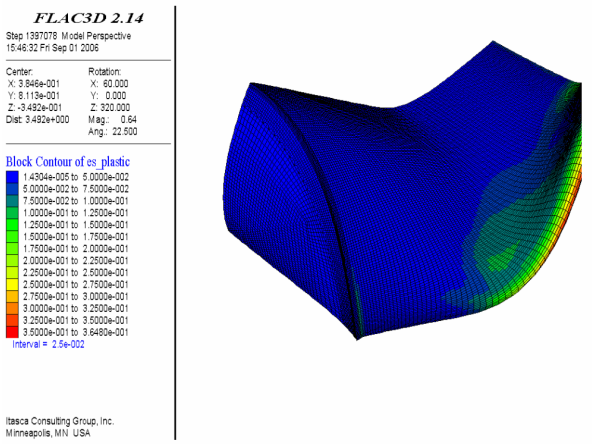

c) Strain, View 2

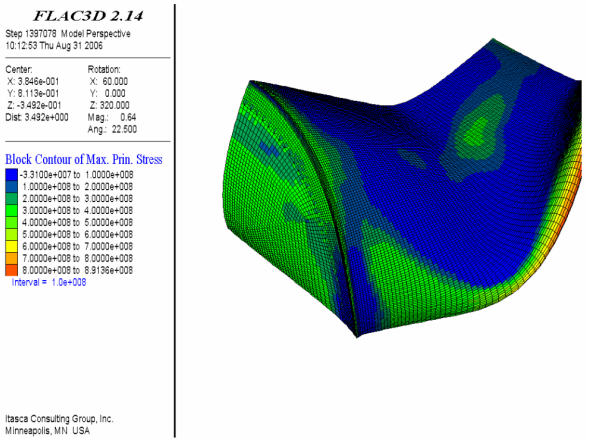

d) Stress (Pa), View 2

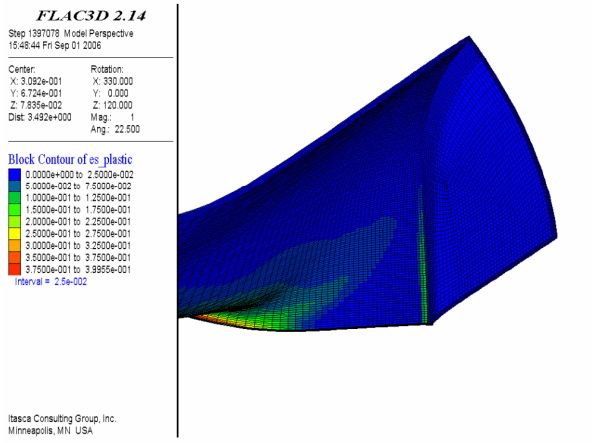

e) Strain, View 3

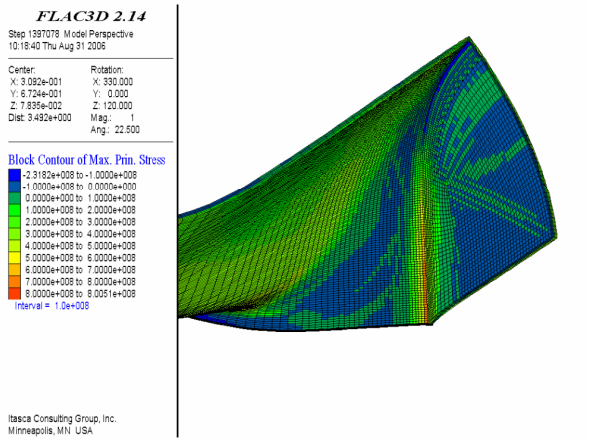

f) Stress (Pa), View 3

Output DTN: MO07043DWPFAIL.000, file *3D/18mm/wp3dstate2.pcx.*

NOTE: Strains greater than 0.20 are not contoured. The maximum strain exceeds 1.10.

Figure D-3. Different Views of Strain and Stress Due to Uniformly Distributed Load in a Three-Dimensional Representation of the Waste Package: State 2 During Collapse

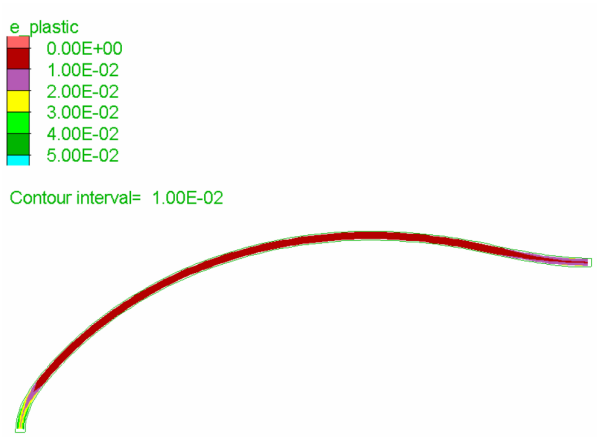

a) Strain, View 1

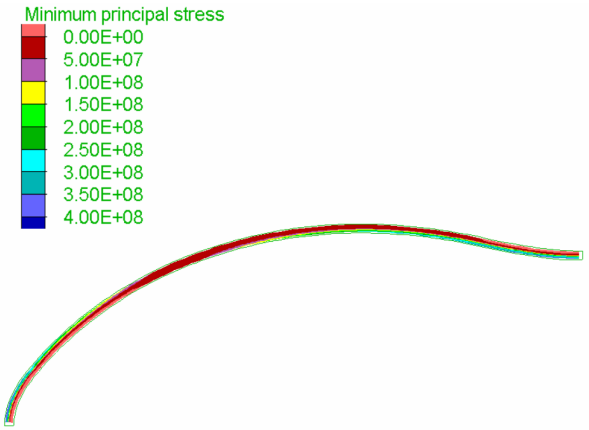

b) Stress (Pa), View 1

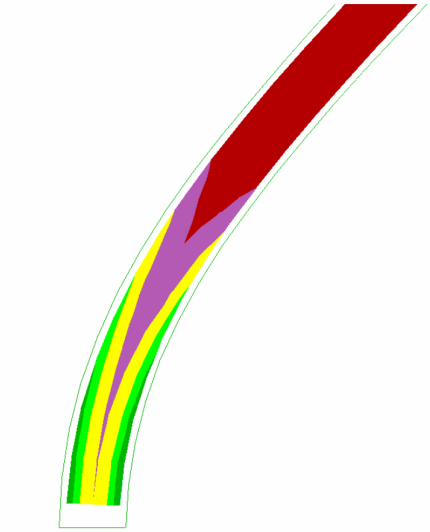

c) Strain, View 2

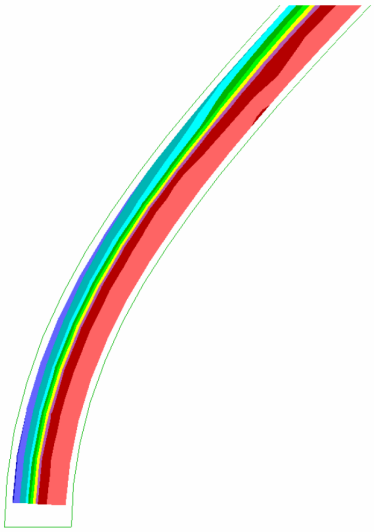

d) Stress (Pa), View 2

Output DTN: MO07043DWPFAIL.000, file *\2D\18mm\wp2Dstate1.pcx*.

Figure D-4. Different Views of Strain and Stress Contours Due to Uniformly Distributed Load in a Two-Dimensional Representation of the Waste Package: State 1 During Collapse

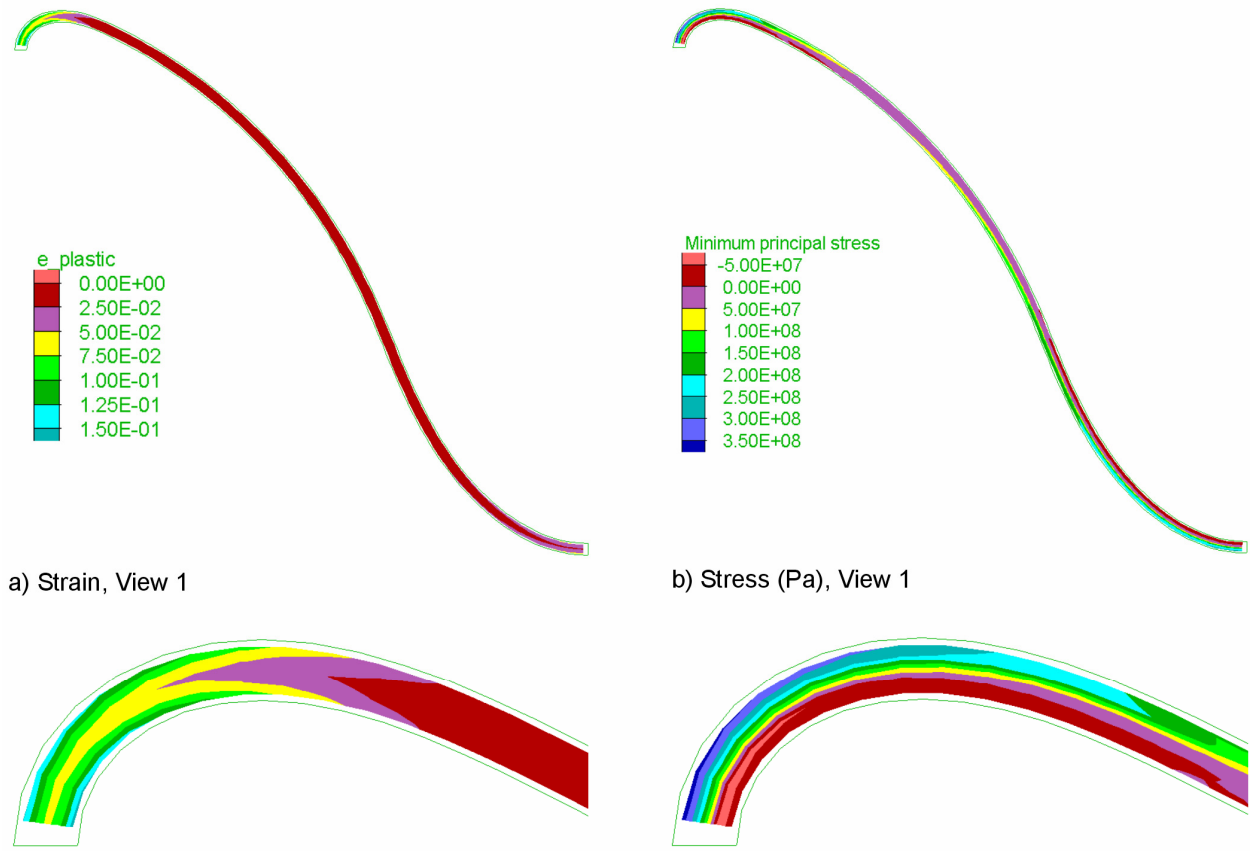

a) Strain, View 1

b) Stress (Pa), View 1

c) Strain, View 2

d) Stress (Pa), View 2

Output DTN: MO07043DWPFAIL.000, file *\2D\18mm\wp2Dstate2.pcx*.

Figure D-5. Different Views of Strain and Stress Contours due to Uniformly Distributed Load in a Two-Dimensional Representation of the Waste Package: State 2 During Collapse

INTENTIONALLY LEFT BLANK

APPENDIX E
INDEPENDENT REVIEW FOR MODEL VALIDATION BY MICHAEL F. HESSHEIMER

APPENDIX E – INDEPENDENT REVIEW FOR MODEL VALIDATION BY MICHAEL F. HESSHEIMER

This review is based on the Reviewer Back Check Copy of the report, dated May, 2007. As of this version, the report is substantially complete. The review was performed by Michael F. Hessheimer, P.E., Sandia National Laboratories.

The analyses described in this report determine how, along with the abstraction of the results, the performance of the Engineered Barrier System will be incorporated into the TSPA-LA model to demonstrate compliance of the repository with the regulatory requirements, accounting for uncertainties in the simulations of performance. Each of the Independent Review Criteria for the *Mechanical Assessment of Degraded Waste Packages and Drip Shields Subject to Vibratory Ground Motion*, specified in the associated TWP (SNL 2007 [DIRS 179869]), is addressed below.

- "*Are the damage models and associated numerical calculations reasonable and appropriate for their intended use? (Is the computational model and its numerical results reasonable and appropriate for its intended use?)*

Conclusion:

Paraphrasing this criteria in terms which are specific to the scope and purpose of this AMR: Do the discrete drift configurations considered in this modeling and analysis effort ensure that the resulting post-seismic event damage states provide a basis to develop damage abstractions which, when interpolated or extrapolated, envelope (or at least provide a 'reasonable' approximation of) the damage surface which represents all possible drift configurations which could occur over the life of the repository?

It is clear to this reviewer, that the work documented in this report represents a conscientious and exhaustive effort to understand and characterize the condition of the waste package and other EBS components prior and subsequent to multiple seismic events. **With consideration to the factors discussed below, it is the opinion of this reviewer, that the estimates of waste package performance documented in this report are reasonable for the TSPA in support of the License Application.**

Additional Considerations:

During the life of the repository, seismic events defined by the seismic hazard curve, can occur at any time with varying levels of probability. At the same time, natural processes and the environment within the repository will result in degradation of the engineered barrier system even without abnormal demands. The condition of the waste packages at the time of a seismic event is, therefore, a complex spectrum of possible states. Because of the complexity and cost of determining the seismic response of the waste package and surrounding elements of the EBS, a small number of discrete states of degradation were considered, assuming that these states can be used to bound the other possible states which might exist.

Obviously, these discrete states represent a simplification of the spectrum of possible states, ranging from a completely intact Outer Corrosion Barrier to a completely corroded OCB and various states of degradation of the internals or external EBS components. For example, the effects of partially degraded internals or a partially degraded pallet with 'sharp' edges, were not considered. The discrete states analyzed were selected, primarily, on the engineering judgment of the team performing the analysis. Only a limited discussion was presented in this report to justify why the combination of states considered envelopes all of the potential states of the waste packages and other engineered barriers. The assumptions regarding the discrete states considered pose one of the first areas where the requirement of providing reasonable assurance of the repository performance may be challenged.

Underpinning the assumptions of the degraded EBS states considered in evaluating damage to seismic events, further assumptions or modeling simplifications are made in evaluating the response of the degraded waste package, drip shield and drift. Throughout the detailed damage calculations and the abstractions (discussed in the Seismic Consequence Abstraction AMR), assumptions and uncertainties in the parameters used in the analyses are justified by claims that many of the assumptions are conservative, and these conservative assumptions compensate for the lack of knowledge of other conditions or model parameters.

> ***Report Author's Explanatory Note:*** *This approach is grounded in the* Yucca Mountain Review Plan, Final Report *(NRC 2003 [DIRS 163274], Section 2.2.1), which states:*
>
> "In many regulatory applications, a conservative approach can be used to decrease the need to collect additional information or to justify a simplified modeling approach. Conservative estimates for the dose to the reasonably maximally exposed individual may be used to demonstrate that the proposed repository meets U.S. Nuclear Regulatory Commission regulations and provides adequate protection of public health and safety. …The total system performance assessment is a complex analysis with many parameters, and the U.S. Department of Energy may use conservative assumptions to simplify its approaches and data collection needs. However, a technical basis … must be provided."

Considering all of this, the challenge for this reviewer is to determine if the approach used in developing the detailed process models and the subsequent abstractions of these process models for input into the TSPA supports the objective of providing a ***reasonable expectation*** of the repository's ability to meet regulatory requirements.

> ***Report Author's Explanatory Note:*** *Reasonable assurance or "Reasonable Expectation" is defined by the NRC in 10 CFR 63.304 [DIRS 180319].*

There is no way of explicitly ensuring that all possible states have been considered, and in fact, it is likely that some conditions which were not considered could result in earlier or more extensive releases. It is also likely that these 'worst case' conditions represent lower probability conditions than the more general conditions considered in this report. Even if the scope of this effort were expanded to consider a broader set of conditions, it would still not be possible to explicitly demonstrate that these would envelope all possible damage states. In the extreme, the only way to ensure this would be to completely disregard the presence of the EBS in evaluating repository performance. Since it has also already been acknowledged

that the integrity of the waste packages is important to the performance of the repository, this extreme assumption is not realistic, nor is it appropriate.

- *For given inputs, are the outputs of the damage model reasonable?*

Conclusion:

The analyses documented in this report represent a comprehensive suite of non-linear dynamic finite element analyses of the engineered barrier system (EBS), comprised of the TAD and Co-Disposal waste packages, emplacement pallets/invert, Drip Shield, and discrete element analyses of drift collapse subjected to a suite of seismic ground motions which represent the full range of intensities anticipated for the repository. As noted above, these calculations were performed for a few discrete states, but given these states **the outputs of the damage models, in terms of excessive residual stress or rupture of the waste package OCB are, in the opinion of this reviewer, reasonable and conservative**.

Some of the conclusions of the report are self evident (i.e. higher levels of ground motion result in higher levels of damage to the EBS components) while others are not as convincing. The conclusion that rupture occurs only under the most extreme combination of corrosion and ground motion may be correct but it also suggests to this reviewer that there may be configurations of the EBS and conditions that have not been considered.

Additional Considerations:

Despite the availability and utilization of state-of-the-art computational resources, direct evaluation of the response of multiple deformable EBS components to the full suite of ground motions prescribed for the TSPA is not feasible. Subsequently, a two step approach was used. The first step utilizes simplified representations of the Waste Package and Pallet to calculate the kinematic response (or more precisely, rigid body dynamic response) in terms of the impact velocity between the EBS components. In the second step, more highly refined models of individual Waste Packages are subjected to a variety of single impacts at a range of velocities to determine the resulting response. The results of these two steps are combined to determine the potential for direct breach of the waste package and, if rupture does not occur, the extent of damage to the OCB, in terms of residual plastic stress. The total damaged area, i.e. the area where residual surface stress exceeds a threshold value, for each seismic event is then used in the TSPA model (via the Seismic Consequence abstractions) to determine the total surface area susceptible to stress corrosion cracking and subsequent advective flow of moisture through the waste package and release of radionuclides to the environment.

There are a number of assumptions in both steps of these calculations and in the manner in which the results are combined, which suggest that this approach will ultimately result in an over-estimate of radionuclide release.

Nevertheless, some questions remain regarding the 'accuracy' or realism inherent in the two step approach to determine the amount of damage to the surface area of the OCB. One of particular concern to this reviewer is the fact the affect of previous damage, occurring either earlier in a seismic event or in a previous seismic event, is not adequately accounted for, either in the effect on the subsequent dynamic response or by the accumulation of damage at a discrete location, i.e. by multiple impacts at the same location. This is more of a concern for rupture of the OCB where plastic strains may accumulate to exceed the ultimate strain limit, rather than for stress corrosion cracking which is reported to depend only on residual stress levels.

Report Author's Response: *The accumulation of damage on waste packages is considered for both damaged areas and rupture, both during a single seismic event and multiple seismic events. During a single seismic event, damaged areas are accumulated from multiple impacts (see Section 6.3.3.1). These damaged areas are also accumulated for multiple seismic events in* Seismic Consequence Abstraction *(SNL 2007 [DIRS 176828]) and TSPA. Probabilities for rupture of the waste package are based on multiple impacts during a single seismic event (see Section 6.3.3.2) and are also considered in* Seismic Consequence Abstraction *(SNL 2007 [DIRS 176828]) and TSPA for multiple seismic events. The total damage from multiple seismic events is defined as the sum of the damage from the individual seismic events. This approach most likely conservatively overestimates the damaged areas.*

An effort was made to address this question by subjecting the detailed representation of the waste package to one of the suite of ground motions. Unfortunately, the seismic realization chosen for this comparison was one which resulted in zero or negligible damage in both the two step and direct analysis. While these results are encouraging, this does not necessarily demonstrate the equivalence of these methods or the conservatism of the two-step method for more severe ground motions.

Report Author's Response: *Tables 7-1 and 7-2 in Section 7.3.1.1.2 list the three realizations and two PGV levels used for comparison between the two-step kinematic analysis approach and detailed single waste package analyses. These realizations were selected because they had the largest predicted damaged areas for the two-step kinematic analyses where the waste package was free of any impacts with the drip shield or other waste packages. Tables 7-3 and 7-4 show that there are substantial damaged areas predicted by the two-step kinematic analyses and smaller damaged areas predicted by the detailed single waste package analyses, ranging from zero or negligible to a factor of 3 less than damaged areas predicted by the two-step approach.*

The damage from the single waste package calculations is expected to be less than from the two-step kinematic approach because the finite element mesh for the rigid body dynamics is necessarily limited, resulting in a higher number of impacts due to the coarse discretization. This difference is expected to be greatest at small PGV levels and to decrease at higher PGV levels. This effect has not been quantified at higher PGV levels, as noted by the reviewer, but is a reasonable extrapolation from the results to date.

The models used to develop the damage states for input into TSPA, described in Section 6, are 'validated' by comparison with models with different levels of fidelity (at least in terms of the geometric representation and mesh refinement) or which were solved using a different computational program.

For the kinematic ground motion response calculations, the results from LS-DYNA compared favorably with similar calculations performed in UDEC. While the details of the UDEC calculations are not provided, presumably the same input and/or assumptions for the geometry, material properties, boundary conditions and loading were made in both simulations. The favorable comparison of the results, therefore, is more of a validation of the correct (or at least consistent) implementation of the numerical time integration routine in each code, but does not necessarily validate how accurately (or at least conservatively) the model simulates the behavior of the actual waste packages in the repository. This is not to imply that this is not a worthwhile exercise, but it does intend to convey the limitations to this method of validation.

Report Author's Response: *LS-DYNA is a finite-element computer program and UDEC is a distinct element computer program. The comparison of kinematic response to ground motion input is more than an exercise and much more than a validation of the correct implementation of the numerical time integration routine in each code. These codes have fundamentally different algorithms for determining the elemental response and contact between components. Free of experiments to compare with, one of the most valuable methods of validation of a model is to compare the results from two fundamentally different approaches. The "favorable" comparison presented in Section 7.3.1.1.1 provided the authors with confidence that the kinematics of the waste package response to ground motion input was reasonably captured in the LS-DYNA analyses. Note that comparison of results from alternate computer codes is common practice in industry, accepted by the Project as a method of model validation, and is used in concert with additional validation methods.*

Realistically, validation for the ability to simulate prototypical response can only be made against empirical data, which is not available at this time.

The UDEC calculations for the waste package surrounded by rubble are 'validated' by demonstrating the ability of UDEC to simulate the response of the thin-walled tunnel liner to blast induced ground motions in a fractured rock mass. Test data from experiments conducted by DNA, shows the UDEC calculations are capable of reproducing the test results with reasonable accuracy and compares well with other simulation models. Note that these post-dictions benefit from a careful characterization of the initial conditions.

The results of FLAC3D simulations of the drip shield response to rockfall loads are compared to similar simulations performed in LS-DYNA. As with the comparison of the kinematic simulations in LS-DYNA with UDEC, this is also primarily a confirmation of the numerical algorithms used in the code to solve the static and dynamic equilibrium equations. The same cautions mentioned previously apply here as well.

Report Author's Response: *The comparison of FLAC3D simulations with LS-DYNA*

methods. FLAC3D and LS-DYNA are similar in that they are both finite element analysis programs. However, the way each program handles material characterization, application of boundary conditions and loads, and numerical time integration is unique to each program and may differ substantially from one program to another. Comparing the results from these codes is a strong method of validation of the models. Note that both programs are individually qualified for their intended use by the quality assurance process of the Project.

- *Are the limitations of the damage models adequately described?"*

Conclusion:

It is the opinion of this reviewer that the limitations of the damage models are adequately described, subject to the comments noted above.

APPENDIX F
SUMMARY OF ACCELERATIONS OF WASTE PACKAGE INTERNALS DUE TO IMPACTS AND MAXIMUM VELOCITIES OF IMPACT

APPENDIX F – SUMMARY OF ACCELERATIONS OF WASTE PACKAGE INTERNALS DUE TO IMPACTS AND MAXIMUM VELOCITIES OF IMPACT

This appendix provides a summary of the waste package accelerations determined by waste package-to-waste package detailed impact analyses and waste package-to-pallet detailed impact analyses with intact internals and a 23-mm-thick OCB (Section 6.3.2.2). Also included in this appendix is a summary of the maximum waste package-to-waste package impact velocities from the kinematic impact analyses (Section 6.3.2.1). This information is provided as an input to *Seismic Consequence Abstraction* (SNL 2007 [DIRS 176828], Appendix A) which is a cladding damage abstraction to support sensitivity studies for the license application.

Tables F-1 and F-2 list peak accelerations of waste package internals as determined by waste package-to-waste package detailed impact analyses with intact internals and a 23-mm-thick OCB. Tables F-3 and F-4 list peak accelerations of waste package internals as determined by waste package-to-pallet detailed impact analyses with intact internals and a 23-mm-thick OCB. Table F-5 lists the maximum codisposal waste package-to-TAD-bearing waste package impact velocities from the kinematic analyses.

Table F-1. Peak Acceleration (g) of TAD-Bearing Waste Package Internals Determined by Waste Package-to-Waste Package Detailed Impact Analyses

Impact Velocity (m/s)	Waste Package	Location				
		−0.30	−0.15	0.00	0.15	0.30
2.00	WP1	25.8	26.7	16.4	23.8	30.2
	WP2	25.1	23.7	13.6	18.5	25.2
4.00	WP1	47.7	48.7	49.7	49.5	48.7
	WP2	36.0	41.8	44.2	43.1	41.9
6.00	WP1	52.3	59.1	61.5	61.4	52.0
	WP2	42.5	50.9	57.4	51.0	43.1
9.00	WP1	66.6	64.9	72.0	69.1	64.2
	WP2	56.2	67.8	64.6	55.2	58.5

Output DTN: LL0706MG004SPC.001, file *Catalog_analyses_accel.xls,* sheet NavalLongTAD WPWP.
NOTE: WP = waste package.

Table F-2. Peak Acceleration (g) of Codisposal and TAD-Bearing Waste Package Internals Determined by Waste Package-to-Waste Package Detailed Impact Analyses

Impact Velocity (m/s)	Waste Package	Location				
		−0.30	−0.15	0.00	0.15	0.30
2.00	WP1 (CDSP)	14.1	7.8	6.6	8.0	8.3
	WP2 (TAD-bearing)	25.0	24.9	11.5	16.0	22.7
4.00	WP1 (CDSP)	23.6	75.0	32.8	56.0	35.5
	WP2 (TAD-bearing)	40.4	41.9	30.1	39.6	43.5
6.00	WP1 (CDSP)	88.4	107.7	101.9	110.9	90.7
	WP2 (TAD-bearing)	50.2	75.4	70.0	66.4	56.0
9.00	WP1 (CDSP)	145.3	146.7	163.8	162.9	149.3
	WP2 (TAD-bearing)	72.5	79.5	86.3	88.4	71.3
10.00	WP1 (CDSP)	151.3	156.0	174.9	173.8	167.9
	WP2 (TAD-bearing)	76.3	77.1	85.3	88.5	87.9

Output DTN: LL0706MG004SPC.001, file *Catalog_analyses_accel.xls,* sheet CDSP WPWP.

NOTE: CDSP = codisposal; TAD = transportation, aging, and disposal (canister); WP = waste package.

Table F-3. Peak Acceleration (g) of TAD-Bearing Waste Package Internals Determined by Waste Package-to-Pallet Detailed Impact Analyses

Impact Velocity (m/s)	Angle	Location		
		1/8	1/4	1/2
7.00	+0.25 degrees	22.5	29.0	33.0
	+6 degrees	23.5	25.6	28.5
10.00	+0.25 degrees	31.4	33.9	40.5
	+6 degrees	30.6	27.4	37.9

Output DTN: LL0706MG004SPC.001, file *Catalog_analyses_accel.xls,* sheet NavalLongTAD WPP.

Table F-4. Peak Acceleration (g) of Codisposal Waste Package Internals Determined by Waste Package-to-Pallet Detailed Impact Analyses

Impact Velocity (m/s)	Angle	Location				
		1/8	1/4	1/2	3/4	7/8
7.00	+/−0.25 degrees	38.8	38.5	37.5	35.1	34.8
	+/−6 degrees	31.9	31.8	30.4	29.3	28.3
10.00	+/−0.25 degrees	41.5	41.1	43.1	37.5	36.1
	+/−6 degrees	35.4	39.7	38.6	36.9	31.3

Output DTN: LL0706MG004SPC.001, file *Catalog_analyses_accel.xls,* sheet CDSP WPP.

Table F-5. Maximum Impact Velocity (m/s) Between a Codisposal Waste Package and a TAD-Bearing Waste Package in the Kinematic Analyses

Realization	Ground Motion Level			
	0.40 m/s PGV	1.05 m/s PGV	2.44 m/s PGV	4.07 m/s PGV
1	–	–	0.629	1.937
2	–	0.455	1.096	1.729
3	–	2.148	1.840	3.697
4	–	0.848	2.169	4.324
5	–	0.245	1.727	3.487
6	–	–	3.915	5.587
7	–	0.120	1.544	2.354
8	–	0.309	2.234	1.963
9	–	–	0.325	1.199
10	0.394	2.013	2.595	9.637
11	–	0.864	4.165	2.835
12	–	–	1.279	4.013
13	–	0.489	1.208	3.568
14	–	0.564	1.881	3.917
15	–	0.246	2.275	4.203
16	–	–	1.081	1.603
17	–	–	2.061	3.187

Output DTN: LL0706MG004SPC.001, file *Catalog_analyses_accel.xls,* sheet "Max Vel CDSP-NavalLong TAD."

NOTES: Realizations that had zero impacts between a codisposal waste package and a TAD-bearing waste package are indicated with an en dash (–).

PGV = peak ground velocity.

INTENTIONALLY LEFT BLANK